Modelling and investigation of microstructural evolution during solidification and sintering with the phase-field method

Zur Erlangung des akademischen Grades eines

Doktors der Ingenieurwissenschaften

von der KIT-Fakultät für Maschinenbau des
Karlsruher Instituts für Technologie (KIT)

genehmigte

DISSERTATION

von

M.Sc. Marco Seiz

Tag der mündlichen Prüfung:	17.11.2023
Hauptreferent:	Prof. Dr. Britta Nestler
Korreferent:	Prof. Dr. Wolfgang Rheinheimer

Kurzfassung

Die Eigenschaften eines Materials setzen sich zusammen aus seinem thermodynamischen Zustand (Temperatur, Druck, chemische Zusammensetzung, ...) sowie seiner Mikrostruktur. Die Mikrostruktur wiederum hängt stark von der Prozessgeschichte eines Materials ab, wodurch die Optimierung des Herstellungsprozesses eine wichtige Rolle einnimmt. Experimente stellen den klassischen Weg dar, den Prozess zu untersuchen, sind aber sowohl zeit- wie auch kostenaufwendig. Eine andere Möglichkeit den Prozess zu optimieren, ist es diesen per Simulation nachzubilden, um damit mit simplen Parametervariationen die Einflüsse der Variationen zu ermitteln. Weiterhin lassen sich, je nach Simulationsmethode, damit auch wesentlich detaillierte Informationen über die spatiotemporale Entwicklung der Mikrostruktur erlangen als in Experimenten. In dieser Arbeit wird die Phasenfeldmethode benutzt, die ebendiese sogenannten 4D-Informationen (3 Raumachsen + 1 Zeitachse) direkt bereitstellt. Ziel der Arbeit ist es, verschiedene Prozesse unter neuen Aspektpunkten zu betrachten und damit weitere Möglichkeiten zur Prozessoptimierung aufzuzeigen.

Abstract

The properties of a material depend both on its thermodynamic state (temperature, pressure, chemical composition, ...) as well as its microstructure. In turn, the microstructure is heavily dependent on the processing history of the material in question and thus the optimization of the processing route is important. The classical way of investigate the process is to conduct experiments, but these tend to be expensive in terms of both time and cost. Another way of optimization is to reproduce the process with simulations, which allows the variation of individual parameters and thus the determination of their influence. Furthermore, depending on the simulation method, one can gain even more detailed information about the spatiotemporal evolution of the microstructure. Within this work the phase-field method is used, which directly allows the observation of this so-called 4D information (3 spatial + 1 time axis). The goal of this work is to investigate different process under new conditions in order to develop new avenues for process optimization.

Contents

Acronyms and symbols

Acronyms

PF	phase-field
MD	molecular dynamics
GB	grain boundary
MPI	Message Passing Interface
RBM	rigid-body motion
COM	center of mass
HLRS	Höchstleistungsrechenzentrum Stuttgart
KIT	Karlsruher Institute for Technology
LGK	Lipton-Glicksman-Kurz
MSC	marginal stability criterion
MST	microscopic solvability theory
FTA	frozen temperature approximation
ODE	ordinary differential equation
PDE	partial differential equation
CALPHAD	calculation of phase diagrams
IAPWS	International Association for the Properties of Water and Steam
STGB	symmetrical tilt grain boundary
NVE	ensemble of constant particle count, volume and internal energy
NPT	ensemble of constant particle count, pressure and temperature

GBA	grain boundary area
GCS	grain cross section
ADV	advective model

Constants

π	Pi: 3.141 59...
N_a	Avogadro's constant: $6.022\,140\,76 \times 10^{23}\,\mathrm{mol}^{-1}$

Latin symbols and variables

A	area; anisotropy function
e	strain
l	length
$\mathcal{F}$	free energy functional
a	gradient energy density
w	potential energy density
f	bulk energy density
h	weighting function
W	phase-field interface width
D	diffusivity
G	grain size, temperature gradient
c	concentration
M	chemical mobility, grain mobility
D	diffusivity
T	temperature
ΔT	temperature difference, undercooling; solidification interval

n	normal vector, count of atoms/vacancies, exponent
l_d	diffusion length
d_0	capillary length
R	tip radius, particle radius, radius of curvature
v	velocity, pulling velocity
m	phase boundary slope, exponent
k	partition coefficient
p	pressure
V	volume
N	particle amount; number of phase-fields
K	number of species
U	inner energy
H	enthalpy; grain boundary length
S	entropy; surface area
G	Gibbs free energy
g	molar Gibbs free energy; genus; grain boundary identification function
t_r	relaxation time
X	neck radius
$\frac{X}{R}$	relative neck radius
V_m	molar volume
c_p	heat capacity
L	latent heat
x	coordinate; mole fraction
Pe	Péclet number
Z	exponent

z	coordination number
P	porosity; period
F	force
j	flux density
N_c	coordination number; number of neighbours
q	generalized gradient vector
Y_{lm}	spherical harmonic function
u	displacement

Greek symbols and variables

ϕ	phase-field vector
η	phase-field vector
ϕ_α	the αth component of ϕ; the α phase
ϵ	interface width parameter; strain
γ	interface energy
τ	phase-field relaxational coefficient
μ	chemical potential; mean of a normal distribution
δ_i	physical interface width
δ	anisotropy strength
λ	wavelength
Λ	lagrange multiplier
Γ	Gibbs-Thomson coefficient
κ	effective stiffness
Ψ	grand potential
ψ	grand potential density; dihedral angle

σ	interface energy; stress; standard deviation
σ^*	marginal stability constant
Ω	atomic volume
ρ	relative density
κ	curvature; effective stiffness
χ	Euler characteristic
$\frac{\partial c}{\partial \mu}$	thermodynamic factor; generalized susceptibility

Operators and math symbols

∇	gradient, del operator
$\nabla\cdot$	divergence

1 Introduction

Materials processing has long been at the forefront of human culture. From early examples of pottery allowing for durable storage vessels, over the eponymous copper and iron ages and straight into the industrial revolution, for which the large scale production of steel was essential, major steps in cultural evolution were always accompanied by advances in materials. The present "silicon age" would not even have been possibly without a deep understanding of the underlying materials. However, for the vast majority of human cultural evolution the reasons behind the properties of materials were shrouded in mystery. While various manuals in the tradition of alchemy gave recipes for how to produce "good" materials [1], they never delved into why these recipes would improve a material. For example, a steel can be hardened by rapidly reducing its temperature from a sufficiently high starting temperature — what is nowadays called quenching. While this principle was already known to Homer (taken from [2])

> As when a man who works as a blacksmith plunges a
> screaming great axe blade or adze into cold water, treating
> it for temper, since this is the way steel is made strong, even
> so Cyclops' eye sizzled about the beam of the olive....
> Odyssey 9389–9394, translation by R. Lattimore

and other authors[1, 3], the reason for the hardening — martensitic transformation — was not identified until much later. Without knowing the reason for how and why the steel hardens, variations in how rapidly to cool the steel, or whether to cool by plunging it into water or oil or even sand, could only be done blindly and hoping for the best. Or to put it more succinctly in the words of Kurt Lewin:

> There is nothing more practical than a good theory.

This theoretical gap was plugged to a large extent during the 19th and 20th century and continues to be filled to this very day. In essence, the materials properties depend on two main factors: First, its chemical composition and other state variables such as temperature and pressure. This being quite obvious, since water freezes below 0 °C which radically changes its properties via phase transition. But even before a phase transition,

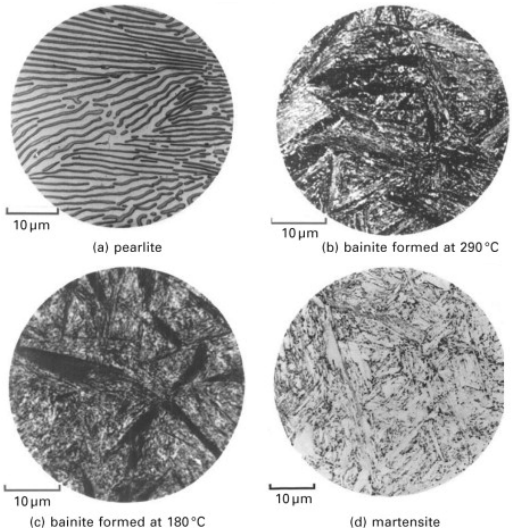

Figure 1.1: Various microstructures observed in steels. Pearlite forms during "slow" cooling, whereas with sufficiently high cooling rate and starting temperature, bainite and martensite can form. Reprinted from [4] with permission from Elsevier.

the everyday property of density already depends on these state variables. Second, if one is concerned about a material with some kind of spatial ordering (generally solids), then the microstructure plays a significant role. The microstructure can be roughly defined as the spatial arrangement and distribution of a material and its defects. Going back to the steel example, a steel cooled down "normally" would exhibit a so-called eutectoid structure formed of ferrite (Fe) and cementite (Fe_3C), plus some excess ferrite or cementite depending on the actual composition. Depending on the processing conditions and the chemical composition, the eutectoid structure can form in either an array of lamellas or in a matrix-fiber geometry, but it usually forms in a lamellar manner called pearlite. If the same steel is cooled down rapidly, instead of the lamellar pearlite, one will find so-called bainite or martensite, depending on how rapidly it was cooled.. These microstructures are depicted in fig. 1.1 and already show quite different geometries. But what is even more relevant than the geometry are the properties of these individual regions, with martensite being far harder than pearlite. The reason for this being that during the transformation to martensite an extremely high number of lattice defects called dislocations are produced. These defects are the origin of plastic deformation, but inhibit each other's motion as well — hence martensite is hard and brittle.

The observant reader will already be tired of the constant mention of "depending on", but understanding how processing conditions influence the microstructure is of great interest

as should be clear from the above. Due to the interdependence of the materials properties and the microstructure, microstructural prediction has garnered much attention over the past century. Early examples of such predictions are the works on dendritic solidification[5–9] and sintering [10–14]. In the case of dendritic solidification, state of the art analytical theories allow the accurate prediction of dendritic operating state [15–17], but are often limited to the prediction of isolate dendrites. For densification during sintering, the earliest models are based on a geometric description of two particles, describing the early stage of sintering. These basically link the diffusive flux of vacancies into the grain boundary to an approach-of-centers of the two particles. Assuming that this describes a unit cell of sintering and extending it to green bodies however was quite unsuccessful, which is why different models of sintering for the so-called intermediate and final stages were developed. While these did qualitatively match experimental observations, their quantitative predictions based on first principles are often wrong, see e.g. [18]. This can be circumvented by employing experiments to determine "true" factors within the theory and allow accurate prediction[19]. However, this approach is limited in that it usually is specific to one combination of material and process, with small changes in e.g. powders characteristics possibly causing large changes in the resulting microstructure[20]. Hence the experimental determination of these factors can become quite expensive in both time and money.

Thus while analytical theory gives valuable clues and serves as an excellent starting point for any investigation, more detailed models are necessary to fully account for nature itself. Simulations bridge the gap between analytical theory and experiments, allowing for the digital re-construction of experiments or even the design of virtual experiments not feasible or possible in nature. One of the most prominent simulation methods for microstructural evolution is the phase-field method, which is employed in this work. It has been shown to be able to model dendritic growth[21–24], eutectic growth [25–28], grain growth[29–32] and sintering [33–36]. Furthermore, dendritic growth via electrodeposition in batteries[37], magnetism's influence on the microstructure formation of magnetic materials[38] as well as the influence of stresses and strains including dislocations[39] can be modelled as well. The citations in previous sentences are by no means exhaustive and just show a small sample of the large amount of literature concerning the application of the phase-field method to microstructure evolution and materials processing.

The goal of the present work is to further the phase-field modelling of solidification and sintering. For solidification, two problems will be considered: First, the coupled growth of dendrites and eutectics, which requires nucleation in some form as well as appropriate processing parameters. Second, the process of freeze-casting, in which discrete, small particles arrange into much larger structures during solidification and thus presents a

challenge in bridging length scales. For sintering, a critical review of the literature models for solid-state sintering is undertaken. This led to novel model developments which eliminate several problems preventing quantitative sintering simulations.

This work is structured as follows: First, the analytical theories of microstructure development pertinent to the processes will be described. These form the basis of further investigation and validation. Next, the necessary phase-field models will be described fully. Some of these models are established literature models, with others having been developed by the author. Based on this groundwork, first the classical problem of alloy solidification will be investigated with the goal of elucidating the coupled growth of dendrites and eutectics. Next, the freeze-casting process will be modelled by employing techniques based on classical solidification, allowing for predictions of microstructural properties. Finally, the sintering process will be investigated by 4D simulations yielding predictions for densification and grain growth in representative volume elements as well as freeze-cast structures based on prior freeze-casting simulations.

2 Theoretical description of microstructural evolution

In this chapter, the processes which determine the microstructural evolution will be descibed for solidification and sintering. First, the fundamental thermodynamic basis will be described. Following this, analytical theories for predicting the microstructural evolution of solidification and sintering in geometrically simple systems will also be described, as these form the basis for numerical validation. The presentation is mostly based on [40] and [41] for thermodynamics, [42–44] for solidification, [45] for freeze-casting and [20, 46] for sintering. Where appropriate, references to prior experimental, theoretical and simulative work are added.

2.1 Thermodynamics and phase diagrams

Thermodynamics concerns itself with heat and work and how these interact with state functions such as energy. A state function is a function describing the state of a system in equilibrium and is independent of how the state was achieved. In contrast, the process quantities of e.g. heat and work depend on the path taken. The system described by these quantities is a mathematical abstraction of a subset of the physical world and is equipped with boundary conditions which define its interaction with the rest of the physical world.
The state functions describing the system are divided into intensive quantities (e.g. temperature), which do not change if a system is duplicated and brought into contact with itself, and extensive quantities which are affected by the previous test (e.g. volume). Extensive quantities have conjugate intensive quantities, which can be interpreted as the potential for change of that extensive property. A specific property akin to a density can be obtained from an extensive property by the division with another appropriate extensive property. This is usually done for materials properties, as e.g. the absolute heat capacity of a block of solid obviously scales with its size. However, the specific

heat capacity is independent of the size of the material in the thermodynamic limit and classifies a physical body of a certain material regardless of its size.

The equilibrium of a system can be calculated by employing equilibrium thermodynamics and hence demanding that the net driving force vanishes. The driving forces for change are differences in the intensive state variables called potentials, e.g. temperature or pressure. Multiplying such a driving force with its conjugate extensive variable yields the energy exchange between the system and its surroundings. Once this exchange is zero, thermodynamic equilibrium is reached. The sum of all such exchanges also represents the change in a thermodynamic potential such as the Gibbs free energy. Which thermodynamic potential to use depends on which quantities are being held constant at the boundary of the system. For constant pressure and temperature, the Gibbs free energy is the potential of choice, since at these conditions the Gibbs free energy is minimized for a single phase single component system.

As a concrete example of equilibrium thermodynamics, the conditions for equilibrium in unary and multicomponent systems of two phases will be derived in the following. This also lays the foundation for calculating phase diagrams which will be repeatedly used in this work.
Consider first the total Gibbs free energy of a single component (unary) system:

$$G = U + Vp - ST \tag{2.1}$$
$$= H - ST \tag{2.2}$$

with the internal energy U, pressure p, volume V, temperature T, entropy S and enthalpy H. The Gibbs free energy's variation reads

$$dG = Vdp - SdT \tag{2.3}$$

and in equilibrium this variation must vanish. From this, pressure p and temperature T are identified as driving forces, with the extensive state functions of volume V and entropy S serving as conjugate extensive functions for these driving forces. Hence in equilibrium, all pressure differences dp and temperature differences dT must vanish; these differences would be associated with corresponding extensive changes of volume and entropy. Furthermore, since an exchange of atoms can happen between the two phases, this net flux must also vanish, as otherwise phase transformation would be ongoing. In

order for this flux to vanish, the chemical potential μ in both phases must also be equal. It is defined by

$$\mu = \frac{\partial G}{\partial N} \tag{2.4}$$

with the number of moles N. Note that all variables except the one being differentiated by are held constant during partial differentiation, with this being omitted for conciseness in this work. In the case of an unary system μ is equal to the Gibbs free energy per mole $g = \frac{G}{N}$, also called molar Gibbs free energy. Hence the condition for the cessation of phase transformation can be written as

$$g_\alpha(p, T) = g_\beta(p, T) \tag{2.5}$$

for the two phases α and β.

In general, as long as a phase transformation is occurring, it will also induce changes in other state variables. Hence the phase transformation equilibrium must be achieved at the same time as pressure and temperature equilibrium, as otherwise another driving force would shift the equilibrium.

A similar train of thought can be used for K-component systems. The variation of Gibbs free energy then reads

$$dG = Vdp - SdT + \sum_i^K \mu_i dN_i \tag{2.6}$$

i.e. besides the pressure and temperature variations, the system also has energy changes associated with variations in mole content between the phases. Note that in this case one of the conjugate pairs is reversed: A change of the *extensive* variable of the number of moles is multiplied with the *intensive* chemical potential. The usual relationship can be recovered with a Legendre transform to the grand chemical potential:

$$\Psi = G - \sum_i^K \mu_i N_i \tag{2.7}$$

$$\rightarrow d\Psi = Vdp - SdT - \sum_i^K N_i d\mu_i \tag{2.8}$$

or equivalently for a density by dividing with the total number of moles N_{tot} within the system

$$d\psi = dg - \sum_{i}^{K} \frac{N_i}{N_{tot}} d\mu_i \tag{2.9}$$

$$d\psi = V_m dp - S_m dT - \sum_{i}^{K} x_i d\mu_i \tag{2.10}$$

with the molar volume V_m, the specific entropy S_m and the mole fraction x_i.

Since $\mu = g$ only holds for $K = 1$, the equilibrium of chemical potential between phases takes a different form: As every component i needs to be in equilibrium across the interface, there are K conditions

$$\mu_{i,\alpha} = \mu_{i,\beta} \tag{2.11}$$

which need to be fulfilled simultaneously. Suppose for a moment that this holds for a component j: This implies that in a diagram of plotting the molar Gibbs free energy g over component j, that a tangent with slope μ_j can be drawn between the two curves representing the Gibbs energy of phases α and β. This is graphically shown in fig. 2.1, together with the equivalent plot in the grand potential space. This tangent can be extended to both axes, at which $x_j \in \{0, 1\}$ and hence a system of either $K - 1$ or 1 components is obtained. The intercept for $x_j = 0$ is given by

$$g_\alpha = g_\alpha(x_{\alpha,j,eq}) - \mu_j x_{\alpha,j,eq} \tag{2.12}$$

which the observant reader will identify with the definition of the grand chemical potential eq. (2.7) for a single component. Since this intercept is the same for both phases, the equilibrium condition for a component j inducing phase transformation can also be written as

$$\psi_\alpha(p, T, \mu_j) = \psi_\beta(p, T, \mu_j) \tag{2.13}$$

as in the unary case, except ψ takes the role of g. This can be repeated for each component j, with the end result being that

$$\psi_\alpha(p, T, \mu) = \psi_\beta(p, T, \mu) \tag{2.14}$$

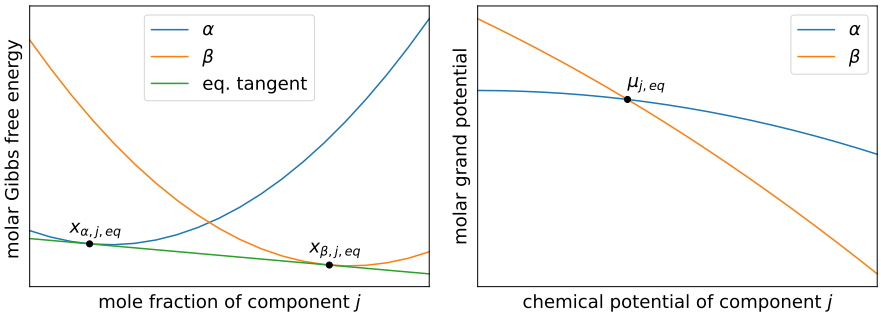

Figure 2.1: The molar Gibbs free energy and grand potential are plotted over their respective natural variables for component j. In the Gibbs energy space, the equilibrium is determined via the double tangent, whereas in the grand potential space an intersection determines the equilibrium.

must hold for a state described by homogeneous (p, T) as well as the chemical potential of each component being equal across both phases. In the binary two-phase case, this is the commonly cited double tangent rule: In the Gibbs energy space, it is tangent, since the chemical potential is equal, and double by virtue of the shared intercept, representing zero driving force for phase transformation. For any choice of (p, T), one can now evaluate eq. (2.14) to arrive at a point (p, T, μ) which describes equilibrium between the two phases, if it exists. However, commonly phase diagrams are not plotted over μ, but rather over the mole fraction x, atomic fraction or weight fraction, since these are independent of temperature whereas μ depends on temperature.

For simplicity, consider only two phases in a binary system at constant temperature T and neglect pressure for conciseness, then the equilibrium conditions can also be written as:

$$g_\alpha(x_\alpha, T) = g_\beta(x_\beta, T) + \mu_\beta(x_\beta, T)(x_\alpha - x_\beta) \tag{2.15}$$

$$\mu_\alpha(x_\alpha, T) = \mu_\beta(x_\beta, T). \tag{2.16}$$

Solving eqs. (2.15) and (2.16) yields the equilibrium phase mole fractions x_α, x_β. Based on these and the total composition x, the lever rule for the phase fractions is defined as

$$V_\alpha = \frac{x - x_\beta}{x_\alpha - x_\beta} \tag{2.17}$$

$$V_\beta = \frac{x_\alpha - x}{x_\alpha - x_\beta}. \tag{2.18}$$

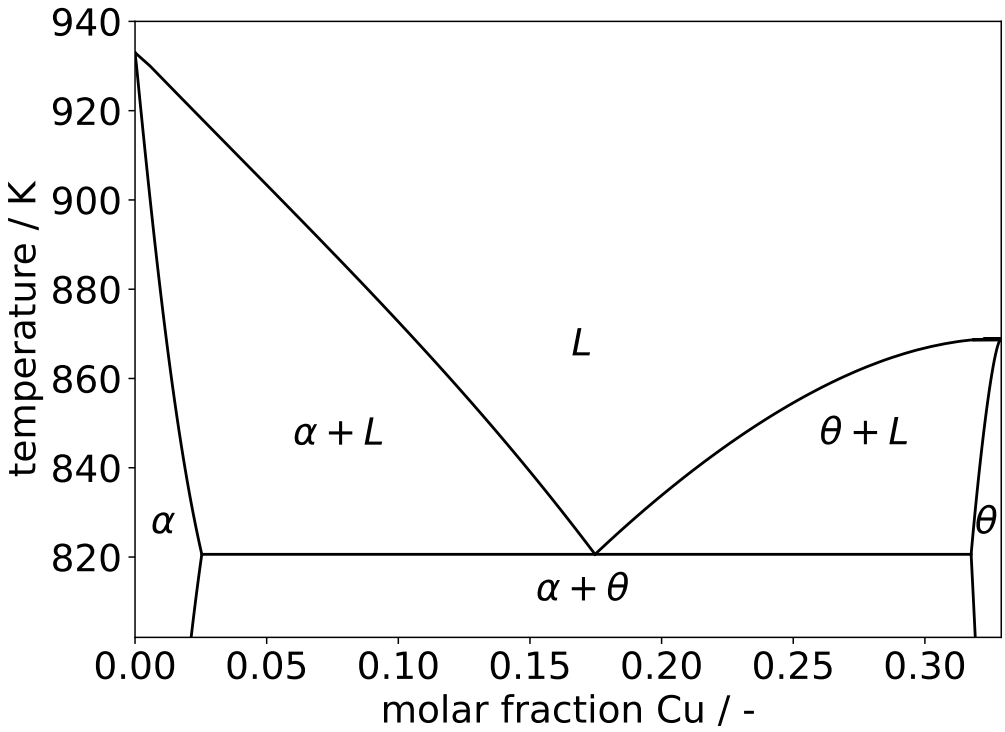

Figure 2.2: Phase diagram of the Al-rich region of the Al-Cu system, assuming that only the α-Al, the liquid L melt and the intermetallic $\theta - Al_2Cu$ phases exist. This primarily changes the phase diagram to the right of $\theta - Al_2Cu$, i.e. ignores the $L + \eta^{'} \rightarrow \theta$ peritectic found in the real system. If the alloy concentration is kept below ≈ 0.33 the peritectic does not occur in the first place and can be safely ignored.

The construction so far only accounted for up to two phases. If the system only has two stable phases, then eqs. (3.127) and (3.128) are sufficient to delineate single phase from two-phase regions for all (T, x) states. However, once more phases are added to the system, the global minimum across *all* these phases and phase mixtures must be found. This is commonly done in so-called CALculation of PHAse Diagrams (CALPHAD) [47, 48] programs. A result of such a calculation for the Al-Cu system is shown in fig. 2.2: The labels within each region identify the phases which are present, with the boundary curves representing the equilibrium concentration of these phases for each considered temperature. The transition between these regions identify reactions of phases transforming into each other. Furthermore, an invariant eutectic reaction identified by a horizontal line can be observed as well.
The slopes of these boundary curves are often employed in theoretical considerations,

especially the liquidus slope $m_{L\beta} = \frac{\partial T_{L\beta}(c)}{\partial c}$ describing the change of concentration within the liquid phase L in contact with a solid phase β. Furthermore, the partition coefficient $k_{L\beta} = \frac{x_\beta}{x_L}$ is also useful for describing whether a phase β tends to reject the species x represents or not. Assuming that x is the minority species, then $k < 1$ implies rejection of that species by the phase β. For dilute alloys in general, $m_{L\beta} < 0$ and $k_{L\beta} < 1$. The former is due to to an increase of entropy (lowering of Gibbs free energy) of the liquid phase due to the solute and the latter due to the solubility in a liquid phase generally being higher than in a solid.

2.2 Solidification

Solidification is one of the most important processing routes, as most metals being used today went through this process. A microstructure which can be obtained by solidification is shown in fig. 2.3 for an Al-Cu alloy, courtesy of Professor Amber Genau of the University of Alabama at Birmingham (UAB). Within the figure a coarse, grey structure is visible, which is an α-Al dendrite growing upwards. A finer, grey-white structure surrounds this dendrite which is a eutectic formed by the α-Al and $\theta - Al_2Cu$ phases. Both microstructures are the result of instabilities which transform a planar front into these complicated structures. In this chapter, classical theories for the prediction of these structures in isolation, as well as a new theory for their combined growth are described.

2.2.1 Dendritic growth

Dendritic growth is very common during solidification and thus its prediction has a long history, stretching from 1700s to the present day, which is summarized well in [43]. In the following, the focus will be on models developed over the past century, which can be used to predict the so-called operating state of the dendrite. The parameters of the operating state are the tip radius R, the tip velocity v and a measure of driving force F, which can be e.g. the undercooling ΔT or the supersaturation Ω[1]. A sketch of an α dendrite growing into a melt L, along with the operating state parameters, is shown in fig. 2.4 to clarify the meanings. The steady-state operating state is achieved after a temporary transient period and thus describes the steady-state growth which is assumed to characterize the majority of solidification time. For simplicity of presentation, only

[1] The actual driving force is scaled by either ΔT or Ω, e.g. $F \sim \Delta G = \Delta H \frac{\Delta T}{T_m}$ for the driving force of a pure substance solidifying.

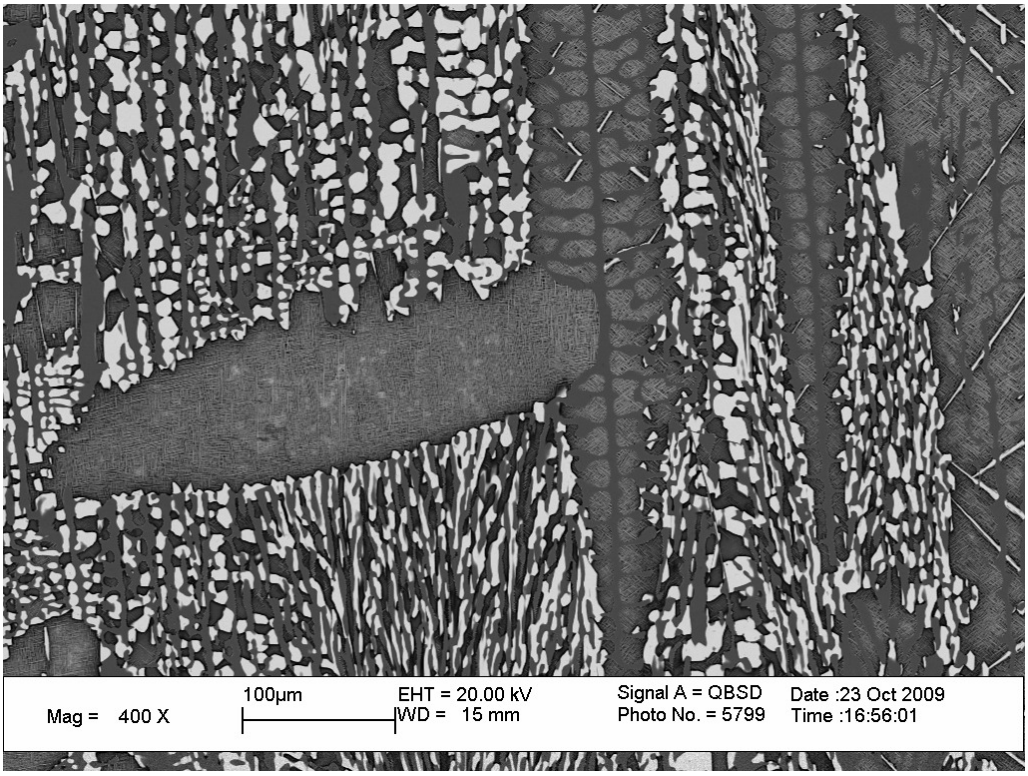

Figure 2.3: A micrograph of a directionally solidified Al-Cu alloy, showing both a coarse dendrite (grey) and a fine eutectic (white and grey) is depicted. The micrograph is provided courtesy of Professor Amber Genau at UAB.

the thermal case, i.e. solidification of an undercooled, unary melt, will be considered in the following.

Only two of the state variables are independent, i.e. $\Delta T(R, v)$ is a uniquely defined function for a single material. The determination of this function is based on two key ingredients: A specification of the diffusion field which results from a shape-preserving solution of the diffusion equation and a selection criterion. The shape-preserving diffusion field solutions were determined by Papapetrou [5] and Ivantsov [6], with these being generally characterized by an equation linking the undercooling ΔT to the Péclet number Pe:

$$\mathrm{Pe} = \frac{Rv}{2D} \tag{2.19}$$

$$\Delta T = \mathrm{Pe}\exp(\mathrm{Pe})E_1(\mathrm{Pe}) \tag{2.20}$$

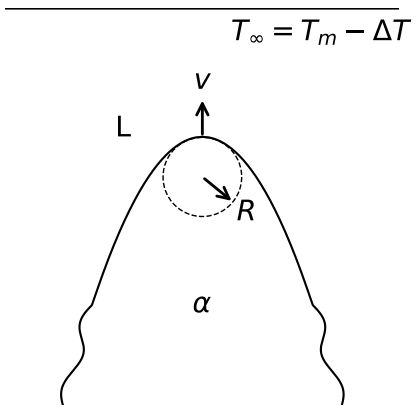

Figure 2.4: A sketch of a thermal α dendrite growing into an infinite, undercooled melt L. The shape approximates a parabola close to the tip, with perturbations occurring further down from the tip. The dendrite is characterized by the tip radius R, its velocity v as well as a driving force, here taken to be an undercooling ΔT specified at infinity.

for a three-dimensional paraboloid, with a diffusivity D and the exponential integral E_1. The right hand-side of eq. (2.20) is nowadays called the Ivantsov function, which is dependent on the shape which is being preserved. Note that this solution does not depend on any interfacial energy considerations, but only what kind of solution grows while being shape-preserving for a diffusion equation. As is obvious from the above, this does not uniquely define ΔT, but rather an infinite spectrum of solutions is defined, as only $Rv = const.$ for a single undercooling.
Zener [49] was the first to propose a maximal velocity criterion, though in the context of solid-state transformations. While this closed the problem, and much development on improving this model was conducted, an experimental test of this took until Glicksman [50] employed a transparently solidifying system to observe dendrite growth directly. None of the models matched these observations and thus new selection criteria were sought. The most prominent criterion is the marginal stability criterion (MSC) of Langer and Müller-Krumbhaar [8]. It states that the tip radius is determined by the wavelength which is *marginally* stable against perturbations:

$$R \approx \lambda_s = 2\pi\sqrt{l_d d_0} \tag{2.21}$$

$$\sigma^* = \frac{l_d d_0}{R^2} = \frac{1}{4\pi^2} \approx 0.025 \tag{2.22}$$

with the diffusion length $l_d = \frac{2D}{v}$ and the capillary length $d_0 = \frac{T_m \gamma}{\Delta T L}$ with the melting temperature T_m, the unit undercooling $\Delta T = L/c_p$, the latent heat L and the specific heat capacity c_p. Note that the stability criterion contains the influence of capillarity, which is one of the ingredients which was missing in the purely shape-preserving solution picture. The selection criterion is characterized by the stability constant σ^* and effectively suggests that $R^2 v = const.$ for a single undercooling. This theory was found to be close to experimental values [50] and thus again sparked a host of improvements. One such improved theory is that of Kurz and Fisher [9] which will be used in this work. By a thorough derivation, they arrive at a cubic equation which is analyzed in a low and high velocity regime, yielding for the tip undercooling

$$\Delta T_d = m c_0 (1 - A_v) \tag{2.23}$$

$$A_v = \begin{cases} \frac{DG}{v \Delta T_0 k} & v < \frac{DG}{\Delta T_0 k} \\ \left[1 - (1-k)\pi \sqrt{\frac{v\Gamma}{D \Delta T_0 k}}\right]^{-1} & v > \frac{DG}{\Delta T_0 k} \end{cases} \tag{2.24}$$

for the two regimes, with the temperature gradient G, the solidification range $\Delta T_0 = m c_0 \frac{1-k}{k}$ and the Gibbs-Thomson coefficient Γ. The low velocity regime describes cells, a related microstructure not further investigated in the present work, whereas the high velocity regime describes dendrites. Based on this relation and geometrical assumptions, the primary spacing can also be estimated, leading to the later power law relationships. For now, note that the undercooling is scaled by the composition c_0, the temperature gradient G and the velocity v.

However, earlier boundary integral results by Nash and Glicksman [7] showed that for an isotropic problem, as had been assumed so far, actually no steady-state solutions exist. This led to the development of microsolvability theory [51–53] (MST), which solved the isolated dendrite problem without the need for any assumptions: In essence, the continuum of solutions suggested by eq. (2.20) are broken into a discrete set by the singular perturbation induced by an anisotropy e.g. in the surface energy. This also explains the symmetry dendrites exhibit, as the anisotropy of the growing crystal is the determining factor. In the small Péclet number limit and for a four-fold anisotropy, MSC and MST are related with

$$\sigma^* \propto \delta^{1.75} \tag{2.25}$$

with the anisotropy strength δ. It should be noted that MST also predicts $R^2 v = const.$ for small Péclet numbers and thus in this limit the only difference between MSC and MST is the exact value of σ^*. Furthermore, Karma and Rappel [22] could show

that phase-field simulations match MST quite closely once the appropriate thin-interface limit is constructed. The complex shapes resulting from solidification, which can be captured with relative ease by employing phase-field methods, together with this ability of matching analytical theories made the phase-field approach the method of choice for solidification simulations. Hence a host of publications, a small selection being given via [22, 23, 37, 54, 55], exist concerning the simulation of dendritic growth with the phase-field method.

While the theory so far describes the growth of an isolated dendrite into an infinite melt, in real system multiple dendrites or even other morphologies grow competitively. Furthermore, in a completely solidified microstructure of an alloy, there is hardly any trace of the tip radius as could be determined with the previously described theories. Rather, what one can observe are inhomogeneities in the composition caused by dendrites impinging on each other or by secondary arms. This is commonly called microsegregation and is undesired. Finally, the dendrites do not have a uniform orientation and thus form grain boundaries when contacting each other, also affecting the materials properties [56].

The grain size is linked with the primary dendrite arm spacing (PDAS) λ_d and the microsegregation to the secondary dendrite arm spacing (SDAS). Based on previous theory and some geometrical assumptions of how a dendritic array is ordered, it is possible to build a theory for estimating the PDAS. In general, the PDAS can be approximated by a power law relationship [9, 57]:

$$\lambda_d = A\Delta T_0^n v^m G^o \tag{2.26}$$

with a lumped material parameters constant A and previously defined parameters. The solidification range ΔT_0 can be directly replaced with the alloy composition c_0. Typically, m and o are negative, i.e. higher gradients and velocities refine the structure. In contrast, n is positive and hence more highly concentrated alloys (with larger solidification range) produce coarser structures. For the high-velocity regime of [9], $n = \frac{1}{4}$, $m = -\frac{1}{4}$, $o = -\frac{1}{2}$. The experimentally observed ranges for m are about -0.19 to -0.75 and for o from -0.3 to -0.55 [58]. If convection is mostly avoided, $n \approx 0.25$ can be observed [58].

2.2.2 Eutectic growth

The history of eutectic growth theory is shorter than for dendrites, as these often form finer structures than dendrites and thus were observable only with higher resolution

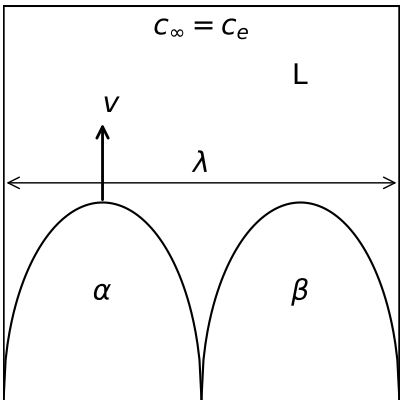

Figure 2.5: A sketch of the unit cell of lamellar eutectic growth is depicted. The eutectic consists of two solid phases α and β, growing into an undercooled melt L whose composition at infinity is assumed to be the eutectic concentration c_e. A steady lamellar spacing λ develops, with the eutectic front at $T = T_e - \Delta T_e$ advancing at a velocity v.

microscopes. The term *eutectic* refers to a type of reaction present in multicomponent systems of the form

$$\mathrm{L} \rightarrow \alpha + \beta \tag{2.27}$$

i.e. a liquid melt decomposing into two[2] solid phases. The eutectic point is the composition-temperature point at which all three phases are in equilibrium and is also the lowest melting temperature of alloys with compositions between the two solid phases. A sketch of the resulting morphology is depicted in fig. 2.5 with the relevant parameters. As with dendrites, the spacing λ between the resultant phases influences the materials properties.

The history of eutectic growth theory is similar to that of dendritic growth theory, though a quantitative theory was arrived at earlier due to anisotropy playing somewhat of a lesser role. The key ingredients are, again, a specification of the diffusion field ahead of the front and a selection criterion. Based on the earlier works of Scheil [59], Brandt [60],

[2] For more than two components, these binary as well as higher order eutectic reactions exist.

Zener [49] and Hillert [61], Jackson and Hunt [62] could formulate a quantitative theory of eutectic growth:

$$\Delta T_e = K_1 v\lambda + \frac{K_2}{\lambda} \tag{2.28}$$

$$\lambda^2 v = \frac{K_2}{K_1} \tag{2.29}$$

with materials and composition dependent parameters K_1 and K_2. The latter equation also defines the eutectic scaling law

$$\lambda^2 v = const. \tag{2.30}$$

which characterizes a materials system. The specifics of the constants change with the morphology, which for a binary eutectic can either be a lamellar arrangement of both phases or a matrix-rod composite. Which of these morphologies forms depends on which grows at the higher velocity, with this being strongly influenced by the mass fractions of the phases. However, anisotropy enters the problem here: A lamellar structure can form in such a way that the plane separating the phases is a low energy plane, whereas a matrix-rod composite necessarily contains boundary planes of variable orientation, including high energy planes [62]. Hence even though the mass fraction, assuming isotropic energies, would predict a matrix-rod composite, anisotropy can shift the morphology to a lamellar one.

In contrast to the quite wide spread of processing condition exponents for the resulting spacing of dendrites, the wavelength of eutectics generally follows the scaling given by eq. (2.30) as long as growth is diffusion-limited as shown in e.g [62–64]. As with dendritic growth, the phase-field method is quite attractive [65–68] for the simulation of eutectic growth, with this being another small selection of the literature.

2.2.3 Coupled dendritic-eutectic growth

The previously described theories analyze the microstructure in isolation. In a real casting, and as visible in fig. 2.3, dendrites and eutectics can form and grow alongside each other. Since these can influence each other and thus invalidate the previous predictions, a qualitative theory of coupled growth is developed in this section, based on the author's work [69]. It is based on the common assumption [70, 71] that coupled growth of dendrites and eutectics is delineated by their growth temperatures being equal. It will later be

employed to test how coupled growth influences the operating state of both dendrites and eutectics.

In order to build a qualitative model, the possible influence of one type of microstructure on the other is ignored for now. If this model gives an accurate estimate for the transition between the observed morphologies, then the dependence can indeed be assumed to be negligible. The basis of the model is the assumption that the microstructure growing at the higher temperature is the dominant one, which implies that the transition from one dominant microstructure to the other occurs when both microstructures grow at the same temperature. Thus accurate estimates for the temperature of either microstructure are necessary. These will not be based on a model involving material parameters, but rather with parameters obtained by data fitting, which allows a higher accuracy w.r.t. the simulation results. Based on [9, 70], the dendrite temperature model reads

$$T_{df} = T_l(c_0) - \Delta T_d \tag{2.31}$$

$$\Delta T_d = A\frac{G}{v} + B(c_0 v)^{0.5} + Cc_0 \tag{2.32}$$

i.e. the dendrite front temperature is the liquidus temperature $T_l(c_0)$ at the composition c_0, minus an undercooling. The parameters A, B, C will be fitted based on simulation data, with the dependence on the processing parameters G, v and c_0 being inspired by the earlier model eq. (2.23). A simplification of this model is to remove the composition dependence of the undercooling, with the corresponding equation being

$$\Delta T_d^s = A\frac{G}{v} + Bv^{0.5} \tag{2.33}$$

which will be compared with the composition-dependent model later. For eutetics the expression due to Jackson and Hunt [62]

$$T_{ef} = T_e - \Delta T_e \tag{2.34}$$

$$\Delta T_e = E(c_0)v^{0.5} \tag{2.35}$$

$$E(c_0) = 2\sqrt{K_1(c_0)K_2(c_0)} \tag{2.36}$$

is employed, with concentration-dependent K_1 and K_2 of eqs. (2.28) and (2.29) also being fitted to data.

Equating both front undercoolings results in an equation for a boundary curve separating the microstructures, given by

$$T_l(c_0) - A\frac{G}{v} - B(c_0 v)^{0.5} - Cc_0 = T_e - E(c_0)v^{0.5} \tag{2.37}$$

which will be solved numerically in a later section after the constants have been determined.

Simulative works concerning coupled dendritic-growth are much more rare [72–74] compared to the pure forms of the solidification morphologies. In [72] an Al-Si alloy with trace contents of P and Sr was investigated with the phase-field method. The strong anisotropy of the Si phase is considered in detail and also includes the effect of Sr on its anisotropy. Nucleation was achieved by designating random sites for potential nucleation and evaluating a barrier condition on these sites as the simulation proceeded. After a primary Al dendrite grew into a finite domain, Si nucleates and first grows in a blocky manner before coarse eutectic growth between Si and Al starts. It could be shown that once enough Sr is added, the eutectic grows in a finer fibrous morphology, due to the modification of the anisotropy of Si. The eutectic nucleated after large portions of the finite domain had been encompassed by the dendrite. In [73] the complete solidification process of a hypereutectic Al-Si alloy was simulated. The strong anisotropy of Si is also considered in detail. No detailed description of the nucleation was given, but since the same software as in [72] was used, it is likely that fixed nuclei were also placed. The authors could observe that after an initial transient growth of blocky Si, the Si blocks were completely encased in nucleated Al after which eutectic growth was partially observed. In [74] the cellular automaton approach was employed to calculate the complete solidification of an Al-Si alloy. Again, special attention is paid to the strong anisotropy of Si. Nucleation was achieved by a continuous nucleation distribution, which basically specifies the density of nuclei as a function of undercooling. This effectively represents a probability for a cell containing liquid to transform into solid. The authors conducted a series of large-scale 3D simulations for different processing conditions: The initial Al grains grow in a dendritic manner, but also interact with each other which reduces their growth speed. Once sufficiently below the eutectic temperature, Al and Si nucleate into the interdendritic liquid. The morphology within the eutectic was compared against experiments and agreed well with these.

2.3 Freeze-casting

Freeze-casting [45] is a novel manufacturing method employing the way a liquid solidifies to generate solid patterns. It typically employs colloidal suspensions with a liquid, which is later frozen, and a particulate, insoluble solid. As the liquid freezes, the insoluble particles are pushed into the regions between the solidification pattern. The freezing liquid can be roughly treated with the dendritic solidification theory described earlier. For simplicity in the following, water will be assumed to be the liquid and hence the solidified structure is ice. After the freezing step, the ice is sublimated and the remaining solid structure is effectively the negative of the complex solidification pattern: This results in a large range obtainable porous microstructures if the liquid is changed, since the anisotropy of the liquid determines the solidification pattern.
The final step in the freeze-casting process is sintering, since the particle packing itself is not particularly durable. Two important characteristics of the final microstructure are the pore widths, where once the ice was, as well as the wall thickness, where particles are concentrated — for the usual reasons of these affecting the materials properties. The materials produced in this way can be used for example as bone replacements, membranes or as a thermal insulation material [45].

The solidification of colloidal suspensions was investigated theoretically and experimentally by Peppin et al. [75–78] in a series of papers. The basic idea for the theoretical thermodynamic investigation is to treat the suspension as a homogeneous mixture, with the solids loading ϕ taking the role of concentration c. The advancing ice front is assumed to perfectly reject particles, i.e. its partition coefficient k vanishes. Since the ice is effectively a unary system, its chemical potential is given by a function of (T, p) only. The suspension contains particles, which cause an osmotic pressure Π in the suspension, which in turn changes the chemical potential with solids loading. Hence the condition for chemical equilibrium may be written as

$$\mu^p_{ice}(T,p) = \mu^p_{water}(T,p) - \frac{\Pi(T,\phi)}{\rho} \tag{2.38}$$

with the superscript p indicating the value for a pure phase and ρ being the density of water in this case. Assuming that the osmotic pressure is equivalent to that of a suspension of hard-spheres, one can write

$$\Pi(\phi) = \frac{\phi}{v_p} k_b T z(\phi) \tag{2.39}$$

with the volume of a hard sphere v_p, Boltzmann's constant k_b and the compressibility factor z accounting for the details of the hard-sphere interaction. These relations can then be solved to yield a liquidus curve of the form

$$T_l = \frac{T_m}{1 + m\phi z} \tag{2.40}$$

with an accumulation of constants m describing the suspension. This curve achieves the melting temperature T_m of the pure fluid at $\phi = 0$. Due to the compressibility expression for a hard sphere suspension, the curve diverges for the random close packing (RCP) fraction $\phi_{RCP} = 0.64$.

The relationship between processing conditions and the resulting microstructural lengths is similar, but not identical to that of dendrites. Experimentally observed exponents for the dependence of the wavelength ($\approx$ PDAS) are in the interval $[-0.33, -1.3]$ [45], i.e. higher velocities always refine the structure, but the degree of refinement differs significantly. Classical dendrite theory would predict an exponent of $n = -0.25$.
There are many reasons for freeze-casting deviating from the dendrite theory: Suspensions are often stabilized with additives, but these can potentially segregate to interfaces and control the local evolution. The resulting phase diagram is also highly nonlinear, i.e. contains strongly variable liquidus slopes and partition coefficients. In contrast, classical dendrite theory works with linear phase diagrams only. Furthermore, the diffusivity of the particles depends on their size as well as concentration, neither of which enters the theory either. Finally, often the experimental determination of actual freezing velocity is quite difficult and hence only the velocity of the applied temperature field or only the cooling rate are given, with estimates for the gradient to arrive at a freezing velocity. Many experiments also do not control for the temperature gradient, although it has a significant influence on the wavelength. Hence some experimental deviation might also be simply attributable to changes in the temperature gradient, which is not measured, being accounted for by an exponent change in the velocity.

The freeze-casting process has only been rarely investigated with the phase-field method with [79–81] being more or less the complete literature[3]. In all these cases, the particles/solute are homogenized over resulting a continuous concentration field. In [79] the authors employed a standard free energy previously described by [83] and thus disregarded the thermodynamic effects of particle size. They also employed a simple four-fold anisotropy function, which does not describe the anisotropy of ice. While they reported

[3] If one considers particles interacting with a front, without forming dendrites, freeze-casting, then there are studies such as [82] as well.

good matching with experiments, they did not provide scaling laws for variable processing parameters. The present author included the thermodynamic effect of particle size, i.e. an osmotic pressure induced by the particles which varies with their total volume fraction and individual volume, following Peppin [76] in [80] and also approximated the complex anisotropy of ice by using spherical harmonics. More specifically, the osmotic pressure leads to a change in chemical potential within the suspension, which then allows the calculation of a liquidus line separating the pure suspension from a two-phase region of suspension and ice. Scaling laws were provided, detailed in-depth in chapter 5, showing that the wavelength was roughly independent of solids loading, with deviations in both the velocity and temperature gradient dependence from classical growth theory. The authors of [81] employ a classical solidification model as well and specialize it to approximate the phase transitions in a chitosan-acetic-acid-water solution, which again discards the suspension character of freeze-casting. A constant partition coefficient and a constant liquidus slope were assumed in a dilute alloy approximation. The anisotropy was modelled by combining a sixfold spherical harmonic in the basal plane and a regularized version of a sharply cusping, twofold function normal to it. This basically predicts sixfold symmetry in the basal plane and plate-like growth normal to it, similar to the description employed in chapter 5. Special attention was paid to the correct thin-interface asymptotics, in contrast to previous works: The kinetic coefficient, modifying steady-state temperature of the moving interface, was made to vanish in the basal plane and achieve a finite value normal to it. This accounts for the fast kinetics within the basal plane, whereas normal to it growth can become limited by attachment kinetics. Scaling laws consistent with classical growth theory were observed. The combination of these results, as well as the experimentally observed large scatter, might suggest that the thermodynamic pecularities of the suspension-based freeze-casting are inconsistent with the simplifying assumptions employed for classical dendrite growth models, i.e. constant partition coefficient k and liquidus slope m.

2.4 Solid-state sintering

The solid-state sintering process is applied in the manufacturing of many products, from the humble coffee cup straight to complex products such as solar cells [84–86], in which the sintering process is usually used to form the front electrode. Thus it is of great importance to understand the process, predict the properties of sintered materials and thereby improve the products themselves. In the simplest case, the process is conducted by heating a so-called green body sufficiently, which then begins to change its microstructure via transport processes. These processes lead to both densification, reducing the porosity of

the body and the size of the body, as well as coarsening, which causes the grains which compose the body to grow. Both processes are driven by energy minimization, with densification reducing surface area and coarsening reducing grain boundary area via grain growth. Densification increases the relative density ρ with grain growth increasing the grain size G. The relative density ρ is relative to the density of the material in question entirely free of pores. Since this work only concerns itself with relative densities, the qualifier of "relative" will be dropped henceforth. The grain size G measures the dimension of a grain in a single dimension. Occasionally it is also useful to consider the grain area or grain volume, as these might not require geometrical assumptions to convert a corresponding measurement to the grain size.

These variables are interesting as they are the main factors determining the effect of the microstructure on the materials properties. A denser material will generally be stiffer and tougher, but also heavier. Fine-grained structures are harder, but are also more susceptible to creep. Hence in the following an overview of modelling and characterization approaches is given for densification as well as grain growth.

Early theoretical developments focused on simple geometrical models from which the densification of complete green bodies was predicted, but observed to be quite wrong. Thus more complex models focusing on specific parts of the process — initial, intermediate and final — were developed. These typically predict the qualitative response of the process to a change of processing parameter correctly, but their quantitative predictions, without being fitted to experiments, are often not accurate [18].

While the early geometric models fail at scale, their predictions for the initial stage can be reasonably compared with experiments. Thus these can also be used to test if a simulation follows their prediction and by transitivity approximates the experiments. These models are generally based on analyzing the geometric evolution of two particles of equal radius R, sketched in fig. 2.6 for an initial and equilibrium state. The two key ingredients are a specification of an atomic flux into the sintering neck — where particles meet — and a geometric assumption which changes the neck radius X and distance between the center of masses (COM) of the particles in reaction to the flux. The motion of the COM can be both by simple diffusion as well as vacancy absorption at the grain boundary acting as a vacancy sink. The geometric assumptions also define whether the COM can move in the first place, with non-densifying geometries keeping the COM fixed whereas densifying geometries allow its movement. Different diffusion paths are available to the system, with them being depicted in fig. 2.6c. The paths 1, 3 and 4 represent different volume diffusion paths, 2 represents diffusion along the grain boundary, 5 represents diffusion along the surface and 6 the evaporation-condensation path. The flux along these paths

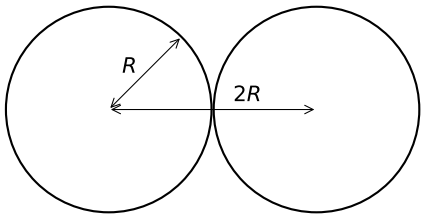

(a) initial state of a two particle model

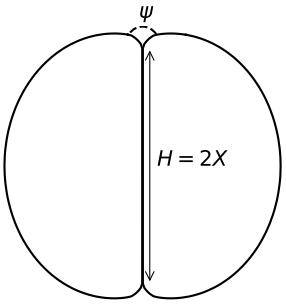

(b) equilibrium state of a two particle model

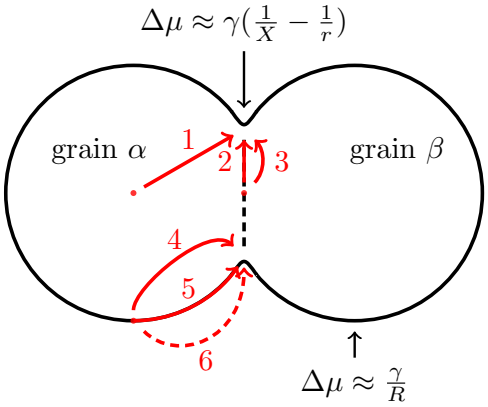

(c) diffusion paths during the kinetic evolution

Figure 2.6: The two particle model employed for the development of initial stage sintering models is depicted. The geometrical models usually assume infinite neck growth, but actual neck growth is limited by the dihedral angle ψ as shown on the right. The volume contained in both states is the same. The evolution from the initial to equilibrium state is facilitated by various diffusion paths (red) shown in fig. 2.6c, based on [35]. The chemical potential gradient induced by different curvatures drives these diffusive fluxes. The neck surface curvature has contributions from both radial $\frac{1}{X}$ and axial $\frac{-1}{r}$ curvature components.

is driven by chemical potential differences between the points considered, originating from the Gibbs-Thomson effect. In the figure, chemical potential differences w.r.t. a flat surface, due to this effect, are given. Within the geometric model, the neck is of circular cross-section, but also has an axial, concave curvature of $r \propto \frac{X^2}{R}$. This relationship allows the elimination of r as an independent geometric parameter, but also limits the applicable range of neck radii. If only a single path is considered, then it is possible to determine the time evolution of the neck region by approximating the flux into the neck region.

More specifically, based on the previously mentioned flux and geometric assumptions, power laws for the relative neck radius $\frac{X}{R}$ and the strain $\epsilon = \frac{\Delta L}{L_0}$

$$\frac{X}{R} = At^{1/n} \tag{2.41}$$

$$\frac{\Delta L}{L_0} = Bt^{1/m} \tag{2.42}$$

can be derived, with $m = n/2$, but $B = 0$ if a non-densifying geometry is assumed. The values of the constants A and B depend on the material and geometry, with the exponents n and m depending on the dominant transport mechanism, listed in table 2.1. By virtue of the geometric assumption only a limited region of the evolution — usually taken to be up to 0.3 of the relative neck size X/R [20] — can be approximated.

Furthermore, these models generally assume a vanishing grain boundary energy, which implies infinite neck growth. Neck growth is actually limited by the dihedral angle

$$\psi = 2\arccos(\frac{\gamma_{gb}}{2\gamma_s}) \tag{2.43}$$

with the grain boundary energy γ_{gb} and the surface energy γ_s. Based on the thermodynamic treatment of [87], the grain boundary length $H = 2X$ in equilibrium is given by

$$H = \frac{\frac{\pi}{r'} + r'(\psi - \pi + \sin(\psi))}{(2\cos(\psi/2))} \tag{2.44}$$

$$r_d = (\frac{\pi}{\pi - \psi + \sin(\psi)})^{1/2} \tag{2.45}$$

$$r_{nd} = \frac{1}{\cos(\psi/2)} \tag{2.46}$$

for the case of an infinite, linear chain of cylinders. The value reached within a two-particle geometry will differ from this, since the particles' resulting equilibrium shape

Table 2.1: Plausible values for the exponent n in eq. (2.41) based on [20].

dominant mechanism	exponent n
surface diffusion	7
grain boundary diffusion	6
lattice diffusion	4-5
vapor transport	3
viscous flow	2

will be different. Depending on whether *d*ensification or *n*o *d*ensification is assumed, a different non-dimensional equilibrium radius $r^{'} = r_{d,nd}/R$ is obtained. This also implies a limit on the strain for the densifying case

$$\epsilon = 1 - r^{'} \cos(\psi/2) \tag{2.47}$$

for this geometry.

Another approach for characterizing sintering, not necessarily limited to the initial stage, are Herring's scaling laws [11]. These are based on assuming a constant grain size and that the microstructure evolves self-similarly. Based on these assumptions one can derive a relation [11, 20]

$$\frac{\Delta t_2}{\Delta t_1} = (\frac{R_2}{R_1})^Z \tag{2.48}$$

which relates the time span Δt for an equivalent microstructural change, e.g. reaching a certain density or strain, to the particle size R. The constant Z is again specific to the process being considered, with the possible values being listed in table 2.2. This relation can be used whenever the dominant transport mechanism does not change. Furthermore, the relation can be used to identify whether the effect of scale has been completely included in a model by measuring the model's prediction and comparing it to the analytical prediction. The eqs. (2.41), (2.42) and (2.48) will be used in later chapters for simple validation of sintering models.

As the necks grow and contacts form, the geometry deviates significantly from the two-sphere contact model and hence requires a change in geometric description. This description originates mostly with Coble [88] who approached it for both intermediate and final stage sintering. It requires the specification of a space-filling geometry of grains and pores as well as the vacancy fluxes. The vacancy flux originates from the pores situated between grains and it is assumed that this flux is efficiently absorbed by GBs. Since

Table 2.2: Plausible values for the exponent Z in eq. (2.48) based on [20].

dominant mechanism	exponent Z
surface diffusion	4
grain boundary diffusion	4
lattice diffusion	3
vapor transport	2
viscous flow	1

the pores can be thought to consist of vacancies, vacancy absorption implies a reduction of pore volume and thus shrinkage. This generally yields a specification of the porosity $P = 1 - \rho$ of the form

$$P = \frac{A}{G^Z}(t_f - t)^k \tag{2.49}$$

in which A lumps material parameters (diffusivity, surface energy, ...), G is the grain size, t_f is the time of pore disappearance, and Z and k are exponents depending on the geometry and flux specifications. The exponent Z is generally the same as for Herring's scaling laws and thus suggests a dominant transport mechanism. In contrast to the earlier direct power laws, the inclusion of a time to pore disappearance specifies a natural end state of zero porosity.

Note that the geometry changes significantly once open porosity is eliminated, since there is no longer a continuous network of pores, but rather only isolated pores attached to grain boundaries or within bulk grains. This transition is also generally used to differentiate intermediate stage sintering from the final stage, with the latter having little to no open porosity left. The transition from open to closed porosity is usually assumed to be due to a Plateau-Rayleigh type of instability. Nichols and Mullins [89] analyzed the morphological instability due to infinitesimal perturbations of an infinite cylindrical pore and could show that there exists both a stability limit and a fastest growing instability. Both are characterized by being a wavelength of instability relative to the cylinder radius, i.e. larger pores are more stable. When grain boundaries connect to the cylinder, the instability is often initiated by the GBs instead of perturbations since their rate of growth is faster [90]. Hence the geometrical configuration of the grain boundary network relative to the pore network plays a key role in determining when pore closure occurs. Typically, pore closure should be delayed as long as possible, since the amount of gas enclosed in a pore determines its pressure which affects its resistance to further densification.

If an isolated pore is attached to a grain boundary, then the gases it contains can typically dissolve [91] and diffuse [92, 93] much more readily along GB paths than in the bulk material[4]. Thus if a pore stays attached, it is possible to transport its gases outside of the green body proper and hence eventually eliminate the pore. However, if grain growth occurs pores can become detached and trapped within grains. Once this occurs, these pores cannot be eliminated on processing timescales without applying pressure to forcefully dissolve the gases into the grain. If this is done, then at a sufficiently high temperature the dissolved gases will nucleate as porosity again. Hence grain growth will be considered next.

During the intermediate and especially the final sintering stage grain growth occurs. It can be described with a power law of the form [20]

$$G(t)^n - G(0)^n = kt \tag{2.50}$$

with the time-dependent grain size G, an exponent n and a constant related to geometry and GB properties k. For ideal grain growth, if it is limited by interface reactions, $n = 2$ [20], though depending on various factors (porosity [95], solute drag [96], ...) exponents deviating from this can be observed. In the ideal case, a difference in curvature is the only driving force which applies homogeneously to the entire GB. This driving force is due to curvature κ affecting the chemical potential via

$$\Delta\mu = \gamma\Delta\kappa \tag{2.51}$$

with the interface energy γ and the difference in curvature κ between two points, and as described in section 2.1, differences in chemical potential imply the existence of driving forces F. Furthermore, it is assumed that there is a linear relationship between driving force and boundary velocity, with the GB mobility M being the proportionality constant. From these, the relations

$$F = \gamma\Delta\kappa \tag{2.52}$$

$$v = MF \tag{2.53}$$

$$\rightarrow \frac{dr}{dt} = M\gamma\frac{1}{r} \tag{2.54}$$

[4] The specifics, as always, depend on the material and diffusing species in question. For example, while hydrogen generally dissolves more easily in grain boundaries than in the bulk, its diffusivity in the bulk is often faster than through grain boundaries, see e.g. [91, 94].

are derived, with the last expression assuming a circular grain embedded within a larger grain, such that the curvature of the larger grain is effectively zero which sets $\Delta\kappa \approx \frac{1}{r}$. Integration yields the ideal growth law with $G(t) \propto r(t) \propto \sqrt{t}$, i.e. parabolic growth. An alternative approach is to consider that the volume change of a grain is proportional to the net flux across its boundaries, i.e.

$$\frac{dV}{dt} = jA\Omega \tag{2.55}$$

with an averaged net flux density j, the boundary area A and the atomic volume Ω. The volume and area can be related with a shape assumption, e.g. for a sphere

$$\frac{4\pi}{3}\frac{dr^3}{dt} = 4\pi r^2 j\Omega \tag{2.56}$$

and assuming $j = \frac{M}{r}$ for the flux, integration yields a parabolic law as well[5]. Equation (2.55) reveals a missing part in the simpler description of a small grain embedded in a large grain: Even if there is a large flux density due to large differences in curvature, if the flux is restricted to only a small area, grain growth will be slow. This is the case in the initial stage of sintering, where the sintering neck and hence the area across which this flux flows is only beginning to form. This is one of the reasons why grain growth is generally not observed in the initial stage of sintering.

Both approaches only describe the growth of a single grain embedded in another, larger grain. A real microstructure however has many grains sharing faces and higher order junctions and so topological effects should be included as well. Furthermore, the grains will obviously no longer have a uniform size distribution after some grains have grown at the expense of others. This is taken into account by so-called mean field theories [20] pioneered by Hillert [97]. These generally contain a growth law, which has a critical grain size G^* above which grains grow and below which grains shrink. Furthermore, it is possible to derive steady-state grain size distributions for these.

Grain size and porosity are often found to be correlated in experiments [46, 98, 99], specifically the expression

$$G = k\frac{G_0}{\sqrt{P}} \tag{2.57}$$

[5] The specific shape assumption does not change the scaling as can be shown with dimensional analysis; only the prefactors will be changed.

is often found to fit experimental data well, with materials and green body parameters absorbed in k and the initial grain size G_0. This effectively captures the phenomenon of concurrent grain growth and reduction of porosity across a wide range of materials and processes. An affine variant of this relation can be analytically derived based on the earlier models for densification and grain growth [98] while assuming that grain growth and densification are controlled by processes occurring on grain boundaries.

During the entire process, the grain structure does not only change in size but also in shape. The grain shape moves from the initial one, usually assumed to be a sphere, to a polyhedron[6] due to impingement by other grains, resulting in e.g. the truncated octahedron for the model of Coble [88], which is characterized by its 14 faces and hence is also called tetrakaidecahedron. As the density increases, previously unconnected grains impinge on each other and their coordination number N_c also changes accordingly. It is linked to the density with

$$N_c = 2 + 11\rho \tag{2.58}$$

following a fit of literature data by German [100]. Note that even at 100% density, this does not yield $N_c = 14$ as would be expected from the truncated octahedron.

Another way of describing the sintering process is by focusing on the evolution of the surface [46, 101]: Since the driving force for densification is the minimization of surface energy, the free surface area must be reduced as density increases. Hence a relationship between density ρ and surface area S exists of the form

$$\frac{S}{S_0} = a - b\rho \tag{2.59}$$

with the initial surface area S_0. If S measures only the internal surfaces, then $S = 0$ describes the fully dense state and implies elimination of open and closed porosity[7] If the method for determining S measures the outer surface as well, then some non-zero S dependent on the sintered body size and shape will characterize the fully dense state.

[6] If a grain boundary is moving the faces will not necessarily be planar.

[7] As a practical note, if surface area is measured with methods only characterizing open porosity, e.g. gas absorption, then $S = 0$ also doesn't necessarily imply full density.

A closely related measure is the Euler characteristic χ

$$\chi = \frac{1}{2\pi}(\int_S K dS + \int_{\partial S} k_g ds) \tag{2.60}$$

$$= V - E + F \tag{2.61}$$

with the Gaussian curvature K of a surface S, the geodesic curvature k_g of the boundary ∂S of S, as well as the number of vertices, edges and faces which make up a polygonal mesh of S. The characteristic is related to the genus g

$$\chi = 2 - 2g \tag{2.62}$$

which describes the number of holes in S. Since sintering starts from a continuous network of pores, then proceeds to isolate and close them, both g and χ should be able to describe how far the sintering has proceeded. More specifically [101, 102], the initial stage is characterized by a negative and decreasing value of χ. Once the characteristic increases, the intermediate stage is entered until a positive, maximum value is attained, which describes pore closure. In the final stage, these pores vanish with time and $\chi = 0$ is achieved for a pore-free body.

This wide range of available descriptions for the sintering process should make it clear that sintering is typically more complex than solidification. In solidification, closed, analytical theories exist for isolated solidification geometries and match quite closely with experiments for the entire solidification process. In sintering, the entire process has to be divided into stages, in which separate theories typically only yield qualitative guidance for process optimization. This is both due the complex, variable geometry resulting from many particles interacting as well as multiple, overlapping processes competing against each other.

The phase-field method has been employed for the simulation of solid-state sintering in a multitude of papers, with two different approaches being practised: One approach simply adds additional diffusion pathways [35, 103, 104], whereas the other also adds advective terms to the field equations being solved [33, 36, 105–112]. The first practical comparisons of these approaches were conducted by [36, 107], with both showing that densification progresses more slowly if no advective terms are included. However, this alone does not imply the necessity of advective terms for the simulation, since densification speed can just as well be adjusted by changing a diffusion coefficient. The present author could show in [113] that if no advective terms are included, there is a severe dependence of densification speed on the system size. This is obvious nonsense and hence advection should always be included. However, the manner in which the velocities which

are calculated in order to advect the fields also plays a large role, as again shown by the present author [114, 115]: If a grain's velocity only depends on its interaction with its nearest neighbours, as previously practised, then there still is a significant dependence of densification speed on system size. This was be remedied by linking the velocity (or equivalently displacement) of all grains in a system of equations, effectively allowing displacement generated in one part of the green body to propagate through the system without resistance.

3 Phase-field modelling

In this chapter the employed phase-field models will be described. The models described in section 3.1 are based on literature, whereas the extensions and developments in section 3.2 consist of original work[69, 80, 114–116]. In section 3.3 an overview of how to approach parametrization of real systems as well as the nondimensionalization is given.

The principal idea behind phase-field models is to approximate a free boundary, whose interface is sharply defined, with a smooth field variable which describes the position of the interface. This allows the solution of a class of mathematical problems called free boundary problems which are highly relevant for materials processing, as e.g. the boundary separating solid and liquid during casting is constantly moving and changing shape. If the solution were sought with a sharp interface, that interface needs to be tracked and the computational mesh adjusted to its local evolution, with topological changes requiring careful handling. The phase-field approach avoids the explicit tracking and accounting for topological changes at the cost of solving another partial differential equation (PDE) for the interface position. This PDE is usually based on a variational derivative of a free energy functional, as this should represent the minimization of free energy w.r.t. the so-called phase-field variable. The variation is then assumed to be linearly related to the change of the phase-field in the spirit of small deviations from equilibrium allowing for a linear expansion around the equilibrium.

3.1 State of the art of phase-field models of materials processing

In this section the state of the art for phase-field models of materials processing, pertaining to solidification and sintering, is recapped. The focus will be on the models employed within the later work.

3.1.1 Phase-field model of alloy solidification

The phase-field model of alloy solidification employed herein is based on the works [25, 117]. The approach starts with a free energy functional

$$\mathcal{F} = \int_V \epsilon a(\phi, \nabla\phi) + \frac{1}{\epsilon} w(\phi) + \psi(\phi, \mu, T) dV \tag{3.1}$$

which describes the total energy contained in the volume V. The phase-field vector $\phi = (\phi_0, \phi_1, \ldots, \phi_{N-1})$ describes the local volume fractions of the N phases ϕ_α. These phase-fields represent the local microstructure and thus their spatial distribution can be compared to experimental microstructures. The chemical potential vector $\mu = (\mu_0, \mu_1, \ldots, \mu_{K-1})$ similarly describes the local chemical potential of the K components and is related to the concentration vector $c = (c_0, c_1, \ldots c_{K-1})$. The local temperature is given by T. Note that within the present work, c will be used in the sense of both molar concentration and mole fractions. This is permissible because in binary systems they are linearly related with the molar volume which is always assumed to be constant for a single material system. Furthermore, if molar concentration is nondimensionalized employing the constant molar volume, then the resulting non-dimensional equations are the same as if mole fraction had been used from the start. Finally, the summands within the integral should be in units of energy per volume. Hence if the energy is specified in energy per mole, it will be divided by the molar volume to arrive at the correct unit. Though as with the concentration, if a constant molar volume is assumed, volumetric and molar energy density are equivalent after nondimensionalization. This is shown explicitly in appendix A.1.

The variables (ϕ, μ, T) appearing in the functional are space-time dependent, but this dependency is dropped for conciseness. For the same reason, the vectorial nature of these variables is dropped, with indices indicating single components of these. Vectorial notation will only be used for vectors if the vectorial nature does not follow from surrounding operators. Hence a gradient of a scalar obviously implies a vector in space in higher dimensions, but the symbol v for velocity is ambiguous and thus will be marked as $\vec{v}$ to emphasize the vectorial nature. Another notational simplification is to not always specify the limits of sums: If the sum is over the phase-field vector ϕ, then the implicit lower limit is 0 and the implicit upper limit is $N-1$. Similarly for sums over the concentration vector c, in which the limits are 0 and $K-1$.

The gradient energy density a and the bulk energy density w are defined as

$$a(\phi, \nabla\phi) = \sum_{\alpha} \sum_{\alpha<\beta} \gamma_{\alpha\beta} A^{\gamma}(q_{\alpha\beta})^2 |q_{\alpha\beta}|^2 \tag{3.2}$$

$$w(\phi) = \begin{cases} \frac{16}{\pi^2} \sum_{\alpha} \sum_{\alpha<\beta} \gamma_{\alpha\beta}\phi_{\alpha}\phi_{\beta} + \sum_{\alpha} \sum_{\alpha<\beta} \sum_{\alpha<\beta<\delta} \phi_{\alpha}\phi_{\beta}\phi_{\delta}\gamma_{\alpha\beta\delta}, & \phi \in \mathcal{GS}^N \\ \infty, & else \end{cases} \tag{3.3}$$

and include contributions due to surface energy. Furthermore, these describe the equilibrium properties in lieu of any driving force. As will be shown later, the term $\gamma_{\alpha\beta}$ directly represents the interface energy of an $\alpha\beta$ interface, with the function $A^{\gamma}(q_{\alpha\beta})^2$ representing the anisotropy of this interface w.r.t. orientation of the interface[1]. In turn, the orientation is described with the generalized gradient vector $q_{\alpha\beta} = \phi_{\alpha}\nabla\phi_{\beta} - \phi_{\beta}\nabla\phi_{\alpha}$. The following anisotropy functions for a single $\alpha\beta$ interface will be considered:

$$A_{iso} = 1 \tag{3.4}$$

$$A_4 = 1 + \delta_{\alpha\beta}(3 - 4\frac{|q_{\alpha\beta}|_4^4}{|q_{\alpha\beta}|^4}) \tag{3.5}$$

$$A_{sph} = 1 + \sum_{l} \sum_{m} \delta_{\alpha\beta,lm} Y_{lm}(q_{\alpha\beta}) \tag{3.6}$$

which describe respectively an isotropic interface eq. (3.4), a fourfold symmetrically anisotropic interface approximating a weakly anisotropic cubic crystal eq. (3.5), and a sum of spherical harmonics Y_{lm} used to approximate the anisotropy of ice eq. (3.6). The $\delta_{\alpha\beta}$ terms describe how strong the anisotropy is, with the terms dependent on $q_{\alpha\beta}$ describing the dependence on the interface orientation. The shorthand expressions of eq. (3.5) read as $|v|_4^4 = \sum_i v_i^4$ and $|v|^4 = (\sum_i v_i^2)^2$ [25] with the index i running over the spatial dimensions. The specifics of the anisotropy of ice will be given in chapter 5.

The chosen bulk energy density w is an obstacle type of potential. It consists of dual interactions terms, accounting for the two-phase interfacial profile, and a triple interaction term which reduces the appearance of so-called ghost phases along interfaces[119, 120]. The obstacle potential can reduce the computational effort when solving the phase-field equations by constricting the nontrivial phase-field values to only a narrow range called the *interface*. Thus computations in which the volume and its neighbours all contain

[1] By multiplying only the gradient energy with the anisotropy function the actual effect is to change the interface *width* with orientation and not the interface *energy* [118]. In terms of how anisotropy affects e.g. dendritic growth this approach suffices and is quite standard.

the same phase-field values (called *bulk*) of either 0 or 1 can be skipped altogether, as no change is possible for these. This is allowed by forcing the phase-field vector ϕ to lie within the N-dimensional Gibbs simplex

$$\mathcal{GS}^N = \{\phi \in \mathcal{R}^N : \sum_\alpha \phi_\alpha = 1, \phi_\alpha \geq 0\} \tag{3.7}$$

via declaring the energy outside of this simplex to be infinite. This requires a projection step in the numerical solution, as the evolution equation derived later does not guarantee that ϕ stays in $\mathcal{GS}^N$.

The driving force is described by

$$\psi(\phi, \mu, T) = \sum_\alpha h_\alpha(\phi)\psi_\alpha(\mu, T) \tag{3.8}$$

with the grand potential densities of the individual phases ψ_α and a weighting function $h_\alpha(\phi)$ with the properties $h_\alpha(0) = 0, h_\alpha(1) = 1, \frac{dh_\alpha}{d\phi}(\phi \in \{0, 1\}) = 0, \sum_\alpha h_\alpha = 1$. These properties ensure that the driving force for other phases β vanish within the bulk of an α phase. The function

$$h_\alpha(\phi) = \frac{\phi_\alpha^2}{\sum_\beta \phi_\beta^2} \tag{3.9}$$

will be employed in this dissertation, based on [121].

The temporal evolution of the phase-field is assumed to be represented by the variational derivative

$$\tau(\phi, \nabla\phi)\epsilon\frac{\partial\phi}{\partial t} = -\frac{\delta\mathcal{F}}{\delta\phi} - \Lambda \tag{3.10}$$

$$\begin{aligned}\tau(\phi, \nabla\phi)\epsilon\frac{\partial\phi}{\partial t} = &-\epsilon\left(\frac{\partial a(\phi, \nabla\phi)}{\partial\phi} - \nabla\cdot\frac{\partial a(\phi, \nabla\phi)}{\partial\nabla\phi}\right)\\ &-\frac{1}{\epsilon}\frac{\partial w(\phi)}{\partial\phi}\\ &-\frac{\partial\psi}{\partial\phi} - \Lambda\end{aligned} \tag{3.11}$$

which evolves the state of ϕ to a minimum of the free energy $\mathcal{F}$, subject to the constraint $\sum_\alpha \phi_\alpha = 1$ which is accounted for by the Lagrange multiplier Λ. This evolution is non-conservative and thus suited to model phase transformations and originates from Allen

and Cahn [122]. The timescale on which the evolution happens is determined by the relaxation coefficient

$$\tau(\phi, \nabla\phi) = I_\tau(A^\tau_{\alpha\beta}(q_{\alpha\beta})\tau_{\alpha\beta}) \tag{3.12}$$

whose anisotropy function $A^\tau_{\alpha\beta}$ need not be the same as that of the gradient energy. I_τ is an interpolation function, which is either the arithmetic mean or the harmonic mean of all individual $\alpha\beta$ terms: For values of $\tau_{\alpha\beta}$ within a few factors of each other, as commonly found in solidification, the arithmetic mean will be employed. For larger factors, as can be found in sintering, the harmonic mean will be employed as this reduces the artificial effect of triple point pinning observed for the arithmetic mean formulation[123].

For a one-dimensional system of two phases, with one phase-field defined in terms of the other $\phi_\beta = 1 - \phi_\alpha$, the evolution equation can be concisely written as

$$\frac{\partial\phi_\alpha}{\partial t} = \frac{2\gamma}{\tau}\frac{\partial^2\phi_\alpha}{\partial x^2} - \frac{1}{\tau\epsilon^2}\frac{\partial w}{\partial\phi_\alpha} - \frac{1}{\tau\epsilon}\frac{\partial\psi}{\partial\phi_\alpha}. \tag{3.13}$$

From this expression it is quite clear that the phase-field equation describes a reaction-diffusion system with a diffusivity $D_\phi = \frac{2\gamma}{\tau}$ and two reaction terms. The first reaction term is derived from w, with zero change if $\phi_\alpha \in \phi_b = \{0, 1\}$, with the second term describing the driving force, which is not expanded for clarity. The Lagrange multiplier vanishes because the assumption $\phi_\beta = 1 - \phi_\alpha$ already fulfills the constraint. The equilibrium profile can be calculated by assuming a steady state and setting the driving force to zero:

$$0 = \frac{2\gamma}{\tau}\frac{\partial^2\phi_\alpha}{\partial x^2} - \frac{1}{\tau\epsilon^2}\frac{\partial w}{\partial\phi_\alpha} \tag{3.14}$$

which is in fact an ordinary differential equation (ODE) and can be solved analytically. For the solution boundary conditions need to be specified, which are taken to be zero gradient conditions at infinity for simplicity.

From this equation, one can already give a relation between the phase-field derivative and the bulk potential by a series of transformations (dropping the multiplicative factor τ):

$$2\gamma\frac{\partial^2\phi_\alpha}{\partial x^2} = \frac{1}{\epsilon^2}\frac{\partial w}{\partial \phi_\alpha}| \cdot \frac{\partial \phi_\alpha}{\partial x} dx \tag{3.15}$$

$$2\gamma\frac{\partial}{\partial x}(\frac{\partial\phi_\alpha}{\partial x})^2 = \frac{1}{\epsilon^2}\frac{\partial w}{\partial x}|\int dx \tag{3.16}$$

$$2\gamma(\frac{\partial\phi_\alpha}{\partial x})^2 = \frac{1}{\epsilon^2}w(\phi_\alpha(x)) + C \tag{3.17}$$

$$\frac{\partial\phi_\alpha}{\partial x} = \sqrt{\frac{1}{2\gamma\epsilon^2}w(\phi_\alpha(x)) + C} \tag{3.18}$$

in which the integration constants on both sides are melded to C. In order to determine C we appeal to energy minimization by inserting the relation into the simplified functional:

$$\mathcal{F} = \int_V \epsilon\gamma((\phi_\alpha - 1)\frac{\partial\phi_\alpha}{\partial x} - \phi_\alpha\frac{\partial\phi_\alpha}{\partial x})^2 + \frac{16\gamma}{\pi^2\epsilon}(1-\phi_\alpha)(\phi_\alpha)dV \tag{3.19}$$

$$= \int_V C\epsilon\gamma + R(\phi_\alpha)dV \tag{3.20}$$

in which the remaining terms only depending on ϕ_α are collected in $R(\phi_\alpha)$ for conciseness. Based on this form an energy contribution due to C is evident. Given that ϵ, γ are positive, the contribution of C is minimized for $C \leq 0$. In order to exclude $C < 0$, consider its impact on the root expression in eq. (3.18). The gradient of ϕ_α should be real since ϕ_α is real as well and thus

$$C \leq \frac{w(\phi_\alpha)}{2\gamma\epsilon^2} \tag{3.21}$$

must hold for all values of ϕ_α. Since this includes $w(\phi_\alpha) = 0$, which is achieved for the bulk values ϕ_b, the only admissible value is $C = 0$. Thus a profile which minimizes the free energy is characterized by

$$\frac{\partial\phi_\alpha}{\partial x} = \sqrt{\frac{1}{2\gamma\epsilon^2}w(\phi_\alpha(x))}. \tag{3.22}$$

This generally describes the one-dimensional equilibrium in phase-field models, up to the term multiplying w, as long as the gradient energy density reduces to a Laplacian after

evaluating the variational derivative[2]. A useful corollary of this relation is that if the phase-field gradient is zero, the bulk energy density also needs to be zero and vice versa. For the employed obstacle potential this is only true for the bulk values $\phi_b = \{0, 1\}$, thus the gradient needs to vanish on the transition to the bulk regions.

Proceeding with the determination of the actual ϕ_α profile, the derivative of w reads

$$\frac{\partial w}{\partial \phi_\alpha} = \begin{cases} \frac{16\gamma}{\pi^2}(1 - 2\phi_\alpha) & \phi_\alpha \in [0, 1] \\ \infty, & else \end{cases} \tag{3.23}$$

thus the equation only within the interfacial region follows as

$$\frac{2\gamma}{\tau}\frac{\partial^2 \phi_\alpha}{\partial x^2} = \frac{16\gamma}{\pi^2 \tau \epsilon^2}(1 - 2\phi_\alpha) \tag{3.24}$$

which is a inhomogeneous linear ODE, whose solution is the sum of the general homogeneous solution and a particular solution accounting for the inhomogeneity. Note that the factor $\frac{\gamma}{\tau}$ is common and thus the solution is independent of it, hence it will be dropped in the following. The two trivial solutions of constant $\phi_\alpha \in \phi_b$ are achieved within the bulk and contribute no energy, which is simple to verify by insertion into the functional.

The homogeneous ODE reads

$$2\frac{\partial^2 \phi_\alpha}{\partial x^2} + \frac{16}{\pi^2 \epsilon^2}(2\phi_\alpha) = 0 \tag{3.25}$$

which by quick consultation of integration tables or by inspection of the characteristic polynomial has the general real-valued solution

$$\phi_\alpha^H = A \sin(kx) + B \cos(kx) \tag{3.26}$$

$$k = \frac{4}{\pi \epsilon} \tag{3.27}$$

with the constants A and B depending on boundary conditions. A particular solution is obtainable by variation of parameters, which yields

$$\phi_\alpha^P = \frac{1}{2} \tag{3.28}$$

[2] Well types of potentials avoid the ambiguity with the integration constant as they can use a definite integral to infinity due to the lack of a bulk region.

and thus the general solution to the inhomogeneous ODE describing the interface is

$$\phi_\alpha(x) = A\sin(kx) + B\cos(kx) + \frac{1}{2}. \tag{3.29}$$

Obviously, if there are multiple interfaces, each interface would contribute energy. Thus for the present goal of minimizing the energy, only solutions with one interface are sought. For the above this implies a restriction on the domain of $\phi_\alpha(x)$ as well as strict monotonicity. Suppose that the domain is $[-x_t, x_t]$ with x_t being the transition coordinate to the bulk. Demanding that the transition coordinate is symmetric is possible without loss of generality, as a translation of the coordinates does not change the energy of the solution. Given the restriction to the Gibbs simplex eq. (3.7), the range of $\phi_\alpha(x)$ is [0,1]. Assume for now that that $\phi_\alpha(x)$ is strictly monotonic increasing[3], then the start and end values of the domain and range are connected with the system[4]

$$\phi_\alpha(-x_t) = 0 \tag{3.30}$$

$$\phi_\alpha(x_t) = 1 \tag{3.31}$$

which has the solution $\{A = \frac{1}{2\sin(kx_t)}, B = 0\}$. Thus only x_t remains to be determined. For this the earlier assumption of the existence of a single interface is employed. The solution is periodic so far, with its period given by

$$P = \frac{2\pi}{k} = \frac{\pi^2\epsilon}{2}. \tag{3.32}$$

However, the sine becomes non-monotonic after a quarter period, thus the transition coordinate must be equal to a quarter period since at this point its derivative is also zero:

$$x_t = \frac{\pi^2\epsilon}{8} \tag{3.33}$$

which fully specifies the inner problem. Combining everything we have

$$\phi_\alpha(x) = \frac{1}{2}(1 + \sin(\frac{4x}{\pi\epsilon})) \tag{3.34}$$

[3] Demanding a decrease only swaps the roles of A and B, yielding a cosine profile, which is simply a shifted sine profile and thus contains the same energy.

[4] These can also be seen as the continuity conditions connecting the interface region to the bulk regions.

which describes the interfacial region. By the earlier domain and range arguments, $\phi_\alpha(\pm x_t) \in \phi_b$ and thus the solution is continuous to the bulk region. Without any bulk free energy densities, the bulk regions themselves need to contribute zero energy, which by the earlier functional is only so if they have zero gradients and attain the bulk values. Thus the profile for the entirety of the real line is given by

$$\phi_\alpha(x) = \begin{cases} 0, & x < -\frac{\pi^2\epsilon}{8} \\ \frac{1}{2}(1 + \sin(\frac{4x}{\pi\epsilon})), & |x| \leq \frac{\pi^2\epsilon}{8} \\ 1 & x > \frac{\pi^2\epsilon}{8} \end{cases} \tag{3.35}$$

and hence the interface width W is sharply defined as $\frac{\pi^2\epsilon}{4} \approx 2.5\epsilon$. Note that the x coordinate can be shifted arbitrarily without a change in energy.

A shorter, though somewhat less rigorous, derivation can be done by simply assuming a certain shape function and then determining its parameters based on the minimization of free energy and the boundary conditions. However, this requires sharp intuition or prior knowledge as to what kind of shape function is suitable. Alternatively, and in the spirit of the phase-field simply being a handy variable for solving the free boundary problem, the shape function can be assumed a priori and keeping the bulk potential indeterminate. By employing the method of manufactured solutions a bulk potential w_m can be found such that the shape function minimizes the free energy functional with that specific w_m.

Given the profile, the energy contained within the profile can be determined by inserting it into the simplified two-phase functional:

$$\mathcal{F} = \int_V \epsilon\gamma((\phi_\alpha - 1)\frac{\partial\phi_\alpha}{\partial x} - \phi_\alpha\frac{\partial\phi_\alpha}{\partial x})^2 + \frac{16\gamma}{\pi^2\epsilon}(1-\phi_\alpha)(\phi_\alpha)dV \tag{3.36}$$

$$= \int_{-x_t}^{+x_t} \frac{4\gamma}{\pi^2\epsilon}\left[1 + \cos^2(\frac{4x}{\pi\epsilon}) - \sin^2(\frac{4x}{\pi\epsilon})\right]dx \tag{3.37}$$

$$= \gamma. \tag{3.38}$$

in which the zero energy density of the bulk regions was exploited. This describes the energy contained in a single equilibrium interface between two phases, which is equal to the physical interface energy σ. Thus, the phase-field model parameter γ is equal to the physical surface energy σ. This convenient relation follows from the choice of prefactors for the functions a and w; different prefactors will yield a different expression, but it should never depend on the interface width parameter ϵ.

Any model with a driving force due to arbitrary couplings to other fields should also recover these equilibrium solutions. For this reason the present dissertation employs the so-called grand chemical potential formulation[117, 124], which decouples the chemical driving force from the interfacial properties and thus can be used generically. This primarily changes the way in which the concentration evolution equation is derived. First, species conservation is assumed to hold with

$$\frac{\partial c}{\partial t} = -\nabla \cdot (j_d + j_{at}) \tag{3.39}$$

which contains the contributions of the diffusive flux j_d and the antitrapping current j_{at}. The diffusive flux is defined as

$$j_d = -M \nabla \mu \tag{3.40}$$

in which the mobility M is defined as

$$M(\phi, \mu) = \sum_\alpha \frac{\partial c(\phi, \mu, T)}{\partial \mu} D(\phi) \tag{3.41}$$

$$= \sum_\alpha \frac{\partial c_\alpha(\mu, T)}{\partial \mu} h_\alpha(\phi) D(\phi) \tag{3.42}$$

which will reduce the later evolution equation to Fick's laws in the bulk regions. The diffusivity $D(\phi)$ depends on the phases and species diffusing, with the simplest formulation being

$$D(\phi) = \sum_\alpha D_\alpha g_D(\phi) \tag{3.43}$$

$$g_D(\phi) = \phi, \tag{3.44}$$

i.e. a linear interpolation of the bulk diffusivity D_α. Note that D_α can be taken to be a matrix describing the interdiffusion of a K component system within a phase α. For notational simplicity the diffusivity is assumed to be independent of temperature T. The term $\frac{\partial c}{\partial \mu}(\mu, T)$ is called the generalized susceptibility[124] and can be interpreted to convert a change in chemical potential to a change in concentration. The so-called antitrapping current j_{at}[117] is a phenomenological tool to reduce effects of artificially large interface widths for solidification problems. Its general formulation, assuming zero diffusivity in the solid α, reads

$$j_{at} = Q(g_\alpha(\phi)) \frac{\partial \phi_\alpha}{\partial t} (n_\alpha \cdot n_l)(c^\alpha - c^l) \tag{3.45}$$

in which the change of a phase α is scaled by the dot product of the interface normals $n_\alpha = \frac{\nabla\phi_\alpha}{|\nabla\phi_\alpha|}$, realizing transport from the solid α to the liquid l proportional to how quickly ϕ_α changed ($\frac{\partial\phi_\alpha}{\partial t}$) and thus the interface moved in its normal direction. The details of the individual terms within the expressions are given in [117].

In order to decouple the interfacial properties from the driving forces, the chemical potential μ is taken to be the independent variable, from which the species concentration c is derived. With this choice, the equilibrium concentration profile, defined by constant chemical potential, simply follows from the phase-field profile and hence decoupling is achieved. The concentration is now linked to the functional by another variation[124]

$$c = -\frac{\delta\mathcal{F}}{\delta\mu} \tag{3.46}$$

$$c = -\frac{\partial\psi(\phi,\mu,T)}{\partial\mu} \tag{3.47}$$

$$c = -\sum_\alpha \frac{\partial\psi_\alpha(\mu,T)}{\partial\mu} h_\alpha(\phi) \tag{3.48}$$

$$c = \sum_\alpha c_\alpha(\mu,T) h_\alpha(\phi) \tag{3.49}$$

in which the thermodynamic relation $c_\alpha = -\frac{\partial\psi_\alpha}{\partial\mu}$ is exploited to arrive at the phase-specific concentration $c_\alpha(\mu,T)$. Note that eq. (3.49) precisely shows that the concentration profile follows from a phase-dependent, but constant function in equilibrium and the phase-field variable. Taking the time derivative of eq. (3.49) yields

$$\frac{\partial c}{\partial t} = \sum_\alpha \frac{\partial h_\alpha(\phi)}{\partial t} c_\alpha(\mu,T) + \sum_\alpha h_\alpha(\phi) \frac{\partial c_\alpha(\mu,T)}{\partial t} \tag{3.50}$$

$$= \sum_\alpha \frac{\partial h_\alpha(\phi)}{\partial t} c_\alpha(\mu,T) + \sum_\alpha h_\alpha(\phi) \left[\frac{\partial c_\alpha(\mu,T)}{\partial\mu} \frac{\partial\mu}{\partial t} + \frac{\partial c_\alpha(\mu,T)}{\partial T} \frac{\partial T}{\partial t} \right]. \tag{3.51}$$

Now equate eq. (3.39) to eq. (3.51) and solve for the time evolution of the chemical potential:

$$\frac{\partial\mu}{\partial t} = \left[\sum_\alpha h_\alpha(\phi) \left(\frac{\partial c_\alpha(\mu,T)}{\partial\mu} \right) \right]^{-1} \tag{3.52}$$

$$\left(-\nabla\cdot\left(j_d + j_{at} \right) - \sum_\alpha c_\alpha(\mu,T) \frac{\partial h_\alpha(\phi)}{\partial t} - \sum_\alpha h_\alpha(\phi) \frac{\partial c_\alpha(\mu,T)}{\partial T} \frac{\partial T}{\partial t} \right).$$

The divergence represents the transport by diffusion and the antitrapping current, with the reaction terms accounting for a change in chemical potential due to phase changes and temperature changes. In the present work, only the case of $K = 2$ is considered and thus there is only one independent component c.

Within this work, the temperature will not be solved for explicitly. Rather, only analytic expressions for the temperature will be used:

$$T(x,t) = T_{iso} \tag{3.53}$$
$$T(x,t) = T_{iso}(t) \tag{3.54}$$
$$T(x,t) = T_{start} - G(x - vt) \tag{3.55}$$

with the first two expression describing a purely isothermal condition with and without a time dependence. The last expression is the so-called frozen temperature approximation (FTA), due to Warren and Langer[125], often employed in solidification due to the large difference in transport coefficients between thermal and mass transport. It assumes that a linear temperature profile exists, characterized by its temperature gradient G, which is pulled across the sample with a velocity v, which is also commonly called pulling velocity.

3.1.2 Phase-field model of sintering — diffusion only

The model presented in this section is that of [35]. It is similar to the model in section 3.1.1 as it also employs the grand potential ansatz in order to decouple the driving forces from the interface energy. However, it removes some specifics of the alloy solidification problem and adds some due to the sintering problem. The key changes are as follows

- introduction of interfacial diffusivities
- removing the antitrapping current

with the reasons given in the following. In contrast to solidification in which the melt diffusivity typically controls the speed of the process, sintering is primarily controlled by processes occurring on grain boundaries and surfaces. Thus it is natural to extend the diffusivity to account for these regions specifically. The antitrapping current is necessary in alloy solidification for diffusional contrasts between phases in order to avoid excessive solute trapping. While physical in nature, the magnitude is scaled with the interface width within the phase-field method and hence computationally efficient interface widths

would yield excessive solute trapping. However, if the phase-field interface width is close to the physical width, only small errors will be incurred.

The evolution equations thus read as

$$\tau(\phi,\nabla\phi)\epsilon\frac{\partial\phi_\alpha}{\partial t} = -\frac{\delta\mathcal{F}}{\delta\phi_\alpha} - \Lambda \tag{3.56}$$

$$\frac{\partial\mu}{\partial t} = \left[\sum_\alpha h_\alpha(\phi)\left(\frac{\partial c_\alpha(\mu,T)}{\partial\mu}\right)\right]^{-1} \left(\nabla\cdot j_d - \sum_\alpha c_\alpha(\mu,T)\frac{\partial h_\alpha(\phi)}{\partial t} - \sum_\alpha h_\alpha(\phi)\frac{\partial c_\alpha(\mu,T)}{\partial T}\frac{\partial T)}{\partial t}\right) \tag{3.57}$$

with mostly the same meaning as in section 3.1.1. A general simplification employed for sintering is that only two kinds of phases will be considered, viz. the surrounding vapor ϕ_V, $\mathrm{V}=0$ and solid grains of distinct, arbitrary orientation ϕ_α, $\alpha>0$. The diffusive flux j_d is still calculated as previously, but with a new definition of the mobility

$$j_d = M\nabla\mu \tag{3.58}$$

$$M = M_\alpha + M^{gb}_{\alpha\beta} + M^s_{\alpha\mathrm{V}} \tag{3.59}$$

$$M_\alpha = \sum_\alpha \frac{\partial c_\alpha(\mu,T)}{\partial\mu} h_\alpha(\phi) D_\alpha\phi_\alpha \tag{3.60}$$

$$M^s_{\alpha\mathrm{V}} = \sum_{\alpha>\mathrm{V}} D^s_\alpha\left(\frac{\partial c_\alpha}{\partial\mu}\phi_\alpha + \frac{\partial c_\mathrm{V}}{\partial\mu}\phi_\mathrm{V}\right) I(\phi_\alpha,\phi_\mathrm{V}) \tag{3.61}$$

$$M^{gb}_{\alpha\beta} = \sum_{\alpha>\mathrm{V}}\sum_{\beta>\alpha} D^{gb}_{\alpha\beta}\left(\frac{\partial c_\alpha}{\partial\mu}\phi_\alpha + \frac{\partial c_\beta}{\partial\mu}\phi_\beta\right) I(\phi_\alpha,\phi_\beta) \tag{3.62}$$

in which the symmetry of the $\alpha\beta$ phase description is exploited. Thus the mobility includes the effect of interfaces enhancing diffusion in a scalar manner as found across grain boundaries (gb) and surfaces (s). The function $I(\phi_\alpha,\phi_\beta) = 4\phi_\alpha\phi_\beta$ interpolates the interfacial diffusion across the variable phase-field.

The interfacial diffusivities take into account the physical δ_i and phase-field W interface widths by scaling these values as to match the diffusivity in the physical case:

$$\int_{-\delta_i/2}^{\delta_i/2} D_i^{real}\,dx = \int_{-W/2}^{W/2} I(\phi_\alpha,\phi_\beta) D_i^{sim}\,dx \tag{3.63}$$

$$\rightarrow D_i^{sim} = D_i^{real}\frac{8\delta_i}{\epsilon\pi^2} \tag{3.64}$$

which is equivalent to [126] except for the parametrization of the interface width. The subscript i stands for both the surface diffusion and the grain boundary diffusion and its accompanying interface width. The input values as listed in the later tables always describe D_i^{real} and are transformed to D_i^{sim} on simulation start.

This model effectively assumes that diffusive fluxes alone can fully describe the sintering process. As shown by the author in chapter 6 however, models without advection have a shrinkage which is strongly dependent on the system size. Thus the next section describes a literature model including advective terms.

3.1.3 Phase-field model of sintering — advective

The model presented in this section is that of [33]. Since it differs substantially from the previous model in its energetic description, different variables will be used, consistent with the publication.

Within this model, the free energy functional is written as

$$F = \int f(\rho,\eta) + 0.5\sum_{\alpha}\beta_\eta|\nabla\eta_\alpha|^2 + 0.5\beta_\rho|\nabla\rho|^2 dV \tag{3.65}$$

$$\begin{aligned} f(\rho,\eta) &= A\rho^2(1-\rho)^2 \\ &\quad + B\Big[\rho^2 + 6(1-\rho)\sum_{\alpha}(\eta_\alpha^2) - 4(2-\rho)\sum_{\alpha}(\eta_\alpha^3) + 3(\sum_{\alpha}\eta_\alpha^2)^2\Big] \end{aligned} \tag{3.66}$$

with ρ representing the local density of material and η representing a vector of phase-fields for the α grains. The surrounding vapor as identified in the previous section is only implicitly defined as $1-\sum_\alpha \eta_\alpha$. The bulk energy f in this case is a mix of the terms w, ψ of eq. (3.1) and thus accounts for both the driving force as well as parts of the equilibrium profile. A similar analysis as previously shown can be conducted[30] to relate the free energy parameters to the physical parameters of interest. The evolution equations are derived by combining a non-conservative Allen-Cahn equation and a conservative Cahn-Hilliard equation and adding advective terms:

$$\frac{\partial\eta_\alpha}{\partial t} = -L\frac{\delta F}{\delta\eta_\alpha} - \nabla\cdot(\eta_\alpha\vec{v}_\alpha(\vec{x})) \tag{3.67}$$

$$\frac{\partial\rho}{\partial t} = \nabla\cdot(D(\eta,\rho)\nabla\frac{\delta F}{\delta\rho} - \rho\vec{v}(\vec{x})) \tag{3.68}$$

with L being the grain mobility, $\vec{v}_\alpha(\vec{x})$ the local velocity of an α grain, D representing the local diffusivity and $\vec{v}(\vec{x})$ the local velocity of the density. The diffusivity is formulated as

$$D(\eta,\rho) = D_{vol}\phi(\rho) + D_{vap}(1-\phi(\rho)) + D_{surf}\rho(1-\rho) + D_{gb}\sum_{\alpha}\sum_{\beta\neq\alpha}\eta_\alpha\eta_\beta \tag{3.69}$$

$$\phi(\rho) = \rho^3(10-15\rho+6\rho^2) \tag{3.70}$$

in order to include bulk, surface and grain boundary diffusion.

The velocities are calculated by postulating a force density on the grain boundaries

$$d\vec{F}_\alpha = \kappa\sum_{\beta\neq\alpha}(\rho-\rho_{gb})g(\alpha,\beta)(\nabla\eta_\alpha - \nabla\eta_\beta) \tag{3.71}$$

with the density difference $(\rho-\rho_{gb})$ acting as a kind of spring term, which allows κ to be interpreted as a stiffness. The gradient difference ensures conservation of momentum and the function $g(\alpha,\beta)$ is used to identify grain boundaries via

$$g(\alpha,\beta) = \begin{cases} 1, & \eta_\alpha\eta_\beta \geq \eta_{\alpha\beta}^{th} \\ 0, & else. \end{cases} \tag{3.72}$$

The force density is integrated to determine a resultant force which is assumed to act on the center of mass of the particles

$$\vec{F}_\alpha = \int_V d\vec{F}_\alpha dV \tag{3.73}$$

which would induce a torque if the force density is distributed asymmetrically w.r.t. the line connecting the center of the GB and the center of mass. This effect is dropped here for conciseness as it has no influence on densification[36]. This force is now assumed to cause an instantaneous velocity via

$$\vec{v}_{\eta_\alpha} = \frac{m_t}{V_\alpha}\vec{F}_\alpha \tag{3.74}$$

$$V_\alpha = \int_V \eta_\alpha dV \tag{3.75}$$

i.e. a mobility m_t is introduced and the particle force is scaled with the particle volume V_α. Finally, the velocities obtained thus are interpolated as

$$\vec{v}_\alpha(\vec{x}) = \vec{v}_{\eta_\alpha}\eta_\alpha(\vec{x}) \tag{3.76}$$

$$\vec{v}(\vec{x}) = \sum_\alpha \vec{v}_\alpha(\vec{x}) \tag{3.77}$$

which ensures a smooth transition across interfaces.

3.2 New model developments

In this section the new developments produced during the dissertation are detailed. It collects the developments of the author's papers [69, 80, 114–116].

3.2.1 Nucleation

The phase-field model of alloy solidification described in section 3.1.1 does not naturally incorporate the spontaneous formation of new phases. Thus a nucleation mechanism needs to be modelled and implemented. For this it is assumed that nucleation of new phases happens primarily at existing solid-liquid sl interfaces. At any such point, if the driving force $\psi_{lP}(\mu, T)$ of a trial phase P w.r.t the liquid phase exceeds a critical value $\psi_B(\mu, T)$, then the liquid phase is recolored to the trial phase P. The critical value ψ_B plays the role of a nucleation barrier. Since the scale of the simulation is far above that of classical nucleation theory and heterogeneous nucleation is considered, the classical expression for the nucleation barrier cannot be employed. Instead, the barrier is assumed to be given by the state in which the present interface would begin to melt. This is defined by the equilibrium chemical potential $\mu_{eq,sl}(T)$ of a plane sl interface with the associated barrier being $\psi_B = \psi_{lP}(\mu_{eq,sl}(T), T)$, which is compared against $\psi_{lP}(\mu, T)$, i.e. the actual field value. Furthermore, $\psi_{lP}(\mu, T)$ is enforced to be positive such that there is a driving force for growth of the trial phase P. Mathematically this can be written as

$$\psi_{lP}(\mu, T) = \psi_l(\mu, T) - \psi_P(\mu, T) \tag{3.78}$$

$$\psi_{lP}(\mu, T) > 0 \tag{3.79}$$

$$\psi_{lP}(\mu, T) > \psi_{lP}(\mu_{eq,sl}(T), T) \tag{3.80}$$

with the currently present interface being an sl interface.

A graphical representation of this is given in fig. 3.1 for a eutectic system below its eutectic temperature: The equilibrium points with their associated $\mu_{eq,sl}$ are depicted with the black circles, with their bounding polygon describing the region where eutectic growth is possible. Outside of this region one of the solid phases will start to melt. Since this state is below the eutectic temperature, the other solid phase will still be stable and thus suitable for nucleation.

This tacitly excludes the effect of surface energy and thus nuclei can be eliminated afterwards due to its effects. The effect of surface energy could be included in the spirit of

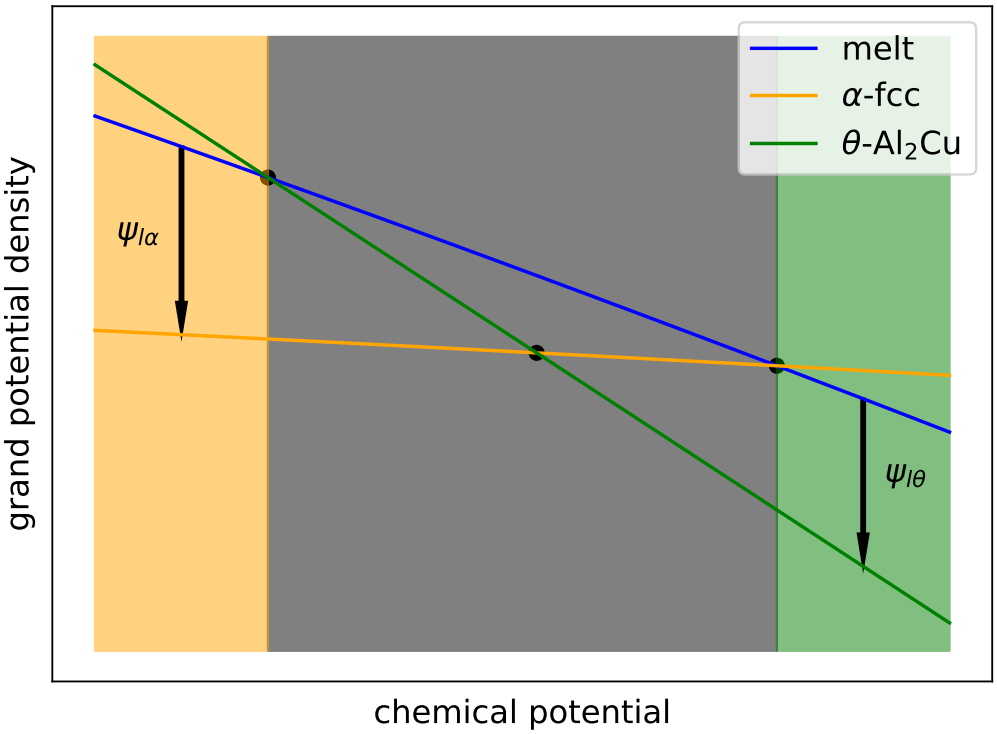

Figure 3.1: The grand potentials of the phases over the chemical potential for a constant temperature are depicted. The shaded grey region in the center describes the space in which eutectic growth is possible, with the colored shaded regions indicating where nucleation of the respectively colored phase is possible. The driving force for nucleation of either phase is depicted by arrows for two chosen chemical potentials.

classical nucleation theory by adding a surface energy and curvature dependent barrier term. Furthermore, the fluctuation distribution of a real system could be accounted for by including the appropriate random distribution in the driving force.

3.2.2 Improving sintering models

As will become clear upon reading chapter 6, the currently most popular[5] phase-field model for solid-state sintering [33] has several defects which need to be addressed. These defects are

1. non-monotonic reduction of free energy
2. change of dihedral angle
3. unshrinkage
4. implicit compression and rarefaction
5. non-convergence of densification with system size

and will be addressed in order in the following subsections. The first three defects stem from the fact that the force terms in eq. (3.71), rewritten here for further use with the concentration c instead of the density ρ

$$d\vec{F}_\alpha = \kappa \sum_{\beta \neq \alpha} (c - c_{gb}) g(\alpha, \beta)(\nabla \eta_\alpha - \nabla \eta_\beta) \tag{3.81}$$

have no connection to the energy functional from which the rest of the evolution equations are derived from. More specifically, these force terms lead to a non-vanishing advection velocity in states which are supposedly equilibria according to the energy functional. The term c_{gb} is identified as the main factor for this. It is classically interpreted as the "grain boundary equilibrium concentration" c_{gb}^{eq}, but cannot be taken to have this sense with the energy functional assigning no different concentration to grain boundary regions. This directly leads to a non-monotonic reduction of free energy and its accompanying change of the equilibrium dihedral angle. The effect of unshrinkage, i.e. the lengthening of a sample over time even though it is not favourable to do so, is linked to this: If the fluxes due to the energy functional increase the concentration c on the grain boundary above c_{gb}, then $d\vec{F}_\alpha$ will be oriented *away* from the grain boundary and hence the advection fluxes will *stretch* the sample. These points are also discussed in-depth in chapter 6. The implicit compression/rarefaction behaviour is due to the interpolation of the velocities. Finally, densification does not converge because the displacement originating somewhere in a body is not propagated correctly through the system.

[5] Based on the number of citations determined by a search for "phase-field sintering" on Web of Science, which yielded 190 citations for [33] at the time of writing, with the next phase-field model being [127] with 68 citations.

3.2.2.1 Fixing the equilibrium

A quite generic method of choosing c_{gb} such that these problems are resolved is by approximating it with the present simulation state S in a suitable sense such that a value close to the true c_{gb}^{eq} is obtained. Two methods for this will be investigated, both based on the approximation

$$c_{gb}^{eq} \sim c_\alpha(\mu_{eq} + \Delta\mu, T) \tag{3.82}$$

i.e. the grain boundary equilibrium concentration is equivalent to the equilibrium concentration of a bulk α grain, plus a deviation from e.g. curvature effects. In the first method, the deviation is approximated by

$$\Delta\mu = \gamma_s \kappa, \tag{3.83}$$

i.e. the Gibbs-Thomson equation is employed. The curvature κ is approximated based on the particle volume and the assumption of a circle (two dimensions) or sphere (three dimensions).

For the second method it is assumed that the chemical potential on a particle's surface is an approximation of $\Delta\mu$, with its average

$$\hat{\mu}_\alpha = \frac{\int \mu \phi_\alpha \phi_\mathrm{V} dV}{\int \phi_\alpha \phi_\mathrm{V} dV} \tag{3.84}$$

taking into account local variations. Note that if the equilibrium chemical potential μ_{eq} of a plane α surface is not zero, this chemical potential needs to be subtracted from $\hat{\mu}_\alpha$.

Both methods obtain an approximation $\Delta\mu_\alpha$ per grain, but the value of $c_{gb}(S)$ should be symmetric w.r.t. the grains since it describes a pairwise interaction. A simple averaging of both values per grain boundary guarantees this symmetry. The effects of these methods will be shown in chapter 7.

An alternative method, not considered within the present work, is to use a related dynamic variable, e.g. mass flux into the GB, for specifying the deviation from equilibrium. This variable should of course vanish in equilibrium and should be well-defined across the bulk, interface and triple point regions consisting of a GB and the vapor phase. The last condition is important, as any initial contact between grains in a phase-field model will be described by regions more akin to triple points than GBs.

3.2.2.2 Compression and rarefaction

Consider the formulation due to Wang [33], reproduced in section 3.1.3, for adding rigid-body motion to a phase-field model of sintering of eqs. (3.67) and (3.76), in one dimension:

$$\frac{\partial \eta_\alpha}{\partial t} = -L\frac{\delta F}{\delta \eta_\alpha} - \nabla \cdot (\eta_\alpha v_\alpha(x)) \tag{3.85}$$

$$v_\alpha(x) = v_{\eta_\alpha}\eta_\alpha(x) \tag{3.86}$$

and let us drop the variational derivative, so we can focus on the effect of advection:

$$\frac{\partial \eta_\alpha}{\partial t} = -\nabla \cdot (\eta_\alpha v_\alpha(x)) \tag{3.87}$$

$$= -\nabla \cdot (\eta_\alpha^2 v_\alpha) \tag{3.88}$$

which is in fact the inviscid Burgers equation up to a multiplicative factor v_α. Thus it naturally allows for regions to be compressed or rarefied, possibly leading to shock formation or smearing the interface more than would be expected. To show this effect in a simple example, the hyperbolic PDE solver ClawPack[128–130] was employed to

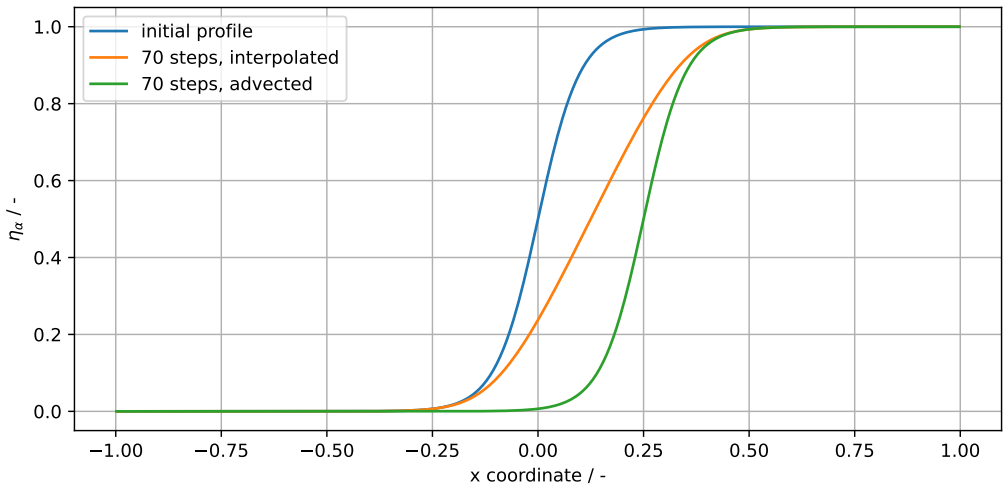

Figure 3.2: Comparison of employing eq. (3.88) (velocity interpolated) and eq. (3.89) (constant velocity advection). The initial profile is severely distorted by eq. (3.88) due to rarefaction, whereas advection leaves the profile undistorted.

calculate the profile evolution across a particle-vapor interface with eq. (3.88) as well as with simple advection

$$\frac{\partial \eta_\alpha}{\partial t} = -\nabla \cdot (\eta_\alpha v_\alpha) \tag{3.89}$$

and employing non-reflecting outflow boundary conditions, up to some arbitrary time. The results are shown in fig. 3.2 and it is quite evident that the initial profile is severely altered (rarefied) by eq. (3.88) but not by eq. (3.89). A compression effect would be observed if the velocity profile across a grain boundary would be employed. Given that solids are often assumed to be incompressible[6], these effects should not be present.

A direct way to exclude these effects when advecting grains is not to interpolate in the first place, but to directly use the rigid-body velocity v_α for advection. This reduces the grain advection to eq. (3.89) and thus does not contain any compression or rarefaction effects. However, the concentration equation still contains the same problem. Here a bit more care is required, as the kind of phase-field profile employed plays a role. For a hyperbolic tangent as occurs in the model described in section 3.1.3, the suggestion of [109]

$$v_\alpha(x) = \begin{cases} v_\alpha, & \eta_\alpha(x) > \eta_{th} \\ 0, & else \end{cases} \tag{3.90}$$

$$v(x) = \sum_\alpha v_\alpha(x) \tag{3.91}$$

can be employed, which basically decomposes the domain into regions of constant velocity with jumps in between, according to the threshold value of η_{th}. For the obstacle potential as employed in the majority of the dissertation a simple interpolation scheme which reduces this effect is

$$v_c(x) = \frac{\sum_{\alpha!=\mathrm{V}} v_\alpha \phi_\alpha(x)}{\sum_{\alpha!=\mathrm{V}} \phi_\alpha(x)} \tag{3.92}$$

which exploits the fact that the vapor phase V is explicitly tracked and that bulk regions are defined by constant values. This also results in jump functions for the velocity across particle-vapor interfaces, but allows for some compression within the grain boundary since vacancy annihilation there should lead to a temporary density increase.

[6] A case can be made for the presence of compression on the grain boundary as long as vacancies are being absorbed, since this implies a density change.

The model modifications presented so far will be employed in chapter 7.

3.2.2.3 Convergence of shrinkage

The problem of non-convergence of shrinkage with system size stems from the inhomogeneous shrinkage implied by the model for calculating velocities, as shown in chapter 7. More specifically, if the model of section 3.1.3 is employed, only particles on the edge of a body can densify w.r.t. any particles on the inside of a body, as these have missing neighbours. In order to develop a model which avoids this problem, molecular dynamics (MD) simulations are conducted to determine rules of motion for grains during the sintering process. The simulations leading to the model are detailed in chapter 8, with the observed rules being recounted here, followed by the model development. Key to these studies was the capability of explicitly identifying a link between the displacement of individual grains and the number of vacancies which are absorbed at grain boundaries. By considering several geometric variations, the following qualitative rules are obtained:

1. the displacement of individual atoms is largely homogeneous within each grain (rigid-body assumption)
2. the grain displacement due to vacancy absorption scales linearly the grain boundary area
3. the grain displacement due to vacancy absorption does not scale with the grain length
4. the grain displacement due to vacancy absorption scales linearly with the number of absorbed vacancies
5. the displacement due to vacancy absorption at individual GBs can be overlaid via superposition

The first rule is already present in the model for velocity calculation. The second and third rule are violated, as the grain volume is assumed to be the determining factor and not the grain boundary area. However, this violation only scales the absolute magnitude of velocities, which does not have any effect on the non-convergence with system size. While the number of vacancies absorbed is not identified explicitly by the model, the construction of the force terms $c - c_{gb}$ effectively imply a kind of relaxation towards an equilibrium concentration of vacancies, thus can be roughly interpreted as a scaled number of vacancies absorbed given the linear relation between number density and

concentration. The superposition rule is not present in the model and will be shown to be the factor which allows convergence.

It is useful to split the application of these rules into two parts: First, a model relating the displacement jump $\Delta u_{\alpha\beta}$ across a grain boundary to its properties will be determined. Second, the displacement jumps are correlated to each other in a system of equations whose solution gives individual grain displacements u_α.

Consider an $\alpha\beta$ bicrystal, whose grain boundary absorbed ΔN vacancies. Assume that each vacancy contributes a volume change equivalent to the atomic volume Ω. Now split this volume change into an area — identified to be the grain boundary area A_{gb} — and a length change ΔL. Thus we have

$$\Delta V = \Omega \Delta N = A_{gb} \Delta L \tag{3.93}$$

$$\Delta L = \frac{\Omega \Delta N}{A_{gb}} \tag{3.94}$$

with ΔL representing the length change of the entire bicrystal, with $\Delta L > 0$ implying vacancy absorption and thus shrinkage. This relation accounts for rules 1–4. Since we are dealing with a bicrystal whose grains move rigidly, the length change ΔL is related to the individual displacements:

$$u_\alpha - u_\beta = \Delta L \tag{3.95}$$

$$= \Delta u \tag{3.96}$$

which is also simply the displacement jump Δu across the grain boundary. By employing the superposition property this should hold for all grain boundaries simultaneously, yielding a matrix equation

$$\mathrm{C}u = \Delta u. \tag{3.97}$$

The contact matrix C consists of rows with zeros except for two entries of $+1$ and -1, representing the sign of the displacement jump and the orientation of the grain boundary plane within the laboratory frame. The grain boundary plane enters the problem, as the grains should move *towards* the grain boundary for vacancy absorption and v.v. for generation.
Equation (3.97) is, in general, overdetermined as the number of grain boundaries B will tend to be larger than the number of grains N. For the special case of a linear chain of grains, we have $B = N - 1$. Accounting for conservation of momentum adds another equation, which makes the matrix C square. Since the equations in this special case

are linearly independent, the matrix C is also of full rank and thus the system is also uniquely solvable. The structure of the matrix, excepting conservation of momentum, can also be thought of as a finite difference matrix between grains. Hence the action of matrix can be thought to be differentiation, with its inverse being the integration of Δu across space.

For the more general case of arbitrary systems of grains, eq. (3.97) can be solved, in principle, with a least-squares approach. As will become clear from the following adjustment of the model for the phase-field model, a direct least-squares approach will be computationally inefficient. Before proceeding to this however, the present model will be investigated as to whether its shrinkage is independent of system size.

Consider a chain of N equally-sized cuboid grains of individual length l and constant grain boundary area A. Assume that each of the $B = N - 1$ GBs has just absorbed ΔN vacancies, which induces a displacement jump Δu across each GB. By the superposition property, the solution is the sum of all solutions only dealing with a single GB. Thus without loss of generality, assume that only the first GB absorbed vacancies. This results in the system

$$u_1 - u_2 = \Delta u \tag{3.98}$$

$$\sum_i u_i = 0 \tag{3.99}$$

with conservation of momentum employing the equal grain size assumption. The first equation directly resolves to $u_2 = u_1 - \Delta u$. Since there is no displacement jump between grains 2 and 3, 3 and 4 and so on, we must necessarily have

$$u_2 = u_3 = u_4 = \ldots = u_1 - \Delta u \tag{3.100}$$

and inserting this into conservation of momentum yields

$$u_1 + (N-1)(u_1 - \Delta u) = 0 \tag{3.101}$$

$$N u_1 = (N-1)\Delta u \tag{3.102}$$

$$u_1 = \frac{N-1}{N}\Delta u \tag{3.103}$$

$$u_2 = (\frac{N-1}{N} - 1)\Delta u \tag{3.104}$$

This procedure can easily be repeated for every grain boundary yielding a similar expression for the grain displacement. The displacements will always be weighted by how

many grains are to the left and to the right of the grain boundary[7] absorbing vacancies, i.e.

$$u_i = \frac{N-i}{N}\Delta u \tag{3.105}$$

$$u_{i+1} = (\frac{N-i}{N} - 1)\Delta u \tag{3.106}$$

with all grains left of grain i exhibiting the same displacement as grain i and v.v. for grains right of grain $i+1$. The superposition property now lets us sum over all these problems to arrive at the solution to our original problem. For simplicity, we only consider the leftmost grain

$$u_1^{SP} = \sum_{i=1}^{N-1} \frac{N-i}{N}\Delta u \tag{3.107}$$

$$= \frac{\Delta u}{N} \sum_{i=1}^{N-1} N - i \tag{3.108}$$

$$= \frac{\Delta u}{N}\left[N(N-1) - \frac{(N-1)N}{2}\right] \tag{3.109}$$

$$= \frac{\Delta u(N-1)}{2} \tag{3.110}$$

and note that there are only $N-1$ GBs and thus limit the sum to $N-1$. As a sanity check, consider $N=2$ in which the above formula yields $u_1^{SP} = \frac{\Delta u}{2}$ which is also the result of solving eqs. (3.98) and (3.99) by hand. It is entirely sufficient to only consider the leftmost grain since the displacement field should be point symmetric w.r.t. the total center of mass (conservation of momentum) and thus $u_N^{SP} = -u_1^{SP}$. Furthermore, the total length change of the chain is simply $u_1^{SP} - u_N^{SP} = \Delta u(N-1)$. Hence we have with the definition of strain

$$e = \frac{\Delta L}{L} \tag{3.111}$$

$$= \frac{\Delta u}{l}\frac{N-1}{N} \tag{3.112}$$

which converges to a constant ($\frac{\Delta u}{l}$) as N goes to infinity.

[7] In effect the grains with non-absorbing boundaries can be lumped together with their adjacent, absorbing grain.

This would imply some finite dependence of the strain on the system size (here number of grains N) as a whole. However, each contact experiences the same strain $\frac{\Delta u}{l}$. The apparent non-convergence at low N results from the choice of end-to-end distance as the reference length. If the reference length is taken to be measured between center of masses, then N cancels out and constant strain independent of system size is achieved.

3.2.2.4 Translation into the phase-field model

Now that the shrinkage or equivalently strain has been shown to be convergent we can translate the earlier model, specified in terms of what is available on the MD scale, to a phase-field model. The matrix equation of eq. (3.97) linking the grain displacements to the displacement jumps can be directly translated as-is, with the grain boundary plane being identified with the one-sided grain boundary unit normal $\vec{n}_{\alpha\beta}$ defined below.

The remaining problem is the specification of the displacement jump Δu in terms of variables accessible within the phase-field. For this the relations

$$V_{\alpha\beta} = \int_{GB} 4\phi_\alpha\phi_\beta dV \tag{3.113}$$

$$A_{\alpha\beta} = \frac{V_{\alpha\beta}}{l_0} \tag{3.114}$$

$$\vec{\Delta u}_{\alpha\beta} = \frac{1}{V_{\alpha\beta}} \int_{GB} 4\phi_\alpha\phi_\beta \frac{\Omega}{A_{\alpha\beta}} \Delta n_{\alpha\beta}\vec{n}_{\alpha\beta} dV \tag{3.115}$$

are employed. First, the grain boundary volume $V_{\alpha\beta}$ is determined and divided by the unit grain boundary width $l_0 = \int_0^1 4\phi_\alpha\phi_\beta dx = \frac{\pi^2\epsilon}{8}$ to obtain the grain boundary area $A_{\alpha\beta}$. Next, the grain boundary "phase" weighted number density of absorbed vacancies $\Delta n_{\alpha\beta}$ is integrated over each $\alpha\beta$ grain boundary separately, which with the atomic volume Ω yields the volume generated/destroyed via vacancy generation/absorption. The orientation of the grain boundary is taken into account by employing the grain boundary unit normal $\vec{n}_{\alpha\beta} = \frac{\nabla(\phi_\alpha - \phi_\beta)}{|\nabla(\phi_\alpha - \phi_\beta)|}$ in the spirit of [33]. The number density n can be expressed with the concentration c via

$$n = \frac{N_a}{V_m} c \tag{3.116}$$

with Avogadro's constant N_a and the molar volume V_m.

Note that this description requires tracking the pairwise interactions $V_{\alpha\beta}$, $\Delta n_{\alpha\beta}$ and $\vec{n}_{\alpha\beta}$. In a naive implementation these would be N^2 matrices, which would need to be held for each parallel process. Hence excessive memory and communication requirements

would follow from this naive approach. Instead, these matrices are distributed across the processes and only a fixed number of neighbours is assumed to exist for each phase α: This effectively results in a constant memory usage per parallel process. However, due to the distributed nature of these matrices, the solution speed of eq. (3.97) is limited by communication. Since the matrix C effectively represents differentiation, the spatial distribution of Δu determines the shape of u. Assuming that all grain boundaries have similar vacancy absorption behaviour, then the spatial dependence of Δu can be taken to be a constant function, plus some local variations which do not affect the overall solution shape. Hence a linear ansatz $u(x) = m(x - x_m)$ can be employed for u, with a slope m, each particle's position x and the total center of mass x_m. This massively reduces the calculation and communication requirements and is described in greater detail in chapter 8.

The final piece is the calculation of $\Delta n_{\alpha\beta}$. For this a relaxation ansatz with a relaxation time t_r is employed

$$\frac{\partial n}{\partial t} = -\frac{n - n_{eq}^{gb}}{t_r} \tag{3.117}$$

with the "equilibrium grain boundary number density" n_{eq}^{gb} defined via eqs. (3.82) and (3.84) in terms of the mole fraction c.

3.2.3 Influence of stress on densification

Stress is often applied in sintering in order to speed up densification. The present model allows a quite simple way of including part of this mechanism: Within the model, the speed of densification is controlled by the vacancy absorption rate of eq. (3.117). It is dependent on the equilibrium GB vacancy concentration c_{eq}^{gb} which is calculated based on an estimated capillary pressure eqs. (3.82) and (3.84). Hence one can simply shift this pressure by an externally applied stress. An uniaxial stress state on the GBs can be achieved by projecting the applied stress direction onto the grain boundary normal, i.e.

$$c_{eq}^{gb}(S) = c_\alpha(\mu_s + \sigma(\vec{n}_{\alpha\beta})) \tag{3.118}$$

$$\sigma(\vec{n}_{\alpha\beta}) = \sigma(\vec{v}_\sigma \cdot \vec{n}_{\alpha\beta}) \tag{3.119}$$

with the direction of uniaxial applied stress $\vec{v}_\sigma$. In the case of an isotropic pressure the projection step can be skipped. This approach is in the spirit of Coble[131] in that

the driving force for sintering, capillary pressure, is summed together with the external pressure.

As creep and sintering are deeply related phenomena, a sintering model should also be naturally be able to approximate the creep process. This will be tested in chapter 9 by applying uniaxial tensile stress to almost dense bodies.

3.3 Parametrizing real systems

The parameters given in the previous sections can be related to real systems, allowing for the generation of a digital twin. The easiest parameter given the current model is the surface energy σ, which is exactly the model parameter γ as previously shown. The interface width parameter ϵ can be related to the physical interface width, but fixing it to the physical width is not necessary. This is because the phase-field is an approximation to a free boundary problem and as long as this approximation holds, the actual width is only a numerical parameter.

The situation is more complex for the relaxation coefficient τ. If a pure phase-field problem is considered, it can be easily related to the interfacial mobility[132] as measurable e.g. for grain growth. For phase-field problems involving other fields, the appropriate kinetic boundary conditions need to be retrieved if τ is to be related to a measurable parameter. If it is simply taken to be a numerical parameter, then it should be chosen such that the controlling field is not altered. For example, in a diffusion-controlled process such as sintering, it should be chosen such that the phase-field relaxes much faster than the diffusion field, effectively hiding the kinetic influence of the phase-field at a smaller time scale. While practical, this sets a limit on the ratio between diffusive and kinetic speeds which can be employed. It can also lead to restrictive time step sizes if an explicit scheme is employed.

A more quantitative treatment is possible with an asymptotic analysis[117]: This method can be used to show that the phase-field model derived in section 3.1.1 recovers the kinetic Gibbs-Thomson condition for near-equilibrium one-sided solidification as

$$\Delta T = \bar{\beta} v \tag{3.120}$$

$$= \frac{T}{L}\Big[\tau - \epsilon A \frac{(c_\beta(\mu_{eq}, T) - c_\alpha(\mu_{eq}, T))^2}{D_\beta \frac{\partial c_\beta(\mu_0, T)}{\partial \mu}}\Big] v \tag{3.121}$$

with the effective undercooling ΔT, the sharp interface kinetic coefficient $\bar{\beta}$, the temperature T, the latent heat L and a constant dependent on the chosen interpolation functions A. This predicts that the apparent kinetic coefficient depends on both the interface width ϵ and other parameters of the energetic and kinetic description of the system. In order to approximate a situation with zero kinetic undercooling, representing slow solidification, the bracketed term can be set to zero, yielding

$$\tau = \epsilon A \frac{(c_\beta(\mu_{eq}, T) - c_\alpha(\mu_{eq}, T))^2}{D_\beta \frac{\partial c_\beta(\mu_0, T)}{\partial \mu}} \tag{3.122}$$

for the phase-field relaxation coefficient τ. If the kinetic coefficient is known, the full expression can be used to calculate a τ such that the kinetic coefficient is recovered.

The specification of the driving forces is simpler and more complex at the same time. They enter the problem simply as-is given appropriate interpolation functions but their actual values depend on the local state. While they can be computed by coupling directly to so-called CALculation of PHAse Diagrams (CALPHAD) [47, 48] programs, this coupling is computationally expensive. Instead, in the present work the programs are employed to tabulate the free energies and other thermodynamic variables of interest, based on which an approximate function is determined. Especially for the grand potential model, the general parabolic approach[133] for the Gibbs energy

$$G_\alpha(c, T) = A(T)c^2 + B(T)c + C(T) \tag{3.123}$$

is employed, with $A(T), B(T), C(T)$ being temperature-dependent coefficients which produce a "good" approximation of the data generated by CALPHAD programs.

The straightforward approach of simply minimizing the residuals

$$G_\alpha(c, T) - G_\alpha^{\mathrm{CALPHAD}}(c, T) \tag{3.124}$$

e.g. via a least-squares procedure generally does not necessarily yield good results. While the error in terms of the Gibbs energies will look good by virtue of the fitting procedure, the resulting phase diagram need not be close to the actual phase diagram. This is due to derived properties of the Gibbs energy, e.g. partition coefficients, latent heats or heat capacities, not being close to their actual values. Obviously, the target function G_α places no constraints on these, but is simply the result of the least-squares procedure.

The procedure can easily be enhanced by taking these properties into account however, extending the space over which to minimize:

$$G_\alpha(c,T) - G_\alpha^{\mathrm{CALPHAD}}(c,T) \tag{3.125}$$

$$\mu_\alpha(c,T) - \mu_\alpha^{\mathrm{CALPHAD}}(c,T) \tag{3.126}$$

$$G_\alpha(c_\alpha^{\mathrm{CALPHAD}},T) + \mu_\alpha(c_\alpha^{\mathrm{CALPHAD}},T)(c_\beta^{\mathrm{CALPHAD}} - c_\alpha^{\mathrm{CALPHAD}}) - G_\beta(c_\beta^{\mathrm{CALPHAD}},T) \tag{3.127}$$

$$\mu_\alpha(c_\alpha^{\mathrm{CALPHAD}},T) - \mu_\beta(c_\beta^{\mathrm{CALPHAD}},T) \tag{3.128}$$

with values derived from CALPHAD marked as such. The first two parts simply try to match the Gibbs free energy and the chemical potential of each phase α which is under consideration. The next two parts include the equilibrium states $c_\alpha^{\mathrm{CALPHAD}}, c_\beta^{\mathrm{CALPHAD}}$ derived from CALPHAD. This ensures that the phase diagram derived from a set of fitted Gibbs energies stays close to the one produced by CALPHAD. Since these are directly related to further derivatives of the Gibbs energy, latent heat and heat capacity will naturally also be approximated reasonably, given that the their dependence can in principle be represented by the chosen basis functions in (c,T).

A somewhat more convoluted approach is necessary if no CALPHAD data is available, as in the case of freeze-casting. For this, the theoretical model of Peppin[76, 78] is employed to generate data of phase equilibria between the suspension and ice. Within the model, the suspension is assumed to be a single phase, not a phase mixture of liquid and insoluble particles. Its state is thus characterized by the volume fraction of particles, which changes its thermodynamic potentials and hence the equilibrium w.r.t. the ice phase. Simply matching these equilibria is possible, but this does not fix the energy scale in terms of latent heat and thus easily results in arbitrarily large free energies. In order to avoid this, the concentration independent term $C(T)$ in eq. (3.123) is fitted to known data of pure water and ice, based on the International Association for the Properties of Water and Steam (IAPWS) formulations[134]. This fixes the energy scale and reproduces the latent heat to a precision of 1.3 %. While keeping this $C(T)$ fixed, the terms $A(T), B(T)$ are fitted to reproduce the phase equilibria of [76, 78]. This procedure will be described in greater detail in chapter 5.

Finally, some considerations on nondimensionalization are in order. The term "nondimensionalization" is used in two senses within the literature: First, the identification of the controlling parameters of a (differential) equation. Second, the scaling of physical parameters such that errors for finite precision calculation are reduced. This is commonly assumed to be in the interval $[0,1]$ and thus the goal of second sense is to map

the nondimensionalized values into this interval. These two senses can coincide, but need not.

In order to identify the controlling parameters, consider for example a simple one-dimensional steady diffusion equation for a temperature T

$$0 = \frac{\partial^2 T}{\partial x^2} \tag{3.129}$$

and inhomogeneous Dirichlet boundary conditions, leading to a solution of the form

$$T(0) = 0 \tag{3.130}$$

$$T(l) = T_1 \tag{3.131}$$

$$T(x) = T_1 \frac{x}{l} \tag{3.132}$$

In terms of the original equation eq. (3.129) there are the variables and their dimensions

$$[T] = \mathrm{K}$$
$$[x] = \mathrm{m}$$

Simply based on these units, there is in fact *no* dimensionless number which can characterize the system, as no combination of T, x can become dimensionless. Equipping the system with boundary conditions, the additional variables

$$[T_1] = \mathrm{K}$$
$$[l] = \mathrm{m}$$

enter the problem. Dimensionless numbers are trivially achieved by choosing $\bar{x} = \frac{x}{l}$ and $\bar{T} = \frac{T}{T_1}$. Based on this one would say that the natural scales of space and temperature for the problem would be l and T_1. The spatial scale on which temperature changes is indeed $\frac{x}{l}$ and thus pure dimensional analysis captured this aspect of the problem. For the present problem, these choices of scales would scale both variables into the interval $[0, 1]$, which is also the goal of the nondimensionalization in the second sense. Do note that the natural scales will change with the boundary conditions and the specifics of the equations being employed. But once nondimensionalization is achieved, *all* solutions have the same form.

Consider now what happens if the equation is in fact time-dependent and has a source term

$$\frac{\partial T}{\partial t} = \alpha \frac{\partial^2 T}{\partial x^2} + kT(1 - T/T_m) \tag{3.133}$$

which introduces new variables t, α, k, T_m with their dimensions

$$\begin{aligned} [t] &= \mathrm{s} \\ [\alpha] &= \mathrm{m}^2\mathrm{s}^{-1} \\ [k] &= \mathrm{s}^{-1} \\ [T_m] &= \mathrm{K}. \end{aligned}$$

Suppose we have some general scales such that

$$\begin{aligned} \bar{T} &= \frac{T}{T_c} \\ \bar{x} &= \frac{x}{x_c} \\ \bar{t} &= \frac{t}{t_c} \\ \bar{\alpha} &= \frac{\alpha}{\alpha_c} \\ \bar{k} &= \frac{k}{k_c} \end{aligned}$$

are all dimensionless. This transforms the original equation to

$$\frac{T_c}{t_c}\frac{\partial \bar{T}}{\partial \bar{t}} = \frac{\alpha_c T_c}{x_c^2}\bar{\alpha_c}\frac{\partial^2 \bar{T}}{\partial \bar{x}^2} + k_c T_c \bar{k}\bar{T}(1 - \bar{T}/\bar{T_m}) \tag{3.134}$$

$$\frac{\partial \bar{T}}{\partial \bar{t}} = \frac{\alpha_c t_c}{x_c^2}\frac{\partial^2 \bar{T}}{\partial \bar{x}^2} + t_c k_c \bar{k}\bar{T}(1 - \bar{T}/\bar{T_m}) \tag{3.135}$$

in which one can cancel the temperature scale, since without boundary conditions the temperature scale is unfixed[8]. The diffusion term is scaled by the dimensionless number $\frac{\alpha_c t_c}{x_c^2}$, whereas the source term by $t_c k_c$. Thus the characteristic time scale of diffusion

[8] By construction of the reaction term a natural choice would be T_m however.

follows as $t_c = \frac{x_c^2}{\alpha}$ and for reaction as $t_c = \frac{1}{k_c}$. Suppose that these time scales are similar, then

$$\frac{x_c^2}{\alpha} = \frac{1}{k_c} \tag{3.136}$$

$$\rightarrow x_c = \sqrt{\frac{\alpha_c}{k_c}} \tag{3.137}$$

which fixes a characteristic length scale x_c[9]. This length scale is independent of the chosen boundary conditions and thus the position scale need not lie in $[0, 1]$. Now, what about the scale for the thermal diffusivity α? Given that there are already scales for length and time, the scale cannot be chosen independently but follows as

$$\frac{x_c^2}{t_c} = \alpha_c \frac{1}{k_c t_c} \tag{3.138}$$

$$= \alpha_c \tag{3.139}$$

with the earlier reaction timescale suggesting that $k_c t_c = 1$. However, the equation is in fact characterized by more dimensionless numbers as can be shown with Buckingham's π theorem: The number p of independent dimensionless variables in a problem described by n physical variables in k independent physical dimensions is $p = n - k$. In the considered equation, the variables are T, t, α, x, k and T_m ($n = 6$) in the dimensions of length, time and temperature ($k = 3$). Thus there are $p = 3$ independent scales, with the missing scale being temperature. Now, consider adding more terms to the equation

$$\tau_2 \frac{\partial^2 T}{\partial t^2} + \tau_1 \frac{\partial T}{\partial t} = \alpha \frac{\partial^2 T}{\partial x^2} + kT(1 - T/T_m) \tag{3.140}$$

which introduces two new physical variables τ_2 and τ_1 but adds no physical dimensions, suggesting $p = 5$ independent scales. However, in terms of basic physical dimensions there are still only length, time and temperature. While the natural choice of these scales will depend on the specifics of the equations, there are still only three values to be chosen, whereas 5 scales characterize the equations. These scales also need no longer map the nondimensional values into the interval $[0, 1]$, which is preferable for a numeric implementation. Thus the worth of identifying the natural scale becomes smaller as the equation(s) to describe contain more and more physical variables. Limiting behaviour,

[9] If instead of temperature one would solve the phase-field equation eq. (3.13) without driving forces, the characteristic length scale would end up being ϵ.

in which some variables are assumed to be more dominant, can be used to still gleam physical behaviour in the appropriate limits, but does not help with the numerical side.

Due to the above considerations, nondimensionalization will be done in a pragmatic way likely to yield nondimensional values on the order of unity. Specifically, the scales will be chosen according to the physical problem to be considered. For example, if a particle of radius r ought to be resolved, then choosing a length scale l_0 on a slightly smaller scale is appropriate. The time scale is chosen relative to the diffusion process (with associated diffusivity D) which controls the process

$$t_0 = \frac{l_0^2}{D_0} \tag{3.141}$$

$$D_0 = D, \tag{3.142}$$

which also maps the diffusivity to 1. The energy scale is chosen depending on whether the process is driven by a phase transformation or by capillary forces. If driven by a phase transformation (e.g. solidification), the volumetric latent heat L is chosen as the energy density scale

$$E_{r,0} = L \tag{3.143}$$

$$\rightarrow E_0 = L l_0^3 \tag{3.144}$$

whereas when capillary forces dominate (e.g. sintering) the surface energy σ is chosen as the surface energy scale

$$E_{s,0} = \sigma \tag{3.145}$$

$$\rightarrow E_0 = \sigma l_0^2. \tag{3.146}$$

In both cases, an energy scale E_0 is derived based on the energy density scales. This also implies a mass scale if the length and time scales have already been defined. If the temperature is constant, the choice of scale is arbitrary. If the temperature is variable, it is chosen to be a temperature for an invariant reaction T_i related to the process being studied, e.g. melting of a pure phase or a eutectic reaction under constant pressure conditions. Finally, the molar volume scale is chosen to be the molar volume of a solid phase. These choices will be reported on in each subsequent chapter which conducts simulations related to a physical system.

4 Solidification of Al-Cu alloys

This chapters focuses on the solidification of Al-rich Al-Cu alloys, investigating the growth of dendrites, eutectics, as well as their interaction. It is based on the author's publication[69] (© Elsevier. Reproduced with permission. All rights reserved), with the additional content of the preprint [135] (temperature gradient influence on the eutectic spacing, complete directional solidification) which were cut from the paper due to length restrictions. The following sections are taken verbatim from the preprint, with only minor linguistic and stylistic changes to account for the move from a paper to a chapter in the present dissertation, as well as some clarifications due to the referees. Numerical details and relevant literature are also given in the paper.
The parametrization of the Al-Cu system was previously tested in [136]. It was successfully compared to both the Lipton-Glicksman-Kurz theory [137] for the dendrite operating state as well as the scaling of the selection parameter σ^* with anisotropy strength following MST in the small Péclet number limit. Hence in the following no further match with dendritic theory is sought. Within [136] first forays into coupled dendritic-eutectic growth were done, with the principal results being that a temperature gradient and nucleation are necessary for its occurrence in phase-field simulations. The present investigation expands this significantly by extending the nucleation mechanism to account for variable temperature (section 3.2.1), formulating a theory delineating eutectic from dendritic-eutectic growth (section 2.2.3), investigating the effect of coupled growth on the individual microstructure as well as taking a more detailed view of the eutectic morphology in three dimensions.

First, the parametrization will be explained. Next, a simple implementation test is done to verify that the correct equilibrium properties are achieved even with nucleation. Based on this, the data necessary for solving the model developed in section 2.2.3 is gathered while also validating the kinetic influence of nucleation with the Jackson-Hunt theory for eutectics. With this data in hand, the boundary curve separating eutectic from dendritic-eutectic morphologies is calculated. This curve is then tested for several states with phase-field simulations, with the resulting microstructures investigated as to whether they are significantly different from the pure morphologies.

The short messages of this chapter are:

- the operating states of dendrites and eutectics are largely unchanged when growing together
- close to the dendrite-eutectic interface, the eutectic has variable phase widths
- secondary dendrite arms can be suppressed by coupled growth
- the three-dimensional morphology of the eutectic is sensitive to solid-liquid anisotropy

4.1 Parametrization of the Al-Cu system

In order to approximate the material system Al-Cu in the phase-field simulations, the energies describing the material system are approximated based on the thermodynamic CALPHAD database from Witusiewicz et al. [138] and by using the parabolic approach described in eq. (3.123). A linear temperature dependence of each coefficient is assumed. The input data includes both Gibbs free energy and chemical potential values as well as phase equilibrium points, both determined via CALPHAD, resulting in a procedure similar to [80]. All concentrations employed are in atomic fraction or equivalently mole fraction of copper, with the assumption of equal molar volumes. The following equations give the resulting functions with 8 significant digits in dimensionless units:

$$\begin{aligned} g_\alpha(c,T) &= (147.73532T - 128.37484)\,c^2 \\ &\quad + (3.5000629T - 53.205937)\,c \\ &\quad - 57.867925T + 27.198937 \end{aligned} \tag{4.1}$$

$$\begin{aligned} g_\theta(c,T) &= (294.11794T - 254.29651)\,c^2 \\ &\quad + (170.96673T - 96.996795)\,c \\ &\quad - 28.930239T + 2.260627 \end{aligned} \tag{4.2}$$

$$\begin{aligned} g_l(c,T) &= (21.442726T - 17.807343)\,c^2 \\ &\quad + (5.587987T - 55.592733)\,c \\ &\quad - 58.655641T + 28.085635 \end{aligned} \tag{4.3}$$

Table 4.1 shows the temperatures and equilibrium concentrations of the eutectic reaction for the system from [138] and from the approximated system, respectively.

Table 4.1: Temperatures and equilibrium concentrations of the eutectic reaction $L \rightarrow \alpha + \theta$ for the binary Al-Cu system from [138] and from the approximated system

	T_e in K	$c_{eq.}$ of α in at.% Cu	$c_{eq.}$ of Al_2Cu in at.% Cu	$c_{eq.}$ of L in at.% Cu
CALPHAD PD [138]	820	2.54	31.8	17.5
reconstructed PD	816	2.59	31.8	18.1

Figure 4.1 shows the Al-rich side of the Al-Cu phase-diagram calculated from [138] (orange) compared with the reconstructed phase-diagram derived from the approximated Gibbs energies of eqs. (4.1) to (4.3) (blue). Excepting conditions close to the melting point of α-Al, good accordance of the phase-transition lines as well as of the position of the eutectic reaction can be found.

The employed nondimensionalization parameters are listed in table 4.2 and the remaining physical parameters in table 4.3. These are generally based on literature values for Al-Cu, except the surface energy, which was chosen much larger in order to allow for high driving forces without suffering from a mushy interface[139].

Table 4.2: nondimensionalization parameters

scale	value
length	$1 \times 10^{-7}\,\mathrm{m}$
time	$5 \times 10^{-6}\,\mathrm{s}$
diffusivity	$2 \times 10^{-9}\,\mathrm{m^2/s}$
velocity	$0.02\,\mathrm{m/s}$
temperature	$820\,\mathrm{K}$
energy density	$1 \times 10^{8}\,\mathrm{J/m^3}$
surface energy	$1 \times 10^{1}\,\mathrm{J/m^2}$
molar volume	$1 \times 10^{-5}\,\mathrm{m^3/mol}$

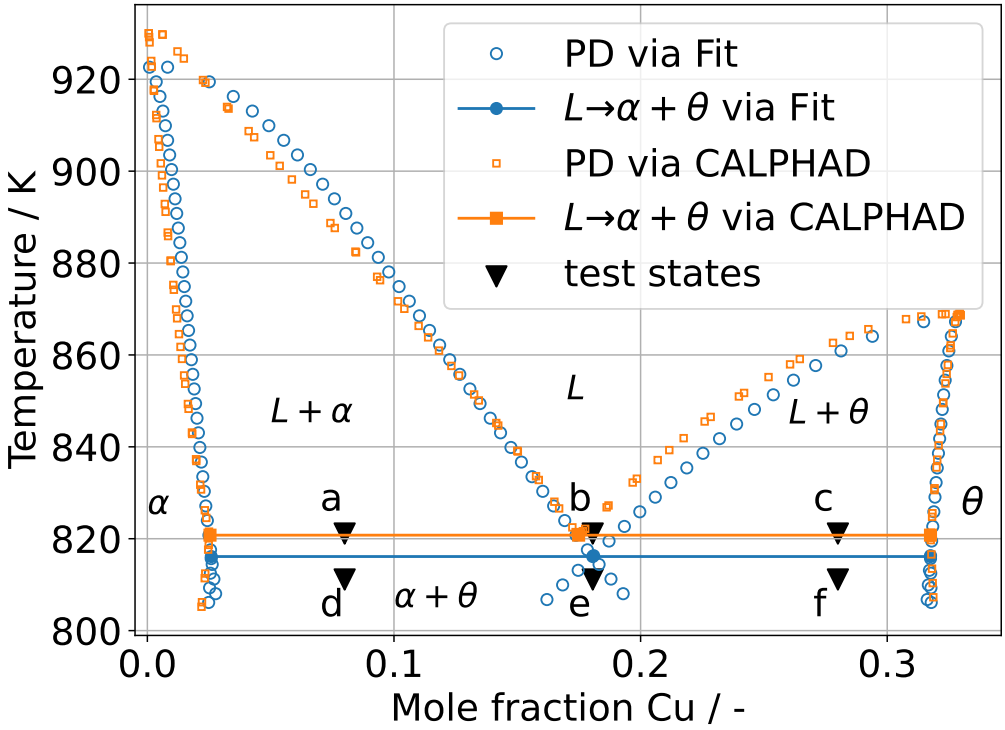

Figure 4.1: Al-rich side of the Al-Cu phase diagram, calculated via CALPHAD based on [138] as well as by the fitted free energies. For the CALPHAD calculation, only the α-Al, θ-Al_2Cu and liquid phases are considered. The fitted free energies show good accordance given the large temperature range. The states which will be investigated as part of the validation are marked by the black triangles (a-f).

Table 4.3: Employed physical and numerical parameters for the simulations.

parameter	simulation value	physical value
Numerical parameters		
grid spacing Δx	1	$1 \times 10^{-7}\,\mathrm{m}$
time step Δt	0.125	$0.625 \times 10^{-6}\,\mathrm{s}$
interface parameter ϵ	$3\Delta x$	$3 \times 10^{-7}\,\mathrm{m}$
interface width W	$7.5\Delta x$	$7.5 \times 10^{-7}\,\mathrm{m}$
Physical parameters		
surface energy $\gamma_{\alpha\beta}$	0.08	$0.8\,\mathrm{J/m^2}$
diffusivity in the melt	1	$2 \times 10^{-9}\,\mathrm{m^2/s}$
diffusivity in the solids	1×10^{-3}	$2 \times 10^{-12}\,\mathrm{m^2/s}$
kinetic coefficient $\tau_{\alpha l}$	0.138	$6.92 \times 10^{8}\,\mathrm{Js/m^4}$
kinetic coefficient $\tau_{\theta l}$	0.0968	$4.84 \times 10^{8}\,\mathrm{Js/m^4}$
kinetic coefficient $\tau_{\alpha\theta}$	0.417	$2.08 \times 10^{9}\,\mathrm{Js/m^4}$
anisotropy strength ζ	0.04	0.04

4.2 Validation and preliminary studies

Before simulating the combined growth of eutectic and dendritic structures within a single phase-field simulation, the implementation is tested, followed by the individual simulation of the processes in order to validate their separate growth. These also deliver the data required for determining the boundary curve.

4.2.1 Implementation test

The implementation of the phase-field model is qualitatively validated by sampling the test states from fig. 4.1 and observing the resulting microstructure. The phase fractions given by the phase diagram should be approximated, given that the phases are present in the domain. In order to ensure the latter, nucleation is allowed. Furthermore, the morphology of the microstructure should depend on the (an)isotropy of the phases: States within a solid-liquid region of the phase diagram should yield dendrites with anisotropy, but seaweed without. Below the eutectic temperature, both solid phases should be present, with a well-developed eutectic at the eutectic composition, but only second-phase linings in the channels between the primary phases for larger deviations from the eutectic composition.

The simulation starts with a circular seed of either anisotropic α or isotropic θ, depending on which side of the eutectic composition the point lies. For the eutectic composition a circular seed of the anisotropic α phase is set. The initial seed concentration is set to the respective phases' eutectic equilibrium concentration, with the melt being set with $c_0 \in \{0.08, c_e, 0.28\}$ respectively and $c_e = 0.181$ being the eutectic composition. The temperature is set to $T_e \pm 5\,\mathrm{K}$, with $T_e = 816\,\mathrm{K}$ being the eutectic temperature. All boundaries in the simulation domain are assumed to be no-flux boundaries. The simulation domain is resolved with 1000 cells in each direction, corresponding to a $100\,\mu\mathrm{m} \times 100\,\mu\mathrm{m}$ physical domain.

The simulations are run until the volume fractions of all present solid phases change by less than 1% when calculated over a 100 ms period. A comparison of theoretical and observed mass fraction is given in table 4.4, showing a good agreement for all investigated states. The composition field for intermediate states of the simulations are shown in fig. 4.2. Black corresponds to pure α, whitish-grey to θ whereas the remaining shades of grey correspond to the melt. This color scheme will also be used in the remaining simulation images. The morphology of the phases fits with theoretical expectations, i.e. the anisotropic α grows as a four-sided dendrite (a,d), whereas the isotropic Al_2Cu phase

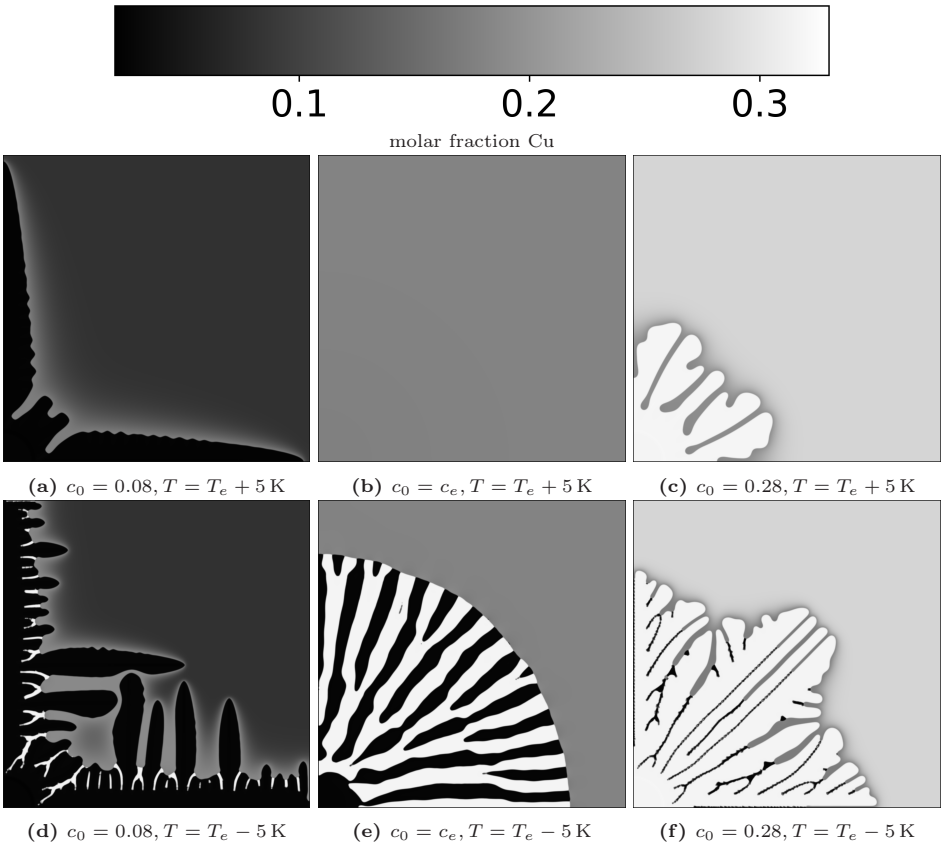

(a) $c_0 = 0.08, T = T_e + 5\,\mathrm{K}$ **(b)** $c_0 = c_e, T = T_e + 5\,\mathrm{K}$ **(c)** $c_0 = 0.28, T = T_e + 5\,\mathrm{K}$

(d) $c_0 = 0.08, T = T_e - 5\,\mathrm{K}$ **(e)** $c_0 = c_e, T = T_e - 5\,\mathrm{K}$ **(f)** $c_0 = 0.28, T = T_e - 5\,\mathrm{K}$

Figure 4.2: Various intermediate morphologies observed in the simulations. The color bar indicates the local molar fraction of copper, based on which the phases are identifiable: Black corresponds to pure α, whitish-grey to θ whereas the remaining shades of grey correspond to the melt. Dendritic, seaweed and eutectic growth is observed as well as second-phase lining of interdendritic/cellular spaces if below the eutectic temperature (d)-(f). All depicted states except for (b,e) were observed at $t = 37.5\,\mathrm{ms}$. In (b) the initial seed vanished around $t = 843\,\mathrm{ms}$, and in (e) the eutectic only started nucleating at around $t = 37.5\,\mathrm{ms}$, hence a later time ($t = 938\,\mathrm{ms}$) was used to show the eutectic pattern.

Table 4.4: Comparison of mass fractions X_i between the phase diagram (PD) and the simulation results (Sim) in the converged state.

	X_α		X_θ		X_l	
	Sim	PD	Sim	PD	Sim	PD
(a)	0.631	0.633	0.000	0.000	0.369	0.367
(b)	0.000	0.000	0.000	0.000	1.000	1.000
(c)	0.000	0.000	0.702	0.701	0.298	0.299
(d)	0.817	0.814	0.183	0.186	0.000	0.000
(e)	0.473	0.473	0.527	0.527	0.000	0.000
(f)	0.127	0.130	0.873	0.870	0.000	0.000

grows in a seaweed-like pattern (c,f). In both cases a lower temperature also increases the growth rate. As expected, the solid phase completely vanishes in (b) since it is in the monophasic liquid region of the phase diagram. For state (e) a radially patterned eutectic is observed since the eutectic nucleates along the circumference of the seed.

4.2.2 Validation of model for eutectic growth simulations

Satisfactorily matching simulation studies of the eutectic growth have been shown previously by several authors for this kind of phase-field model without using a nucleation mechanism [27, 140, 141]. Thus the focus in this section is on validating the proposed nucleation mechanism similar to Kellner et al. [142]. In their work it is shown that simulations at arbitrary domain lengths including nucleation can be mapped back onto a normalized Jackson-Hunt curve for the lamellar spacing. In effect this probes whether the steady-state growth point is recovered even in a nucleating system. This computational experiment is reproduced for the investigated Al-Cu system.

The principal setup of the simulation study is shown in fig. 4.3, along with typical evolutionary states: An initial pair of isotropic α-Al and θ phases is set at the bottom of the domain with the fractions determined by the lever rule (a). The top part of the domain is filled with melt at the eutectic composition c_e, with this composition also being imposed as a Dirichlet condition at the top. At the bottom no-flux conditions are employed, whereas on the sides periodic boundary conditions are applied. The temperature is assumed to be homogeneous. If the spacing λ is sufficiently above the dominant lamellar spacing λ_{JH}, oscillations can be observed (b). Without nucleation, these persist and may lead to one phase overgrowing the other, in which case the simulation is aborted and the data is not taken into account. Nucleation will occur in the concave parts of the front

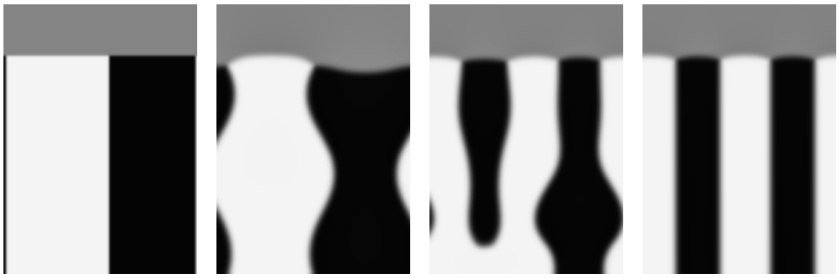

(a) initial **(b)** oscillating **(c)** shortly after nucleation **(d)** long past nucleation

Figure 4.3: Initial setup as well as exemplary evolutionary states during eutectic growth. The domain is cut off slightly above the moving window cutoff in order to emphasize the solid phases.

with the present mechanism, leading to a refinement of the spacing and less oscillatory growth (c,d).

First, several undercoolings $\Delta T \in \{3, 4, 6, 8\}$K will be investigated without nucleation activated. For each considered undercooling, a range of domain lengths is employed to allow different lamellar spacings λ and thus front velocities v. The values for the domain lengths are determined iteratively starting from an estimated dominant lamellar spacing. Following the theory of Jackson and Hunt[62], the curve $v(\lambda)$ should contain a global maximum which represents the dominant lamellar spacing λ_{JH}. Thus if no maximum is observed, additional domain lengths are added in the direction of the slope of the curve. Once a maximum is observed, the set of domain lengths is frozen. Based on these simulations the concentration-independent model of eq. (2.28) is fitted, yielding $K_1 = 0.02696$, $K_2 = 0.05197$ in nondimensional units. Next, simulations with nucleation activated are conducted for each undercooling and its corresponding set of domain lengths, with additional simulations at significantly larger domain sizes than the observed λ_{JH} in order to allow multiple pairs of lamellas to nucleate from a single pair. In total this yields fig. 4.4, showing the solid front velocity over domain width and the final lamellar spacing for all conducted eutectic simulations. The transparent circles denote the nucleationless simulations, whereas the squares represent the simulations with nucleation active. The solid line is the analytical Jackson-Hunt result, based on the previously calculated K_1, K_2. First, the circles match the theory without a selection criterion well, suggesting that the main features of Jackson-Hunt theory are captured with the simulations. Second, the squares map back closely to the curve, suggesting that steady-state growth is not significantly affected by the nucleation mechanism. It should be noted that herein simulations growing at $\geq 2\lambda_{JH}$ did not necessarily exhibit strong oscillations in their

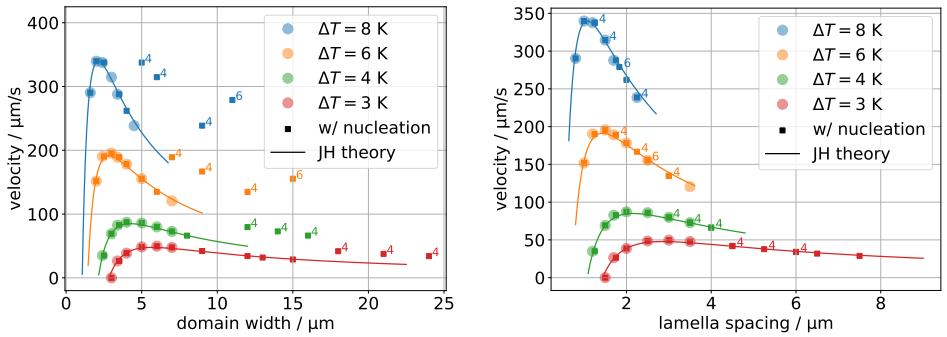

Figure 4.4: Comparison of eutectic theory (lines) and simulations with (squares) and without (circles) nucleation for various undercoolings. The left plot shows the same data as the right plot, but plotted over the domain width instead of the lamellar spacing. The initial configuration always consists of a single pair of α and θ, representing two lamellas. The number besides the squares indicates how many lamellas are observed in steady-state, with no number indicating two lamellas. Matching behavior between theory and simulation is observed over the entire undercooling range. Furthermore, the simulations with nucleation fall onto the curve described by JH theory and achieve similar steady-state velocities to simulations without nucleation.

growth. This leads to only minor solute excess in front of the solid phases which inhibits nucleation. Hence the squares will tend to cluster not around λ_{JH} but rather around a spacing somewhat larger, similar to [142] in which simple concentrations differences were assumed to give the nucleation potentials.

In order to determine the influence of off-eutectic compositions on the undercooling, further simulations are conducted. For these, the frozen temperature approximation eq. (3.55) is employed. The velocities and domain lengths are based on the maxima from the previous study and the melt concentrations $\{0.12, 0.13, 0.15, c_e\}$ are employed, i.e. three hypoeutectic concentrations and the eutectic concentration. The gradient is chosen to be 99 K/mm in order to speed up convergence of the temperature field. The simulations are run until the velocity differs by less than 2% from the imposed velocity. Plotting the difference of the off-eutectic front temperature to the eutectic front temperature for these simulations yields fig. 4.5a. It is easy to see that the front temperature is decreasing with increasing distance from the eutectic composition. The eutectic constant E is calculated for each composition and then a parabola is fit to this data, with fig. 4.5b showing that the fit matches the data well. Thus the eutectic undercooling model reads $\Delta T_e = (0.376c_0^2 - 0.142c_0 + 0.08714)v^{0.5}$. The effective value of E at the eutectic composition is $428\,\mathrm{Ks}^{0.5}/\mathrm{m}^{0.5}$ which compares well with the investigations at the eutectic composition, which yields a value of $434\,\mathrm{Ks}^{0.5}/\mathrm{m}^{0.5}$.

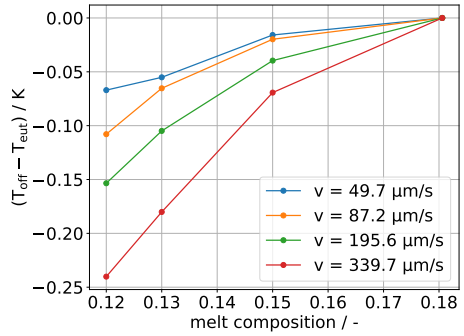

(a) Difference of front undercooling for the off-eutectic simulations to the eutectic simulation. With increasing distance from the eutectic composition, the front grows at an increasingly lower temperature.

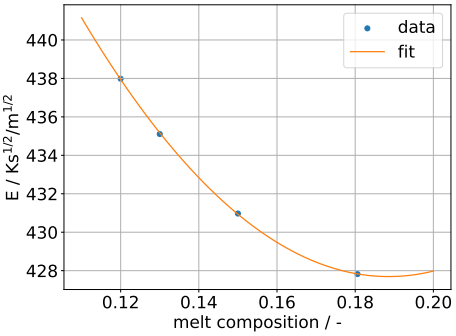

(b) The concentration dependence of the growth constant E in $\Delta T_e = Ev^{0.5}$. A quadratic polynomial seems to describe the dependence satisfactorily.

Figure 4.5: Results of the off-eutectic simulations.

4.2.3 Determination of dendrite model parameters

The simulations for the determination of the constants within the dendrite tip undercooling model eq. (2.32) will now be described. An initial periodic, anisotropic α-seed is placed at the bottom of the domain inside of a homogeneous melt of concentration c_0. The frozen temperature approximation eq. (3.55) is employed again. A quasi-infinite domain is simulated by employing the moving-window technique. Various temperature gradients $G \in \{24.7, 99.0\}$K/mm, velocities $v \in \{80, 160, 320, 640\}$µm/s as well as melt concentrations $c_0 \in \{0.06, 0.08, 0.1\}$ are employed. Nucleation was allowed for all simulations, but no nucleation was observed since it is energetically unfavorable for the investigated parameters. The simulations are run until the front velocity differed by less than 2% from the imposed velocity. This yields tuples of (T_i, v, G, c_0) values which are used to fit the undercooling formulation of eq. (2.32), with the interfacial undercooling $T_l(c_0) - T_i$ as the dependent variable. The nondimensionalized coefficients are given by $A = 0.957, B = 0.788, C = 0.288$ for the melt concentration dependent model and $A = 6.58, B = 0.370$ for the model without an explicit melt concentration dependence. A scatter plot of the measured undercoolings over the velocity is shown in fig. 4.6, with the two models indicated as lines. The non-monotonic behavior of the concentration independent model at lower velocities is expected[70]. The concentration dependent model shows this as well for even lower velocities. The mean unsigned error defined by $\sum \frac{|\Delta T_{observed} - \Delta T_{estimated}|}{N}$ is 5.81 K for the concentration-independent model and 1.05 K

for the concentration-dependent model. In total one can observe that the explicit inclusion of melt concentration increases the model accuracy significantly.

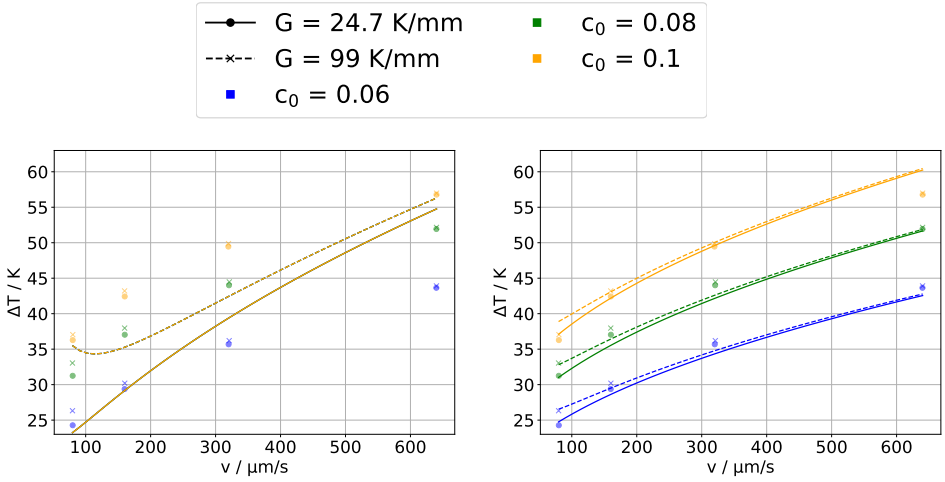

(a) fit without c_0-dependence

(b) fit with c_0-dependence

Figure 4.6: A scatter plot of the interfacial undercooling over the imposed velocity is depicted. The observed undercooling (markers) rises with velocity, composition (color) and gradient (marker type). The same data is shown in both plots, with the lines indicating the predictions of the different models for the dendrite tip undercooling, varying similarly for velocity, composition (color) and gradient (line style). The composition dependent model generally matches the data better than the composition independent model. Note that the concentration independent model only produces two lines, as any choice of c_0 will lead to the same line for the same G.

4.2.4 Boundary curve of the coupled zones

Now that the undercooling models for dendrites and eutectics are fully specified, the boundary curve between the two morphologies can be calculated. For each (G, v) point, the resulting nonlinear equation in c_0 is solved numerically. Three gradients ($G \in \{6.18, 24.7, 99.0\}\mathrm{K/mm}$) are chosen, for which the range of cooling rates Gv from $3 \times 10^{-2}\,\mathrm{K/s}$ to $40\,\mathrm{K/s}$ is sampled. The resulting set of points is plotted as a $c_0 - G/v$ diagram in fig. 4.7 as suggested by [70]. The curves separate the eutectic range to the right from the coupled dendritic-eutectic range to the left. The eutectic range is always increased by increasing the gradient. If G/v is sufficiently high, i.e. at low velocities, the influence of gradient diminishes and the extent of the eutectic range is only weakly dependent on the gradient. In the high velocity regime there is a significant effect of the gradient on the

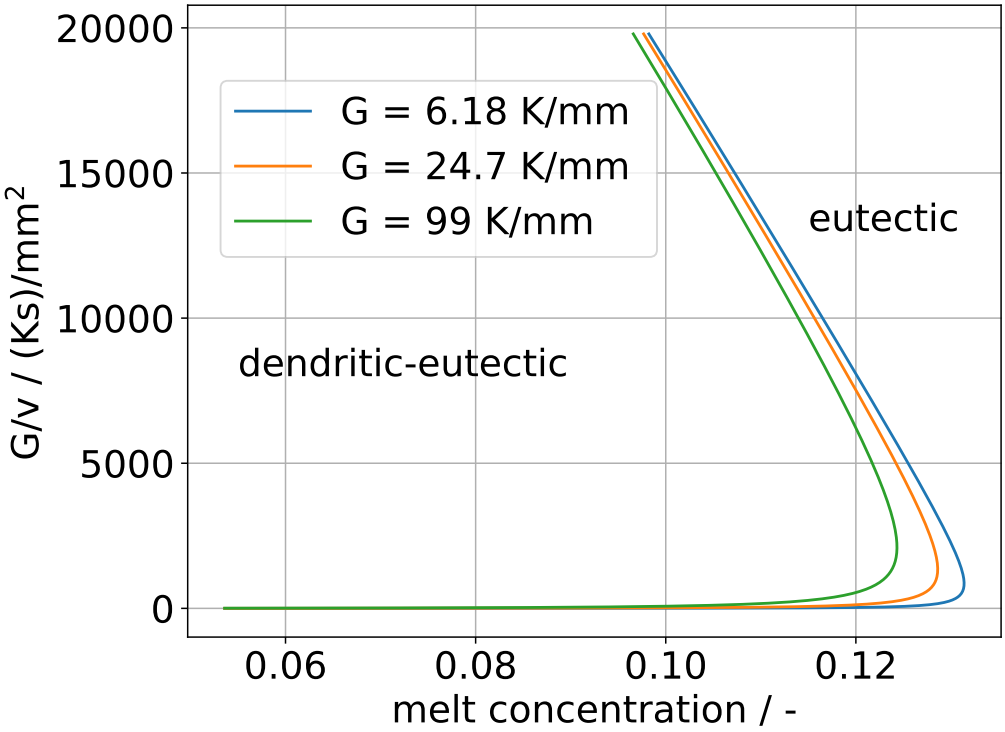

Figure 4.7: Numerically calculated boundary curves between pure eutectics and a mixed dendritic-eutectic microstructure.

eutectic range. Further to the left one would expect a purely dendritic microstructure once the melt composition is around the solubility limit. This microstructure will not be separately considered in the present work, but can also be easily simulated with the present model. The majority of the simulations will be conducted around the "knee" of these curves in order to probe the minimal extent of the eutectic range.

4.3 Results for coupled dendritic-eutectic growth

In this section novel results investigating the conditions for dendritic-eutectic growth and its influence on the microstructure are presented and discussed. Additional videos of some of the simulations are deposited with [143].

4.3.1 Boundary curve validation & microstructural influences

Given that the boundary curve is now known, processing conditions which are likely to yield dendritic-eutectic growth can be set. Specifically, simulations with gradients $G \in \{6.18, 24.7, 99.0\}$K/mm, pulling velocities $v \in \{80, 160, 320\}$µm/s and melt compositions $c_0 \in \{0.1, 0.11, 0.12, 0.13\}$ are conducted. The initial and boundary conditions are similar to the setup of pure dendritic growth in the previous section. The starting temperature $T_0 = T_e - 2\,\mathrm{K}$ is now below the eutectic temperature. The domain height of 5000 cells corresponds to 500 µm and the width of 2500 cells corresponds to 250 µm. The moving window cutoff is set at 250 µm, i.e. there are at least 250 µm between the front and the boundary at all times. The diffusion length for the smallest velocity corresponds to 25 µm and thus there are at least 10 diffusion lengths between the front and the boundary, mimicking an infinite melt. Unless mentioned otherwise, the simulation images always depict a region of size 280 µm × 250 µm, i.e. the whole width of the domain and slightly above the solidification front in terms of height. This is done to emphasize the solid structure. The simulations are continued until either the eutectic is shifted outside of the domain, a eutectic front stabilizes or the height difference between the dendrite tip and the eutectic becomes constant. The former two conditions are based on the observation that once one of the morphologies becomes dominant, the other morphology will not appear without external influence again. The latter condition is employed instead of a velocity convergence criterion as multiple fronts are advancing at different velocities. Usually, the primary dendrite will reach a converged velocity first, with the eutectic still adjusting its position w.r.t the dendrite tip.

Figure 4.8 shows exemplary simulation results. Purely dendritic (D, fig. 4.8a), dendritic-eutectic (D+E, fig. 4.8b) and purely eutectic (E, fig. 4.8c) structures are observed, depending on the melt composition c_0. Note that in the case of dendritic-eutectic structures, the θ lamellas close to the dendrite are thicker than in the middle. This is due to the melt composition close to the dendrite being enriched in Cu which is rejected by the dendrite, which is also easily observed with the composition field being slightly brighter (more Cu) closer to the dendrite. Simulations in which only dendrites remain will be counted as dendritic-eutectic in the following. This is due to the fact that if a sufficiently higher moving cutoff were to be used, the eutectic would not be shifted out of the domain and hence both morphologies would be observed, as long as the melt composition is larger than the corresponding solidus composition. Generally, if dendritic-eutectic growth is the goal of the simulation, then the simulation needs to be able to span the temperature difference between the dendrite front temperature T_{df} and the eutectic front temperature T_{ef}. With the frozen temperature approximation (eq. (3.55)) this suggests that the

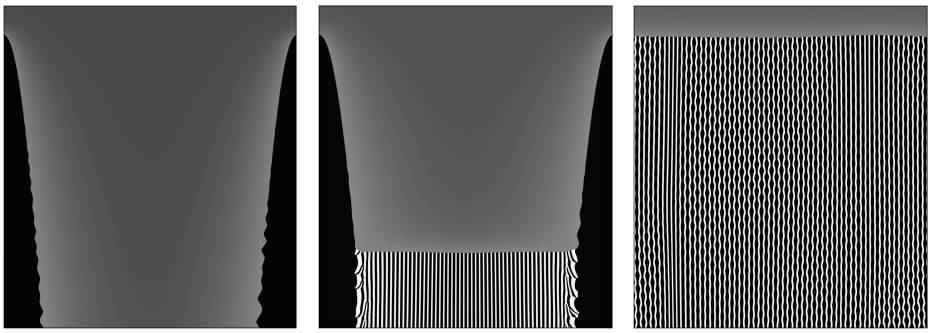

(a) $c_0 = 0.11$ **(b)** $c_0 = 0.12$ **(c)** $c_0 = 0.13$

Figure 4.8: Observed microstructures for $v = 160\,\mu\text{m/s}$, $G = 24.7\,\text{K/mm}$ and various melt compositions. Both purely dendritic as well as eutectic structures are found as well as simulations in which both morphologies grow within the moving window concurrently.

physical domain up to the moving window cutoff should be at least $L = \frac{T_{df} - T_{ef}}{G}$. If this length is negative, it also implies that the eutectic should be the dominant morphology. Note that this is a necessary but not sufficient condition, as the initial conditions have an effect on the resulting morphology as will be shown later.

The results can be displayed succinctly in a $\{c_0 - G/v\}$ plot as suggested by [70]. This is done in fig. 4.9, displaying the results for all simulations at once along with the boundary curves calculated based on the theory described in 2.2.3. All eutectics, represented by circles, lie to the right of their respective boundary curves. Similarly, the dendritic-eutectic structures are observed to the left of the curves, suggesting that the maximum temperature condition for the transition between eutectic and dendritic-eutectic morphologies describes the boundary curve well. This also implies that the front undercooling of the individual morphologies is either not significantly changed compared to their isolated growth or changed by the same value. Due to the choice of $G - v$ pairs, several points result in the same G/v value but with different gradients and different morphologies. Thus the full specification of solidification conditions ($\{v, G, c_0\}$) is necessary to determine the morphology.

The observed growth conditions ($\Delta T - v$) can be compared to the models which were determined earlier. This is shown in fig. 4.10. While there is a systematic underprediction of the undercooling by the model, it is of similar magnitude as to the isolated growth conditions which were used to determined the model parameters. Thus there is no significant effect of coupled growth on the underlying undercooling-velocity relationship.

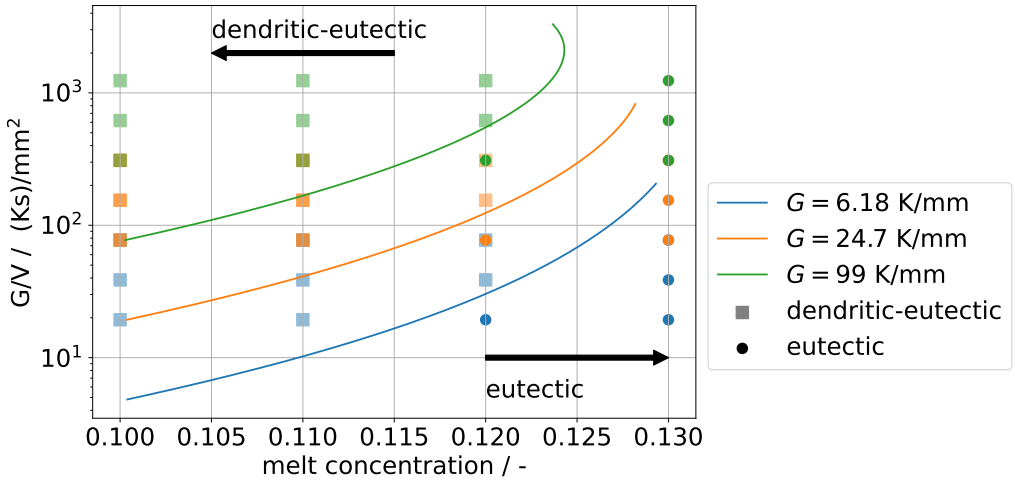

Figure 4.9: The microstructure map differentiating the eutectic range from the dendritic-eutectic range. The theoretical boundary curve clearly separates the two observed morphology regimes.

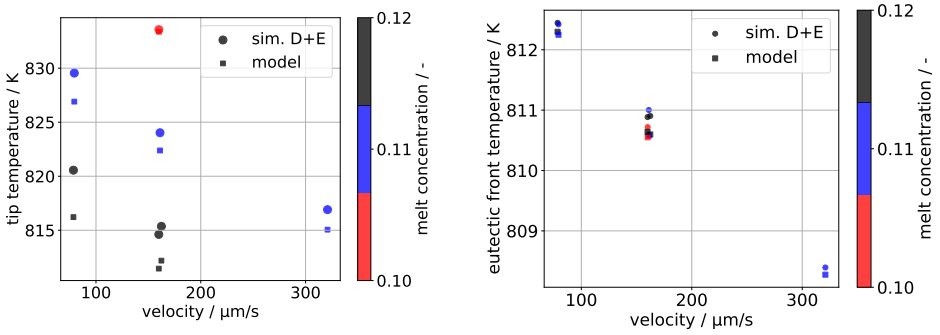

Figure 4.10: Comparison of observed front temperatures during dendritic-eutectic growth and the prediction of the respective isolated growth models. There is a systematic underprediction of front temperature, but of similar magnitude as the earlier deviations (figs. 4.4 and 4.6) between data and the model. Thus the coupled growth does not seem to affect the undercooling-velocity relationship significantly.

Next, the influence of dendritic-eutectic growth on the microstructural lengths is investigated. The relevant microstructural lengths of the dendrite are the primary dendrite arm spacing (PDAS) and secondary dendrite arm spacing (SDAS). In the present setup one cannot make statements about the PDAS as usually only a single dendrite is contained within the simulation domain. However, a qualitative statement regarding the SDAS is possible: If the eutectic grows sufficiently close to the dendrite tip, secondary arms cannot develop fully before being enveloped by the eutectic. Thus the SDAS will tend to be smaller than for purely dendritic growth.

The eutectic spacing however can be easily investigated for the present simulations, as large numbers of lamellas are contained within the eutectic and dendritic-eutectic simulations. A bit of preprocessing is necessary for dendritic-eutectic simulations in order to exclude the dendrite and its closest neighboring θ lamellas from the analysis: Specifically, the α and θ phases are separated and segmented[144] on their own. For the α phase, the isotropic and anisotropic variants are added together. It is assumed that any segments larger than four times the median are dendrites, which are henceforth excluded from the analysis. Furthermore, small segments of e.g. failed nucleation are excluded as well by using a minimum segment size of 100 cells. For the θ phase the lamellas close to the dendrite need to be excluded as these are severely thicker. Since a simple size threshold is hard to define for these, only the θ segments past the second and before the second to last α lamella are analyzed, with the same small segment filter applied as for the α phase. The remaining segments are put together to form an image of a "well-formed" eutectic, which is analyzed with the same procedure as for purely eutectic simulations. In the present case, the individual phase widths w_α, w_θ perpendicular to the growth direction are analyzed, with their sum being the spacing λ.

The results of analyzing the simulations containing a eutectic are shown in fig. 4.11 with a scatter plot of the theoretically calculated and measured spacings. If there is no influence of the dendrite on the growing eutectic, then the results should cluster around the line $y = x$. This is generally observed, with a slight scatter upwards. The eutectic simulations tend to be above the line, due to a combination of factors: First, many of the α lamellas are represented by the dendritic phase, as these lamellas originally branched off from the dendrite. Thus these have a different surface energy and also triple point angles. Second, as explained in the validation, the nucleation mechanism tends to generate slightly larger spacings than predicted by the minimum undercooling criterion in the JH theory. When comparing the dendritic-eutectic to the purely eutectic simulations, the presence of a dendrite tends to slightly decrease the spacing. One possible explanation for this is that the dendrite itself tends to increase the Cu content in the melt ahead of the eutectic, altering the far-field the eutectic is growing against. In order to estimate

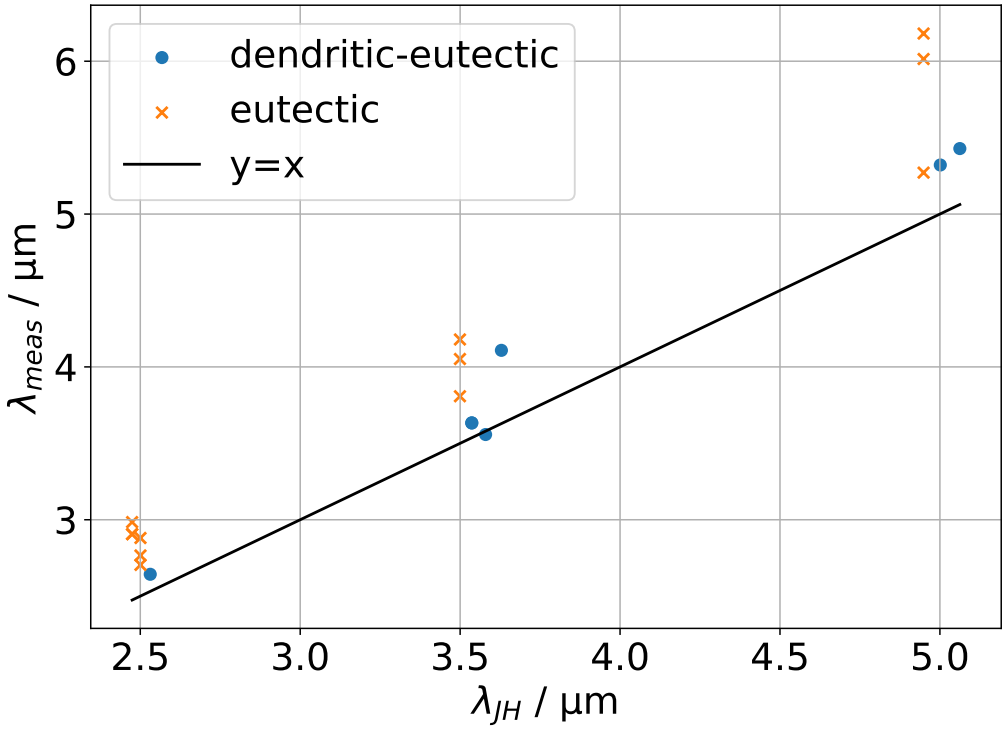

Figure 4.11: A comparison between the theoretically expected spacings λ_{JH} and the measured spacings λ_{meas}. The black line serves as a guide for the eye. The dendritic-eutectic simulations tend to be above this line but roughly parallel to it. The eutectic simulations tend to deviate more.

the effective far-field concentration, the fraction of θ within the eutectic is evaluated. The total composition leading to this fraction is then iteratively determined and thus an estimate for the effective far-field concentration obtained. This would theoretically lead to refinements on the order of 0.01 µm to 0.1 µm for the present simulations, with the actual refinement ranging from 0.1 µm to 0.5 µm. Thus only a part of the observed deviations can be explained with far-field effects. The remaining effect might be due to structural effects of the dendrite on the eutectic, which will be the subject of further research.

Furthermore, the present data can also be analyzed as to whether the temperature gradient has any influence on the eutectic spacing relationship, since this is excluded in the theoretical considerations. Plotting the spacings for the eutectic simulations over the gradient yields fig. 4.12, which shows individual bands of spacings for each velocity. Excepting the slowest velocity, there is little difference between spacings obtained at the

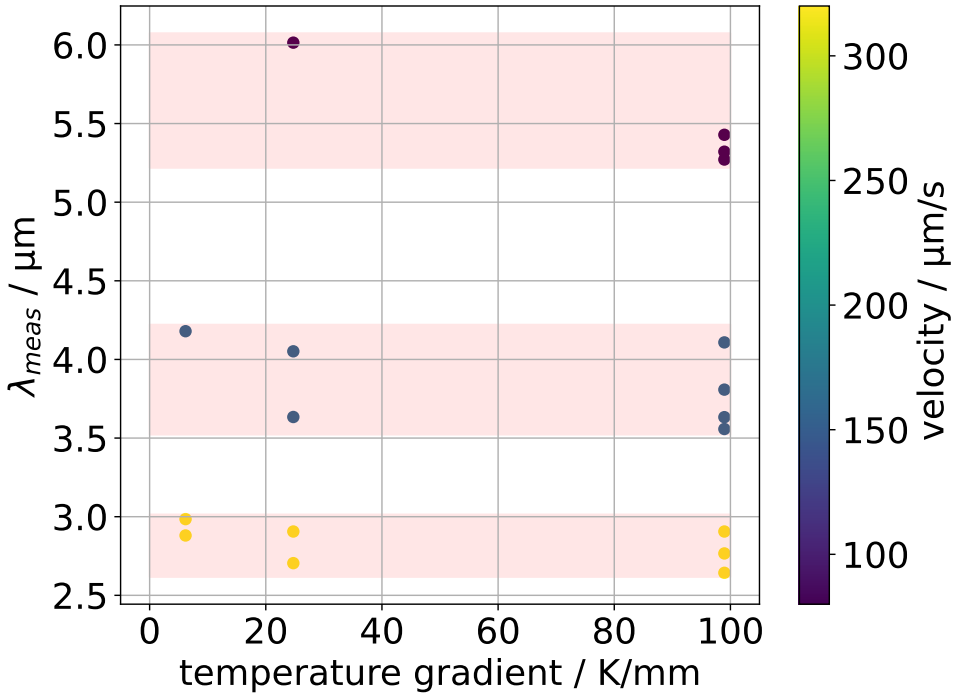

Figure 4.12: The measured lamellar spacing for all simulations containing eutectic is plotted over the employed temperature gradients. For each employed velocity, a band of spacings is spanned by the system, indicated by the shaded regions. Excepting the smallest velocity, there is little difference between spacings at the lowest and highest gradients.

highest and lowest gradients. The smaller velocities and temperature gradients tend to show larger oscillations in the lamellar structure, making the measurement less reliable for these. In total however there seems to be no significant influence of the temperature gradient on the spacing within the simulations.

4.3.2 Influence of velocity variation

Next, simulations will be conducted in order to investigate transitions between the morphologies by abruptly changing the velocity of the temperature field.
The first transition is for a gradient of 24.7 K/mm and a melt concentration of 0.12, with the velocity jump being from 160 µm/s to 320 µm/s. This should move the simulation from a dendritic-eutectic growth regime into a purely eutectic growth regime.

Figures 4.13a to 4.13c show the results for speeding up a dendritic-eutectic front. The eutectic slowly grows upwards until it overtakes the dendrite, resulting in a flat eutectic front. During this process the eutectic becomes finer, as would be expected from theory. After a flat eutectic front is obtained, the jump is done in the other direction as to test for hysteresis effects on the morphology. While the eutectic coarsened after the second jump, the eutectic front stayed stable with no dendrites forming. Thus there is a certain dependence of prior microstructural history on which morphology is observed. Since the prior simulations always started from a dendrite, the "easy" direction of morphological change was available and thus the boundary curves could be confirmed. However, if the simulations were started from a eutectic front, it is likely that the eutectic range would be extended beyond the theoretical boundary curve. Usually, primary solidification takes place before the eutectic grows and thus the morphological hysteresis should not play a role for experiments.

The spacing and velocity of the eutectic are analyzed during the whole process and are shown in fig. 4.13d, with the black vertical line separating the two different imposed velocities. It is observed that while the velocity begins adjusting almost immediately, the eutectic spacing lags behind. After the original velocity is reached again, a similar spacing is observed again, confirming that the eutectic spacing is not subject to hysteresis effects[63].

The second transition is for a gradient of 99 K/mm and the same melt concentration of 0.12, with the velocity jump being from 320 µm/s to 20 µm/s, moving a eutectic into the dendritic-eutectic regime. Due to the priorly observed hysteresis, a much larger velocity jump is employed in this case. Sufficient space between the solidification front and the boundary is kept by extending the domain height to 1000 µm, yielding about 7.5 diffusion lengths. Figure 4.14 shows the results for the second case of slowing down a eutectic front. After a short initial period, α overgrows the eutectic front and forms a band. This band then undergoes a Mullins-Sekerka type of instability, with θ nucleating in concave regions. The convex regions can grow into dendrites. In the present case only a single dendrite grows, with a coarse eutectic growing around it. The simulation is not run to convergence as the small velocity would necessitate excessively long simulations. For this reason and because the eutectic nucleates anew above the destabilized band, the eutectic spacing is not analyzed in this case.

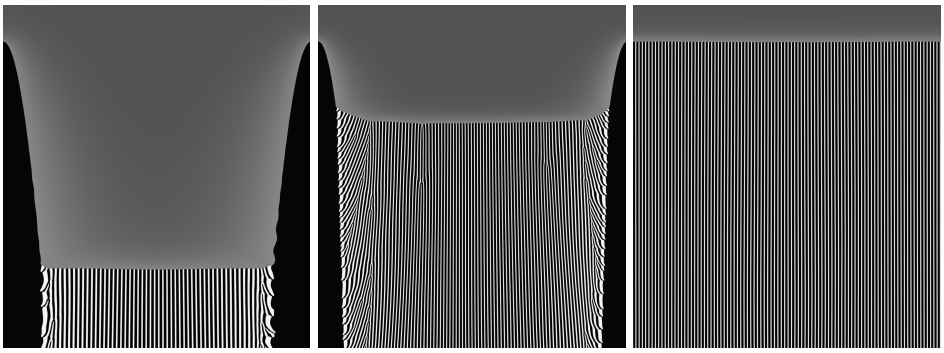

(a) $t = 0\,\mathrm{s}$ **(b)** $t = 1.875\,\mathrm{s}$ **(c)** $t = 5.5\,\mathrm{s}$

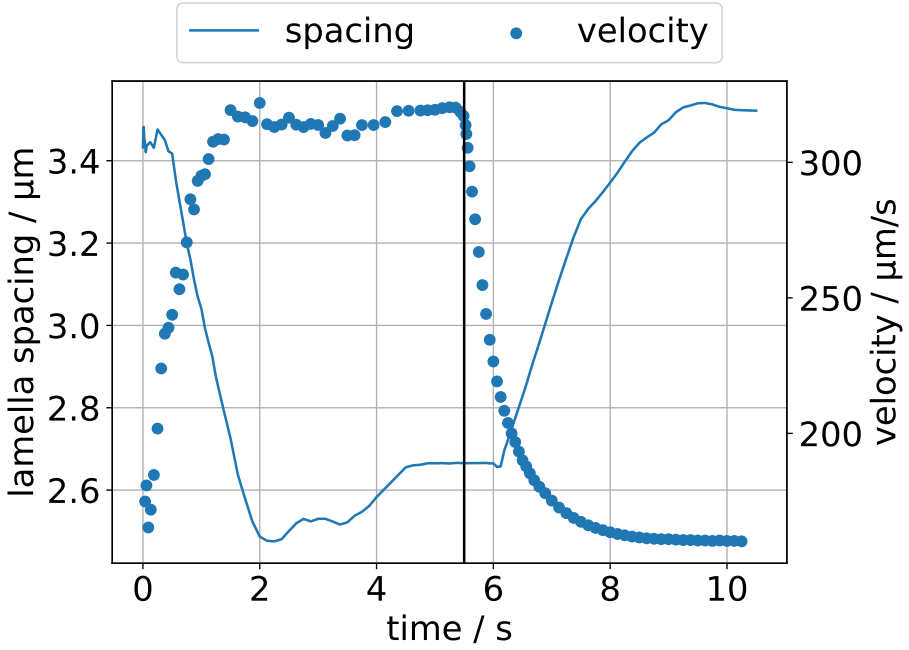

(d) Lamella spacing and velocity over time.

Figure 4.13: The top row shows simulation states for a jump from 160 µm/s to 320 µm/s, up to the point where the jump is reverted. The eutectic grew at a constant distance from the dendrite tip prior to the jump. After the jump, it slowly creeps upwards towards the dendrite tip before enveloping it and establishing a flat eutectic front. At the bottom, the lamellar spacing and eutectic velocity during the entire process is shown, with the black vertical line separating the two velocity regimes. The velocity begins adjusting almost immediately, with the lamellar spacing lagging behind in its adjustment. There tends to be an over/undershoot in the spacing before a stable spacing is reached.

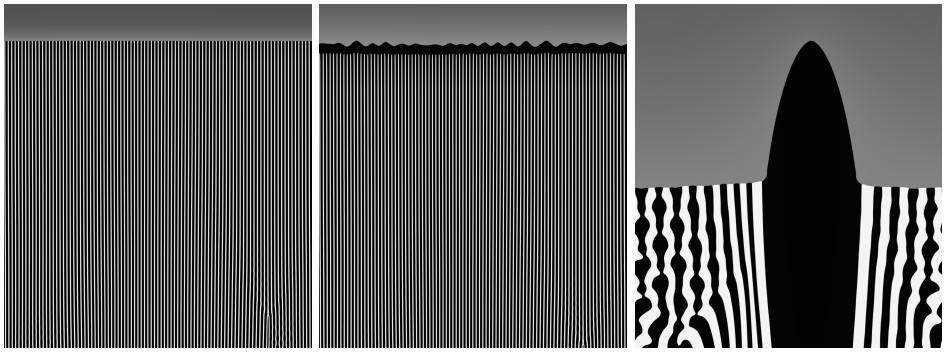

(a) $t = 0\,\mathrm{s}$ **(b)** $t = 0.313\,\mathrm{s}$ **(c)** $t = 16.5\,\mathrm{s}$

Figure 4.14: Intermediate simulation states for a velocity jump from 320 µm/s to 20 µm/s. Shortly after the velocity jump a band of α forms above the eutectic front. This band undergoes a Mullins-Sekerka instability allowing for a single dendrite to emerge surrounded by coarse eutectic.

4.3.3 Complete directional solidification

Three simulations approximating complete directional solidification, from below the liquidus down into the eutectic region, are performed. The previous simulations start out with the front temperature below the eutectic temperature, in which case there should already have been a dendritic structure for the eutectic to grow into. For these simulations the moving window technique is deactivated and the domain height is extended to 1500 µm and the width to 500 µm. The first two simulations should contain mostly one morphology, with the parameters $v = 320\,\mu\mathrm{m/s}$, $G = 24.7\,\mathrm{K/mm}$ being employed for both simulations, but two different melt compositions $c_0 \in \{0.08, 0.12\}$ being used. The former should yield a primarily dendritic structure, with the latter exhibiting a primarily eutectic structure based on the calculated boundary curve. As an example of a primarily dendritic-eutectic structure, a third simulation with $v = 160\,\mu\mathrm{m/s}$, $G = 24.7\,\mathrm{K/mm}$ and $c_0 = 0.12$ is conducted. The starting temperature $T_0 = 836\,\mathrm{K}$ for these simulations is chosen well below the respective liquidus temperatures but above the eutectic temperature. On one hand this allows a substantial amount of primary solidification while on the other hand cooling below the eutectic temperature is achievable with a reasonable amount of computational effort.

In fig. 4.15 the time-resolved microstructure for $c_0 = 0.08$ is shown. It can easily be observed in (a) that primary solidification occurs via dendrites which grow until they reach the top of the domain (b, c). Secondary arms are clearly visible (a), but as solidification progresses a significant number of secondary arms retracts towards the

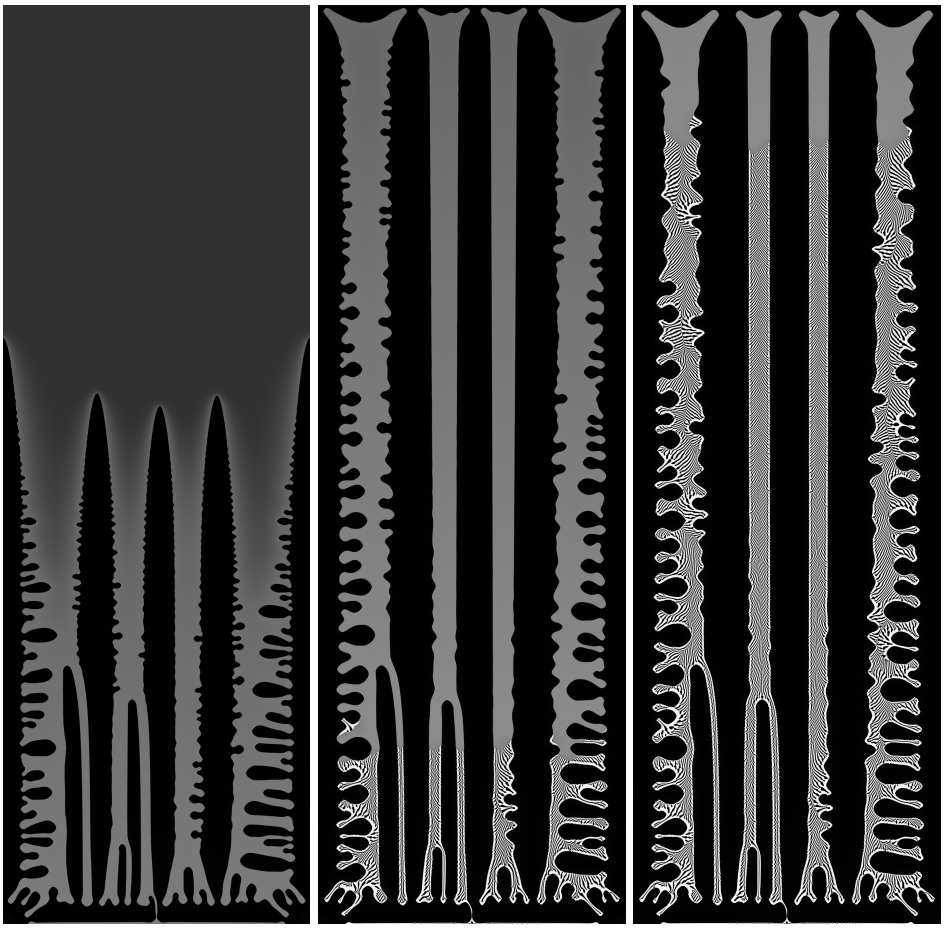

(a) $t = 1.81\,\mathrm{s}$, $T_b = 821\,\mathrm{K}$ **(b)** $t = 4.31\,\mathrm{s}$, $T_b = 802\,\mathrm{K}$ **(c)** $t = 7.38\,\mathrm{s}$, $T_b = 778\,\mathrm{K}$

Figure 4.15: Intermediate simulation states for a complete solidification of a Al-8at%Cu alloy from below the liquidus line across the eutectic line with $v = 320\,\mu\mathrm{m/s}$. The gradient in color from between the dendrites (black) to the top liquid is due to the interdendritic melt being enriched in copper, as copper is mostly rejected by the α phase. First, primary dendrites grow in the direction of the temperature gradient until the top of the domain is reached. Afterwards, the dendritic branch structure coarsens and at about 4 K below the eutectic temperature the eutectic nucleates near the bottom of the domain. This eutectic grows upwards, but new eutectic tends to nucleate faster in the side branch structure than the front can grow. Hence different orientations of somewhat lamellar structures are observed.

primary dendrites (b). The eutectic starts off nucleating near the bottom of the domain and then grows upwards in the side channels of the dendrites, but this is not the only mode of growth (b,c). Rather, the eutectic front tends to be nucleated anew in the Cu-rich pockets formed by dendritic sidearms and then grows towards the main channel, partially closing it off to the eutectic growing up from the bottom of the channel. Thus if an alloy crosses both the primary crystallization regime and the eutectic line during solidification, then eutectics of different dominant orientation should be found around dendritic structures. One should be mostly aligned with the dendritic growth direction, whereas the other with the growth direction of the side arms.

In fig. 4.16 the completely eutectic structure is shown. While a dendrite does grow initially, major parts of it are soon overtaken by the eutectic (a). The dendrite itself gets progressively thinner as the eutectic grows upwards until it is engulfed by the eutectic. The eutectic front is observed to be strongly curved during this overgrowth process (a,b), with some curvature still remaining after the overgrowth process (c). Beyond the initial primary arms, no secondary arms can be observed. The eutectic structure itself tends to contain oscillating waves (d) which travel across the structure at a roughly 30° offset from the growth direction. This kind of travelling oscillatory wave was also found experimentally in [145] with a 35° offset from the growth direction. These are also sometimes observed in the simulations with the moving window technique. It should be noted that regions with oscillating lamellas tend to grow at a slightly lower temperature compared to those with straight lamellas. Hence there is likely a correlation between the front curvature and the oscillating lamellas, though the determination of cause and effect of this correlation will be the topic of further research.

The last complete directional solidification simulation is shown in fig. 4.17. Similarly to the dominantly eutectic one, the dendrite grows first followed by eutectic. However, a constant distance between the dendrite tip and the eutectic front is established and the two morphologies continue to grow in parallel. The primary dendrite does not develop significant side arms, with the bumps quickly being covered by the eutectic. While there are again oscillations in the eutectic structure, these do not travel across the structure and are rather localized. In the closeup (d), the eutectic front can now also be observed to be curved close to the dendrite. In the previous simulations with the moving window technique, only the lamellas directly adjacent to the dendrites were observed to grow at a different temperature. This was assumed to have negligible effect on the structure as a whole but might be part of the structural influence leading to the observed refinement between eutectic and dendritic-eutectic structures.

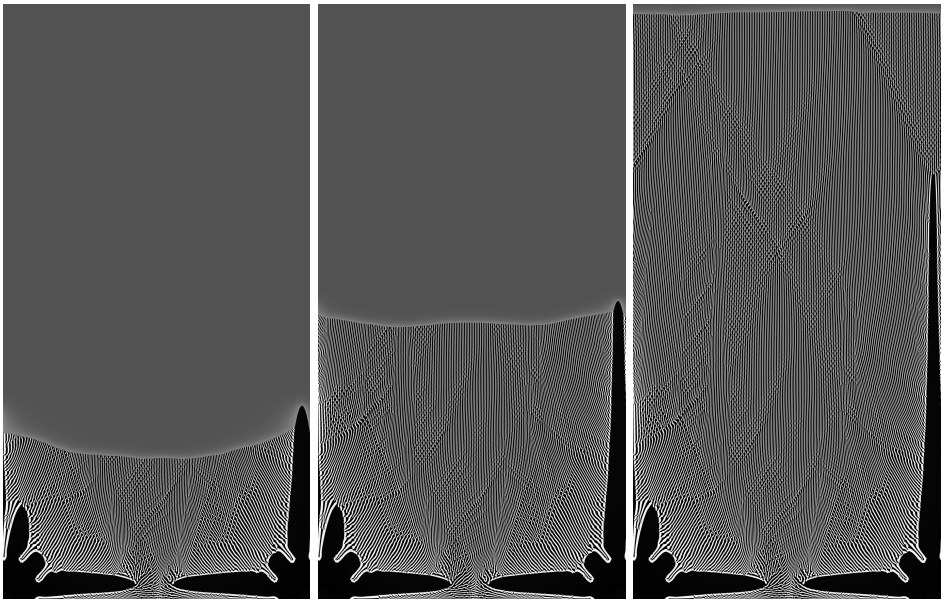

(a) $t = 4.31\,\mathrm{s}$, $T_b = 802\,\mathrm{K}$ **(b)** $t = 4.94\,\mathrm{s}$, $T_b = 797\,\mathrm{K}$ **(c)** $t = 6.5\,\mathrm{s}$, $T_b = 785\,\mathrm{K}$

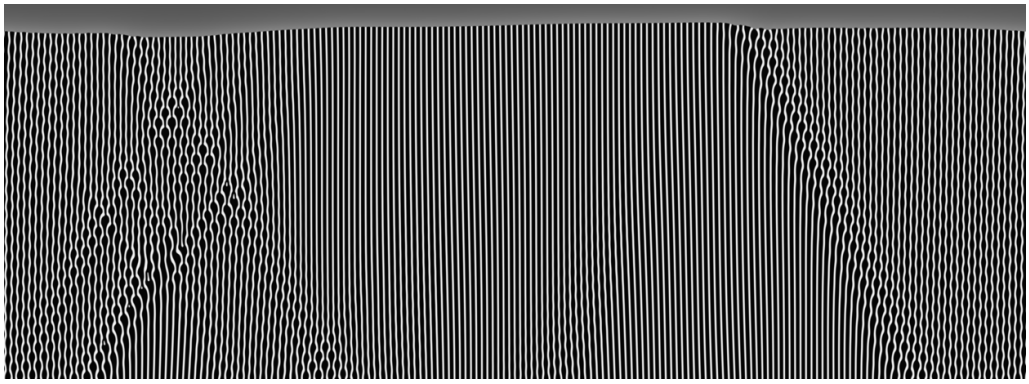

(d) $t = 6.5\,\mathrm{s}$, $T_b = 785\,\mathrm{K}$, closeup of the eutectic front

Figure 4.16: Intermediate simulation states for a complete solidification of a Al-12at%Cu alloy from below the liquidus line across the eutectic line with $v = 320\,\mu\mathrm{m/s}$. The images are cropped to slightly above the final position of the eutectic front, with the remaining size being $970\,\mu\mathrm{m} \times 500\,\mu\mathrm{m}$. First, a primary dendrite grows slowly until eutectic starts forming. The eutectic creeps up the dendrite, forcing the dendrite to taper off until overgrown. Oscillations which travel across the eutectic structure are clearly visible in the closeup. Even after the dendrite is eliminated, the eutectic front is still observed to be slightly curved.

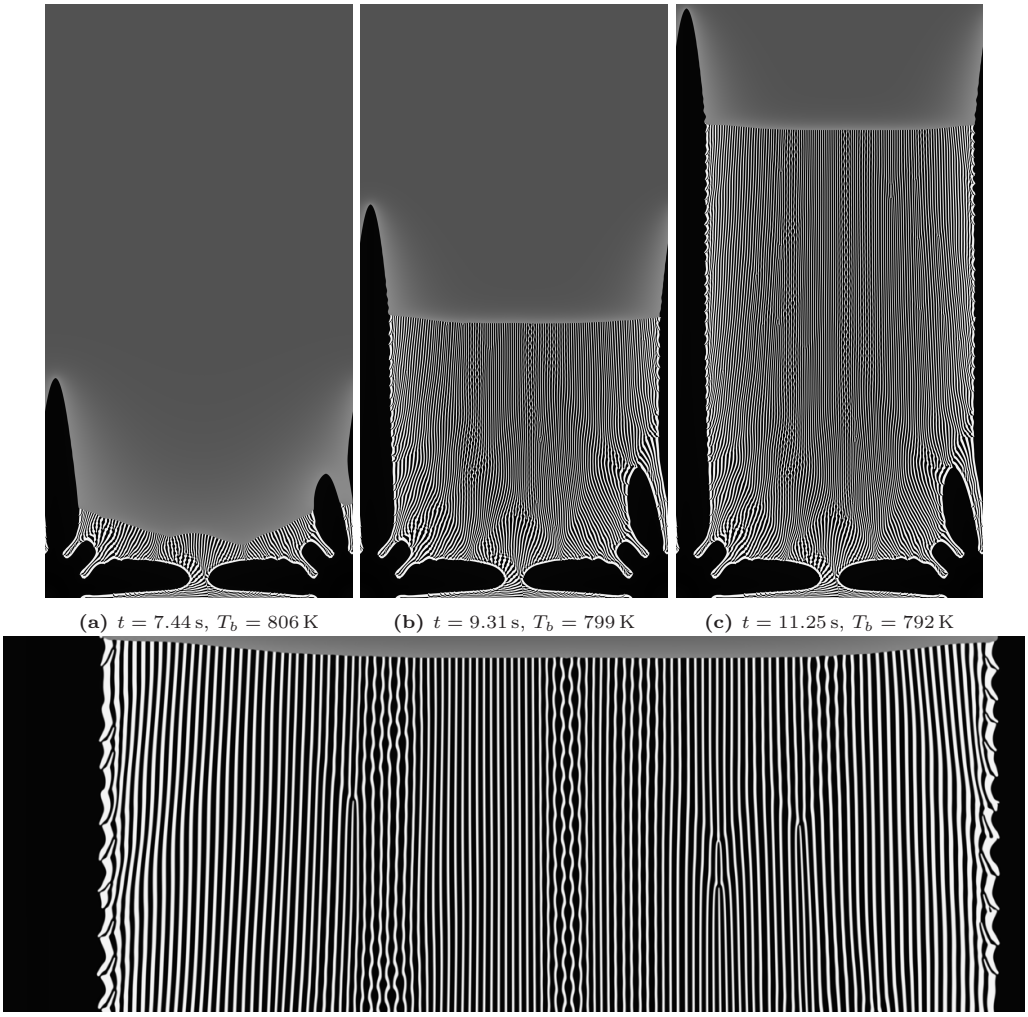

(a) $t = 7.44\,\mathrm{s}$, $T_b = 806\,\mathrm{K}$ **(b)** $t = 9.31\,\mathrm{s}$, $T_b = 799\,\mathrm{K}$ **(c)** $t = 11.25\,\mathrm{s}$, $T_b = 792\,\mathrm{K}$

(d) $t = 11.25\,\mathrm{s}$, $T_b = 792\,\mathrm{K}$, closeup of the eutectic front

Figure 4.17: Intermediate simulation states for a complete solidification of a Al-12at%Cu alloy from below the liquidus line across the eutectic line $v = 160\,\mu\mathrm{m/s}$. The images are cropped to slightly above the final position of the dendrite, with the remaining size being $970\,\mu\mathrm{m} \times 500\,\mu\mathrm{m}$. First, a primary dendrite grows slowly until eutectic starts forming. The eutectic creeps up the dendrite, overgrowing secondary arms but is unable to reach the dendrite tip. A constant distance between the eutectic front and the dendrite tip is observed in the later stages. The eutectic front is observed to be curved when close to the dendrite.

4.3.4 Eutectic morphology in 3D dendritic-eutectic growth

Finally, the influence of the dendritic-eutectic growth on the eutectic morphology is investigated. Since the two-dimensional simulations can only show lamellar eutectics, a set of three qualitative three-dimensional simulations is conducted. The three simulations differ only in their initial conditions: One starts with a Voronoi tesselation of the isotropic α-Al and θ phases, the second with a Voronoi tesselation of the anisotropic α-Al and the isotropic θ phases. The last one starts with a periodic anisotropic α-Al sphere as a dendrite seed together with a Voronoi tesselation of the isotropic α-Al and θ phases as a eutectic seed. With this, the effect of the anisotropy on the eutectic can be separated from that of the dendrite, as the morphological hysteresis will force the simulations without an initial dendrite seed into a purely eutectic structure. The previous two-dimensional simulations were ran at a grid spacing Δx of 1, which would lead to excessive computational effort in three dimensions. Thus a grid spacing of 2 is employed and the interfacial width is increased to 6 to keep a diffuse profile. These steps are taken to reduce the computational effort which will lead to mainly qualitative simulations. The simulation box size is $700 \times 500 \times 500$ cells, corresponding to real dimensions of $140\,\mu m \times 100\,\mu m \times 100\,\mu m$, with periodic boundary conditions on the basal plane, a no-flux condition on the bottom and a Dirichlet condition at the top. The processing parameters are $v = 160\,\mu m/s$, $G = 99\,K/mm$ and $c_0 = 0.14$. The composition is taken to be higher than would be expected to form a dendritic-eutectic structure, as three-dimensional dendrites grow more quickly at the same undercooling compared to their 2D counterparts, whereas a dimensional change has little effect on the eutectic.

The mass fractions at the composition c_0 are 60.9 % α and 39.1 % θ, which suggests that both lamellar and α-matrix-θ-fiber structures should be found[146]. The results for the two eutectic simulations are shown in figs. 4.18a and 4.18b. The α phase is represented as metallic silver, with the θ phase as metallic orange. The isotropic eutectic shows a mostly matrix-fiber structure with a few small lamellas remaining. However, the anisotropic variant shows only lamellas, as also observed by [28, 147], although in the present case only one of the solid-liquid interfaces is anisotropic. The mass fraction of α-Al in the isotropic variant is 59.2 % and 60.0 % for the anisotropic variant. While close to the lever rule, the remaining difference is likely due to capillary and far-field effects as there is a significant composition gradient left in the system. In fig. 4.18c the final state of the 3D simulation starting with a dendritic seed is shown. During growth, θ is primarily nucleated in the concave parts of the dendrite. As growth proceeds, these θ patches meet the main eutectic, forming new pairs of anisotropic α-Al and isotropic θ lamellas. These eventually overtake the isotropic eutectic seed, resulting in the observed lamellar

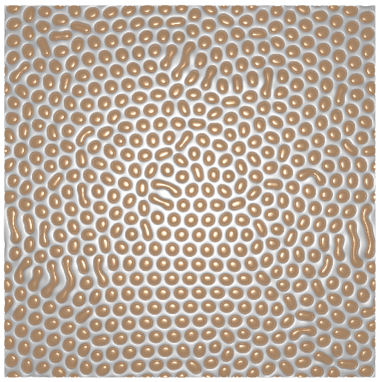

(a) Starting from an eutectic seed with isotropic α-Al and isotropic θ results in a matrix-fiber structure.

(b) Starting from an eutectic seed with anisotropic α-Al and isotropic θ results in a lamellar structure.

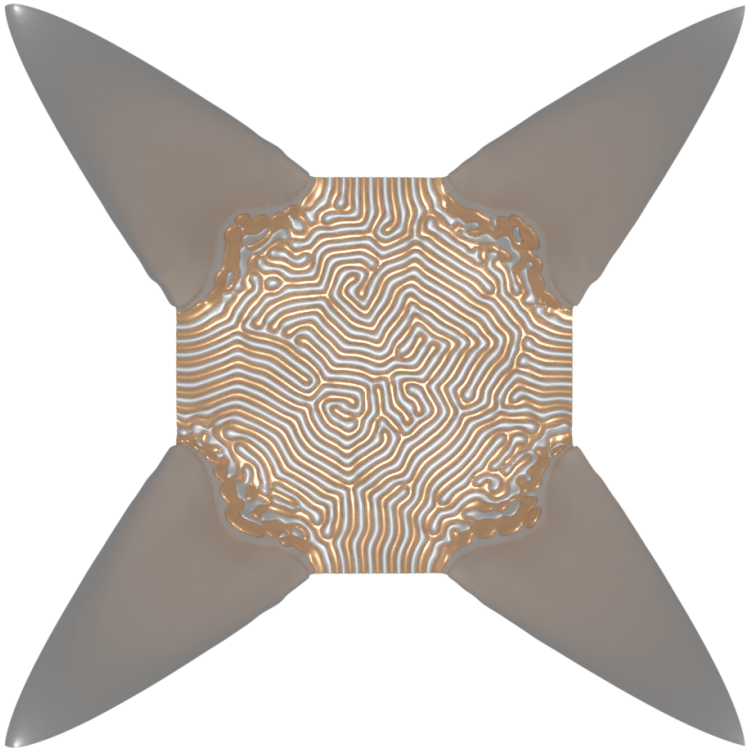

(c) Starting from a dendritic seed and an eutectic seed with isotropic α-Al and isotropic θ results in a lamellar eutectic being observed between the dendrite.

Figure 4.18: Final states of 3D simulations, showing the distribution of the solid phases in the entire domain. The camera is oriented antiparallel to the solidification direction to emphasize the eutectic pattern. This makes it seem as if fig. 4.18c does not have the same size as the other simulations, since the height difference between the dendrite and the eutectic includes a perspective effect.

structure. The α-Al mass fraction within the eutectic only is 53.0 % and thus significantly lower than for the eutectic morphologies. It is likely that if an isotropic or a much more weakly anisotropic interface were present, this would cause a shift to a more lamellar morphology, instead of it being due to the anisotropic interface. Furthermore, the mass fraction of θ is also enriched around the dendrite compared to the middle of the domain. The average lamellar spacing can be roughly estimated by dividing the volume of the region of interest by the surface area of the lamellas. The former is directly obtained by geometry, with the latter being related to the integral of the solid interphase boundary $\int_V \phi_\alpha \phi_\theta dV$. This yields a spacing of 3.49 µm for the dendritic-eutectic structure and a spacing of 3.56 µm for the purely eutectic structure, which compares well with the two-dimensional eutectic spacing results at the same velocity ($\lambda_{2D} \sim 3.5$ µm). The difference is even smaller than for the two-dimensional simulations and thus deemed to be insignificant.

4.4 Conclusion for coupled dendritic-eutectic growth

In this work dendritic, eutectic as well as dendritic-eutectic growth are simulated. This is achieved by combining a grand potential type of phase-field model with an empirical nucleation mechanism based on the local grand potential difference. It is validated by showing that a eutectic system with nucleation yields a Jackson-Hunt curve close to that of a system without nucleation. The dendritic growth is shown to qualitatively match an approximate undercooling model. Based on both of these validations, an approximate boundary curve between dendritic-eutectic growth and eutectic growth is determined. This curve is used to determine the processing conditions for simulations to show either dendritic-eutectic growth or pure eutectic growth. In each case, the observed simulated microstructure is found to agree with the prediction of the boundary curve, with the undercooling-velocity relationship not being appreciably changed by dendritic-eutectic growth.

By analyzing the spacing of the eutectic in the dendritic-eutectic simulations, a slightly refined spacing relative to pure eutectic structure at the same speed is found. Close to the α dendrite, the θ eutectic lamellas are found to be significantly thicker. Going further, the stability of the dendritic-eutectic regime is investigated by employing velocity jumps. When increasing the solidification speed of a dendritic-eutectic simulation, the eutectic regime is easily entered. During this increase, the eutectic continuously refines its spacing. Decreasing the speed back to the original value however does not yield a

dendritic-eutectic structure, but rather only a coarsened eutectic with a spacing similar to that of the original dendritic-eutectic simulation. Thus the spacing is not significantly affected by processing history, but the morphology is observed to depend on the prior processing history.

Finally, qualitative 3D simulations showed that the eutectic morphology is strongly influenced by the presence of interfacial anisotropy. For the same solidification conditions, isotropic interfaces yielded a fiber-matrix morphology, whereas if even one phase has a four-fold interfacial anisotropy, a lamellar structure is observed. This extends to the dendritic-eutectic case, in which a lamellar structure between primary dendrites is observed. While the lamellar spacing did not differ significantly between a 3D lamellar eutectic and the 3D dendritic-eutectic, the mass fractions of α-Al and θ within the eutectic are observed to differ significantly. Furthermore, the presence of the dendrite changes the spatial distribution of phase widths, with these differing significantly close to the dendrite compared to the bulk of the eutectic, suggesting significant spatial heterogeneity of properties if coupled dendritic-eutectic growth occurs. In total this work lays the groundwork for further investigations into solidification microstructures containing different kinds of morphologies evolving at different length scales.

5 Freeze-casting with the phase-field method

This chapter is based on the author's paper [80] (© Elsevier. Reproduced with permission. All rights reserved). The following sections are taken verbatim from the paper, with only minor linguistic and stylistic changes to account for the move from a paper to a chapter in the present dissertation, as well as some clarifications due to the referees. Numerical details and relevant literature are also given in the paper.

This chapter uses the model described in section 3.1.1, with specially crafted Gibbs free energy terms which approximate the freeze-casting process including the effect of particle size. First, the parametrization of the system with special focus on the construction of these Gibbs free energies is given. Based on the Gibbs energies, directional solidification simulations are conducted and the microstructural lengths L of interest — tip distance λ, ice trunk diameter d_{ice} and suspension channel diameter d_{sus} — measured. Power laws relating these individually to the process parameters are established and analyzed.

The short messages of this chapter are:

- homogenizing over the particles is a viable approach for simulating freeze-casting
- the microstructure during freeze-casting is significantly influenced by velocity v, temperature gradient G and solids loading c_0
- the temperature gradient's influence on the suspension channel's diameter lessens with increasing particle size

5.1 Parametrization of the freeze-casting system

The key in linking the phase-field evolution to a specific material lies in its parametrization in terms of energies and kinetics. In this section, the focus will be on the energetic

part, specifically the complex anisotropy of the ice-water interface and the grand potential density of colloidal suspensions. The energetic contribution consists of the interfacial and the bulk energies. Many experimental studies ([148–150] and references in [151]) exist for the determination of the interfacial energy between ice and water, with values ranging from $25\,\mathrm{mJ/m^2}$ to $45\,\mathrm{mJ/m^2}$ — for the purpose of simplicity a value of $30\,\mathrm{mJ/m^2}$ is assumed, which is close to the data of Hardy [150]. This value describes the *isotropic* behavior, but ice is an anisotropic material. For its capillary anisotropy the function a_{cap} is expanded into a sum of spherical harmonics Y_{lm}:

$$\begin{aligned} a_{cap}(\vec{q}_{\alpha\beta}) &= \sum_{l,m} \epsilon_{lm} Y_{lm}(\vec{q}_{\alpha\beta}) \\ &= 1 + \epsilon_{4,0}^{cap} Y_{4,0}(\vec{q}_{\alpha\beta}) + \epsilon_{6,6}^{cap} Y_{6,6}(\vec{q}_{\alpha\beta}), \end{aligned} \tag{5.1}$$

which yields a smooth, weak hexagonal capillary anisotropy with the coefficients $\epsilon_{4,0}^{cap} = -0.045, \epsilon_{6,6}^{cap} = 0.0015$. This choice is due to relatively small difference in interfacial energies according to [152–154][155, p. 440]. Furthermore, [156] showed that below a critical undercooling the interface is smooth, implying that the typical hexagonal shape is due to kinetic effects rather than capillary ones, hence the weak capillary anisotropy. This, together with the different kinetics along the basal and prismal planes [157], is reproduced via the kinetic anisotropy function a_{kin}:

$$a_{kin}(\vec{q}_{\alpha\beta}) = 1 + \epsilon_{2,0}^{kin} Y_{2,0}(\vec{q}_{\alpha\beta}) + \epsilon_{4,0}^{kin} Y_{4,0}(\vec{q}_{\alpha\beta}) + \epsilon_{6,6}^{kin} Y_{6,6}(\vec{q}_{\alpha\beta}) \tag{5.2}$$

with coefficients $\epsilon_{2,0}^{kin} = -0.66, \epsilon_{4,0}^{kin} = -0.34, \epsilon_{6,6}^{kin} = 0.15$ yielding a strong hexagonal anisotropy in the basal plane with a marked reduction in growth kinetics normal to the basal plane. The isotropic value $\tau_{\alpha\beta}$ is chosen such that diffusion-controlled growth is ensured.

The bulk energetic contribution enters the phase-field model from the previous section by the grand potential differences, which are related to differences in Gibbs free energy. For pure ice and water, the International Association for the Properties of Water and Steam (IAPWS) formulations [134] provide extensive thermodynamic information, including the enthalpy and Gibbs energy as a function of temperature. These allow the fitting of the concentration-independent term $C_\alpha(T)$ in eq. (3.123) for ice and water. The volumetric enthalpy of each phase α can be derived from the Gibbs energy by

$$h_\alpha = g_\alpha - \frac{\partial g_\alpha}{\partial T}. \tag{5.3}$$

Both the enthalpy and Gibbs free energy are fitted against data provided by the IAPWS formulations with the `LSSolve` function of Maple. Back-calculating from the fitted enthalpy for the latent heat showed excellent agreement with a relative error of 1.3 %.

However, to the author's knowledge there is no experimental data for the enthalpy or Gibbs free energy in aqueous colloidal suspensions. Hence the model of Peppin et al. [76, 78] is utilized in order to extend the description from pure water and ice to aqueous suspensions, specifically aqueous suspensions of bentonite. The liquidus curve

$$T_l(c) = T_m(1 + mc\frac{1 + a_1c + a_2c^2 + a_3c^3 + a_4c^4}{1 - c/c_p})^{-1}, \tag{5.4}$$

with the coefficients of [78] and $c_p = 0.64$ being the random dense-packing density (RDP), describes the temperature below which a coarse-grained suspension begins to separate into a solid ice phase and the remaining suspension enriched in colloids. The factor $m = \frac{k_b T_m}{V_p \rho_f L_f}$ with the Boltzmann constant k_b, the melting temperature of the pure substance T_m, the volume of an individual particle V_p, the fluid density ρ_f and its melting enthalpy L_f incorporates the effect of differently sized particles. The origin of the dependence on the particle volume is its inclusion in the osmotic pressure of a suspension of hard spheres, which is employed by Peppin et al. [76] to derive eq. (5.4). The particles are assumed to be spherical and thus $V_p = \frac{4}{3}\pi r^3$ with r being the radius of an individual particle. From this it can be seen that the liquidus curve in the model of Peppin et al. depends significantly on the radius of the suspended particles, with smaller particles resulting in steeper liquidus curves.

The connection between the liquidus curve and the chemical equilibrium conditions is exploited in order to establish a least-squares problem for the functions $A_\alpha(T), B_\alpha(T)$ in eq. (3.123) for both phases. For the temperature range of interest, the equilibrium conditions

$$g_s(c_s, T) + \mu_s(c_s, T)(c_i - c_s) - g_i(c_i, T) = 0 \tag{5.5}$$

$$\mu_s(c_s, T) - \mu_i(c_i, T) = 0 \tag{5.6}$$

are evaluated on the liquidus curve points (c_s, T) and the solidus curve points (c_i, T) for the suspension phase's Gibbs energy g_s and the ice phase's Gibbs energy g_i respectively. This yields a matrix of squared residuals whose minimization gives the functions $g_s(c, T), g_i(c, T)$ which generate a phase diagram with the minimal distance from the given phase boundaries. Again, the `LSSolve` function of Maple is employed, this time with an additional constraint that the curvatures of the Gibbs energy curves are to be positive for the employed temperature ranges. The solid ice phase is assumed to be largely

Table 5.1: Employed physical and numerical parameters for the simulations.

parameter	simulation value	physical value
Numerical parameters		
grid spacing Δx	1	$1 \times 10^{-6}\,\mathrm{m}$
time step Δt	0.025	$2.5 \times 10^{-4}\,\mathrm{s}$
interface width W	$2.5 \cdot 5 \cdot \Delta x$	$12.5 \times 10^{-6}\,\mathrm{m}$
Physical parameters		
surface energy $\gamma_{\alpha\beta}$	0.097879	$0.03\,\mathrm{J/m^2}$
diffusivity in suspension	1	$1 \times 10^{-10}\,\mathrm{m^2/s}$
diffusivity in ice	1×10^{-3}	$1 \times 10^{-13}\,\mathrm{m^2/s}$
kinetic coefficient $\tau_{\alpha\beta}$	33	$1.01\,\mathrm{Js/m^4}$
melting temperature T_m	1	$273.15\,\mathrm{K}$

stoichiometric, with its solidus curve given by $c_i = (T_m - \frac{T}{5})/100$ in non-dimensional temperature T and non-dimensional melting temperature T_m. This slight dependence of the ice composition on the temperature is included for numerical stability.

This procedure can be executed for any desired particle radius, yielding Gibbs energy curves approximating a binary phase diagram according to the theory of Peppin et al. In contrast, the prior work of Huang [79] does not consider the particle size at any time during model formulation or parametrization. Three particle radii r (250 nm, 375 nm and 500 nm) are studied in this paper, with the free energy parameters of each tabulated in the employed precision in appendix A.2. The resulting phase diagrams for all particle sizes are shown in one plot in fig. 5.1. As the solidus curve does not differ much between the particle sizes, only a single one was drawn. Generally the liquidus curve becomes flatter and moves towards the RDP with increasing particle size.

Furthermore, table 5.1 shows the remaining numerical and physical parameters necessary to conduct the simulation. The parameters were nondimensionalized by choosing the length scale $l_0 = 1\,\mu\mathrm{m}$, the diffusion scale $D_0 = 1 \times 10^{-10}\,\mathrm{m^2/s}$, the temperature scale $T_0 = 273.15\,\mathrm{K}$, the energy density scale $E_0 = 3.065 \times 10^5\,\mathrm{J/m^3}$ and the molar volume scale $V_{m,0} = 2 \times 10^{-5}\,\mathrm{m^3/mol}$. Based on these the remaining scales of time, surface energy and kinetic coefficient can be derived. For each physical parameter, its dimensionless value is determined by dividing it by its corresponding scaling parameter.

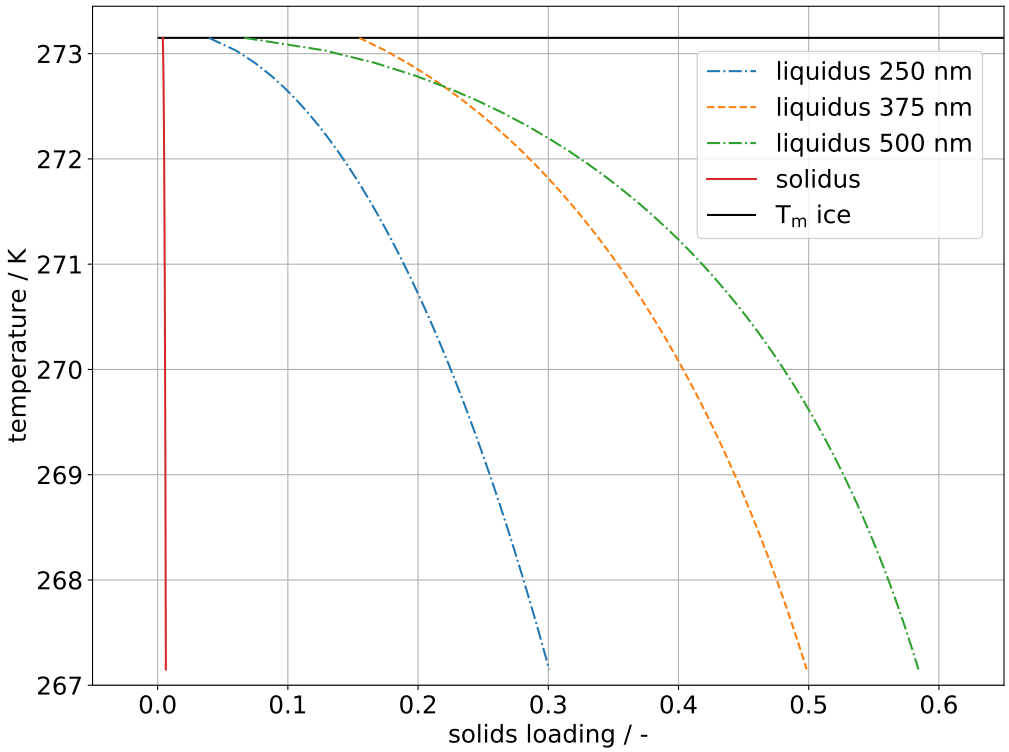

Figure 5.1: Back-calculated phase diagrams of freeze casting for three different particle sizes with the parameters from appendix A.2. Since the solidus curves are very close together only a single line is drawn. However, the liquidus curves differ significantly for each particle size. The larger the particle radius, the flatter the liquidus curve becomes.

5.2 Simulation setup

The simulations are conducted as follows: A planar ice front is put in the left part of the domain and the rest of the domain is filled with the suspension at the investigated solids loading c_0. Periodic boundary conditions are applied on the top and bottom sides, whereas zero flux conditions are applied on the left (solid) side. On the right (liquid) side of the domain the phase-field has zero flux conditions and the solids loading is fixed to c_0 with a Dirichlet boundary condition. A moving window technique is applied in order to simulate a quasi-infinite domain in the growth direction. The planar ice front is set such that this moving window starts immediately. A graphical overview of the simulation setup can be seen in fig. 5.2a. Within this and following figures, yellow indicates the ice crystal and blue the suspension with the red-orange part indicating

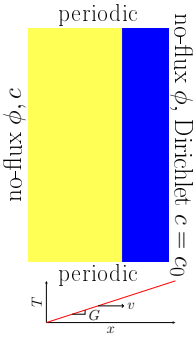

(a) Simulation setup for the directional solidification of the suspension.

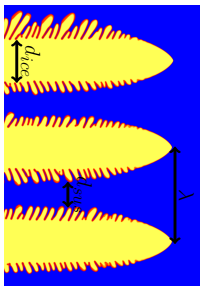

(b) Exemplary part of a steady-state simulation. λ is the tip distance, d_{ice} the ice trunk diameter and d_{sus} the suspension channel diameter.

Figure 5.2: Initial and boundary conditions of the simulation as well a subregion of an exemplary steady-state simulation. Yellow indicates the ice crystal and blue the suspension, with the red-orange part being the diffuse interface.

the diffuse interface. Additionally in fig. 5.2b the considered microstructural lengths are shown: The tip distance, or wavelength, λ, the ice trunk diameter d_{ice} and the suspension channel diameter d_{sus}. For the trunk and channel diameters the straight regions of pure ice and pure suspension are determined. Hence the region of side branches is excluded from the measurement which leads to $\lambda > d_{ice} + d_{sus}$.

5.3 Overview of results

Simulations are conducted with the following solidification conditions: Solids loading $c_0 \in \{0.075, 0.1, 0.15\}$, pulling velocity $v \in \{3.2, 6.4, 12.8\}$µm/s and temperature gradient $G \in \{1.5, 24\}$K/mm for the parameter sets for 250 nm, 375 nm as well as 500 nm particle suspensions, resulting in 54 simulations. The first temperature gradient is similar to the one found in experiments [158] with the second one chosen for quicker convergence of the microstructure. The simulations are continued until no dendrite is moving significantly out of the moving window. Figure 5.3 gives an overview of the final simulated microstructure for various parameters. Several observations are evident: The microstructure is refined by higher pulling velocities v and dendritic side branches are less developed. The latter effect is likely caused by the distance between dendritic trunks decreasing which causes diffusion-mediated suppression of the side branches. In contrast the solids loading directly changes the mass fraction of ice to suspension, with an increase of the solids loading causing a widening of the suspension channels and a narrowing of the ice trunks. Furthermore, dendritic side branches become more prominent for higher

solids loading as the trunk distance grows. Finally, increasing the particle size generally lessens side branching by decreasing the trunk distance. Simulation snapshots of all conducted simulations in their final state are available in appendix A.2.

5.4 Influences on the microstructural lengths

The tip distance λ, the ice trunk diameter d_{ice} and the suspension channel diameter d_{sus} are measured as the microstructural length parameters in each simulation. In order to build a relationship between the processing parameter set $\{c_0, v, G\}$ and the output microstructural length, it is assumed that a power law relationship holds for each parameter and that the parameters' effect can be separated, i.e. their product yields the microstructural length up to a constant multiplier. Hence the results will be fitted to the model

$$L = Ac_0^n v^m G^o \tag{5.7}$$

with L being any of the microstructural lengths. This model is similar to analytical models for dendritic growth in alloy solidification [9], except that the solids loading c_0 takes the place of the solidification range ΔT_0. In the following, the model is fitted to the different simulated microstructural lengths and the results discussed. The main thrust of this discussion will be on the scaling laws and hence the prefactor A will not be discussed, but reported for completeness' sake. Table 5.2 provides an overview of the predicted, observed and fitted results for scaling laws from literature as well as this work. In the following, the fitting results will be discussed and compared to theoretical and experimental results.

First, the results for particles of 250 nm radius are used for parametrizing this model. Fitting the simulation data for the wavelength λ against this model yields the parameters plus-minus the standard deviation $A = 4729\,\mu\text{m} \pm 956.0\,\mu\text{m}$, $n = -0.07088 \pm 0.06306$, $m = -0.6058 \pm 0.03714$, $o = -0.2675 \pm 0.01658$, with v in µm/s and G in K/m. The velocity exponent m is close to the range of experimentally reported values $[-0.67, -1.3]$[158–160]. Note that as [159] mentions the velocity exponent depends on the particle size, the effect of which will be shown shortly. However, none of the experimental studies systematically studied the influence of the temperature gradient on the structural wavelength. The aforementioned model by Kurz et al. [9] predicts an exponent of -0.5, whereas here a temperature gradient exponent o of roughly half this value is observed. While this difference remains to be investigated, it does imply that care should be taken to control

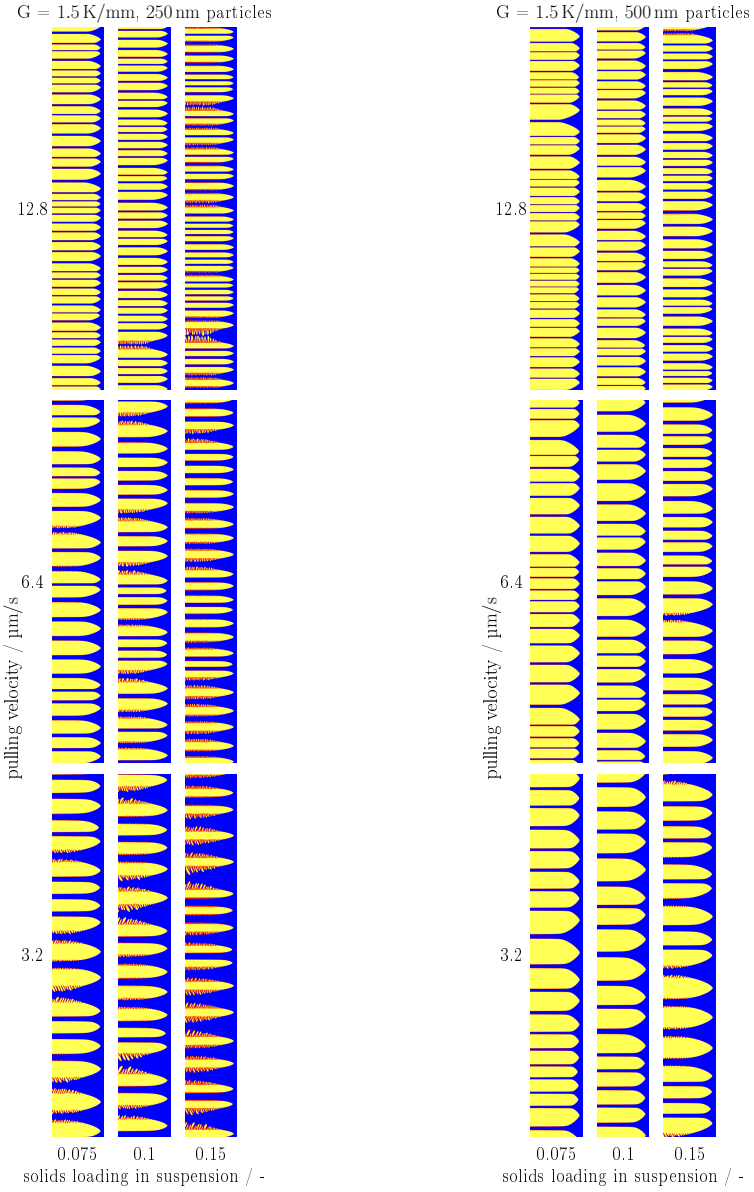

Figure 5.3: Overview of simulation results for suspensions of 250 nm and 500 nm particles being directionally solidified in a 1.5 K/mm temperature gradient. Increasing the pulling velocity refines the structure in general. Increasing the solids loading roughens the side structure of the ice dendrite and decreases the fraction of ice trunk diameter to suspension channel diameter. Freeze-cast suspensions with larger particles tend to show less dendritic features.

Table 5.2: Predicted, observed and fitted parameters to eq. (5.7).

L predicted/fitted/observed	n in c_0^n	m in v^m	o in G^o
λ predicted by Kurz et al. [9]	-	-0.5 (cells), -0.25 (dendrites)	-0.5
λ observed by Waschkies et al. [158]	-	-0.8 to -1.3	-
λ observed by Deville et al. [159]	-	-0.67 to -1	-
λ fitted in this work, 250 nm particles	-0.07088 ± 0.06306	-0.6058 ± 0.03714	-0.2675 ± 0.01658
λ fitted in this work, 375 nm particles	$+0.04561 \pm 0.03953$	-0.5699 ± 0.02304	-0.2317 ± 0.009860
λ fitted in this work, 500 nm particles	$+0.08709 \pm 0.04294$	-0.5847 ± 0.02525	-0.2037 ± 0.01029
d_{sus} fitted in this work, 250 nm particles	$+0.3733 \pm 0.1037$	-0.6995 ± 0.06473	-0.4193 ± 0.03747
d_{sus} fitted in this work, 375 nm particles	$+0.5611 \pm 0.05328$	-0.7520 ± 0.03389	-0.1699 ± 0.01207
d_{sus} fitted in this work, 500 nm particles	$+0.6485 \pm 0.09631$	-0.7754 ± 0.06159	-0.05052 ± 0.01963
d_{ice} fitted in this work, 250 nm particles	-0.7147 ± 0.09337	-0.3119 ± 0.04442	-0.1488 ± 0.01882
d_{ice} fitted in this work, 375 nm particles	-0.4091 ± 0.07633	-0.4488 ± 0.04028	-0.2590 ± 0.01902
d_{ice} fitted in this work, 500 nm particles	-0.1987 ± 0.05944	-0.3877 ± 0.03151	-0.2134 ± 0.01415

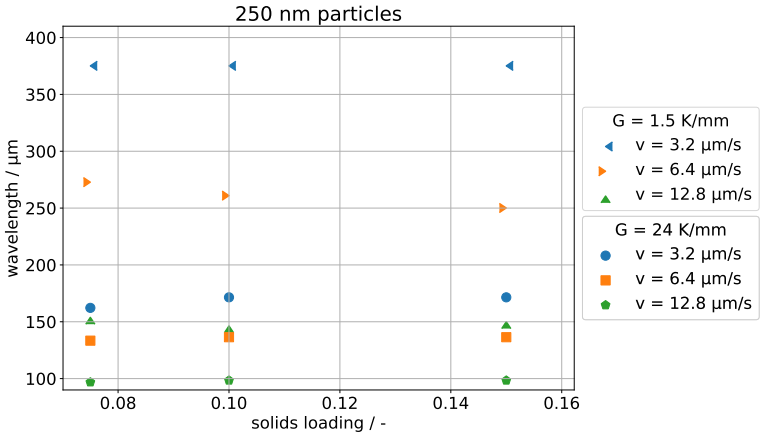

Figure 5.4: Scatter plot of the solids loading and observed wavelength with 250 nm particles. The triangular symbols indicate the observations for $G = 1.5\,\mathrm{K/mm}$ and the rest for $G = 24\,\mathrm{K/mm}$. The solids loading only has a minor effect on the observed wavelength compared to the pulling velocity and temperature gradient. Furthermore, its effect apparently reverses direction for the higher gradient.

the temperature gradient during freeze casting, as it has a significant influence on the wavelength of the microstructure. The exponent n for the solids loading c_0 is harder to compare with existing models as these typically employ the solidification range ΔT_0. However, drawing a scatter plot of the solids loading and the observed wavelength for several velocities, as shown in fig. 5.4, helps to interpret the result: The wavelength is mainly determined by the pulling velocity v and the temperature gradient G, with the solids loading showing only a minor effect. The direction of this effect even changes for the higher gradient, hence the small value for n and its comparably large standard deviation can be interpreted as the solids loading having close to no correlation to the structural wavelength for this particle size.

Fitting the model with measured suspension channel diameter d_{sus} yields the parameters $A = 10.48\,\mathrm{mm} \pm 3.953\,\mathrm{mm}$, $n = 0.3733 \pm 0.10364$, $m = -0.6995 \pm 0.06473$, $o = -0.4193 \pm 0.03747$. The velocity exponent now crosses into the range of experimentally observed exponents and the temperature gradient exponent is closer to the model by Kurz et al. [9]. However, the exponent for the solids loading has changed appreciably. In order to interpret this, consider that the suspension channels are closely related to the dense part of the structure after the freeze-casting process is finished. The density, or equivalently porosity, has been experimentally shown [160] to depend linearly on the solids loading of the suspension, which would correspond to a solids loading exponent of $n = 1$ for the dense part of the structure. However, the suspension channels in the simulation do not

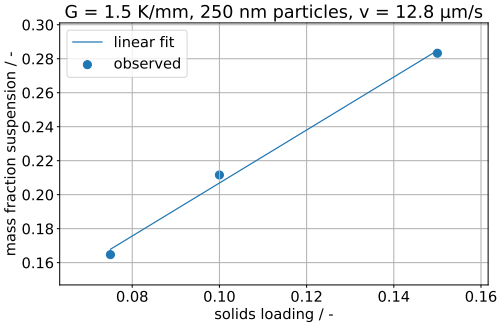

Figure 5.5: The mass fraction of the suspension below the dendrite tips vs solids loading for $\{G = 1.5\,\mathrm{K/mm}, v = 12.8\,\mu\mathrm{m/s}\}$ with 250 nm particles.

correspond exactly to the solid walls within the freeze-cast structure, as the solidification is not finished and the channel diameter disregards the ambiguous region of side branches. Furthermore, the suspension channel diameter itself is modulated by the wavelength λ. In order to show the linear relationship between density and solids loading, the observed mass fraction of the suspension below the dendrite tips is plotted over the solids loading in fig. 5.5 along with a linear fit to the data for a velocity of $12.8\,\mu$m/s. The fit is also calculated for the remaining velocites and gradients, all of which show good correlation ($R^2 \geq 0.995$), suggesting that the model reproduces the linear relationship between solids loading and density as found in experiments.

Finally, applying the model to the ice dendrite trunk diameter d_{ice} yields the parameters $A = 148.5\,\mu\mathrm{m} \pm 41.61\,\mu\mathrm{m}$, $n = -0.7147 \pm 0.09337$, $m = -0.3119 \pm 0.04442$, $o = -0.1488 \pm 0.01881$. These are very different from the previous results and indicate that the ice trunk diameter is less sensitive to changes in the gradient and the solidification velocity but more sensitive to changes in the solids loading compared to the suspension channel diameter. The sign change of the solids loading exponent directly follows from the ice phase rejecting particles and hence when more particles are present, less space is available for the ice to solidify. Calculating the mass fraction of ice as above also indicates that a linear relationship, now with negative slope, exists between the ice mass fraction and the solids loading of the suspension.

Next, the simulation results for particles of 375 nm radius are used for parametrizing eq. (5.7). The fitting parameters $A = 4471\,\mu\mathrm{m} \pm 555.0\,\mu\mathrm{m}$, $n = 0.04561 \pm 0.03953$, $m = -0.5699 \pm 0.02304$, $o = -0.2317 \pm 0.009862$ are obtained for the wavelength λ. In contrast to the 250 nm particle results, the concentration exponent n is now positive. Furthermore its standard deviation relative to the exponent is smaller, which suggests

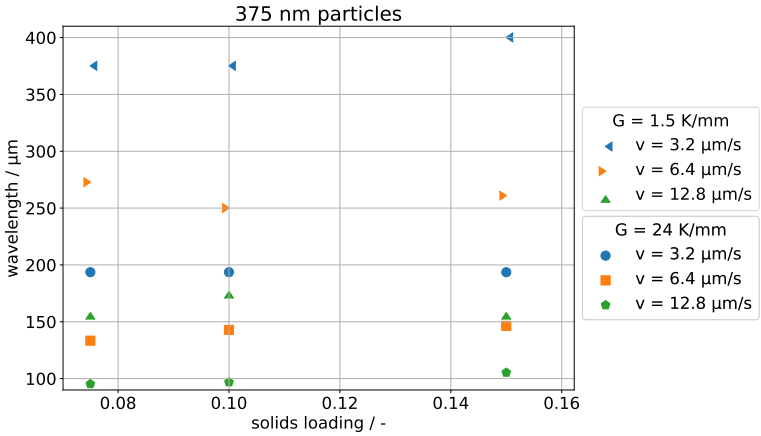

Figure 5.6: Scatter plot of the solids loading and observed wavelength with 375 nm particles. The triangular symbols indicate the observations for $G = 1.5\,\mathrm{K/mm}$ and the rest for $G = 24\,\mathrm{K/mm}$. The effect of the solids loading on the wavelength is still minor compared to the pulling velocity and temperature gradient. However more points tend to trend upwards with a higher solids loading.

that there is a small coarsening effect on the wavelength when increasing the solids loading. The corresponding scatter plot in fig. 5.6 shows mostly irregular behavior again but with more points trending upwards for higher solids loading. Both the velocity exponent m and the temperature gradient exponents o have decreased slightly from the previous case.

Fitting the data for the suspension channel diameter d_{sus} yields $A = 2387\,\mu\mathrm{m} \pm 381.6\,\mu\mathrm{m}$, $n = 0.5611 \pm 0.05328$, $m = -0.7520 \pm 0.03389$, $o = -0.1699 \pm 0.01207$. The solids loading exponent is now closer to the expected value of 1. As can be seen in fig. 5.1, for a given undercooling below the liquidus, the suspensions with larger particles will have an equilibrium solids loading closer to the random dense-packing density of 0.64. The liquidus becomes very steep close to this RDP, similar to the stoichiometric solidus line. Hence a suspension region which achieves this concentration range will stay close to it, even if it is cooled down further. In combination with the stoichiometric solidus line this implies that a constant partition coefficient $k = x_i/x_s$ with the equilibrium solids loading in the ice x_i and the suspension x_s is achieved. Away from this region the partition coefficient is a function of temperature. Thus it is likely that more cells in the growth direction below the moving window point would further move the solids loading exponent to a value of 1, as a bigger part of the simulation domain would have an almost constant partition coefficient. The velocity exponent m increased from the 250 nm particle results whereas the temperature gradient exponent o decreased.

Employing the data for the ice trunk diameter d_{ice} yields $A = 1167\,\mu\text{m} \pm 281.9\,\mu\text{m}$, $n = -0.4091 \pm 0.07633$, $m = -0.4488 \pm 0.04028$, $o = -0.2590 \pm 0.01902$. As with the suspension channel results, the velocity exponent shows a slight increase. Contrary to those results, the temperature gradient exponent o increased. The solids loading exponent is still negative but has decreased substantially.

Finally, the simulations results for particles of 500 nm radius are used for parametrizing eq. (5.7). For the structural wavelength λ, the parameters $A = 3791\,\mu\text{m} \pm 504.5\,\mu\text{m}$, $n = 0.08709 \pm 0.04294$, $m = -0.5847 \pm 0.02525$, $o = -0.2037 \pm 0.01029$ are obtained. As with the 375 nm results, a slight coarsening effect of increased solids loading is present, with even more points trending upwards in a scatter plot. The effect of the temperature gradient on the wavelength seems to decrease slightly with increasing particle size. The velocity exponent is close to that of 375 nm particle suspensions, though slightly larger now. In [159] the authors observed a velocity exponent of 1 for 400 nm particles and one of $\frac{2}{3}$ for 100 nm particles, both suspended in water. The present study shows a minor effect in the other direction, that is the velocity exponent increases as the particle size is reduced. However, the magnitude of this effect relative to the error in the exponent does not suggest that the effect is significant. An explanation for the dependence of the velocity exponent is the concentration and particle size dependent diffusivity [161]. However, the present study assumes a constant diffusivity of particles in the suspension. Hence the variation of the velocity exponent is likely to be largely a function of the kinetics represented by diffusivity, with only minor energetic influences.

For the suspension channel diameter d_{sus} the parameters $A = 965.7\,\mu\text{m} \pm 272.5\,\mu\text{m}$, $n = 0.6485 \pm 0.09631$, $m = -0.7754 \pm 0.06159$, $o = -0.05052 \pm 0.01963$ are obtained. The velocity exponent is now higher than for the suspension with smaller particles, but the ranges including the error overlap again. The trend of increasing solids loading exponent with increasing particle size continues, although in a less significant way as the ranges including the error overlap now. Furthermore, the dependence of the suspension channel diameter on the temperature gradient is significantly smaller than for the suspensions with smaller particles. Scatter plots of the suspension channel diameter against the temperature gradient generally show a refinement effect, with two outliers. One shows almost no refinement and the other a coarsening effect on the suspension channel, whereas both the wavelength and ice trunk exhibit refinement. Excluding those two outliers roughly doubles the exponent, but even at -0.1 there is still a significant difference to the results for suspension with smaller particle sizes which remains to be investigated further.

Lastly, fitting against the results for the ice trunk diameter d_{ice} yields the parameters $A = 1122\,\mu\text{m} \pm 207.6\,\mu\text{m}$, $n = -0.1987 \pm 0.05944$, $m = -0.3878 \pm 0.03151$, $o = -0.2134 \pm 0.01415$. The solids loading exponent has become even smaller at this particle size, continuing the trend of previous particle size variations. In contrast, both the velocity and temperature gradient do not follow the previous trends.

5.5 Conclusion and outlook

A new parametrization of the freeze-casting process with the phase-field grand potential approach was presented. Within this, the complex capillary and kinetic anisotropy of the ice-water interface was qualitatively approximated with sums of spherical harmonics. The as-of-yet experimentally undetermined thermodynamics of an aqueous colloidal suspension were approximated by relying on a previously calculated phase boundary by Peppin et al. [76, 78]. Based on these approximations, simulations in the dendritic morphology regime were conducted for suspensions with particles of radius 250 nm, 375 nm and 500 nm. The wavelength, the suspension channel diameter and the ice trunk diameter were measured in the steady-state regime and connected to the input processing parameters of velocity, temperature gradient and solids loading of the suspension. Qualitatively, observations showed that higher velocities and temperature gradients refined the microstructure for all three considered microstructural lengths. Increasing the solids loading yielded larger suspension channels and narrower ice trunks with the dendritic features becoming less prominent.

A simple power law model was fitted to the simulated data in order to determine scaling relationships between the processing parameters and the microstructural lengths.

The wavelength was shown to depend mostly on the pulling velocity and the temperature gradient, with an increase of either leading to a smaller wavelength. This suggests that temperature gradients should be controlled in experiments in order to make them more comparable. In contrast to e.g. [159], an increase in particle size in the results shows a small reduction of the velocity exponent. Since in this study only the energetic and not the kinetic effects of changing the particle size was considered, the experimental behavior is likely to be largely attributable to kinetic effects such as the concentration and particle size dependent diffusivity. There was little influence of the solids loading on the wavelength for the smallest particle size. For the two bigger particle sizes, increasing the solids loading slightly increased the wavelength.

The suspension channel diameter, which roughly corresponds to the width of the solid walls within the final freeze-cast structure, showed a bigger dependence on the employed pulling velocity with the exponent also being closer to the experimentally observed range. This dependence slightly grew with increasing particle size similar to [159]. While an increase of the temperature gradient also led to smaller suspension channel diameters, the magnitude of the influence seems to strongly depend on the particle size. At the largest investigated particle size, the influence of the temperature gradient was minor compared to both the pulling velocity and solids loading. An increase in the solids loading showed larger suspension channel diameters with its exponent getting larger and closer to 1 with increasing particle size. It was shown that the mass fraction of the suspension phase below the dendrite tips is a linear function of the solids loading with positive slope, as is commonly found in experiments.

Finally, the ice trunk diameter, which roughly corresponds to the pore width within the final freeze-cast structure, showed a smaller dependence on the employed pulling velocity. The magnitude of the pulling velocity dependence changed with the particle size but without an obvious trend. Similar results are found for the temperature gradient. An increase in solids loading showed smaller ice trunk diameters with its dependence becoming smaller for larger particles.

In total the results suggest that coarse-graining the individual particles into a concentration field is a viable approach for simulating freeze-casting. A future study investigating the effect of the particles on the kinetic variables such as diffusivity should be conducted in order to test whether this would reproduce the experimentally observed dependence of the velocity scaling law on the particle size.

6 Effect of advection within phase-field models of sintering

This chapter is based on the author's paper [113] (© Elsevier. Reproduced with permission. All rights reserved). The following sections are taken verbatim from the paper, with minor linguistic and stylistic changes to account for the move from a paper to a chapter in the present dissertation as well as some clarifications due to the referees. Numerical details and relevant literature are also given in the paper. The conclusion was slightly rewritten to account for the already presented information and removing the outlook, as the following chapters will consider aspects of the outlook.

This chapter uses the model described in section 3.1.3, with and without advective terms, in order to determine the influence of advection within phase-field models of sintering. The model with advection will also be referred to as the RBM model, as it includes rigid-body motion.

First, the parameters as employed by [33] will be introduced. Next, the geometry employed for this work will be described alongside some pertinent prior theoretical work. Following this, the simulations are described, their results reported upon and discussed. The short messages of this chapter are:

- adding advection significantly helps with the convergence of shrinkage
- a relaxation ansatz towards a time-independent constant for the calculation of advection velocities is inconsistent with free energy minimization

6.1 General parametrization

The model parameters are the same as in [33], with $\{A = 16, B = 1, \beta_\eta = 1, \beta_\rho = 10\}$ corresponds to values of the surface energy $\gamma_s = \frac{23\sqrt{3}}{18}$, the grain boundary energy $\gamma_{gb} = \frac{2\sqrt{3}}{3}$ and the interface width $W = \frac{2\sqrt{3}}{3}$. The equilibrium dihedral angle given by $\psi = 2\arccos(\frac{\gamma_{gb}}{2\gamma_s})$ is about 150°. The diffusion coefficients are assumed to be $D_{surf} =$

$4, D_{gb} = 0.4, D_{vol} = 0.01$ and $D_{vap} = 0.001$ and the mobility $L = 10$. The parameters influencing the rigid-body motion which will not be varied are $m_t = 500$ and $\kappa = 100$. A spatial discretization of $\Delta x = 0.33$ is chosen, with a stable time step of size $\Delta t = 2.9648025 \cdot 10^{-5}$. As in [33] the parameters do not correspond to a specific material system or thermodynamic conditions. The results are thus generic for material systems exhibiting similar surface energy and diffusion ratios as the ones employed here.

6.2 Benchmark geometry and analysis methods

A finite, linear chain of equally-sized grains is generally considered in this section. For circular grains fig. 6.1 shows a geometric sketch along with the relevant parameters of the number of grains n and the radius r. During sintering vacancies are annihilated at the grain boundary, which yields both neck growth and densification. Assuming that each grain boundary acts independently and absorbs the same amount of vacancies, one would expect that the densification rate at a certain time is independent of the number of grain boundaries in the chain. Based on this reasoning, the densification is taken to be the main parameter of interest in this study, as it should stay invariant with the number of particles n, i.e. the densification-time curves should form a single master curve regardless of n. As a measure of densification the strain $\epsilon(t)$ is used, computed by comparing the distance of barycenters of the leftmost (x_1) and rightmost (x_n) particle (cf. fig. 6.1)

$$L(t) = x_n(t) - x_1(t) \tag{6.1}$$

$$\epsilon(t) = \frac{L(t) - L(0)}{L(0)} \tag{6.2}$$

$$= \frac{\Delta L}{L(0)} \tag{6.3}$$

with the x-coordinate being the linear direction of the particle chain. The strain is positive if the chain lengthens and negative if the chain shrinks. For the simulations with RBM, the individual displacements $u_i = v_i \Delta t$ only due to RBM were also tracked and integrated over time. The length change calculated purely by these advection steps did not differ much from the length change calculated based on the barycenter movement. Their time evolution was highly similar, with the barycenter distance method showing a slightly larger length change due to including the effects of diffusive transport.

The case of an infinite linear chain has previously been investigated via geometric models by several authors [87, 162, 163]. If one simply applies periodic boundary conditions to a two-particle geometry with the grains being cut by the periodic boundary, then

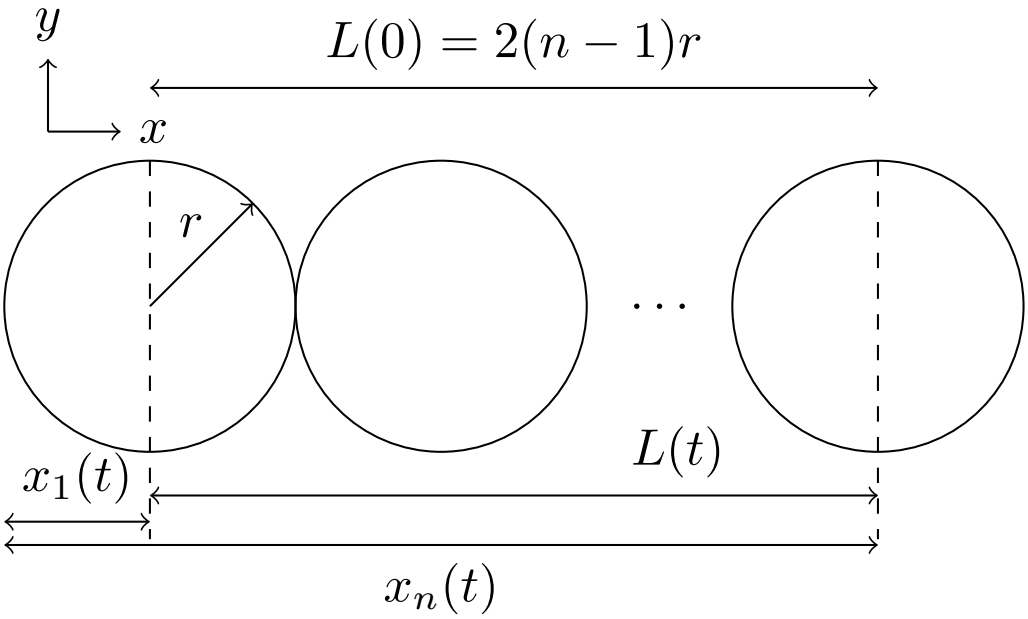

Figure 6.1: Finite, linear chain of n particles of radius r. The coordinate x_i describes the barycenter of the ith particle along the chain axis. The length of the chain is represented by the center-to-center distance of the first and last particle.

the net velocity as calculated by the model of section 3.1.3 will always vanish. Thus a direct comparison with these is not possible. However, a common point in these analyses is whether the geometry can be considered densifying or not, which leads to different equilibrium shapes. Specifically, Kellet and Lange[87] showed for an infinite chain of cylinders that their equilibrium shape could be described with three variables, viz. the equilibrium dihedral angle ψ, the grain boundary length h and the radius r of the truncated sphere connecting two grain boundaries. They distinguished two cases, one in which the particle centers are fixed (non-densifying) and one in which they are allowed to move (densifying). In the densifying case, the non-dimensional equilibrium radius $R = r/r_i$ is given by $R^d_{eq} = (\frac{\pi}{\pi-\psi+\sin(\psi)})^{1/2}$ whereas in the non-densifying case it is given by $R^{nd}_{eq} = \frac{1}{\cos(\psi/2)}$, with the initial radius r_i. In both cases, the non-dimensional grain boundary length $H = h/r_i$, or twice the neck radius X, is given by $H = \frac{\frac{\pi}{R}+R(\psi-\pi+\sin(\psi))}{(2\cos(\psi/2))}$. Based on the resulting geometry, the shrinkage strain in equilibrium can be computed via $\epsilon = 1 - R\cos(\psi/2)$, which yields 0.5466 for $\psi = 150°$.

Plotting the grain boundary length over the dihedral angle yields fig. 6.2, in which it is easy to see that densifying geometries generally yield longer grain boundaries than

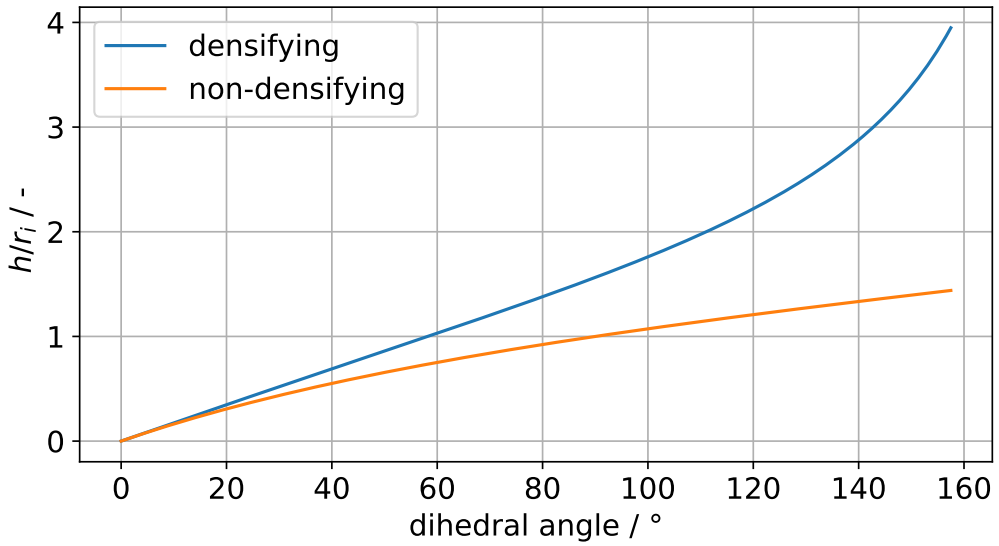

Figure 6.2: Equilibrium grain boundary length h normalized by the initial grain radius r_i over the equilibrium dihedral angle ψ. For increasing dihedral angle the grain boundary gets longer, with the densifying geometry generally exhibiting longer grain boundaries than the non-densifying geometry.

non-densifying ones. Specifically for a dihedral angle of 150° the non-densifying grain boundary length should be about $1.39r_i$ and the densifying one $3.38r_i$. It seems reasonable that this result transfers to finite chains, with some error induced by the end particles taking on a different shape. Thus if a system is densifying, one would expect much longer grain boundaries than in a non-densifying system, which allows the classification of phase-field models according to whether they describe a densifying geometry or not. In order to calculate the grain boundary length h the grain boundary area A is divided by the interface width W. The neck length then follows as $X = h/2$. The grain boundary area between the grains described by order parameters η_α and η_β can be computed based on the phase field by $A = \int 4\eta_\alpha\eta_\beta dV$.

6.3 Chain length and densification

The initial radius for the circular particles is chosen to be $r = 40$ cells, with at least 20 cells left empty between the particles and the grain boundary. Chain lengths of 2, 4, 6 and 8 particles are considered, with and without RBM. For this study, the RBM parameter set $\{\rho_{gb}, \kappa\}$ is kept fixed at $\{\rho_{gb} = 0.9816, \kappa = 100\}$ as in the original paper by

Wang. On the boundary gradient-zero conditions for all phase-fields η_α and the density ρ are employed.

In order to avoid pairing of particles due to the natural boundary effect of the first and last particle, the first 10^4 time steps of $4 \cdot 10^5$ are calculated without RBM. After the first $4 \cdot 10^5$ steps, corresponding to a simulation time of 11.8592, the simulations were analyzed and continued for another $32 \cdot 10^5$ steps in order to start investigating the long-time behavior.

The time evolution of a 4 particle chain which is continued with RBM is shown in fig. 6.3. Both neck growth and shrinkage are observed, with an apparent unshrinkage being observed from (c) to (d) in the long-term simulation.

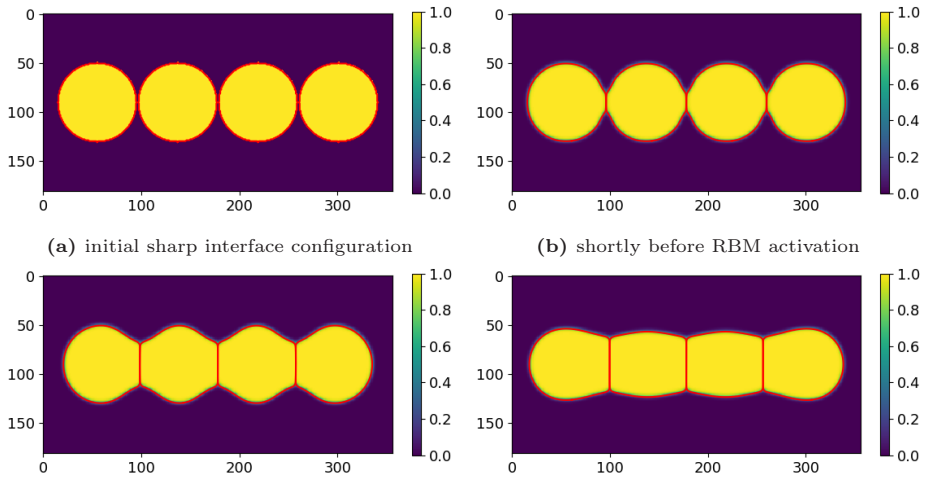

(a) initial sharp interface configuration

(b) shortly before RBM activation

(c) state at normal end of simulation, $t = 4 \cdot 10^5 \Delta t$

(d) state at long end of simulation, $t = 3.6 \cdot 10^6 \Delta t$

Figure 6.3: Time evolution of the sum of grain phases $\sum \eta_\alpha$ in a 4 particle chain with rigid body motion activated after $t = 10^4 \Delta t$. The $\eta_\alpha = 0.5$ contour lines of individual grains are drawn as red lines. From the start (a) to the activation of RBM (b) no significant densification is observed, but a neck is formed. At the regular end of the simulation (c), a significant densification is observed relative to the initial configuration (a). If this simulation is continued then material apparently flows towards the boundary (d) instead of the center of the chain.

The length change ΔL of the sample and the absolute value of the strain $|\epsilon(t)|$ are plotted in fig. 6.4. For the purely diffusive simulations the length change ΔL at any particular time is almost independent of chain length and thus a variable strain is observed. Incorporating RBM yields increased length changes with increasing chain size, leading to

almost the same strain being observed at any particular time for more than two particles. This suggests that the strain rate, or equivalently densification rate, does almost not depend on system size if RBM is included. Note that even with the inclusion of RBM there is a slight decrease of strain with chain length.

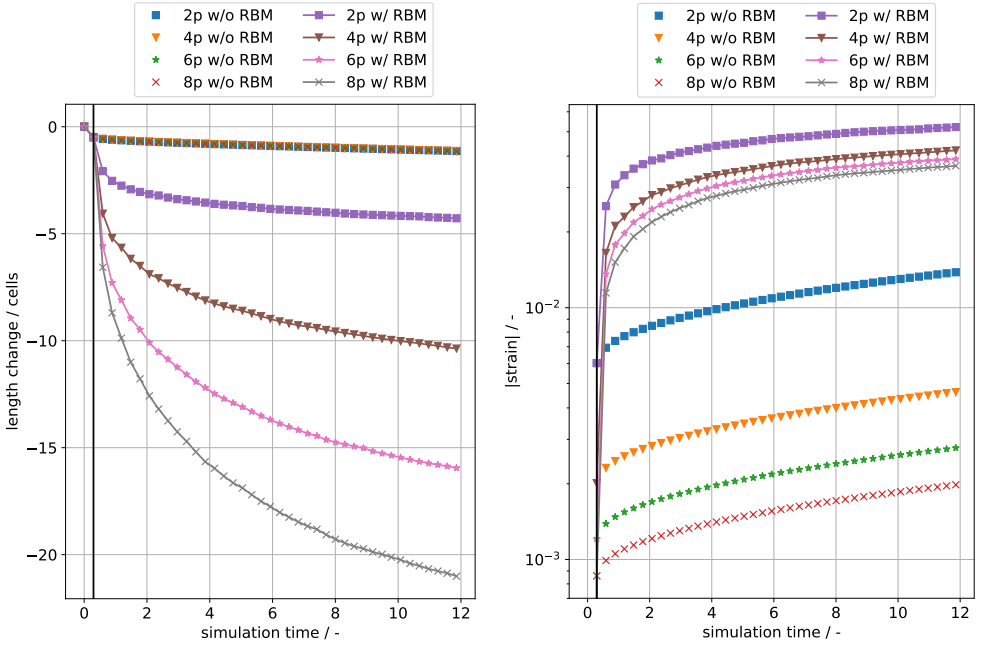

(a) length change **(b)** strain

Figure 6.4: Length change and absolute value of the strain for particles chains of various lengths with and without RBM. Lines with markers indicate simulations with RBM, whereas only markers indicate simulations without RBM. The label describes how many particles were in the chain as well as whether RBM was active. The black vertical line indicates the time at which RBM was activated. The strain is plotted on a semilogarithmic scale for better visibility of the differences without RBM. Simulations without RBM show a length change independent of chain length, whereas simulations with RBM have an almost linear increase in length change with increasing chain length. Thus the strain is variable for simulations without RBM and almost constant for those with RBM.

These results suggest that RBM is indeed a necessary ingredient for a physically sensible phase-field model of sintering, as the kinetic pathway taken should obviously not depend on the system size. However, the manner in which the rigid body velocity of each particle is calculated is also of great import. This is revealed by looking at the long-term simulations, in which eventually a kind of unshrinkage occurs, shown in fig. 6.5, which is accompanied by an increase in free energy. This is due to the phase-specific

velocities v_{η_α} no longer being oriented towards the total center of mass, but rather away from it. Once the velocity points outwards it will transport mass towards the boundary and unshrinkage can occur. The instantaneous velocity of the leftmost particle for the 4 simulations with RBM is shown in fig. 6.6, with a positive velocity pointing towards the total center of mass and a negative one away from it. The view is restricted to the dimensionless velocity range of $[-0.1, 0.1]$ in order to emphasize the occurrence of long periods with negative velocities; these are the cause behind the observed unshrinkage. The jumps of the instantaneous velocity are caused by the filtering function g, since new cells with large force densities are added to the resultant force in an abrupt manner. Note that this particle velocity is used for the spatial interpolation (eq. (3.76)) and hence does not need to be continuous.

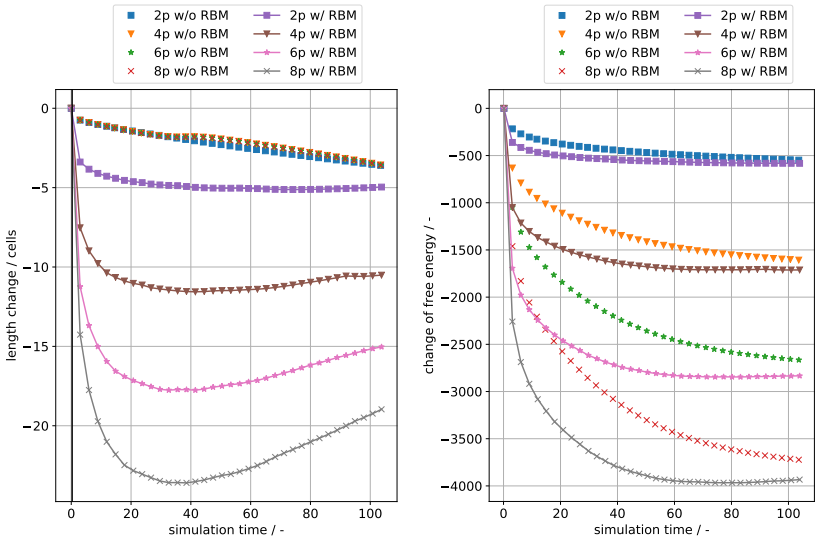

(a) length change **(b)** change of free energy after $t = 2000\Delta t$

Figure 6.5: Long time behavior of simulations with and without RBM. Simulations with RBM eventually show unphysical unshrinkage. This also causes the free energy to increase which is inconsistent with the minimization of free energy.

Before proceeding to investigate the reason for the sign change in the velocity, the influence of particle size is considered shortly. Two additional particle sizes, 50 and 60 cells, were simulated for chains of length 2, 4, 6 and 8 thus yielding another 8 simulations. Their length changes and strains are depicted in fig. 6.7. The length change is barely affected by the change in particle size, which in turn causes the densification to decrease

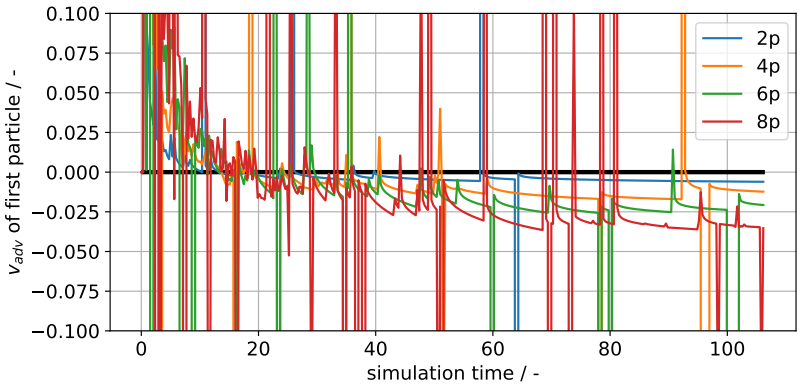

Figure 6.6: The rigid-body velocity of the leftmost particle over time. A positive velocity point towards the total center of mass and thus causes densification. While it is initially positive and thus densifying, the velocity becomes negative for extended periods of time during later stages, thus causing the observed unshrinkage. Since the velocity is calculated instantaneously based on the resulting force it has discontinuous jumps due to the filtering function g.

as the particle size is increased. The larger particles tend to experience less unshrinkage in total.

In order to determine whether particle size influences when unshrinkage starts, the relative neck radius X/r_i, i.e. the neck radius divided by the initial particle radius, is evaluated at the onset of unshrinkage. The onset of unshrinkage is assumed to be the global minimum of the length change curve. Figure 6.8 shows the dependence on the particle size as well as the number of particles in the chain. The relative neck radius at the start of unshrinkage tends to decrease as the particle size is increased. Furthermore, more particles in the chain seem to also incentivize unshrinkage, but not in a strictly monotonic way as the particle size.

In the following section the reason for the sign change in the velocity will be determined with theoretical considerations as well as sensitivity studies on the RBM parameters.

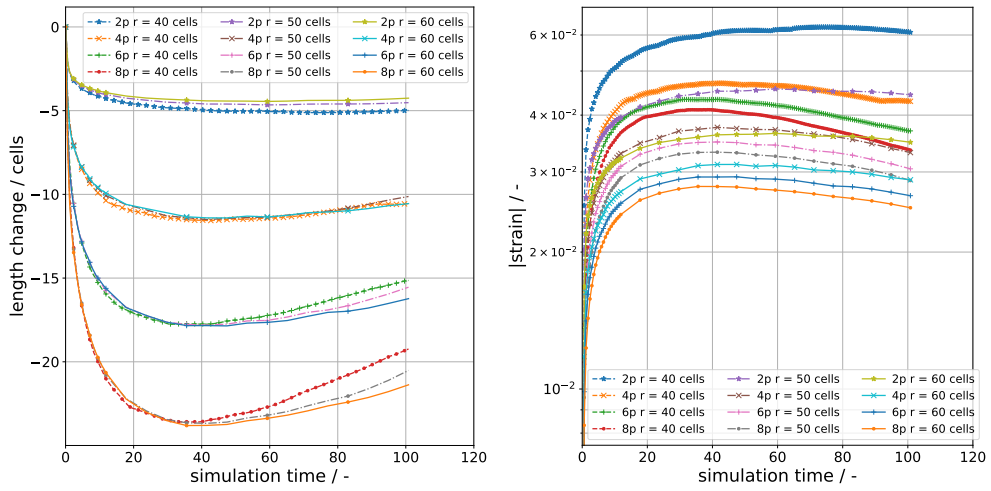

(a) length change **(b)** strain

Figure 6.7: Length change and absolute value of the strain for particles chains of various lengths and particle sizes with RBM. The length change is barely affected by the particle size, but this induces a large variation in observed strain.

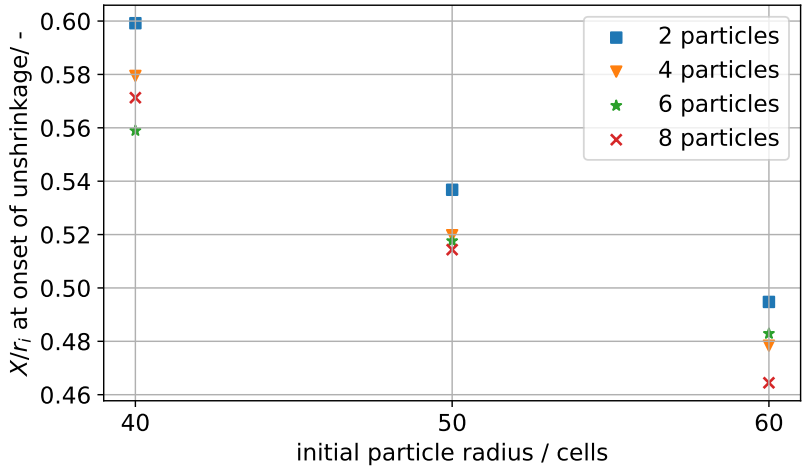

Figure 6.8: The geometrical state, described by the relative neck radius X/r_i, at the onset of unshrinkage for the conducted simulations. Unshrinkage is observed at relatively smaller necks as particle size is increased, or when the number of particles in the chain is increased. However, the latter influence is not observed to be monotonic.

6.4 Shrinkage in equilibrium

The analysis is started by considering the simplest possible case, i.e. a one-dimensional system with two grains occupying the intervals $(-\infty, 0]$ and $[0, \infty)$. The equilibrium phase-fields (vanishing $\frac{\delta F}{\delta \eta_\alpha}$) are given by

$$\eta_1(x) = 0.5(1 + \tanh(\frac{x}{W})) \tag{6.4}$$

$$\eta_2(x) = 1 - \eta_1(x) \tag{6.5}$$

with a uniquely determined interface width W and the grain boundary at position $x = 0$. The grains are characterized by a constant density of $\rho = 1$ and evaluating the chemical potential $\mu = \frac{\delta F}{\delta \rho}$ yields zero everywhere. These results only consider the energy functional itself, without any influence from RBM. If RBM is now introduced, there will be a net force and hence net velocity acting on the grains. This is due to $\rho = 1$ being found on the grain boundary, whereas the net force would only vanish for $\rho = \rho_{gb}$. For the left grain η_2, the force density is described by $dF_2 = \kappa(\rho - \rho_{gb})g(\eta_2, \eta_1)(\nabla\eta_2 - \nabla\eta_1)$. Since ρ is 1 everywhere in equilibrium the density difference $\rho - \rho_{gb}$ is of positive sign. Thus the direction of the force is initially given by $(\nabla\eta_2 - \nabla\eta_1)$ which points towards the bulk of η_2, i.e. in the negative x direction and away from the grain boundary. By Newton's third law, the same but opposite force acts on the grain η_1 and hence both grains *repel* each other. This leads to the negative velocities observed in fig. 6.6 which finally lead to the observed unshrinkage. This conclusion can also be reached by considering that the force density will only vanish once $\rho = \rho_{gb}$ is achieved within the grain boundary, which necessitates transporting mass away from the grain boundary. The implication of both arguments is also that generally the thermodynamic equilibrium state based on the functional is not the same as the equilibrium state in which the RBM term vanishes. Hence nontrivial equilibrium states of this kind of model are generally dynamic with a spatially variable density and chemical potential field. Only for the case $\rho_{gb} = 1$ the equilibrium state in 1D for both models overlap and hence a static equilibrium can be reached.

This obviously raises the question of why there is enhanced densification with RBM in the simulations above, when the simplest case already shows unshrinkage. The values of the density ρ on the grain boundary are of key importance and hence the value range is explored in the following: The two driving forces for a change in ρ are the RBM flux, in equilibrium for a density of ρ_{gb}, as well as the diffusion flux, equilibriated at $\rho_{eq} = 1 + f(\kappa)$ due to the Gibbs-Thomson effect slightly changing the equilibrium density. Hence the density should lie within the interval $[\rho_{gb}, \rho_{eq}]$ as long as the considered point is within

the grain boundary. The grain boundary itself is attached to two triple points in the benchmark geometry and the density has to drop to 0 once the triple point is left behind and the pure vacuum is entered. Thus regions within the triple point can have density values of $\rho < \rho_{gb}$. The triple point regions need to be considered since the filtering function

$$g(\alpha, \beta) = \begin{cases} 1, & \eta_\alpha \eta_\beta \geq c \\ 0, & else \end{cases} \tag{6.6}$$

can include them, and in fact does for the literature value of $c = 0.14$. Hence the interval is expanded to $[\rho_c, \rho_{eq}]$, with ρ_c being the density at which $\eta_\alpha \eta_\beta = c$ holds. An example of such a profile is plotted in fig. 6.9 for the two-particle simulation with RBM at $t = 11.562$, which still showed shrinkage. Only the region between the intersection of the orange curve and the solid black line contributes to the total force, since values outside of it are filtered away by $g(\alpha, \beta)$. This is visualized with the green line which corresponds to the local force density dF except for the phase-field gradient. The dashed black line indicates $\rho_{gb} = 0.9816$ and thus we can see that $\rho_c < \rho_{gb}$; this will generally hold unless one chooses c very close to 0.25 which is the maximum of $\eta_\alpha \eta_\beta$. The parts of the profile above the dashed black line will cause repulsion of the particles, whereas those below it will cause attraction. Thus if the middle region, the grain boundary, grows long enough the simulation will have net forces acting in a repelling manner. This causes unshrinkage if the absolute value of the advection flux induced by these is larger than the diffusive flux, since the latter always acts in a densifying manner. The volume of the particles enters the problem here, as the force is translated into a velocity with $\vec{v_{\eta_\alpha}} = \frac{m_t}{V_\alpha} \vec{F_\alpha}$ and thus larger particles are less likely to show unshrinkage. In total determining the state when unshrinkage starts is not analytically tractable, as it depends on both time-and-space-dependent density and phase-field profiles as well as the global state via the particle volume. If one only considers the velocity magnitude to be the determining factor for the influence of unshrinkage, one would conclude that larger particles would enter unshrinkage at later simulations stages. This is due to the velocity magnitude being directly antiproportional to the particle size. However, a larger particle size also implies reduced diffusional fluxes which always act densifying and hence would counteract unshrinkage. As shown in the earlier study on particle size, the relative neck radius at the onset of unshrinkage in fact decreases as particle size increases. This is likely due to the diffusional fluxes decreasing more than the advective fluxes when the particle size is increased.

In order to exclude the possibility of unshrinkage, the force and thus velocity need to be kept attractive. The direction of the force is affected by the choice of gradient vectors, the

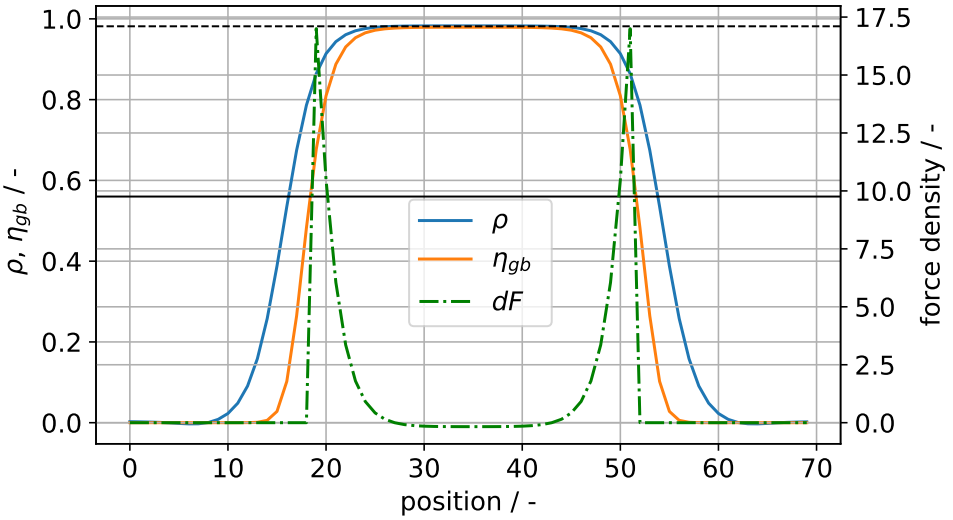

Figure 6.9: Density and grain boundary profile along the grain boundary for a two-particle simulation at $t = 11.562$. The grain boundary η_{gb} is defined as $4\eta_\alpha\eta_\beta$ in order to scale it in the range of $[0, 1]$. The horizontal dashed black line indicates the chosen $\rho_{gb} = 0.9816$ and the horizontal solid black line the threshold value $c = 0.14$ multiplied by 4, accounting for the scaling. The force density dF is non-zero only between the intersections of the solid black line and η_{gb}, as indicated by the dot-dashed line. Note that the region where $\eta_{gb} \sim 1$ exhibits only negative force densities.

regions considered to be a grain boundary via $g(\alpha, \beta)$ and the difference $\rho - \rho_{gb}$. Inverting the direction of the gradient vectors fails directly, as any initial contact between particles will force them apart and no shrinkage at all is possible. Augmenting this by choosing the grain boundary region such that $\rho > \rho_{gb}$ is guaranteed might fix this approach, but it requires a precise calibration of the filtering parameter c in eq. (6.6) such that $\rho_c \geq \rho_{gb}$ is true. A much easier calibration is available for the difference $\rho - \rho_{gb}$: Since the upper limit of ρ within the grain boundary is known to large precision via $\rho_{eq} = 1 + f(\kappa)$, the difference can be forced to be largely of negative sign which will lead to attractive forces. This reduces the problem to finding the average curvature during the simulation or estimating it prior to the simulation if it is expected not to change appreciably. More generally, as long as $\rho_{gb} \geq \rho_{eq}$ holds the grain boundary will tend to attract the adjacent grains. Note that ρ_{gb} is thus unrelated to the physical density of the grain boundary, but rather simply a parameter for ensuring attractive grain boundaries.

In order to verify this procedure without needing to find $f(\kappa)$ for the given energy functional, several two particle-simulations with different values of ρ_{gb} are carried out for up to 300 million time steps, corresponding to a simulation time of roughly 9000. This

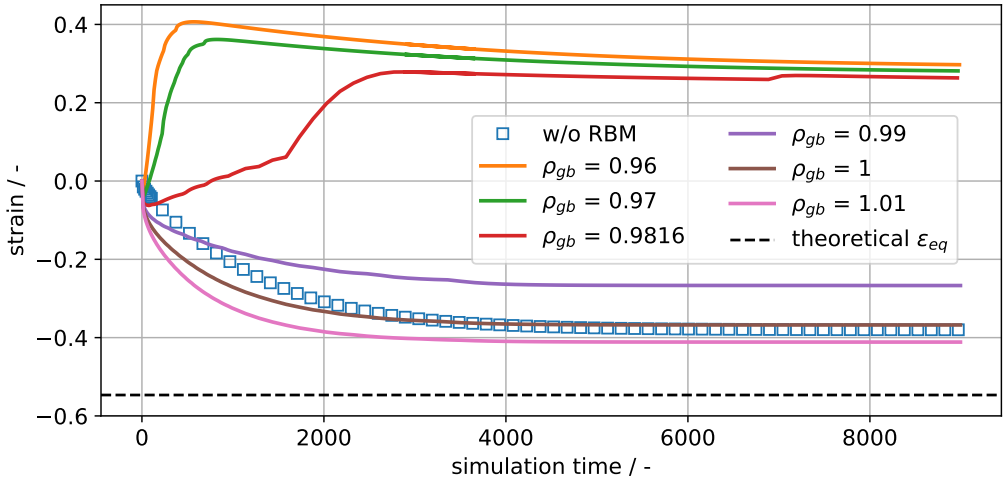

Figure 6.10: Strain of a two-particle system without RBM and with RBM for various grain boundary densities ρ_{gb}. A positive strain corresponds to a lengthening (unshrinkage) and a negative strain to a shortening (shrinkage). For $\rho_{gb} \geq 0.99$ a monotonic behavior is observed as would be expected, but for values below 0.99 unshrinkage is observed. The equilibrium strain is observed to depend on ρ_{gb}.

Table 6.1: Measured and theoretical equilibrium values for densifying simulations.

property	no RBM	$\rho_{gb} = 0.99$	$\rho_{gb} = 1.00$	$\rho_{gb} = 1.01$	theoretical
shrinkage $\lvert\epsilon\rvert$ / -	0.377	0.267	0.368	0.411	0.546
GB length h / r_i	2.38	1.92	2.33	2.55	3.38
estimated h' / r_i ($\psi = 150°$)	3.00	3.42	3.01	2.95	3.38
dihedral angle ψ / °	159	145	157	160	150
estimated h' / r_i (ψ measured)	3.42	3.23	3.38	3.44	3.38

value was sufficient to reach equilibrium for the simulations showing monotonic densification behavior. In general, the effect of the Gibbs-Thomson effect on the bulk density is small. Hence grain boundary density values $\rho_{gb} \in \{0.96, 0.97, 0.9816, 0.99, 1.00, 1.01\}$ were chosen for this test. Furthermore, one simulation without RBM was carried out to long times as well in order to compare the equilibrium grain boundary lengths and hence determine which model more closely approximates the densifying geometry from Kellet and Lange[87]. The results of this simulation study are shown in fig. 6.10. For values of $\rho_{gb} \geq 0.99$ monotonic behavior in the strain is observed, suggesting that for $\rho_{gb} \geq 0.99$ shrinkage is ensured.

In the following, the influence of ρ_{gb} on the shrinkage as well as its relation to the theoretical equilibrium shrinkage is discussed, with the results being collected in table 6.1 to give a concise overview. As can be seen in fig. 6.10 different values of ρ_{gb} lead to different equilibrium shrinkages, when it should be a universal value. This difference is due to the proportionality of the force density to $\rho - \rho_{gb}$ and hence different values of ρ_{gb} will directly change the equilibrium state. Shrinkage values, corresponding to $-\epsilon$, of $0.267, 0.368, 0.411$ are observed for RBM simulations with $\rho_{gb} = 0.99, 1.00, 1.01$ respectively, i.e. a higher ρ_{gb} leads to larger shrinkage in equilibrium. The simulation without RBM achieved a shrinkage value of 0.377, comparable to that of $\rho_{gb} = 1.00$. However, none of these values come close to expected infinite chain shrinkage at 0.546, very likely due to the finite length of the chain. The same behavior and discrepancy is observed for the grain boundary length, which is plotted in fig. 6.11. Since shrinkage and grain boundary length are coupled via mass conservation, one may assume that these differences are correlated. Hence an equivalent equilibrium grain boundary length h', if the infinite chain could be simulated, can be estimated via $h' = h\frac{\epsilon_{infinite}}{\epsilon_{finite}}$. For the simulations with $\rho_{gb} = \{0.99, 1.00, 1.01\}$ the grain boundary lengths $\{3.42, 3.01, 2.95\}r_i$ are calculated and for the simulation without RBM a length of $3.00r_i$ is calculated. Thus the simulation which comes closest to the theoretical value of $3.38r_i$ is that for $\rho_{gb} = 0.99$. While it would be an interesting validation to derive an expression for the equilibrium grain boundary length and shrinkage for finite chains and compare them with the present results, it is out of the scope of the present work. However, additional information can be gained from evaluating the dihedral angle in the simulations, as it enters the theoretical problem as a key value. The results over time are shown in fig. 6.12. There is a deviation from the theoretical value even in equilibrium, but of similar magnitude as others' results[104] for a dihedral angle of 150°. It can be observed that as ρ_{gb} is decreased, the dihedral angle is reduced. Employing the earlier estimation of h' with the observed dihedral angle yields the values $h' = \{3.23, 3.38, 3.44\}r_i$ for RBM simulations with $\rho_{gb} = \{0.99, 1.00, 1.01\}$ respectively and $h' = 3.42r_i$ for no RBM. In this case the simulation with $\rho_{gb} = 1$ matches the infinite chain result rather well. Hence some of the earlier discrepancy is likely due to a different dihedral angle obtained in the simulation compared to theory. The remaining difference in the shrinkage should thus mainly be due to the finite chain length.

In any case, all of the simulations with monotonic shrinkage behavior, including the one without RBM, show grain boundary lengths somewhat comparable to the theoretical result for the densifying geometry. Thus both models approximate the densifying geometry, with the RBM model only doing so if $\rho_{gb} \geq 0.99$ holds for the present setup.

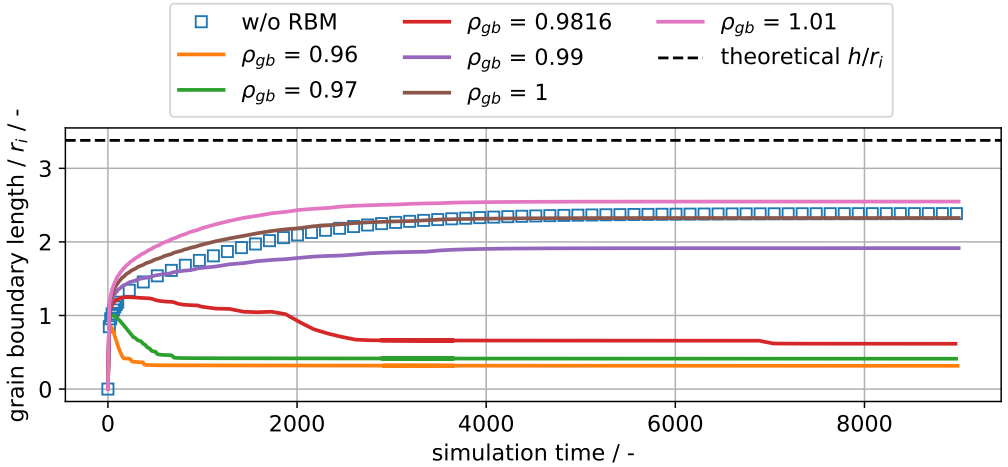

Figure 6.11: Grain boundary length h normalized by the initial grain radius r_i over time for various simulations. Like with the length change, increasing values of ρ_{gb} exhibit longer grain boundaries, as both are correlated via mass conservation. Note that the simulation without RBM reaches an equilibrium length comparable to that of $\rho_{gb} = 1$ and thus is still densifying.

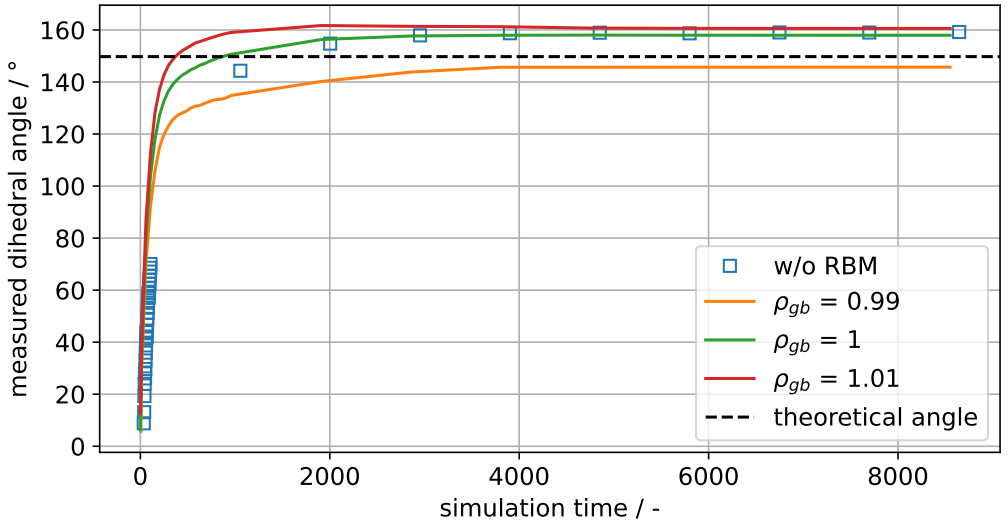

Figure 6.12: Dihedral angle of all densifying simulations as well as the theoretical value. There is a discrepancy for all simulations, with the grain boundary density influencing the dihedral angle. Note that this measurement is done on the field-resolved data and hence has less points than the previous plots which were calculated during the simulations.

6.5 Discussion

The previously shown simulation results and analytical considerations clearly show that some kind of advection term is necessary in order for phase-field models to exhibit sensible shrinkage behavior with more than two particles. The physical background of this necessity is explored in the following: Consider an atom or a vacancy located within an inner particle of the chain and its driving forces for migration. The closer the atom is to a particular neck, the more likely it is to migrate towards it, with an atom perfectly between two necks not having any preferential direction. This implies a symmetry of the mass flux towards both grain boundaries of an inner particle and thus no net movement of the particle center. For the outer particles of the chain there is no such symmetry and thus they account for most of the motion observed in diffusion-only models. In practice the motion of the outer particles causes a slight asymmetry for the inner particles, but as the simulation results have shown, this is negligible on diffusive timescales. Adding an advection term whose velocity points on average to the total center of mass will induce a preferential direction for the mass flux towards the total center of mass of the system. If the magnitude of this mass flux now depends on how many grain boundaries are crossed, then a velocity profile leading to a constant shrinkage independent of chain length can be established. Due to the density field being a conserved field, the effect of the velocity field can be seen as removing vacancies from GBs (increasing density) and generating them on the surface (decreasing density) as the particles are moving. While this effect might be mimicked by a local source term, this would not lead to a preferential direction for the mass flux and thus is unlikely to show shrinkage independent of chain length. Note that the advection term does not have to be based on a rigid-body motion model, it could also originate from solving a momentum transport equation. Hence it would be interesting to verify whether phase-field models for liquid-phase and viscous sintering [164, 165] naturally include the proper scaling with chain length. These models do not introduce additional parameters such as ρ_{gb} or include external forces, but rather can be derived thermodynamically consistently as done by [165] which ensures that the free energy is indeed minimized.

The second part of this work elucidated the reasons behind the observed unshrinkage in simulations if they are continued long enough. It was found that ρ_{gb} is a parameter of key importance, as it controls whether grain boundaries act to repulse or attract the grains they are attached to. Specifically, any value below ρ_{eq} will force the grain boundaries to repulse the grains, but this may be balanced by the attractive force of the triple points. This balancing is very likely the reason why the unshrinkage phenomenon has not been observed previously in phase-field simulations, as the state at which the

balance tips towards repulsion occurs only late into the sintering process. Based on the study on variation of ρ_{gb}, choosing $\rho_{gb} = \rho_{eq}$ is likely to yield the results closest to analytical theories of shrinkage. In general ρ_{eq} is a function of simulation state via the Gibbs-Thomson effect and hence should be estimated during the simulation run if the curvature is expected to change appreciably.

Finally, do all phase-field simulations of sintering, regardless of stage, require the inclusion of an advection term? Certainly those that start from green bodies do, as the majority of densification still needs to occur without any kind of size dependence. However, in the final stage only isolated pores remain and often these include gases which exert a pressure on the surrounding grain structure. Assuming that these pores have reached an equilibrium pressure-size state, then the generation of vacancies on their surface would disturb the equilibrium and hence be energetically unfavorable. Hence if the simulation is only concerned with pressurized, isolated pores, such as in [166, 167], then including an advection term is unnecessary.

6.6 Conclusion

In this work the necessity of including an advection term in phase-field models of sintering was shown by simulation. Specifically a shrinkage rate almost independent of system size was only observed for models with an advection term. Hence, in order to reproduce the correct kinetic scaling of sintering an advection term needs to be included. Furthermore, a sensitivity study on the grain boundary density ρ_{gb} showed that its choice is critical: If ρ_{gb} is chosen below the equilibrium grain density ρ_{eq}, then unshrinkage can occur. The most practical choice of ρ_{gb} is ρ_{eq}, as then the equilibrium states of the energy functional and the RBM model are very close and ρ_{eq} can be calculated based on the energy functional. In the study it could also be shown that regardless of whether RBM is included, simulations will approximate the equilibrium densifying geometries of analytical models[87].

7 Thermodynamically consistent phase-field simulations of sintering

This chapter is based on the author's paper [69] (CC-BY [168] IOP Publishing). The following sections are taken verbatim from the paper, with only minor linguistic and stylistic changes to account for the move from a paper to a chapter in the present dissertation, as well as some clarifications due to the referees. Numerical details and relevant literature are also given in the paper. The conclusion is slightly rewritten to account for the already presented information in section 3.2.2, but is also mostly taken verbatim.

The goal of this chapter is to present simulations of a grand potential phase-field model of sintering, cf. section 3.1.2, including advective terms, which monotonically decreases the free energy with time. The latter condition is, under suitable boundary conditions, equivalent to monotonic increase of entropy which is commonly called thermodynamic consistency via the second law of thermodynamics. In chapter 6 it was already shown that this condition is violated if a constant equilibrium grain boundary concentration c_0 is chosen. This chapter verifies that this holds for a grand potential model as well and then goes on to eliminate this problem as well as the shock problem, with the model details described in section 3.2.2.1 and section 3.2.2.2. Finally, it is observed that the small variation in shrinkage with system size observed in chapter 6 has severe effects on the densification of large three-dimensional green bodies.

The short messages of this chapter are:

- estimating c_0 via the current simulation state can result in a thermodynamically consistent evolution
- nearest-neighbour-only calculation for advection velocities are insufficient for system size independent shrinkage.

7.1 Parametrization for copper

The employed nondimensionalization scales are listed in table 7.1 and the material parameters in table 7.2. The Gibbs free energies are assumed to be given by simple parabolas

$$g_{\mathrm{V}}(c,T) = A_{\mathrm{V}}(T)(c - c_{\mathrm{V}}(T))^2 \tag{7.1}$$

$$g_s(c,T) = A_s(T)(c - c_s(T))^2 \tag{7.2}$$

respectively for the vapour phase V and solid grains s. The exact choice of energies is not particularly relevant if the initial conditions are chosen such that driving forces for phase transformation are small relative to capillary forces. This is generally achieved by setting the initial concentrations to the equilibrium concentration $c_{\mathrm{V}} = 0.02$ and $c_s = 0.98$. The prefactor $A_{\mathrm{V}} = A_s = 50$ is chosen such that the Gibbs-Thomson effect of changing the bulk concentration due to curvature is comparatively small. This also reduces the spontaneous shrinkage of grains within the phase-field context as found by[169]. Strictly speaking, A should be determined based on the observed concentration shift of a particle embedded in a matrix of material. However, this value tends to be quite high, i.e. the shift of concentration due to the Gibbs-Thomson effect via capillary forces is small. In turn, this would severely increase the numerical stiffness of the solution, which is why a pragmatic approach is taken here.

The grid spacing Δx will be repeatedly varied and thus will be mentioned for each set of simulations. The time step is calculated by estimating the stable time step in the explicit time integration scheme as well as the Courant-Friedrichs-Lewy (CFL) condition, with a safety factor of 0.3:

$$\Delta t = 0.3 \min(\Delta t_{\phi,c}, \Delta t_{CFL})$$

$$\Delta t_{\phi,c} = \frac{\Delta x^2}{2 \max(D_\phi, D_c)}$$

$$\Delta t_{CFL} = \Big[\sum_i \frac{\max(|v_i|)}{\Delta x_i}\Big]^{-1}$$

with the effective phase-field diffusivity $D_\phi = 2\frac{\max(\gamma)}{\min(\tau)}$ with the respective maximum and minimum values of γ and τ, the highest diffusivity employed for the concentration equation D_c, i going over the spatial dimensions and $\max(|v_i|)$ being the largest velocity per dimension. Typically though the phase-field step is the limiting factor for stable time integration.

The values of the interfacial energies are based on estimates for pure copper at 700 K, resulting in a dihedral angle of 151°. The grain boundary diffusion value is based on [170], with the surface diffusion value being based on [171]. The bulk diffusion within the grains and vapor will be varied, and thus be mentioned for each simulation set. When employing [171], bulk Cu diffusion would be on the order of $1 \times 10^{-20}\,\mathrm{m}^2/\mathrm{s}$ for 700 K, effectively freezing the diffusion field within the bulk relative to the interfacial diffusivities. Instead of using this tiny value, larger values will be used in order for allow a reasonable amount of relaxation within the grains; this should not significantly influence the qualitative results if faster diffusion mechanisms (grain boundary, surface) are active at the same time. The kinetic coefficient of the surfaces $\tau_{v\alpha}$ is chosen such that the phase-field always relaxes more quickly than the chemical potential, which ensures that the process is controlled by diffusion. Grain growth, if thermodynamically possible, is largely suppressed by taking the kinetic coefficient between grains to be $100\tau_{v\alpha}$. The effective stiffness κ is chosen based on the observations in [36], such that the simulation results become independent of its choice: The advective velocity tends to increase as κ is increased until a plateau is reached. This plateau is determined in a pre-study and found to start at 800, with $\kappa = 3200$ employed in the simulations to ensure that the results are independent of κ. The resulting data and evaluation of this pre-study is available within [172].

This pre-study as well as the small scale validation in section 7.2.1 are calculated on a local machine using GNU parallel[173] for effective job management. The later large scale simulations are calculated on the Hawk supercomputer at the HLRS.

Table 7.1: nondimensionalization parameters

scale	value
length l_0	$1 \times 10^{-8}\,\mathrm{m}$
diffusivity D_0	$1 \times 10^{-12}\,\mathrm{m}^2/\mathrm{s}$
time t_0	$1 \times 10^{-4}\,\mathrm{s}$
velocity v_0	$1 \times 10^{-4}\,\mathrm{m}/\mathrm{s}$
temperature T_0	700 K
surface energy $E_{s,0}$	$1\,\mathrm{J}/\mathrm{m}^2$
energy density $E_{r,0}$	$1 \times 10^{8}\,\mathrm{J}/\mathrm{m}^3$
molar volume $V_{m,0}$	$7.1 \times 10^{-6}\,\mathrm{m}^3/\mathrm{mol}$

Table 7.2: Employed physical and numerical parameters for the simulations.

parameter	nondim. value	physical value
Numerical parameters		
interface parameter ϵ	$4\Delta x$	variable
interface width W	$10\Delta x$	variable
grain boundary cutoff $\phi_{\alpha\beta}^{min}$	0.14	-
Physical parameters		
surface energy $\gamma_{\mathrm{V}\alpha}$	2	$2\,\mathrm{J/m^2}$
grain boundary energy $\gamma_{\alpha\beta}$	1	$1\,\mathrm{J/m^2}$
grain boundary diffusion D_{gb}	55	$5.5 \times 10^{-11}\,\mathrm{m^2/s}$
surface diffusion D_s	169	$1.69 \times 10^{-10}\,\mathrm{m^2/s}$
physical interface width δ_i	0.02	$2 \times 10^{-10}\,\mathrm{m}$
surface kinetic coefficient $\tau_{v\alpha}$	0.08	$8 \times 10^{10}\,\mathrm{Js/m^4}$
grain boundary kinetic coefficient $\tau_{\alpha\beta}$	$100\ \tau_{v\alpha}$	$8 \times 10^{12}\,\mathrm{Js/m^4}$
stiffness κ	3200	-

7.2 Simulation results

In this section the model without the improvements as well as the models with improvements will be compared. The first simulation setup for this purpose is the venerable two-particle model, as it suffices to clarify whether the problems observed in [113] are fixed by the improvements or not. The second setup concerns the scaling of the advective velocity with the green body size. In [113] a small but persistent slowing of the densification speed with the green body size was observed, even with advective terms included. This is explored by employing the most promising model from the two-particle setup in a three-dimensional packing and comparing it to a purely diffusive model.

7.2.1 Equilibria and dynamics for two particles

Two particles of equal radius R are set symmetrically in a simulation box with no-flux conditions on all boundaries. The box size is taken to be $4R + 9\epsilon$ in the direction where the particles touch, ensuring that the phase-field does not initially touch the boundary. Directions perpendicular to this direction are of size $4R$, which is sufficient to ensure that the equilibrium states' phase-fields will not touch the boundary. All phases are set to their equilibrium concentrations initially.

The following models will be considered for the present investigation: A diffusion-only (DO) model, whose advective velocity is always zero. Three models including advective terms (ADV), with the following variations:

- a constant $c_{gb}^{eq} = 0.99$ slightly above the equilibrium bulk concentration (C)
- estimating c_{gb}^{eq} with the particle size (V) eq. (3.83)
- estimating c_{gb}^{eq} with the average chemical potential on the surface (μ) eq. (3.84)

The DO model serves as a reliable baseline for the equilibrium shape, which the ADV models should match if they are consistent with the energy functional. The ADV (ADV-C, ADV-V, ADV-μ) models are expected to have faster neck growth and densification, with differences in their individual dynamics and possibly equilibrium states. For simplicity of presentation, only the case of bulk diffusion will be considered, i.e. the coefficients for grain boundary and surface diffusion are set to zero. The Cu diffusion in the grain is arbitrarily set to $D_b = 1 \times 10^{-12}\,\mathrm{m}^2/\mathrm{s}$, with a value of $D_v = D_b/1000$ being used for the diffusion in the vapor. The equilibrium properties will be independent of these choices for the DO model, while for the ADV models it will depend on whether they are consistent with the energy functional. If these are not, then the choice of diffusion constants will influence the equilibrium. The dynamic evolution will of course differ if the diffusion coefficient is changed, but the scaling with time will be the same. Thus the qualitative aspects should readily transfer to cases with grain boundary or surface diffusion active as well as arbitrary non-zero choices of diffusion constants.

The first investigation is conducted at a constant particle size of $R = 25\,\mathrm{nm}$, resolved with $r = 25$ cells at $\Delta x = 0.1$. An approximation for the chemical potential in equilibrium is given by $\mu_{eq} = \Delta\mu = \gamma_s\kappa$ and assuming $\kappa = 1/R_0$ with the initial radius $R_0 = 25\Delta x = 2.5$, which yields $\Delta\mu = 0.8$. This can be translated into a bulk concentration by $c_\alpha(\mu) = c_s + \frac{\partial c_\alpha}{\partial \mu}\Delta\mu = 0.98 + \frac{0.8}{100} = 0.988$.

The simulations are continued until a state close to equilibrium is reached, with the obtained equilibrium shapes shown in fig. 7.1. While models except for ADV-C show more or less similar equilibrium shapes, the shape of ADV-C is much more oblong due to its severe violation of minimization of free energy. The free energy as well as dihedral angle will thus serve as tests on the consistency with the free energy functional. The change in free energy is shown in fig. 7.2a, relative to $t = 0.0075$ in order to exclude the initial large jump from a sharp to a diffuse interface. It is observed that the models except for ADV-C and ADV-V show a monotonic reduction in free energy. For model ADV-V the non-monotonicity is short-lived and handily overshadowed by the other symbols, but

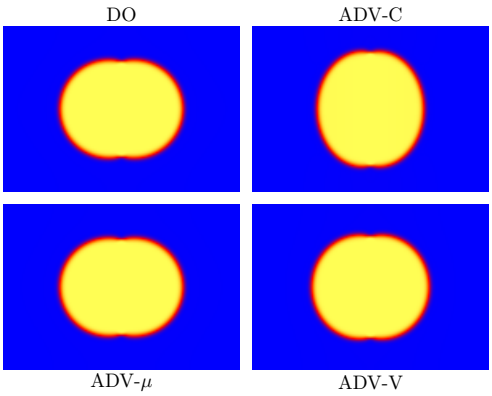

Figure 7.1: Obtained equilibrium shapes represented by the Cu concentration field, with yellow indicating the solid grains, dark indigo the surrounding vapor and reddish-orange their interface. Note that model ADV-C results in a much more oblong shape, with remaining models showing similar shapes. This oblong shape results from the lack of free energy minimization.

simple forward differences showed that it also contains a non-monotonic reduction in free energy. The observed equilibrium concentration (model DO) within the particles is about 0.9868, which compares reasonably with the above simple approximation. The remaining difference is easily explained, as multiple interfaces with different interface energies exist, which the estimate for $\Delta\mu$ doesn't take into account.

Although $c_{gb}^{eq} = 0.99$ lies above this equilibrium concentration as suggested by [113], an increase in free energy is observed. As shown in [113], the force density within the grain boundary region defined by $\phi_\alpha\phi_\beta > 0.14$ has repulsive (grain boundary) and attractive (triple point) regions. During transient growth of the neck, the advective flux tends to decrease itself by lengthening the repelling grain boundary until it matches the diffusive flux. Given that the diffusive flux acts densifying for dihedral angles below the equilibrium value, this implies that the advective flux has to increase the grain boundary length and thus dihedral angle beyond their equilibrium values in order to match the diffusive flux. Models ADV-μ and ADV-V can potentially avoid this problem by decreasing the advective flux not by a grain boundary lengthening, but by decreasing the force density within the grain boundary. The difference in free energies in equilibrium between models DO and ADV-μ are due to the spatially variable chemical potential field for ADV-μ. There is a finite, but small velocity remaining even for ADV-μ which balances out the diffusive flux within the grain boundary.

The dihedral angle θ is shown in fig. 7.2b. The DO and ADV-μ models achieve the same equilibrium dihedral angle $\theta = 150.4°$, missing the theoretical value by $0.6°$. However,

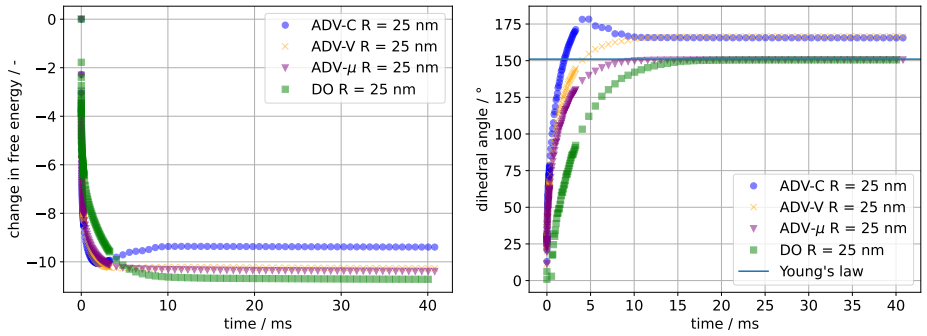

(a) change of free energy

(b) evolution of the dihedral angle

Figure 7.2: The models ADV-C and ADV-V show a non-monotonic evolution of the free energy, whereas models ADV-μ and DO show a monotonic drop in free energy. The theoretical dihedral angle is closely approximated by ADV-μ and DO as well, while models ADV-V and ADV-C significantly increase the angle.

both ADV-V and ADV-C increase the dihedral angle to about 166°. As previously observed in [113], the equilibrium dihedral angle is modified by a constant c_{gb}^{eq} and thus this was to be expected. At first glance, model ADV-V increasing the dihedral angle would seem odd, given that the simulation state is employed for estimating c_{gb}^{eq}. However, the model for predicting $\Delta\mu$ assumed constant γ for the interfaces, whereas in the simulation the surface and grain boundary energy are different. This leads to a different equilibrium, which in the present case by happenstance is close to the ADV-C equilibrium. It is likely that model ADV-V would perform much better for equal surface and grain boundary energy, but it seldom happens that these are equal. In total, the only advective model that is observed to be consistent with the free energy functional is ADV-μ.

All models will also be tested for adherence to Herring's scaling law. For this, the radius R will be varied by increasing the number of cells employed to resolve the particle r as well as by changing the grid spacing Δx. This is done as to verify that size effects have been fully included. If the physical size $R = r\Delta x l_0$, with the nondimensionalization length l_0, is the same between two simulations with differing Δx, then similar curves should be obtained, with the difference entirely attributable to the discretization error. The number of cells employed to resolve the particle r is in the set $\{25, 50, 100\}$, with two grid spacings $\Delta x \in \{0.1, 0.2\}$ being used. Thus a range of physical particle radii R from 25 nm to 200 nm are resolved, with 50 nm and 100 nm being represented by two different combinations of cells and Δx.

The time evolution of the relative neck radius X/R, scaled according to Herring's scaling law, is shown in fig. 7.3. The data is filtered such that a parabolic profile in the chemical

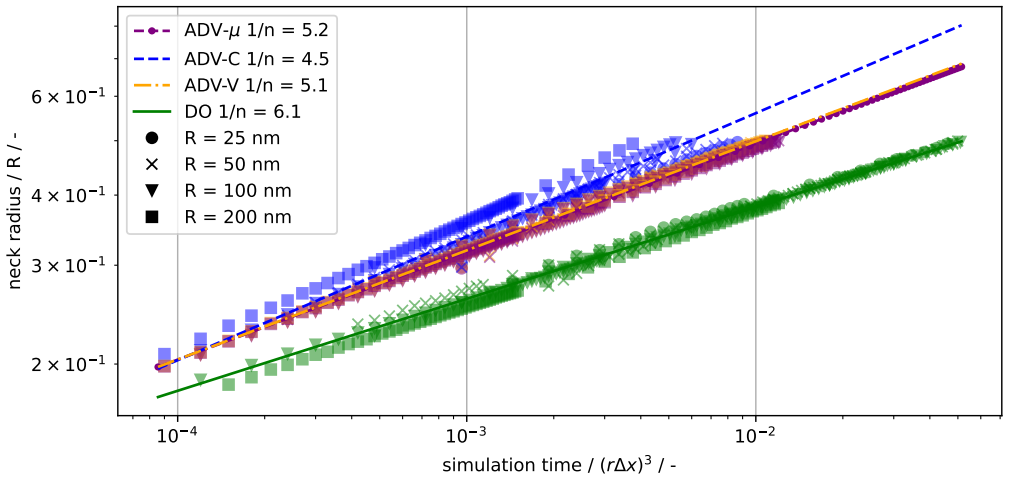

Figure 7.3: Neck size evolution up to $X/R = 0.5$, with the time scaled following Herring's scaling law. The ADV models' exponent $1/n$ clusters in the expected range of 4-5, but the DO model shows an unexpected value of 6. All models except for ADV-C scatter closely and randomly around their master curve and thus follow Herring's scaling law. Model ADV-C tends to scatter upwards as particle size is increased.

potential is present within the grain boundary and for $X/R < 0.5$. The former ensures that the simulation matches the theoretical expectation and that the interface is well-developed. The latter excludes the approach to equilibrium, which the scaling laws do not represent and thus there is no sense in including that regime. The regime is taken to be larger than the usual $X/R < 0.3$, as [162] still observed quite close matching up to $X/R = 0.5$ for a similar dihedral angle. As expected, the DO model shows the slowest evolution, whereas ADV-C shows the quickest evolution. There is little difference in the evolution between the ADV-V and ADV-μ models, though as seen earlier, different equilibria will be obtained. Models excluding ADV-C show mostly random scattering around their respective master curve, regardless of the chosen particle radius R. For model ADV-C, the line tends to move upwards as the particle size is increased. Thus a fixed choice of c_{gb}^{eq} might not follow Herring's scaling law, though the present set of simulations allows no conclusive decision. Furthermore, the slopes of curves differ from the classical two-particle model expectation of 1/5[20]. The deviation is of similar magnitude as observed by other phase-field models of sintering[33, 34]. Interestingly, the present DO model seems to replicate the observed $n \sim 1/6$ of [33] rather closely, whereas the models including advection hit much closer to the expected $n = 1/5$. It might be that the factors employed by [33] led to an evolution which was more dominated by diffusion rather than advection.

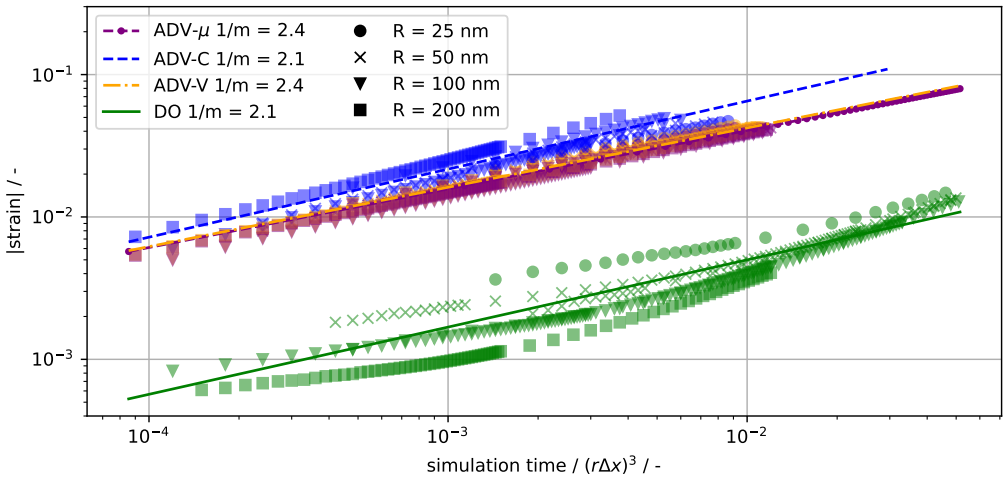

Figure 7.4: Absolute strain $|e|$ up to $X/R = 0.5$. The expectation that $1/m = 2/n$ for the strain is roughly observed, with the strain values for the DO model probably being too small to allow for a trustworthy evaluation. The upwards drift of model ADV-C with increasing particle size is observed again.

The effect of a change of Δx while keeping the physical radius R constant is that the curve is moved upwards, especially for shorter simulation times. Excepting model ADV-C, these simulations approach each other for larger times and thus the size dependence should be completely included.

The absolute strain $|e|$ is shown in fig. 7.4. The expectation that the observed exponent is half that of the neck growth law is roughly confirmed for the models with advection. A similar deviation from Herring's scaling law is observed for model ADV-C. Model DO tends to scatter strongly, likely due to its small amount of strain in the first place, so the value of the fitted exponent is likely wrong. The equilibrium strain (0.333 for models DO and ADV-μ, 0.366 for ADV-V and 0.429 for ADV-C) could be observed for the simulations from the first study. This is below the strain predicted by Kellett[87] for an infinite chain of cylinders, as also observed in [113], and is likely explainable by finite size effects.

In total, the model ADV-μ seems to produce the most sensible results and thus will be employed in the next study.

7.2.2 Large-scale three-dimensional simulations

In chapter 6 a small but persistent decrease in densification rate is observed as the number of particles in a chain is increased. Since the chain geometry is quite restricted in its movement and does not contain porosity to fill, a small number of large-scale 3D simulations will be conducted to probe this effect further. The initial conditions are generated by employing [174] as a discrete element simulation tool. A periodic box of fixed size is filled with spheres of uniform size with a random velocity distribution, followed by letting the system evolve in an NVE ensemble while accounting for the translational and rotational degrees of freedom of the three-dimensional particles. The particle interaction is described with a Hertzian contact law. The resulting packing is then sliced to various extents, with larger slices always containing the smaller slices as subdomains. The cuboid slices will be of size c^3 with $c \in \{200, 400, 800\}$nm, which with $\Delta x = 0.1$ corresponds to domain sizes of 200^3, 400^3 and 800^3 cells respectively. The simulation volume c^3 will henceforth be used directly as a simulation label. The individual particles are resolved with a radius of 12 cells ($R = 12\,\text{nm}$), ensuring that there are bulk cells for each particle while allowing a large number of particles to be contained within the simulation domain. A particle is only voxelized into the domain if its outer edge is at least 15 cells from the global boundary in order to exclude boundary effects from the phase-field. This results in 262, 3445, and 34459 particles for the 200^3, 400^3, and 800^3 domains respectively. No-flux conditions are applied on all boundaries for all fields. Each simulation is preprocessed by running the DO model for 5000 steps with equal bulk and vapor diffusivities of $D = 1 \times 10^{-12}\,\text{m}^2/\text{s}$. This is done to ensure that interfaces have already been established, as to reduce the influence of the grain boundary filtering function g on the initial evolution. After this step, all simulations are run with the parameters listed in table 7.2 for at least an initial run of 300 000 time steps, with more depending on the observed evolution. Grain growth is mostly suppressed by the choice of a small grain boundary mobility. For the longest-running simulation, the mean grain size changed from 11.84 nm to 13.95 nm, with less change for simulations running for a shorter time. Given the small change in grain size, its effect on the density evolution should be negligible compared to other effects present.

Exemplarily, the surface of the structure at simulation start and simulation end for the 400^3 domain is shown in fig. 7.5 along with 2D slices through the domain showing the grain structure. While there is significant neck growth, barely any movement inwards is observed. Furthermore, the 2D slices reveal that the inner part of the green body densifies much less quickly than the outer parts. It should be noted that the entire green

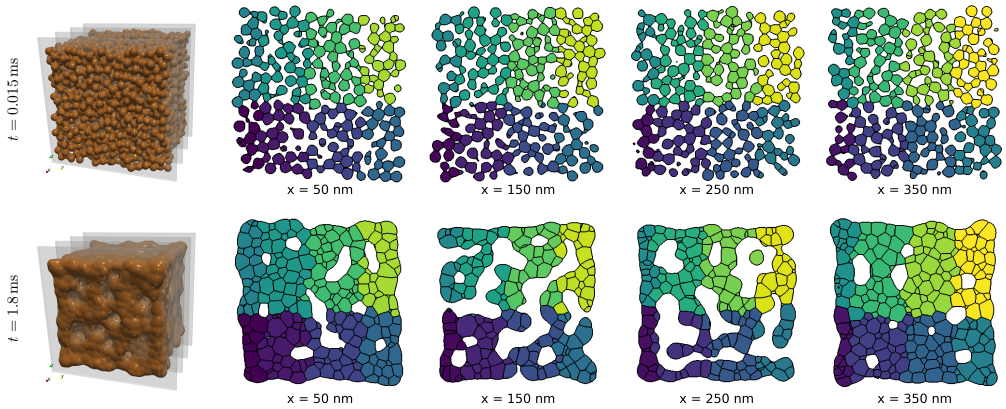

Figure 7.5: The 3D green body as well as 2D slices of the 400^3 domain calculated with model ADV-μ close to simulation start and at simulation end are shown. The slice positions are indicated with the transparent planes. Within the 2D slices, the surrounding vapor is depicted as white, any interfaces as black and the grain number with a colormap without physical meaning. While initially the structure is homogeneous, as time progresses the outer edges become denser than the inner part of the green body.

body stays connected during the process; videos of complete scans through the green body are deposited with [172].

The density evolution observed for this study is shown in fig. 7.6. It can easily be seen that the DO model has a strong dependence of its densification on the green body size. Furthermore, while the ADV-μ model does densify more quickly, it also has a strong dependence on the green body size.

Thus the hypothesis stated in chapter 6 is confirmed, in that the model for calculating advection velocities is lacking a part which eliminates this dependence. The most relevant quantity to observe here is the spatial distribution of velocities. Densification in principle means the reduction of occupied volume. In the language of continuum mechanics, this is nothing more than demanding that the dilatation $\delta = \frac{\Delta V}{V_0} = tr(e)$ is negative, with the trace of the strain tensor e. Differentiating this by time yields the same property for the strain rate tensor and its trace $tr(\dot{e}) = \nabla \cdot v$ which ought to be negative for densification to take place. Thus for any control volume to densify, its $\nabla \cdot v$ needs to be negative. Note that this should hold for macroscopic control volumes containing multiple particles. It does not need to hold on a local basis, as e.g. $\nabla \cdot v$ is zero everywhere within the bulk of the particles due to the rigid body assumption.

Thus in order for a body to densify uniformly, its strain rate needs to be homogeneous, suggesting that its velocity is a linear function of position. Of course, if a green body

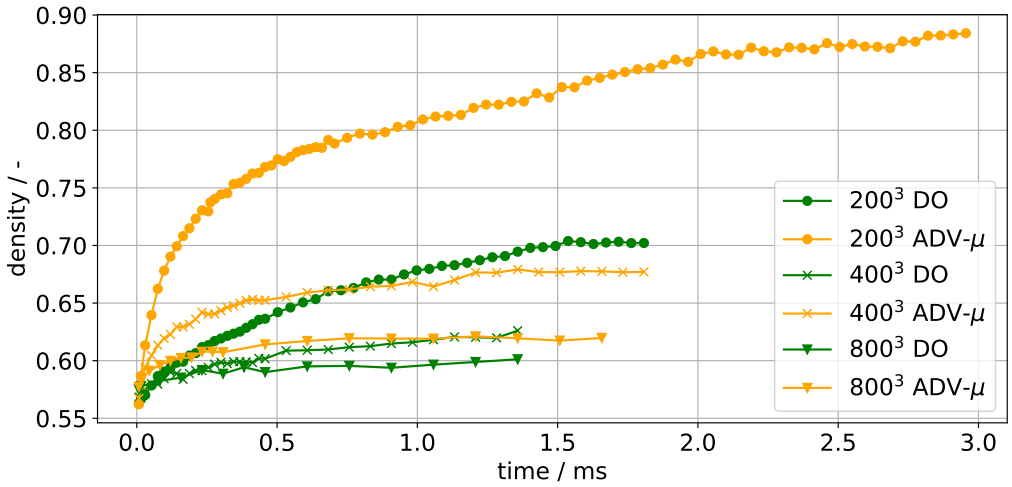

Figure 7.6: Density of the green bodies over time, for models DO and ADV-μ and various packing sizes. While model ADV-μ does densify more quickly than model DO, its densification rate is also strongly dependent on the system size.

were nonhomogeneous in its vacancy absorption rate, this need no longer hold. In the present case however all properties are isotropic and homogeneous to the extent that the structure is homogeneous; thus there is little reason for a deviation from linearity. The velocity components are depicted over their particle's spatial coordinates in fig. 7.7 within the 800^3 domain, for every 10th particle. Given the above discussion of the relationship between densification and velocity distribution, it is obvious that the present model will preferentially densify the outer edges, with the inner part showing almost no densification. This is indeed observed as shown in fig. 7.5. Due to this non-uniform densification, no RVE can be found for this model, as the controlling parameter for the density evolution is now the ratio of inner particles to outer particles, which will not converge for finite domain sizes.

It should be noted that this conclusion is independent of how c_{gb}^{eq} is determined, as the particle velocity will still only depend on local interactions. A similar thought experiment as was conducted in chapter 6, for why a diffusion-only model fails to scale correctly with the number of particles in a chain, shows this easily: Consider a control volume of sufficient size to be considered homogeneous on the inside of the packing: Since only local interactions are taken into account and it is homogeneous, neighboring control volumes will have a similar magnitude and sign of the velocity. Thus for neighboring control volumes there is little to no velocity gradient, which implies *little to no densification* as per the above discussion. Now consider a control volume on the edge of a packing: Since

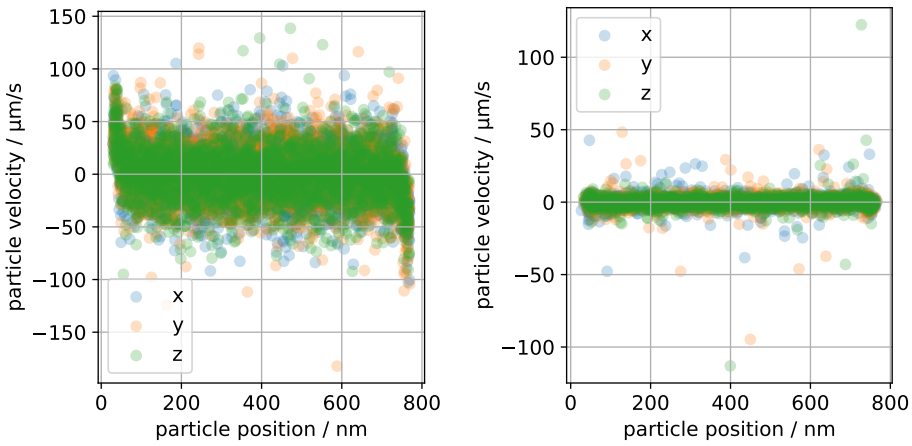

(a) t = 0.045 ms

(b) t = 1.4 ms

Figure 7.7: Particle velocities over their respective barycenters for the 800^3 domain and model ADV-μ for two times. The outer particles have significantly larger velocities, whereas any correlation between position and velocity is lost within the green body proper. This decorrelation becomes more pronounced as the simulation progresses, with local interactions causing high individual particle velocities.

the particles there have missing neighbours, they will have a significant nonzero velocity gradient to any control volume only containing inner particles and thus can densify w.r.t the inner control volumes. What this implies is that the outer particles are *implicitly* treated differently from the inner particles, which is the origin of the nonhomogeneous densification. The only feature of the model necessary to arrive at this conclusion is that only local interactions enter the velocity calculation for a fixed time, and thus the precise value of c_{gb}^{eq} is irrelevant.

7.3 Conclusions

Based on the model extensions described in section 3.2.2, except for the convergence of shrinkage, phase-field simulations of sintering with multiple new models were conducted. The new models are compared by testing the free energy evolution, the equilibrium state, as well as their dynamic evolution. It is observed that among the advective models, only ADV-μ, which estimates the grain boundary equilibrium density by averaging the surface chemical potential, is consistent with the free energy functional. All advective models roughly reproduce the expected scaling laws of the neck size with time, both in

terms of the time and particle size dependence. Furthermore, the approach of centers as quantified by the strain is observed to also reproduce the expected scalings. Based on these results, the most promising model ADV-μ is employed in order to simulate large scale 3D structures in order to seek representative volume elements. However, it is observed that even this model shows a strong dependence of the densification on the green body size and thus no RVEs could be identified. The spatial distribution of the velocity is identified as the likely origin of this dependence, as densification would imply a negative dilatation rate ($\nabla \cdot v$), but the model exhibits a dilatation rate of approximately zero in the green body proper.

8 Unravelling densification during sintering by multiscale modelling of grain motion

This chapter is based on the author's paper [115] (CC-BY [168] Springer). The following sections are taken verbatim from the paper, with only minor linguistic and stylistic changes to account for the move from a paper to a chapter in the present dissertation, as well as some clarifications due to the referees. Numerical details and relevant literature are also given in the paper. The outlook part of the conclusion has been removed, as it is addressed in the next chapter.

The goal of this chapter is to establish a model for the calculation of advection velocities for mesoscopic models of sintering with the help of molecular dynamics (MD). Hence the first part will employ MD in a specially crafted geometry which allows the isolation of absorption processes on GBs and how these affect the motion of the grains. The data is then analyzed to build a model describing the grain motion in reaction to vacancy absorption. The model is then translated into a phase-field context and embedded into the previously described model of chapter 7. Following a short validation that the appropriate model properties are still present, three-dimensional green bodies of increasing size are computationally sintered to determine representative volume elements (RVEs). Furthermore, the resulting data is compared against eq. (2.58) to establish a first qualitative link to experiments. The short messages of this chapter are:

- motion due to vacancy absorption on grain boundaries is superimposable
- due to the above, sintering models with RBM but without global coupling of motion do not have RVEs
- once global coupling is established, a few hundred particles are sufficient to reach RVEs for densification in homogeneous packings

8.1 Molecular dynamics

Molecular dynamics (MD) is a method in which the dynamics of individual atoms under the influence of an interaction potential can be simulated. The individual atoms are assumed to follow Newton's laws of motion, with the interaction potential determining what kind of material is being simulated. Sintering has previously been investigated with MD by various authors[175–178], but with a general focus on identifying the sintering mechanisms at the nano-scale rather than determining rules of motion for coarser spatial methods. The present study is somewhat similar to Hawa and Zachariah's work [175, 176], in which they investigated how a chain of amorphous Si sintered and considered the influence of chain length and particle size and how these affect the velocity distribution and sintering time.

For the present investigation LAMMPS[179] is used to conduct MD simulations. As a model material copper is employed by using EAM potential developed by Foiles et al. [180]. A comparison with more recent copper EAM potentials was conducted. While the quantitative results did change, the qualitative trends did not and the employed potential was much faster to calculate. The timestep employed within the MD simulations is generally 0.004 ps.

The primary goal of the following simulations is to predict the sample length change ΔL during sintering, parametrized by variables accessible on the mesoscopic phase-field scale. For this purpose the geometry depicted in fig. 8.1 is developed. It contains a chain of rectangular cuboid grains of alternating, different orientations, with both ends of the chain being free as to allow movement. On each of the grain boundaries a pore may be

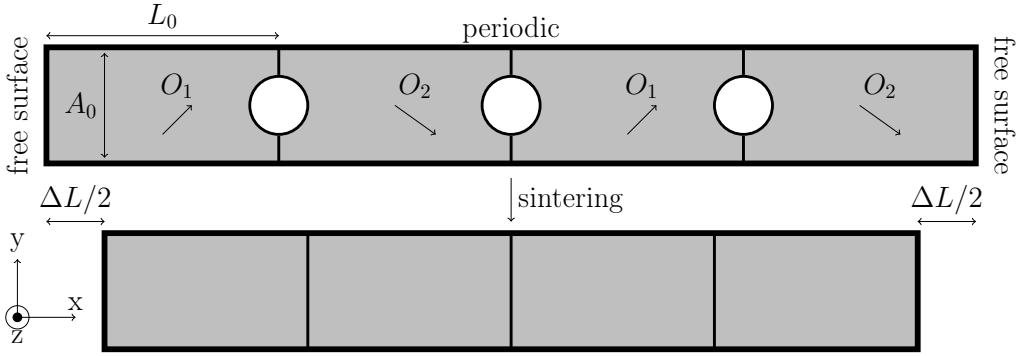

Figure 8.1: Two-dimensional sketch of the considered geometry in the MD simulations. Grains of different orientation O_1, O_2 are placed in a row, with pores on grain boundaries. The ends of the chain are free surfaces, with directions perpendicular to these being periodic.

placed, which then vanishes during the sintering process, which in turn induces movement of the grains. By employing cuboid grains extending to the periodic boundary, the grain rotation as commonly found in MD simulations of sintering[178] is largely suppressed. This makes the tracking of the pore region much simpler. It also makes the calculation of rigid displacements simpler because no rotational displacement needs to be removed.

The following results will be mainly based on placing spherical pores of radius $\approx 1.2\,\mathrm{nm}$, but the qualitative trends of the results do not change when the size is varied or when a cylindrical pore is placed. The visualization of the results is done with OVITO[181] and matplotlib[182]. The view of the simulations will be from the positive z direction as indicated in fig. 8.1, unless mentioned otherwise.

The system is prepared as follows: First, a bicrystal of size (nL_0, mA_0) is prepared with a base length $L_0 = 141\,\text{Å}$ and base area $A_0 = 1306\,\text{Å}^2$ with free surfaces along the [100] axis (x-axis) of the simulation cell. n, m are positive integers, which will be varied. The main grain boundary orientation relationship which will be investigated in the present study is the (210)/[001] STGB. It is a symmetrical tilt grain boundary (STGB) with a misorientation angle of $\theta = 53.1°$ about the [001] tilt axis, with the grain boundary plane being (210). Additional GBs for which the simulations were conducted are the (310)/[001] STGB and an asymmetrical tilt grain boundary with the left/right grain boundary planes being the (100) and $(2\bar{1}0)$ planes, with a 26.56° rotation around the [001] axis. These GBs are chosen because they were easy to directly construct within LAMMPS. After the atoms are set, a conjugated gradient minimization at 0 K is conducted, followed by an constant number of atoms N, pressure $p = 0$ and temperature T (NPT) ensemble heating run from 1 K to the target temperature $T = 700\,\mathrm{K}$ over 200 ps, followed by another 320 ps of equilibration at constant target temperature $T = 700\,\mathrm{K}$. This condition of $p = 0$ and $T = 700\,\mathrm{K}$ will also be held for the rest of the chapter. The system is then copied and shifted until the desired chain length is reached and equilibrated for a period of 400 ps to allow the system to relax the newly constructed grain boundaries. Once the system is ready, regions on the grain boundaries are defined and the atoms removed in order to place pores. By counting the number of atoms within these regions during the simulation, it is possible to obtain an estimate of the number of absorbed vacancies. Furthermore, the center of mass (COM) of the individual grains is tracked as to allow calculation of grain displacements and the total length change. The grain displacements are calculated directly by subtracting the center of mass $x_i(t)$ of grain i at time t from that at time $t = 0$. The total length change in a direction is assumed to be the length change of the vector connecting the center of mass of the first and last grain in the chain. It is taken to be *positive* for a shortening of the vector. The sintering simulations on structures with pores are generally run in increments of 8 ns. If a pore is observed to have vanished, the

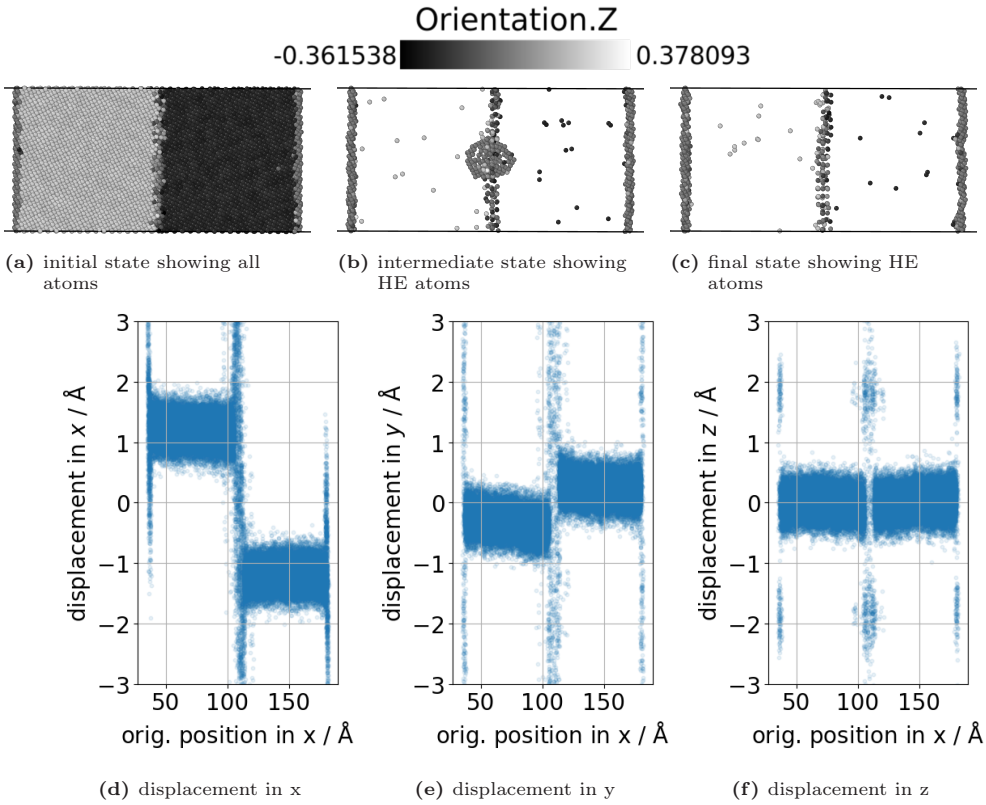

(a) initial state showing all atoms

(b) intermediate state showing HE atoms

(c) final state showing HE atoms

(d) displacement in x

(e) displacement in y

(f) displacement in z

Figure 8.2: Simulation results exemplarily depicted for $L = 2L_0$, $A = 2A_0$ and a cylindrical pore. The color in the top row indicates the local orientation in the viewing direction (Z), calculated via polyhedral template matching[183], allowing to distinguish the grains. In the last two two images, only high energy (HE) atoms (potential energy of $> -3.2\,\mathrm{eV}$) are shown, revealing the interfaces. The displacement of the atoms in the x (d), y (e) and z (f) directions after the pore has vanished are plotted over the original atomic position on the bottom. The displacement range is fixed to [-3, 3]Å since the large displacements on the surfaces would obscure the behaviour within the grain. The inner parts of the grains are generally homogeneously displaced, with the interfaces showing large deviations. Similar plots are obtained for all other simulations.

simulation run may be terminated early. Not all simulations are run to complete pore elimination as the goal of the study is to find rules which are also applicable during the process and not only after it.

A typical simulation result, starting with a cylindrical pore, is shown in fig. 8.2 with the displacement per atom on the bottom. As expected, the pore vanishes over time and its vanishing is correlated to an inwards movement of the free surfaces. The displacement per atom is observed to be largely homogeneous within the grains, with large deviations

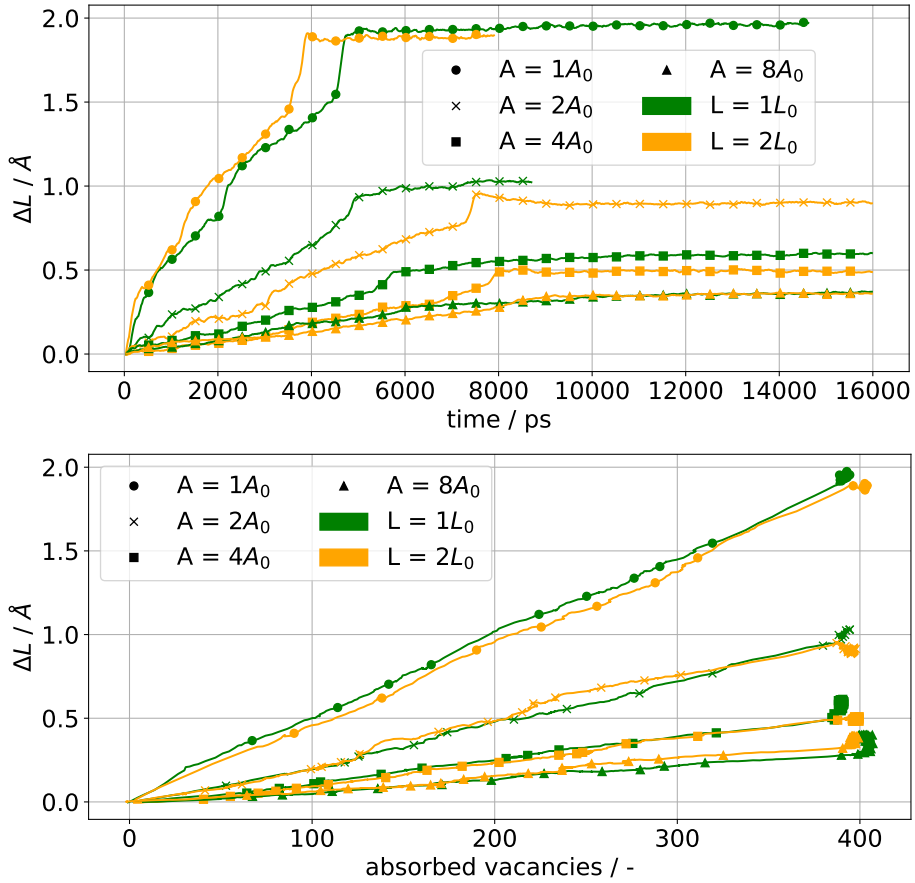

Figure 8.3: Length change ΔL of a bicrystal containing a (210)[001] STGB for various geometries, over time and over the number of absorbed vacancies. The length change is observed to be strongly dependent on the area, with only a weak dependence on the total length. The pore elimination time, roughly given by when ΔL becomes constant, is slightly dependent on total length. A linear dependence of ΔL on the number of absorbed vacancies is also observed.

only found close to interfaces, lending credence to the common assumption of rigid-body motion during sintering. The displacement in x, the shrinkage direction, generally directly scales with the pore size and is influenced by the area of the grains. While there were differences for the displacement in y, they generally did not show any monotonic relationship to pore size or grain geometry. In the shown simulation a gradient for the y displacement seems to exist, though this did not always manifest in the other simulations. Interestingly, the displacement in z did not show a sign difference between the grains. This might be due to the tilt axis being the z axis, though further research in this direction should be conducted. For the present chapter we shall focus on the displacement in the shrinkage direction and assume that it is described by a rigid-body motion.

Next, the influence of grain geometry on the length change is investigated in a bicrystal. In fig. 8.3 the results are shown for various grain lengths and areas. In this and the following plots, only every 25th point is marked unless mentioned otherwise; the line always indicates all data points. It is easily observed that the results are clustered by the grain area, whereas the grain length has no consistent influence on the results. The small influence of the grain length is likely due to excess stress caused by finite size effects. This also causes the pore to vanish at different times. Note that there is a linear relationship between vacancy absorption and displacement. By only plotting the system response over the number of absorbed vacancies, differences in kinetics can be removed from the problem.

As the present setup does not allow the differentiation of the GB area (GBA) from the grain cross section (GCS), a second series of simulations is performed. In these the area around the grain boundary is largely removed, effectively decoupling the GB area from the grain cross section. This is achieved by leaving only a rectangular area of size GBA in a region of length 50.61 Å around the grain boundary. Thus new surfaces are introduced to a thin region between the grains, which need to be relaxed. This relaxation is done for 16 ns before a spherical pore is placed on the GB, followed by another run for up to 16 ns. It should be noted that the newly generated surfaces can also act as vacancy sink/source, whose contribution to the supposed absorbed vacancy count is not easily accounted for. Thus the relationship between displacement and vacancies shown in fig. 8.4 will differ from that of the previous results. More specifically, more vacancies are being absorbed than plotted which also causes a larger displacement[1]. The squares and triangles show results for which GCS = GBA, whereas those in which GCS $\neq$ GBA are marked with

[1] Using the later model eq. (8.3) and presuming that the volume change is caused by both area and length changes $\Delta V = A\Delta L + L\Delta A$ yields a bit more than twice as many vacancies being absorbed, which fits quite well with these results.

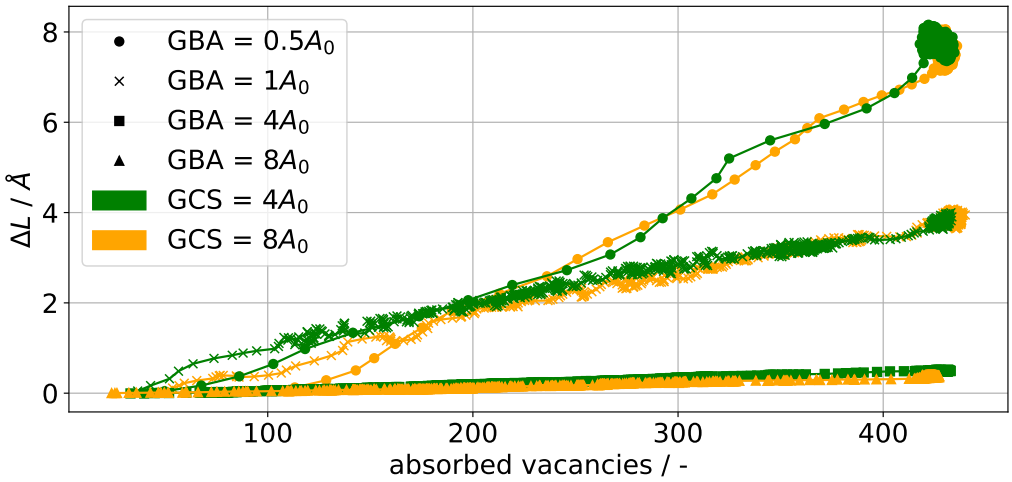

Figure 8.4: The length change ΔL of a bicrystal containing a (210)[001] STGB for two grain cross sections (GCS) and four grain boundary areas (GBA). Once GBA is independent of GCS, it is the determining factor of ΔL. Due to the quick pore removal for GBA $= 0.5A_0$ every point is marked in this plot.

crosses and dots. The length change seems to be mainly influenced by GBA instead of GCS.

Hence we may formulate the first two rules of motion: The length change of a bicrystal sample due to vacancy absorption is *antiproportional* to the grain boundary area of the sample. The length change of a sample due to vacancy absorption is *proportional* to the number of absorbed vacancies.

Next we shall consider the influence of adding more grains, and hence grain boundaries and pores, to the system. The results of investigating chains with up to 8 grains are depicted in fig. 8.5. For consistency, two grain boundary areas were considered and the first rule of motion is confirmed again. If one follows the line described by a smaller simulation, one can then reasonably predict the length change observed in the larger chain. Hence the displacement induced by the vacancy absorption on each grain boundary tends to be transported along the whole chain without any resistance. This can be interpreted as a kind of superposition property inherent in the solution, i.e. for a system containing multiple vacancy absorption sites, the total solution is the sum of all single vacancy absorption site problems. This is verified by running seven simulations for a chain with 8 grains, but with only a single pore being placed on a different grain boundary each time. The seven individual solutions are then added together and compared against the full solution, shown in fig. 8.6. The calculated solution and measured solution match

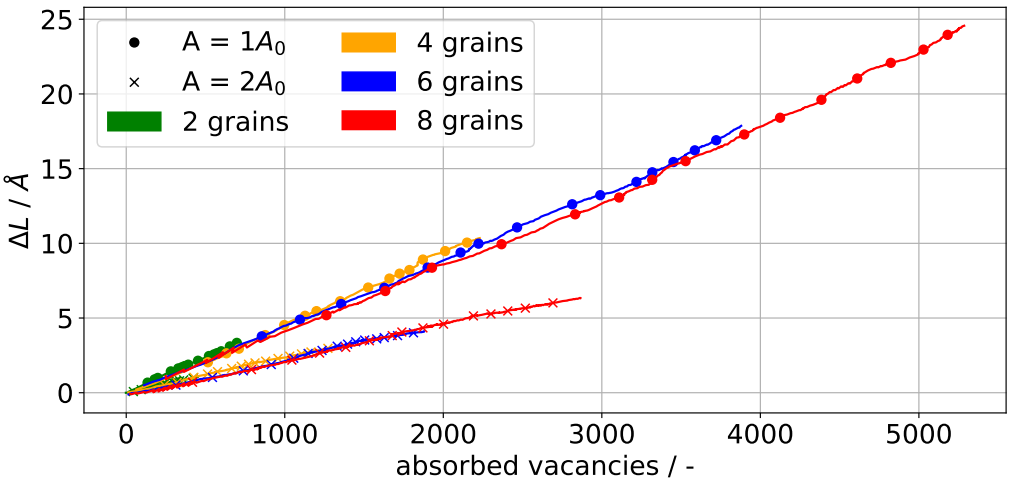

Figure 8.5: Total length change for two areas and up to 8 grains / 7 pores in the chain, with $L = 2L_0$. A linear relationship between vacancies absorbed and the length change is observed. The results for longer chains roughly behave as if lying on the same line as for the smaller chains.

well, hence we may define the third rule of motion: The total length change of a system is determined by the superposition of all length changes due to vacancy absorption sites.

Recapping these rules we have the following properties:

1. the length change is *antiproportional* to the grain boundary area and *independent* of the grain length
2. the length change is *proportional* to the number of absorbed vacancies within the system
3. the length change of a system with multiple vacancy absorption sites is the *superposition* of the individual length changes

In the following we shall shortly derive a model which contains all these properties. In spirit it is rather similar to DeHoff's theoretical developments in the 1980s[184, 185], but without requiring the grain structure to be decomposed into a space-filling cell structure. First, based on item 2 we assume that each vacancy contributes a certain volume change dV proportional to the atomic volume Ω, with dN being the number of vacancies which have just been absorbed. Second, we assume that this volume change is due to a rigid

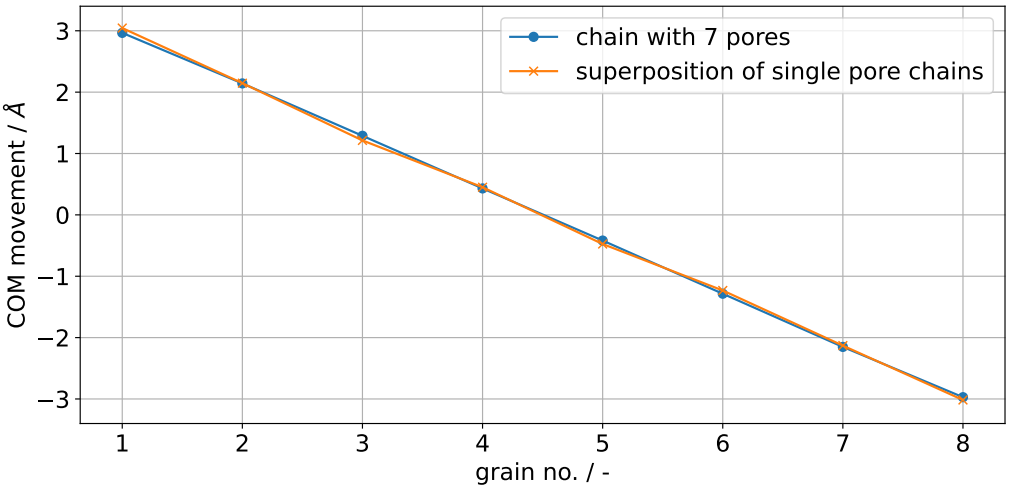

Figure 8.6: Comparison of a 8 grain chain with 7 pores and the solution via superposition. A good match for the total length change as well as the grain-specific displacements is observed.

movement of the entire crystal lattice of magnitude dL, i.e. $dV = AdL$ with the grain boundary area A, motivated by item 1 Thus one may write

$$\Omega dN = AdL \tag{8.1}$$

$$\leftrightarrow dL = \frac{\Omega}{A} dN \tag{8.2}$$

$$\int \leftrightarrow \Delta L = \frac{\Omega}{A} \Delta N \tag{8.3}$$

with the length change ΔL taken to be positive for a shortening of the sample. This model is verified by testing it not only against the already presented data, but also several grain boundary types, grain lengths, grain boundary areas, pore shapes, pore sizes, and numbers of pores. The grain boundary area A of each simulation is estimated based on the equilibrated area before the pore is placed. The atomic volume Ω is determined by observing the volume of an fcc lattice of copper atoms in a periodic box at $T = 700\,\mathrm{K}$ employing an NPT ensemble with $p = 0$, resulting in $\Omega = 1.22 \times 10^{-29}\,\mathrm{m}^3$ which is close to the value given by [186]. The number of absorbed vacancies is known via measurement and thus the length change can be determined. The result of the comparison is shown in fig. 8.7 which shows a good match for all data, though with a slight underprediction in the length change.

The presented model so far seems to only describe the total length change ΔL and not the motion of individual grains described by their displacements u_α, or equivalently

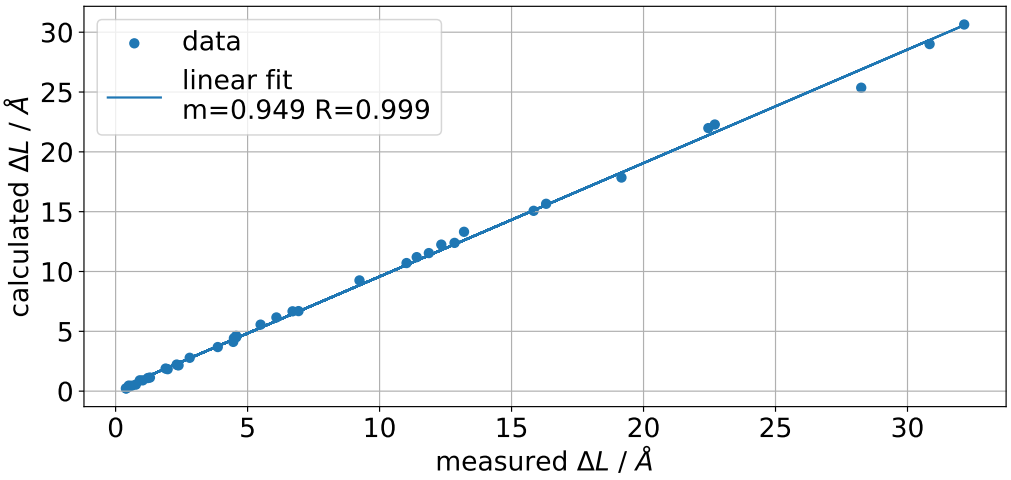

Figure 8.7: The measured length change is plotted against the calculated length change based on eq. (8.3). A general match is observed, with the fitted line's slope (m) indicating a slight underprediction (5%) of the model.

velocities, as required in a field-resolved method as the phase-field method. In order to resolve this, consider the implication of a length change ΔL in an effectively one-dimensional bicrystal $\alpha\beta$: Since both grains move as rigid-bodies, the length change is the sum of the individual displacements and thus is given by

$$u_\alpha - u_\beta = \Delta L \tag{8.4}$$

$$= \Delta u_{\alpha\beta} \tag{8.5}$$

which is also the displacement jump $\Delta u_{\alpha\beta}$ across the grain boundary. The superposition property item 3 is now exploited to enforce this simultaneously for all grain boundaries, leading to

$$\underbrace{\mathrm{C}}_{B\times N}\ \underbrace{u}_{N} = \underbrace{\Delta u}_{B} \tag{8.6}$$

which is a usually overdetermined linear system of equations. The matrix C consists of rows with zeros and only one $+1$ and -1 each and acts on the unknown N grain displacements $u = (u_1, \ldots, u_N)^T$. The sign of the entries is determined by the one-sided grain boundary plane vector $n_\alpha = -n_\beta$ in the laboratory frame, with n_α being normal to the $\alpha\beta$ grain boundary and pointing out of the α grain. The right-hand side vector is determined by eq. (8.3) for each of the B grain boundaries. This system may be solved e.g. in a least-squares sense, with the conservation of momentum accounted for

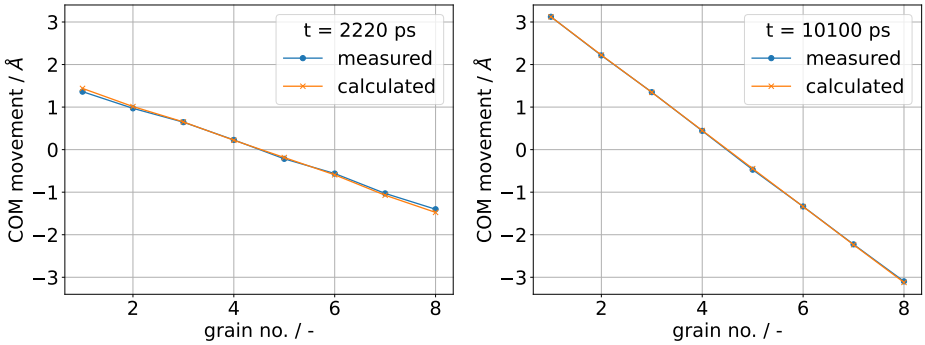

Figure 8.8: Comparison of solving eq. (8.6) and the observed data for two simulation states. A good match is observed for both.

afterwards by subtracting the mass-weighted average displacement from the solution u. For the special case of a linear chain of grains, there are $B = N - 1$ grain boundaries. Adding conservation of momentum to the system of equations makes the matrix C square and since the individual rows are linearly independent[2], it also is of full rank and thus uniquely solvable. Furthermore, this formulation only accounts for motion due to vacancy absorption. If other processes inducing displacement occur, e.g. grain boundary sliding, then these will require a separate treatment.

As a first test of this, we use the time-dependent data of one MD simulation and input these as the right-hand sides of the system of equations. The contacts between grains which fill the matrix C are also determined from these. Since the chain is linear, including conservation of momentum makes it uniquely solvable. The system is solved by direct matrix inversion since it is rather small, with a comparison of the calculated grain movement and the observed grain movement shown in fig. 8.8 for two simulation states. As the figure shows, there is a close match between the calculation and measurement, giving a measure of confidence in this approach.

[2] A new unknown is introduced by each row and thus cannot be represented as a linear combination of previous rows. Conservation of momentum doesn't add a new unknown, but cannot be constructed from prior rows.

8.2 Phase-field model and simulations

In this section a new phase-field model will be described, following by a small-scale validation to ensure that the green body size effect is no longer present before large green bodies are calculated.

8.2.1 Phase-field model with advection

The model in the following is based on [114, 187], with the advection velocity being calculated with a model based on the MD results. This new model in its entirety is dubbed MDi, as it is *i*nspired by MD. The evolution equations for the fields are the same as in [114]:

$$\begin{aligned}\frac{\partial \phi_\alpha}{\partial t} + \nabla \cdot (\vec{v}_\alpha \phi_\alpha) = \frac{1}{\tau(\phi)\epsilon}\Big[&- \epsilon \left(\frac{\partial a(\phi, \nabla\phi)}{\partial \phi_\alpha} - \nabla \cdot \frac{\partial a(\phi, \nabla\phi)}{\partial \nabla \phi_\alpha} \right) \\ &- \frac{1}{\epsilon}\frac{\partial w(\phi)}{\partial \phi_\alpha} - \sum_{\beta=0}^{N-1} \psi_\beta(\mu, T) \frac{\partial h_\beta(\phi)}{\partial \phi_\alpha} \Big] - \lambda,\end{aligned} \tag{8.7}$$

$$\begin{aligned}\frac{\partial \mu}{\partial t} = &\left[\sum_{\alpha=0}^{N-1} h_\alpha(\phi) \left(\frac{\partial c_\alpha(\mu, T)}{\partial \mu} \right) \right]^{-1} \\ &\left(\nabla \cdot \Big(M(\phi, \mu, T) \nabla \mu - \vec{v}(x) c \Big) - \sum_{\alpha=0}^{N-1} c_\alpha(\mu, T) \frac{\partial h_\alpha(\phi)}{\partial t} \right).\end{aligned} \tag{8.8}$$

This represents the evolution of the N phase-fields ϕ_α and the chemical potential μ for one independent component, taken to be copper in the present chapter. The phase-field tuple ϕ distinguishes the surrounding vapour ($\phi_\mathrm{V}, \mathrm{V} = 0$) from copper grains of arbitrary orientation ($\phi_a, a > 0$). The evolution of the chemical potential μ accounts for the species conservation via the concentration c and takes into account the effect of phase changes due to changes in ϕ. For further particulars of the terms the interested reader is referred to [114, 187].

The calculation of the grain velocities follows the ideas outlined in the previous section. This will be formulated in terms of instantaneous displacement u and number density of absorbed vacancies Δn to be consistent with the MD section. The instantaneous velocity v is linearly related to u as $v = \frac{u}{\Delta t}$ with the time interval Δt. The concentration c is related to the number density n as $n = \frac{N_a}{V_m} c$ with Avogadro's constant N_a and the molar volume V_m. Each grain boundary $\alpha\beta$ absorbs an amount $\Delta N_{\alpha\beta} = \int_{GB} \Delta n_{\alpha\beta} dV$

of vacancies in a time interval Δt, with the density of absorbed vacancies $\Delta n_{\alpha\beta}$. This is related to the vectorial displacement jump

$$V_{\alpha\beta} = \int_{GB} 4\phi_\alpha\phi_\beta dV \tag{8.9}$$

$$A_{\alpha\beta} = \frac{V_{\alpha\beta}}{l_0} \tag{8.10}$$

$$\vec{\Delta u}_{\alpha\beta} = \frac{1}{V_{\alpha\beta}} \int_{GB} 4\phi_\alpha\phi_\beta \frac{\Omega}{A_{\alpha\beta}} \Delta n_{\alpha\beta} \vec{n_{\alpha\beta}} dV \tag{8.11}$$

in which the orientation of the grain boundary plane was taken into account by a similar approach as Wang[33], but employing normalized phase-field gradients representing the normal vector, i.e. $\vec{n_{\alpha\beta}} = \frac{\nabla(\phi_\alpha - \phi_\beta)}{|\nabla(\phi_\alpha - \phi_\beta)|}$ instead of just the phase-field gradients. Note that $\vec{n_{\alpha\beta}}$ needs to be chosen consistently with the later input to the matrix equation. It is always taken to be from the lower α index to the larger β index, defining a unique orientation for each $\alpha\beta$ pair. The grain boundary region GB is defined to be the region in which $g = \phi_\alpha\phi_\beta \geq g_T$ holds, i.e. only the region where both grain phases have significant volume fractions. In the following the value $g_T = 0.14$ is chosen. The grain boundary area $A_{\alpha\beta}$ is resolved by dividing the grain boundary volume $V_{\alpha\beta}$ by the equilibrium grain boundary width $l_0 = \int_0^1 4\phi_\alpha(x)(1-\phi_\alpha(x))d\phi = \frac{\pi^2\epsilon}{8}$ for the employed obstacle potential. The remaining $4\phi_\alpha\phi_\beta$ and $V_{\alpha\beta}$ terms act as a weighted average to assign higher weight to regions which contain more grain boundary phase $4\phi_\alpha\phi_\beta$.

Equation (8.11) still contains an unknown, namely the number of absorbed vacancies. For this we assume that a grain boundary has a certain equilibrium number density of atoms n_{eq}^{gb} and that it relaxes towards this number density:

$$\frac{\partial n}{\partial t} = -\frac{n - n_{eq}^{gb}}{t_r} \tag{8.12}$$

which allows the calculation of the number density of absorbed vacancies $\Delta n = -\frac{\partial n}{\partial t}\Delta t$. Since this describes a relaxation process, one can consider the term $n - n_{eq}^{gb}$ as the driving force for this process — once it vanishes, densification via advection stops. Note that this assumes atoms and vacancies are both conserved quantities. Only the number of atoms is actually conserved, with vacancies and lattice sites being destroyed and generated during absorption to accommodate the volume change. However, this rough treatment suffices to show the capabilities of the model and is in fact quite standard in phase-field modelling of sintering[33–35, 104, 114]. In spirit this is similar to Wang's model[33] but the relaxation time t_r is identified explicitly here, which can in turn be determined via molecular dynamics. In the MD simulations t_r was observed to depend strongly on the

grain boundary orientation relationship; it is strongly related to the efficiency of a grain boundary at absorbing vacancies such as described in [188]. In the following simulations, all grain boundaries are assumed to be of a (210)/[001] STGB (53.1°) type. Furthermore, n_{eq}^{gb} does not have the meaning of a "grain boundary equilibrium density" in this context. Specifically, if it is below the bulk density as one would expect based on physics, it will *push apart* grains instead of attracting them. This phenomenon has been investigated in-depth in [113, 114]. Based on the suggestions therein, n_{eq}^{gb} is calculated based on the observed average chemical potential on the particle surface $\hat{\mu}$, which should approximate the capillary pressure. This ensures that the resulting velocities are consistent with the free energy functional and the theoretical dihedral angle is recovered[114]. Note that this allows a rather trivial addition of an external isotropic pressure to the system, as the capillary pressure can simply be shifted by the external pressure.

It should also be noted that properties such as $\vec{\Delta u}_{\alpha\beta}$ and $V_{\alpha\beta}$ need to be tracked for each grain boundary individually and thus their memory and communication requirements scale as $O(nN^2)$ if implemented naïvely, with the number of parallel processes n and number of phase-fields N. While this is not a problem for a few hundreds of grains, once thousands or tens of thousands grains are resolved this will dominate the memory and communication costs. This is resolved by only storing the actual contacts (thus being a sparse representation) and distributing it across all parallel processes. The message passing interface (MPI) is employed for the parallelization and updates to this distributed matrix are realized via one-sided communication. The details of this scheme will be published in a separate paper.

The displacement jumps are used to solve for the particle displacements u, for each direction separately, by building a system of equations

$$\mathrm{C}u = \Delta u \tag{8.13}$$

in which the matrix C is filled according to the connectivity determined during the simulation. The structure of the matrix is clarified by the following example: Consider a 2x2 grid of grains, depicted in fig. 8.9. Each particle has two contacts, one along each dimension. These are always taken to be from the lower grain index a of ϕ_a to the higher one, i.e. we have the contacts described by the ordered set $\{C_{1,2}, C_{1,3}, C_{2,4}, C_{3,4}\}$. The size of this set is equal to the number of grain boundaries B in the system. A matrix C_d of dimension $B \times N$ is constructed per dimenions d, with a corresponding RHS Δu_d of size B. For each contact a row is added to the matrix, with only non-zero entries for those grains which are connected by this contact. The magnitude of the entries is always 1, but the sign is determined consistently with $\vec{n_{\alpha\beta}}$ in this direction, going consistently

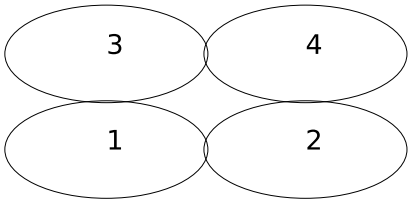

Figure 8.9: Example 2x2 setup of grains for clarifying the matrix structure. The number within the circles indicates the grain index.

from the lower to the higher index. The right-hand side displacement jump is already in a vector form and therefore can be easily split into its components Δu_d. Thus eq. (8.13) can be written, for the x dimension, as

$$\begin{pmatrix} 1 & -1 & 0 & 0 \\ -1 & 0 & 1 & 0 \\ 0 & -1 & 0 & 1 \\ 0 & 0 & 1 & -1 \end{pmatrix} \begin{pmatrix} u_{x,1} \\ u_{x,2} \\ u_{x,3} \\ u_{x,4} \end{pmatrix} = \begin{pmatrix} \Delta u_{x,1,2} \\ \Delta u_{x,1,3} \\ \Delta u_{x,2,4} \\ \Delta u_{x,3,4} \end{pmatrix}$$

with the sign on the left-hand side determined based on the grain boundary normal. If the grain boundary normal has no component in a dimension, the sign within the matrix plays no role as the right-hand side will be zero. This effectively says that no relative motion occurs. Note that this matrix, although square, is singular, since e.g. the fourth row can be constructed by adding the first and second row and subtracting the result from the third row. Conservation of momentum is accounted for afterwards by subtracting the mass-weighted average displacement from each grain displacement.

The resulting system of equations is usually overdetermined and only in the special case of a linear chain of particles can be solved exactly if conservation of momentum is included in the system. However, the system can be solved in a least-square sense. This could be done with e.g. an Alternating Direction Method of Multipliers approach[189], which requires a collective reduction of N scalars per iteration. Alternatively, the matrix C and its transpose could be partially distributed and then be solved by using some Krylov subspace method (e.g. a block Conjugated Gradient Least Squares method[190]) which would need a collective reduction of a single scalar per iteration. However, both approaches lead to excessive communication time (on the order of entire field sweeps) and thus an approach suited to the present problem is developed.

Typical solutions of the system were sought by generating packings, from which eq. (8.13) was determined while assuming the right-hand side is given by a normal distribution

$$p(\xi) = \frac{1}{\sqrt{2\pi\sigma^2}} \exp(-\frac{(\xi-\mu)^2}{2\sigma^2}) \tag{8.14}$$

with its mean and standard deviation σ. A mean of $\mu = 1$ is generally employed with variable standard deviation σ. A spatial dependence can be included by simply adding a function of particle position to the random sample generated by eq. (8.14). The system is solved employing the Least Squares via QR factorization (LSQR)[191] algorithm.

It was observed that the spatial distribution of the right-hand side tends to determine the shape of the solution. If it is assigned randomly without any spatial dependence, a mostly linear function of position is observed, with local inhomogeneities. If a linear dependence on the position is added, the displacement field becomes a quadratic function of position. This implies that the solution of the system basically integrates the spatial distribution of right-hand sides. This can also be seen from the structure of the matrix C: Each row effectively represents a finite difference formula, with the right-hand side giving the slope, i.e. C is a differentiation operator. Thus its generalized inverse is an integration operator.

Given that the same grain boundary type is assumed for all contacts, with similar initial neighbourhoods, it seems reasonable to assume the displacement field is given by a linear function. Hence one may approximate the full problem by replacing the particle displacements u by the relation

$$u = m(x - x_m) \tag{8.15}$$

with the known center of mass of each grain x, the known total center of mass x_m and an unknown slope m. Hence only m remains to be determined, which can be done exactly in a least-square sense by employing the normal equations:

$$\underbrace{\mathrm{C}}_{C\in\mathbb{R}^{BxN}} u = \underbrace{\mathrm{C}(x - x_m)}_{D\in\mathbb{R}^B} m = \Delta u \tag{8.16}$$

$$Dm = \Delta u \tag{8.17}$$

$$\underbrace{D^T D}_{q\in\mathbb{R}} m = \underbrace{D^T \Delta u}_{p\in\mathbb{R}} \tag{8.18}$$

$$m = \frac{p}{q} \tag{8.19}$$

which only requires a parallel reduction operation for p and q.

This approach is compared against the full solution via LSQR. The error is evaluated with the root-mean-square error (RMSE) and relative RMSE (RRMSE) defined as

$$\mathrm{RMSE} = \sqrt{\frac{1}{N}\sum_i (x_{i,LSQR} - x_{i,lin})^2} \tag{8.20}$$

$$\mathrm{RRMSE} = \frac{\mathrm{RMSE}}{\max(x_{LSQR}) - \min(x_{LSQR})} \tag{8.21}$$

for the solution vectors of the LSQR method and the linear fit ansatz. It is generally observed that the RRMSE is unaffected by the choice of mean μ, while the RMSE changes due to the scale in displacement. For regular packings the (R)RMSE is observed to scale mostly linearly in the standard deviation σ of the random distribution, with errors on the order of machine precision for $\sigma = 0$. The irregular packings employed later for the PF simulations generally show some non-zero error even for $\sigma = 0$, though starting from about RRMSE $\approx 0.16\%$. Even if σ is comparable to the mean of the normal distribution, RRMSE $\approx 1.6\%$ and thus still quite acceptable. A visual comparison for the effect of σ on the displacements in a 3D packing containing 3445 particles is shown in fig. 8.10. As can be seen, the solution shape and scale are always well-preserved. What the fit ansatz obviously cannnot match however is the local variation of absorption activity, modelled by the random distribution of displacement jumps. The interested reader is referred to the Supplementary Material wherein the code employed for this test is published in full, along with the irregular packings employed later for the large-scale sintering simulations.

As a final note, the specification of the vacancy absorption rate is the main weakness of the presented model, since it cannot be completely linked to quantities obtainable via MD. Hence a direct comparison to MD simulations would likely yield a significant mismatch in the temporal evolution. However, if an improved model for the vacancy absorption rate is developed, it can be included easily into the current approach. This is due to the model effectively being split into a kinematic part eq. (8.13) and a dynamic part eq. (8.12) which can be changed independently.

8.2.2 Parameters and data evaluation

The scales employed are listed in table 8.1 and the materials parameters in table 8.2. These are the same as in [114] except for the newly introduced atomic volume Ω and the relaxation time t_r. The relaxation time is determined by running MD simulations

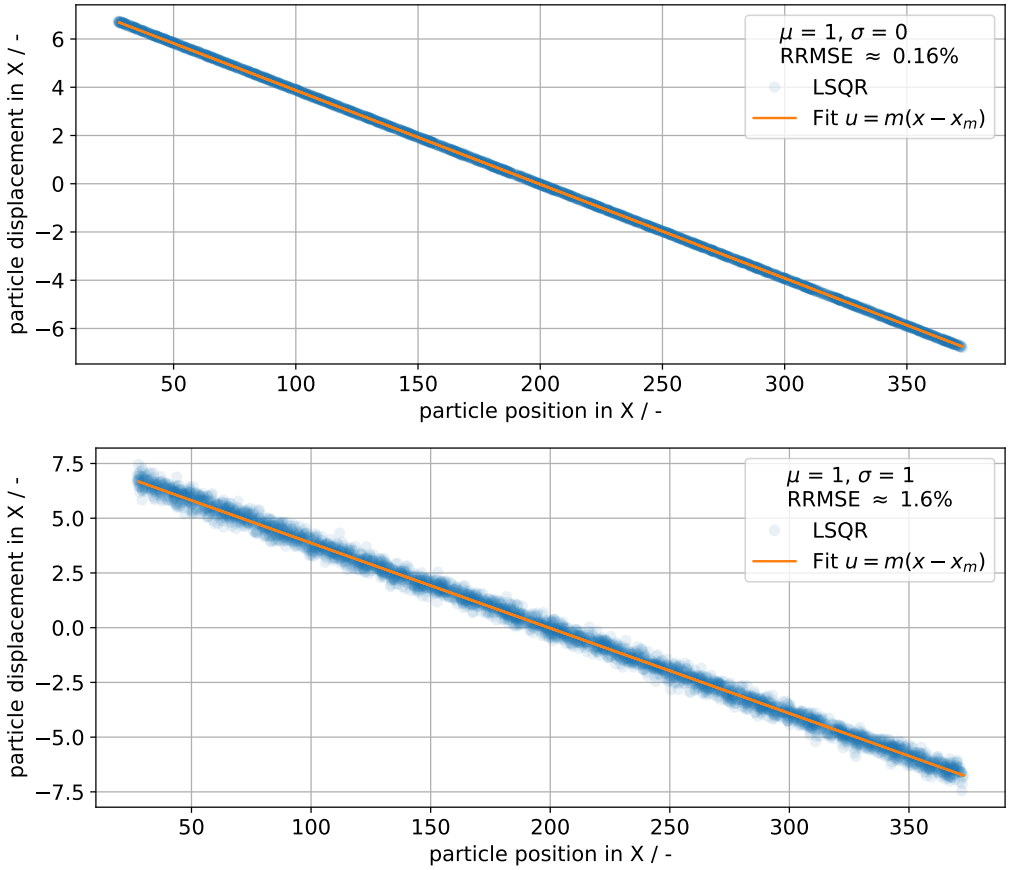

Figure 8.10: Comparison of the full displacement solution calculated via LSQR and fit ansatz for two values of the standard deviation. Each marker indicates a particle's position and its resulting displacement in one dimension of the 3D packing. The shape and scale of the solution are always well-preserved by the fit ansatz.

for a (210)/[001] STGB (53.1°) in which atoms are randomly removed from the grain boundary and observing the time it takes until the atom count within the grain boundary has stabilized. Several such simulations were run and the order of magnitude for the relaxation time then used for the value of t_r. This is more of qualitative approach, but t_r behaves similarly to the stiffness κ in the classical rigid-body motion (RBM) model of Wang[33]: In the classical model, the RBM velocity scales as

$$v \propto \kappa(n - n_{gb}^{eq}) \tag{8.22}$$

whereas in the present model it is rather

$$v \propto \frac{n - n_{gb}^{eq}}{t_r} \tag{8.23}$$

i.e. the velocity is proportional to κ, but inversely proportional to t_r. Shi et al.[36] could show that once κ is sufficiently large, the resulting advection velocity does not change upon a further increase in κ. Hence the proportionality is only applicable to a certain limit, after which other processes control the velocity. Since t_r divides the driving force $n - n_{gb}^{eq}$ whereas κ multiplies it, the same behaviour applies, but reversed: Once t_r is small enough, making it smaller will not change the velocity. One can think of this as saying that the problem ought not to be controlled by the absorption rate and hence the absorption rate should be appreciably faster than the slowest other process. The time step is determined by calculating stable time step widths within the explicit scheme and employing the minimum to ensure stable time integration as described in [114], with the table only listing the largest stable timestep with zero advection velocity.

The evaluation of the data is the same as in [114] in terms of strain and density. The contact number later employed in the three-dimensional simulations is calculated with the package cc3d's[144] function `contacts` on the phase-field label field and the simply counting the pairwise occurrences of labels. The surrounding vapour phase is treated as background, with the phase-field label field being defined pointwise as the label which has the highest phase-field value. Since surface particles always have some missing neighbours, including these would induce a particle size and simulation size bias in the coordination number. These are excluded by determining the bounding box of the green body, then shrinking it by 32 nm in each direction and only averaging over particles contained in this shrunken box. In the 3D simulation this excludes at least two particle layers, removing the surface effect.

The simulations in section 8.2.3 are conducted locally while employing GNU Parallel[173] for efficient job management. The three-dimensional simulations in section 8.2.4 are

calculated on the Hawk supercomputer at the High Performance Computing Center in Stuttgart. Hence the processor employed for the three-dimensional simulations is the AMD EPYC 7742, with 64 cores running at 2.25 GHz. A single core performance of 9.4 GFLOP/s, i.e. 26.1 % of the theoretical peak, is achieved.

Table 8.1: nondimensionalization parameters

scale	value
length l_0	$1 \times 10^{-8}\,\mathrm{m}$
diffusivity D_0	$1 \times 10^{-12}\,\mathrm{m^2\,s^{-1}}$
time t_0	$1 \times 10^{-4}\,\mathrm{s}$
velocity v_0	$1 \times 10^{-4}\,\mathrm{m\,s^{-1}}$
temperature T_0	$700\,\mathrm{K}$
surface energy $E_{s,0}$	$1\,\mathrm{J\,m^{-2}}$
energy density $E_{r,0}$	$1 \times 10^{8}\,\mathrm{J\,m^{-3}}$
molar volume $V_{m,0}$	$7.1 \times 10^{-6}\,\mathrm{m^3\,mol^{-1}}$

8.2.3 Validation

In this section the system size convergence of the present model will be investigated. In effect, this tests whether the superposition rule of motion from the MD simulations has been transferred successfully. As will be shown below, the results for a two-particle model are virtually identical between the present model MDi and a grand potential model including advection, i.e. the model (ADV-μ) of [114]. Hence the accordance with classical theory in terms of neck growth and approach of centers, as well as Herring's scaling laws for a two-particle model as shown in[114], are transferable to the present model. Thus the strain in a system of increasing size will be investigated, first in a particle chain as suggested by [113], then in a rectangular grain geometry. Simulations are run for both models, with the number of particles in the chain given by $n \in \{2, 4, 8, 16, 32\}$. The simulations for the same geometry are all run to the same simulation time t_e. The strain is evaluated based on the movement of the barycenters of the first and last particle, i.e. $e = \frac{L(t)-L(0)}{L(0)}$ with $L(t) = x_{m,last} - x_{m,first}$ and $x_{m,*}$ being the the barycenter of the first/last particle. The geometries considered in this section can also in general be used as a relatively cheap benchmark geometry for determining whether size-independent densification is captured by the model.

Table 8.2: Employed physical and numerical parameters for the simulations.

parameter	nondim. value	physical value
numerical parameters		
grid spacing Δx	0.1	$1 \times 10^{-9}\,\mathrm{m}$
max. time step Δt_{max}	1.5×10^{-5}	$1.5 \times 10^{-9}\,\mathrm{s}$
interface parameter ϵ	$4\Delta x$	$4 \times 10^{-9}\,\mathrm{m}$
interface width $W \approx 2.5\epsilon$	$10\Delta x$	$10 \times 10^{-9}\,\mathrm{m}$
grain boundary cutoff $\phi_{\alpha\beta}^{min}$	0.14	-
physical parameters		
surface energy $\gamma_{v\alpha}$	2	$2\,\mathrm{J\,m^{-2}}$
grain boundary energy $\gamma_{\alpha\beta}$	1	$1\,\mathrm{J\,m^{-2}}$
volume diffusion D	1×10^{-3}	$1 \times 10^{-15}\,\mathrm{m^2\,s^{-1}}$
grain boundary diffusion D_{gb}	55	$5.5 \times 10^{-11}\,\mathrm{m^2\,s^{-1}}$
surface diffusion D_s	169	$1.69 \times 10^{-10}\,\mathrm{m^2\,s^{-1}}$
physical interface width δ_i	0.02	$2 \times 10^{-10}\,\mathrm{m}$
surface kinetic coefficient $\tau_{\mathrm{V}\alpha}$	0.08	$8 \times 10^{10}\,\mathrm{J\,s\,m^{-4}}$
grain boundary kinetic coefficient $\tau_{\alpha\beta}$	$100\ \tau_{\mathrm{V}\alpha}$	$8 \times 10^{12}\,\mathrm{J\,s\,m^{-4}}$
effective stiffness κ	3200	-
atomic volume Ω	1.22×10^{-5}	$1.22 \times 10^{-29}\,\mathrm{m^3}$
GB relaxation time t_r	1×10^{-8}	$1 \times 10^{-12}\,\mathrm{s}$

The strain over time for a chain of circular particles is shown in fig. 8.11a. While model MDi seems to converge at around 16 particles in a chain, model ADV-μ still shows a large change at this particle count. Let us first consider how model ADV-μ fails to converge by looking at the velocity distribution in fig. 8.11b. The velocity is plotted over the relative barycenter $X_{i,r} = \frac{x_{m,i} - x_{m,first}}{x_{m,last} - x_{m,first}}$ which allows the compact viewing of chains of arbitrary physical length. The absolute scale of velocity reached is similar for both models, but while model MDi always yields a linear function by design, model ADV-μ tends to produce curved velocity profiles which directly imply inhomogeneous densification. While a small amount of inhomogeneity is to be expected due to the discussion below, this should drop off rapidly from the outermost particle.

One might ask why model MDi does not instantly converge in this case, given that the model without the phase-field information did so? This is due to the chain not actually being homogeneous and only becoming so at a sufficient number of particles. The simulation geometry at the end of the simulation is depicted in fig. 8.12, showing that the chain ends take up a different shape than inner chain particles. This shape difference

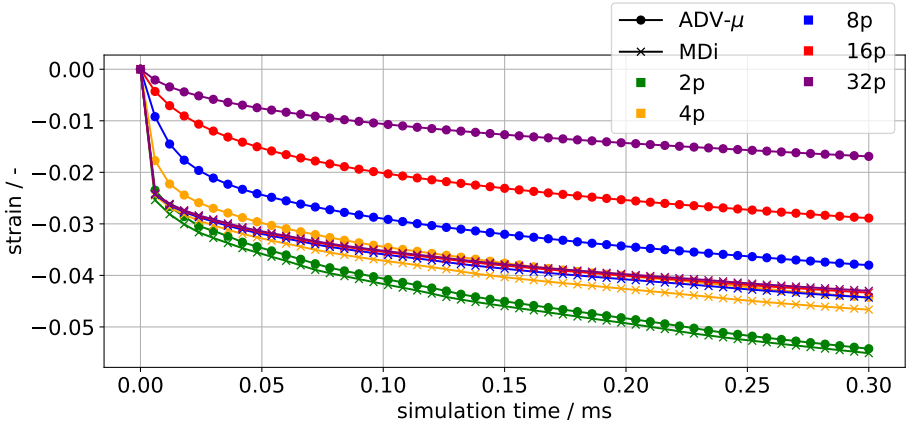

(a) strain over time

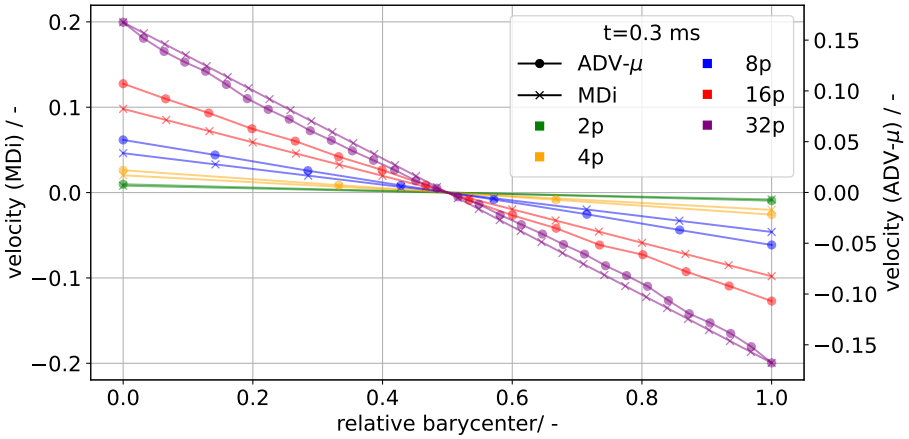

(b) velocity distribution

Figure 8.11: Comparison of the MDi model (crosses) and the model of [114] (circles). The dependence on the strain becomes negligible at around 16 particles for the MDi model but is substantial across all investigated particle counts for model ADV-μ. The velocity distribution shows the inhomogeneous densification (non-constant velocity gradient between the particles) from which this lack of convergence originates.

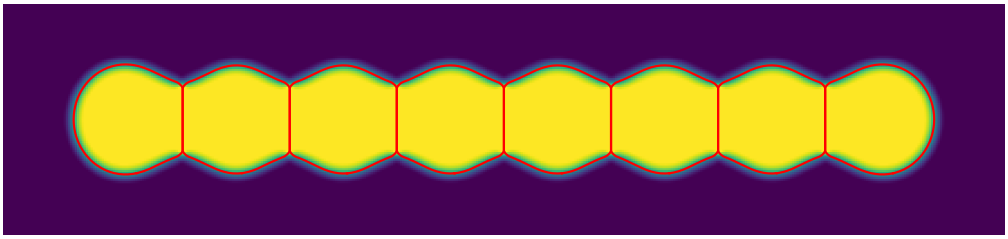

Figure 8.12: The grain field, defined by $1 - \phi_V$, at simulation end for 8 particles and model MDi. Yellow indicates the copper grains, dark indigo the surrounding vapour and green the interface between them. The phase transitions defined by the 0.5-isoline of the phases are represented with red lines.

is simply due to the inner particles being restricted from free movement, whereas the outer particles can easily adjust. This difference will also eventually lead to grain growth.

The chain ends being different can be somewhat mitigated by employing the rectangular grain geometry from the MD simulations and placing pores on the grain boundaries. It will not be fully mitigated, as the absorption rate still depends on the average surface chemical potential, which is different for end grains and for inner grains. However, as fig. 8.13 shows the convergence is sped up with this geometry for the MDi model, but the lack of convergence for ADV-μ becomes even more obvious. It should be noted that the MDi model eliminates the pores on the GBs at similar times, whereas model ADV-μ eliminates them step by step from the outer parts of the chain, with videos showing this being deposited with the Supplementary Material. This is also the reason for the different velocity magnitudes between the two models: Up to the point of pore elimination, the size of the pores in the simulations with model MDi is roughly comparable to that of the outermost pore of ADV-μ at the same time. Thus the pores for simulations with model MDi are on average smaller than for model ADV-μ which implies a larger driving force for vacancy absorption.

Based on these results, one can conclude that at about 16 particles in a one-dimensional chain the model MDi becomes representative. Presuming that this result extends to three-dimensions, one would expect representative simulations to start from about $16^3 = 4096$ particles. However, it is likely that the end geometry problem makes this a significant overestimation, and thus we proceed to three-dimensional simulations to test this.

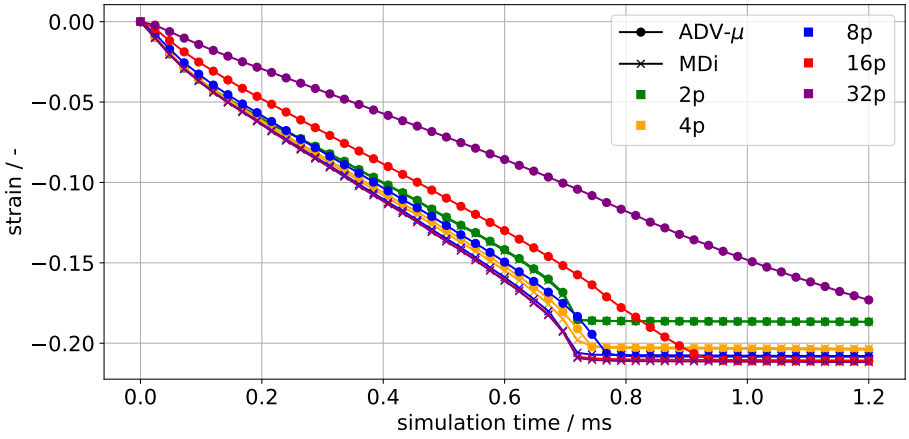

(a) strain over time

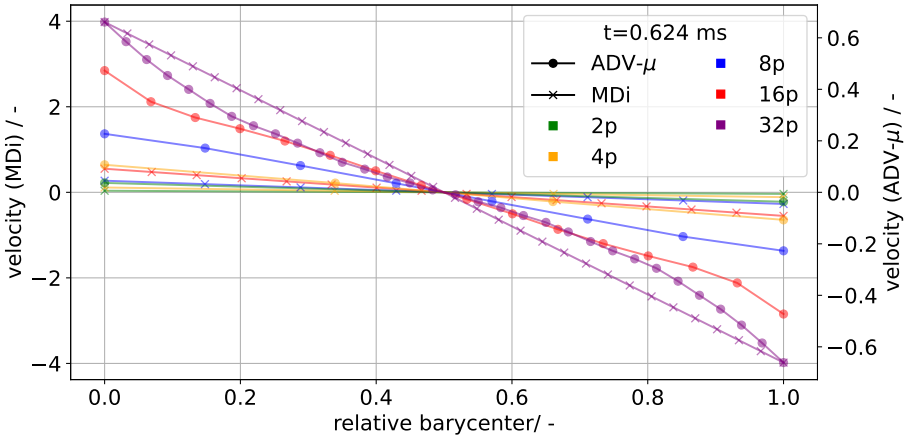

(b) velocity distribution

Figure 8.13: Comparison of the MDi model (crosses) and the model of [114] (circles) when employing the rectangular grain geometry. While the MDi model converges at around 8 particles in the chain, model ADV-μ does not converge at all. The velocity distribution shows that model ADV-μ tends to produce nonlinear velocity profiles.

8.2.4 Large scale three-dimensional simulations

The model will now be employed to simulate three-dimensional green bodies in order to determine representative volume elements (RVEs) by verifying that the densification is independent of the green body size. For this, the packings as described in [114] are employed: A voxel domain of size $N_v^3, N_v \in \{200, 400, 800\}$ is filled based on a packing generated with the discrete element method. In order to minimize boundary effects, it is ensured that there are at least 15 voxels between the outermost edge of a particle and the global boundary. All fields employ zero-flux conditions on the global boundary. The voxelization happens with a fixed number of voxels $R \in \{8, 12, 16\}$ used to resolve the particle radius, allowing the investigation of particle size effects with different simulations. Given the employed non-dimensionalization scales and discretization, these correspond to particles of size $R \in \{8, 12, 16\}$nm. Table 8.3 lists the number of grains N_g within each combination of (N_v^3, R), as well as on how many cores the simulations were run and for how long. Figure 8.14 shows one of the structures at different simulation times; videos of the entire process are deposited with the Supplementary Material. The left side shows a simple visualization of the entire green body, with the right side showing a fracture surface generated with a (011) plane and removing any grains beyond this plane. The mesh visualized here is based on a cellwise maximal value of the phase-field vector excepting ϕ_V. Contour levels $l > 0.5$ of this field cause an etching-like effect to appear starting from the highest order junctions[3]. A contour level of $l = 0.6$ is employed which entirely reveals the triple lines in the three-dimensional structure. In any case, both visualizations show the macroscopic densification of the body, with the fracture surface view also showing that the grains transform from spheres to polyhedra.

The evolution of the density is shown in fig. 8.15, with the present model as well as the results of [114] for a particle size of 12 nm. It can easily be seen that the present model shows highly similar density evolution over all the considered green body sizes. Only for $R = 16$ there is a slight effect of green body size from 200^3 to 400^3, with the following simulations being quite similar again. It is likely that rather than the green body size, a certain minimum number of particles should be contained within a three-dimensional packing, with that threshold lying between 97 particles (200^3, $R = 16$ nm) and 262 particles (200^3, $R = 12$ nm). The particle count likely acts as a proxy variable for whether the geometry is sufficiently homogeneous. Thus green bodies with a polydispserse grain size distribution will likely need a larger number of particles to be representative, but

[3] This can also cause grains on the edge of the packing to look only tenously or not connected at all.

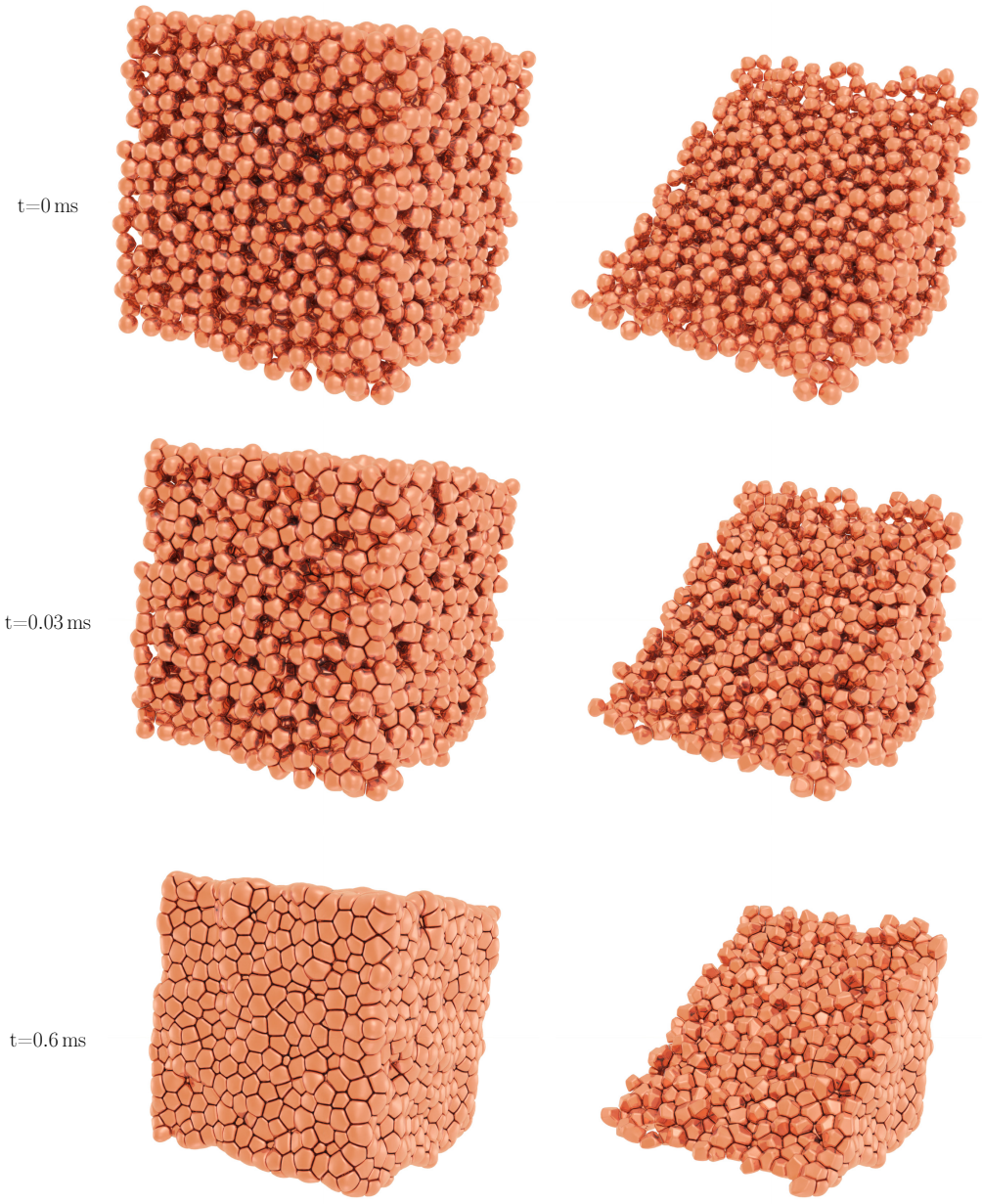

Figure 8.14: Three-dimensional view of the 400^3, $R = 12\,\text{nm}$ simulation for various times using Paraview[192]. The left side shows the entire green body, with the right side showing a (011) fracture surface from the same angle. The dark lines delineating regions can be interpreted as grain boundaries and higher order junctions. The dark smudges on some grains are due to the dark areas being reflected via ray tracing and thus not actually part of the simulation data. Both macroscopic densification and the polyhedralization of the grains are evident.

Table 8.3: Initial grain counts N_g for the employed packings as well as the number of cores C employed and the total runtime T. The longer runtime of larger particles is due to these being run for longer to achieve comparable densities.

N_v^3	R	N_g	C	T
200^3	16 nm	97	128	10.5 h
200^3	12 nm	262	128	8.00 h
200^3	8 nm	1033	128	4.70 h
400^3	16 nm	1361	512	21.7 h
400^3	12 nm	3445	512	16.0 h
400^3	8 nm	12418	512	15.6 h
800^3	16 nm	14113	8192	15.0 h
800^3	12 nm	34459	8192	9.20 h
800^3	8 nm	120132	8192	10.5 h

this will be left to future work. Furthermore, it is easily seen that densification progresses more slowly with larger grains.

Let us shortly revisit why the present model does not fail to reach a RVE: The necessary requirement for densification is for the divergence of velocity $\nabla \cdot v$ to be negative between volume elements. In advection models only employing nearest-neighbour interactions such as [33] and models based on it, the velocity of particles only depends on their immediate neighbours. Since within the green body proper, a grain's immediate neighbours will be similar, the neighbouring volume elements will be similar, with the exception of those volume elements containing the green body boundary. In contrast, in the MDi model the velocity of a single particle depends on *all* particles via solving eq. (8.13). Thus there is nothing forcing neighbouring volume elements to be similar. The simplification of using a linear ansatz for the particle displacement of course forces a constant $\nabla \cdot v$ between neighbouring volume elements. Given that solving the complete system for spatially uncorrelated absorption does result in the particle displacement being a linear function of position, this is quite justified.

The present results also allow to qualitatively test whether the geometries assumed in intermediate stage sintering are found. Coble's classical model [88] assumes a tetrakaidecahedron, i.e. a solid with 14 faces, for the grain shape. Thus the number of neighboring grains, also called the coordination number N_c, should tend towards 14. A more quantitative relation is given by German [100], based on a fit of literature data:

$$N_c = 2 + 11 f^2 \tag{8.24}$$

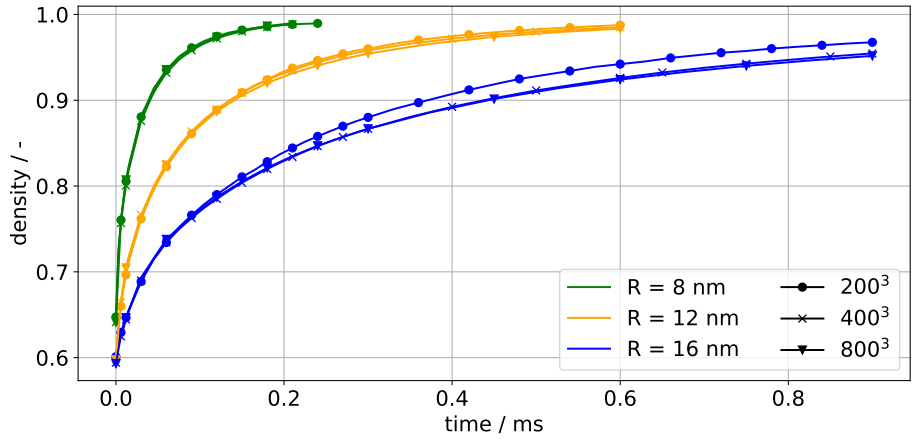

(a) present model MDi

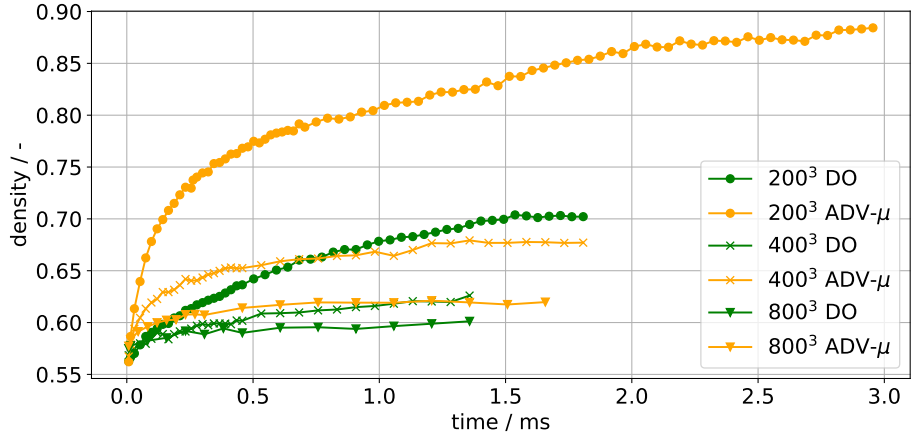

(b) results of [114] ($R = 12\,\text{nm}$)

Figure 8.15: Comparison of densification for the present MDi model and the results of [114] for a diffusion-only (DO) model and a model including advection (ADV-μ) based only on nearest-neighbour interactions. The results of [114] clearly have a strong dependence on domain size, which the MDi model eliminates once a RVE is reached.

with the fractional density f which is equivalent to the present usage of density. The average coordination number of all grains is plotted over density in fig. 8.16, showing a monotonic increase of coordination number with density. After correcting for surface effects, a coordination number of 14 is reached at around 99 % density. This includes the effect of many small contacts, which might not be detected easily in experiments. Hence there is a systematic deviation from German's fit, but the slope is quite comparable. If the fit is shifted vertically by a value of 1.1, which is roughly the difference in starting

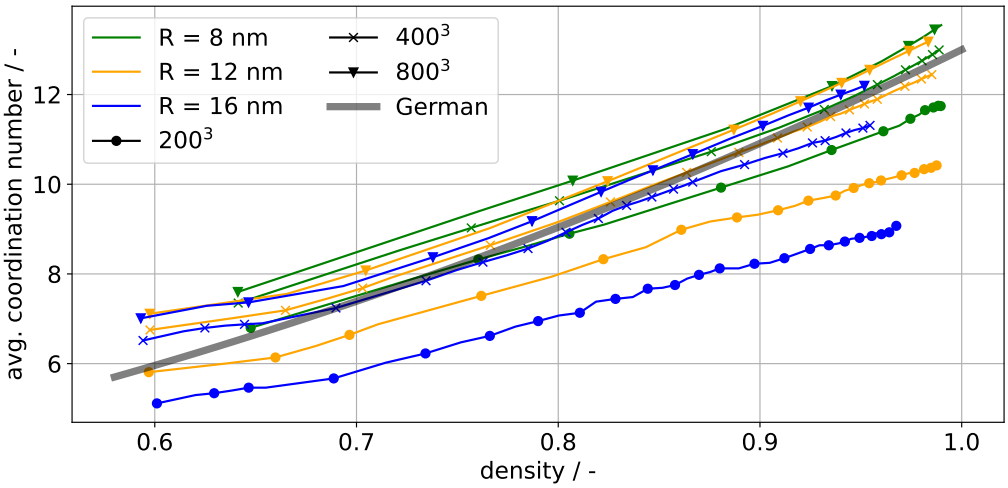

Figure 8.16: The Coordination number over density for all simulations as well as the relation of German eq. (8.24) are depicted. The coordination number rises monotonically with density, but shows a systematic deviation from German's relation. However, the slope of the curve is highly similar, as is shown by also plotting a vertically shifted version of German's relation.

coordination number at 60 % density, then a quite close match is observed. Conversely, the simulation data could also be filtered to exclude contacts with small surface area, also resulting in a reasonable match for higher densities. This is explored in [193] as choosing any one minimum surface area is quite arbitrary. In any case, based on both the experimental fit due to German and the present results, the tetrakaidecahedron shape assumption does not hold in intermediate stage sintering. It can however hold in the final stage.

8.3 Conclusion

In the present chapter molecular dynamics (MD) is employed to investigate the densification behaviour of a chain of grains. The grains are observed to move largely as rigid bodies, i.e. the atomic displacement within a single grain is largely uncorrelated to atomic position. Three rules of motion for this displacement are found: The displacement is proportional to the number of absorbed vacancies, antiproportional to the grain boundary area and superimposable if multiple vacancy absorption sites are present. These rules were used to construct an analytical model which agreed well with the MD results. Following this, a previously published phase-field model (ADV-μ) was extended

with this new model for calculating velocities (MDi). The previously published phase-field model and the new model are then compared in terms of their strain evolution within a linear chain geometry. For the MDi model, the strain as a function of time is observed to become independent of the number of grains between 8 and 16 grains in the chain, depending on the particulars of the geometry. Model ADV-μ did not converge, as previously shown by [114]. Finally, the model MDi is employed to sinter large-scale three-dimensional structures to determine representative volume elements. It is found that between 97 and 262 particles are necessary for densification to become independent of the green body size. Furthermore, the qualitative correct influence of particle size is included in the model, with green bodies consisting of larger particles sintering more slowly. Finally, reasonable agreement with a model linking the coordination number of grains to the density could be shown.

9 Revealing process and material parameter effects on densification via phase-field studies

This chapter is based on the author's preprint [116]. The following sections are taken verbatim from the preprint, with only minor linguistic and stylistic changes to account for the move from a preprint to a chapter in the present dissertation, as well as some clarifications due to the referees. Numerical details and relevant literature are also given in the preprint.

The goal of this chapter is to use the phase-field model which has been developed over the past chapters to sinter large-scale three-dimensional green bodies as to show the wide applicability of the method. First, the effects pressure and stress on grain boundaries' contribution to densification is shown following the model presentation in section 3.2.3. Next, the effects of mobility variations (diffusivity as well as interfacial mobilities) is investigated by a parametric study and using various quantifiers to put the results into the theoretical and experimental context. Finally, the phase-field model of freeze-casting presented earlier was used to calculate a three-dimensional freeze-cast structure, which is then computationally sintered. The parameters for all of these simulations, unless noted otherwise, are shown in table 9.1. The initial conditions for the simulations, unless noted otherwise, are the same as for the 400^3, $R = 12\,\mathrm{nm}$ simulation described in the previous section.

The short messages of the chapter are:

- theoretical prediction and experimental observations are matched by the presented addition of stress
- agreement with trends based on theory and experiment over a large range of quantifiers (density, surface area, grain size, Euler characteristic) is shown
- for reaching full density, surface diffusion is always detrimental and grain boundary diffusion is always beneficial

- grain shapes during intermediate stage sintering generally do not approximate the truncated octahedron suggested by Coble

Table 9.1: Employed physical and numerical parameters for the simulations.

parameter	nondim. value	physical value
numerical parameters		
grid spacing Δx	0.1	$1 \times 10^{-9}\,\mathrm{m}$
max. time step Δt_{max}	1.5×10^{-5}	$1.5 \times 10^{-9}\,\mathrm{s}$
interface parameter ϵ	$4\Delta x$	$4 \times 10^{-9}\,\mathrm{m}$
interface width $W \approx 2.5\epsilon$	$10\Delta x$	$10 \times 10^{-9}\,\mathrm{m}$
grain boundary cutoff $\phi_{\alpha\beta}^{min}$	0.14	-
physical parameters		
surface energy $\gamma_{v\alpha}$	2	$2\,\mathrm{J\,m^{-2}}$
grain boundary energy $\gamma_{\alpha\beta}$	1	$1\,\mathrm{J\,m^{-2}}$
volume diffusion D	1×10^{-3}	$1 \times 10^{-15}\,\mathrm{m^2\,s^{-1}}$
grain boundary diffusion $D_{gb,0}$	55	$5.5 \times 10^{-11}\,\mathrm{m^2\,s^{-1}}$
surface diffusion $D_{s,0}$	169	$1.69 \times 10^{-10}\,\mathrm{m^2\,s^{-1}}$
physical interface width δ_i	0.02	$2 \times 10^{-10}\,\mathrm{m}$
surface inverse mobility τ_{gv}	0.08	$8 \times 10^{10}\,\mathrm{J\,s\,m^{-4}}$
grain boundary inverse mobility τ_{gb}	variable	variable
atomic volume Ω	1.22×10^{-5}	$1.22 \times 10^{-29}\,\mathrm{m^3}$
GB relaxation time t_r	1×10^{-8}	$1 \times 10^{-12}\,\mathrm{s}$

9.1 Sintering under stress

The first foray will consider the influence of stress on sintering, as it is quite simple but also important for densification. Pressure is often applied during sintering in order to either speed up densification or to remove isolated/detached porosity by forcefully dissolving the contained gas into the material. In this section the former effect is investigated by considering the effect of the applied stress on the equilibrium concentration of vacancies on grain boundaries. This effect can be easily included in the model of [115] as shown in section 3.2.3.

The pressures $p \in \{0, 50, 100, 200\}$MPa will be considered. The scale of the pressure is based on the magnitude of the capillary pressure $O(p_c) \sim O(\frac{\gamma_s}{r}) \approx 100\,\mathrm{MPa}$ with the

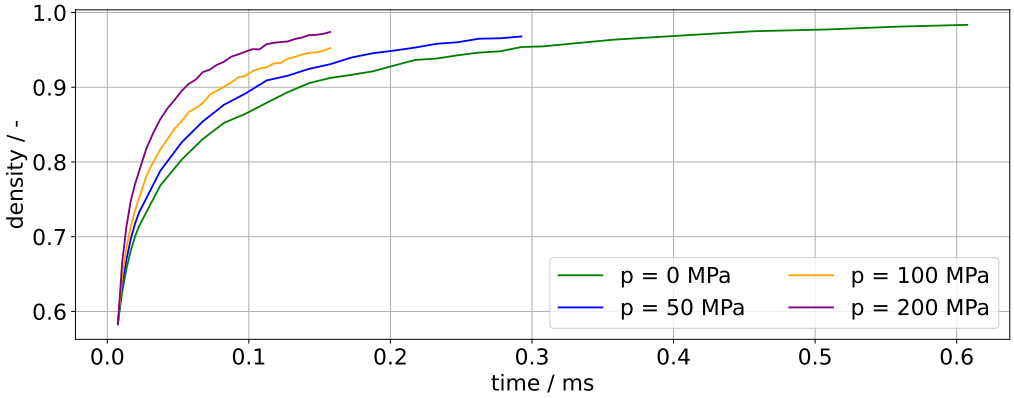

(a) time evolution of density for various pressures

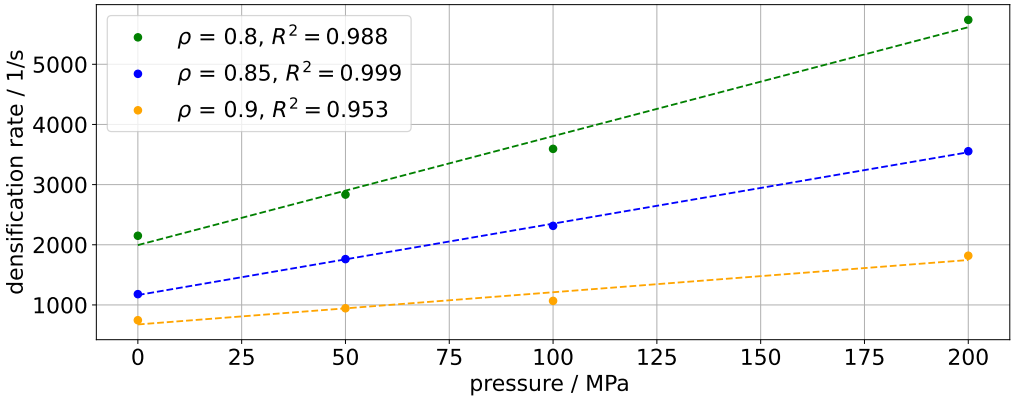

(b) pressure influence on densification rate

Figure 9.1: The influence of pressure on the density evolution is depicted in (a), with its influence on densification rate depicted in (b). With rising pressure, quicker densification is achieved. The dashed lines in (b) indicate linear fits with coefficient of determination R^2 given in the legend. There is a roughly linear relationship between pressure and densification rate as also experimentally observed by [194].

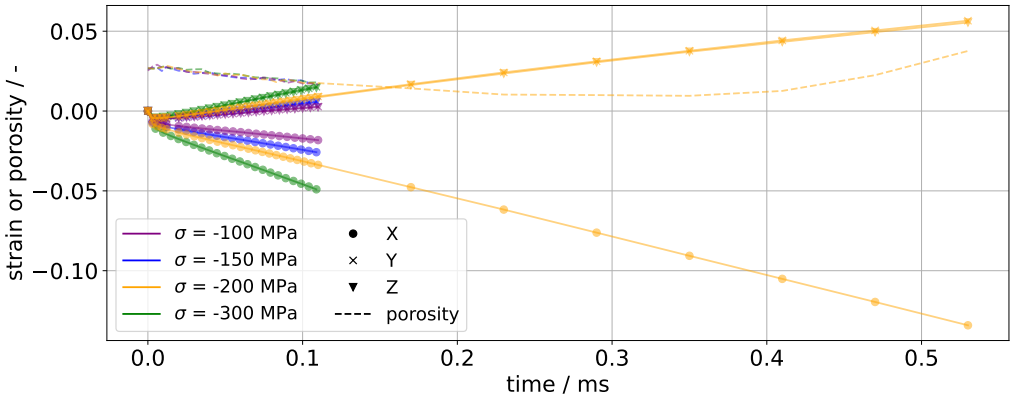

Figure 9.2: Strain and porosity evolution for several creep simulations, with tensile stress being applied in the X direction. After an initial transient, a constant strain rate is observed, characteristic of secondary creep.

surface energy γ_s and the particle radius r. The resulting density over time is shown in fig. 9.1a, with increasing densification rate with higher pressures. In order to determine the qualitative relationship between pressure and densification, the densification rate of the individual simulations is calculated at test densities of $\rho \in \{0.8, 0.85, 0.9\}$. For this, the numerical densification rate, i.e. the slope in fig. 9.1a is calculated, followed by an interpolation across its density space, which then allows the calculation of densification rates at any density within the valid density range. This yields fig. 9.1b which shows a roughly linear relationship between densification rate and pressure, as also observed by experiments [194]. Classical theory e.g. due to Coble [131] also predicts a linear relationship between external pressure and densification rate. Hence this simple addition of pressure compares well against both experiment and theory.

As sintering and creep are intimately related processes, any model of solid-state sintering should also be able to approximate creep. The present model can achieve this by setting the stress to be uniaxial, which will cause vacancy generation on grain boundaries aligned with the tensile stress direction. Four tensile tensile stresses $\sigma \in \{-100, -150, -200, -300\}$MPa in the X direction are considered, with $\sigma = -200\,\mathrm{MPa}$ being run longer than the others to show porosity increase. The simulations are conducted by starting from an almost dense (97%) sintered body produced by prior simulations. The evolution of normal strain in the coordinate directions as well as porosity are shown in fig. 9.2: The samples lengthen (negative strain) in the X direction and shrink in the Y and Z directions, with the Y and Z strains effectively overlapping. After an initial transient, the strain is observed to be a linear function of time as expected of secondary creep. The steady strain rate is observed to be linearly dependent on the applied stress,

as is expected of Coble creep [195]. Porosity is reduced at first, but with sufficient time, the porosity rises and would eventually lead to failure. This suggests that the model extension successfully models the stress dependence of Coble creep.

9.2 Coupling grain growth and densification

Densification and grain growth are intimately related and thus the concurrent simulation of both is of paramount importance for quantitative simulation of sintering. In this section, these coupled processes are investigated by parameter variations of the relevant mobilities. The mobility of an interface is controlled with the inverse mobility τ, for which high values imply low mobility. For the grain-vapor interface a small value of τ_{gv} is chosen such that the evolution is diffusion-controlled. For the grain-grain interfaces, two different values of the inverse grain mobility τ_{gb} are chosen, with their values also serving as simulation labels: Kinetically suppressed grain growth is achieved with $\tau_{gb} = 100\tau_{gv}$ and unsuppressed grain growth with $\tau_{gb} = \tau_{gv}$.

For each of these mobility variations, different diffusion coefficients will be tested. The base case is that of table 8.2, with variations on the surface diffusivity D_s and the GB diffusivity D_{gb} by simple factors, with the factors being chosen arbitrarily. The full set of investigated diffusivity combinations is

$$\{(D_{gb,0}, D_{s,0}), (D_{gb,0}, 0.1D_{s,0}), (D_{gb,0}, 0.01D_{s,0}),\\ (0.1D_{gb,0}, D_{s,0}), (0.1D_{gb,0}, 0.01D_{s,0})\}$$

with the color scheme being used consistently to identify the simulations. The base case $(D_{gb,0}, D_{s,0})$ is identified explicitly, with departures from it being used as labels with the appropriate color. The surface to GB diffusion ratio in the base case of $\frac{D_{s,0}}{D_{gb,0}}$ is about 3, with this being varied from about 1/30 to 30 with the employed factors.

A qualitative, visual comparison of some of these results is given in fig. 9.3 showing the GB network (blue) as well as isolated (grey) and detached porosity (red) for selected densities. It can easily be seen that in the base case without grain growth (left), no pores are detached. For otherwise the same parameters (middle), allowing grain growth leads to a significant fraction ($\approx 80\%$) of detached porosity. Finally, if the GB diffusivity is reduced (right), then densification slows down significantly and within the allotted simulation time the maximum reached density is about 82%, whereas both simulations with quick GB diffusion achieved at least 99% density. As an exemplary quantification, the time to reach 80% density is increased by a factor of 33 even though the GB diffusion

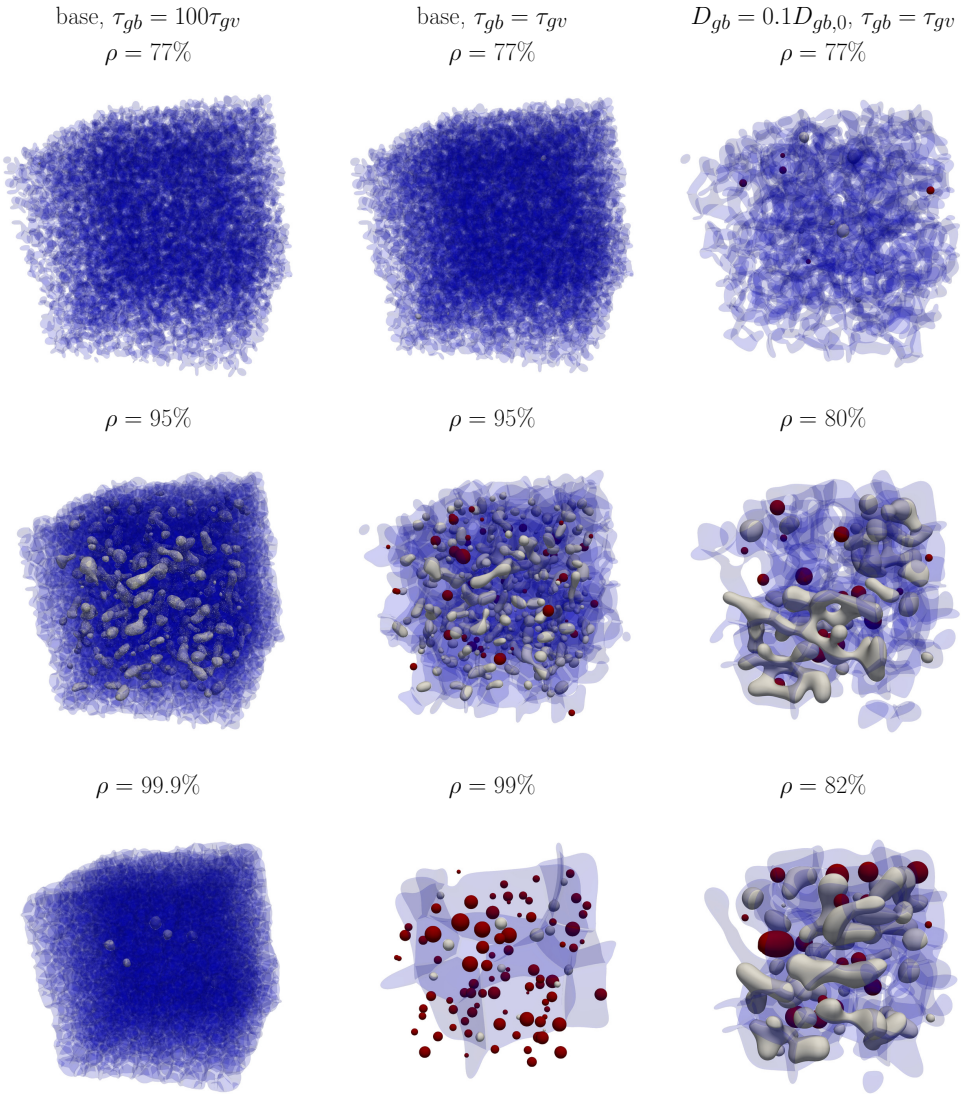

Figure 9.3: Comparison of simulations with suppressed grain growth (left), with grain growth (middle) and a simulation with grain growth and reduced GB diffusivity (right). The GB network is shown in transparent blue, isolated porosity in grey and detached porosity in red. The depicted states were chosen based on their density and can represent different times.

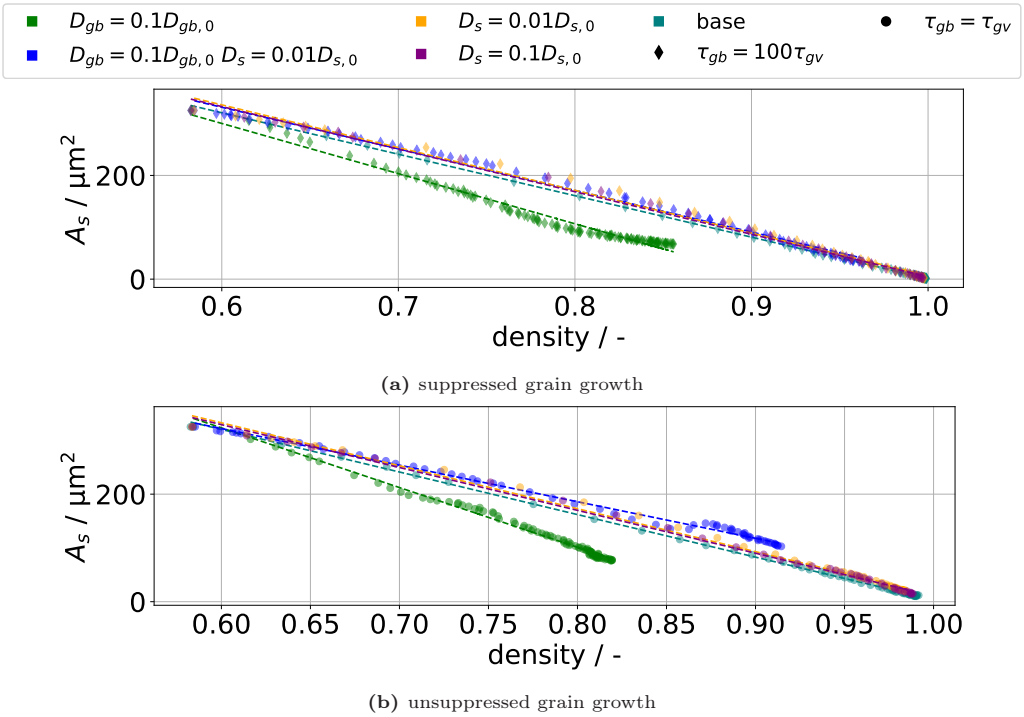

(a) suppressed grain growth

(b) unsuppressed grain growth

Figure 9.4: The relationship between surface area and density is observed to be roughly linear, with the dashed lines indicating best fit linear functions.

was only reduced by a factor of 10. From these images it should also be clear that even at the same density, microstructures need not be comparable. Rather, these are the complex product of the temporal interplay of densification, pore destabilization and grain growth, with a single variable being unable to capture the full picture. Videos of the time evolution, also showing a kind of Plateau-Rayleigh instability of isolated pore channels, are deposited with the supplementary material at [196].

Let us start the quantitative investigation by considering the evolution of surface area with density, as the reduction of surface area is the driving force for densification. It is often observed [46, 101, 197] that surface area and density are linearly related during sintering. This relationship is demonstrated in fig. 9.4 for simulations with and without suppressed grain growth separately. The legend employed will be the same for all following plots, with colors indicating variations in diffusivity and symbols indicating suppressed grain growth (diamond) or unsuppressed grain growth (circle). The main point however is that regardless of the employed parameters, a linear relationship is observed.

The linear fits' (dashed lines) coefficient of determination $R^2 > 0.98$ also shows this in a quantitative manner. Therefore, the model's densification behaviour is in qualitative accordance with experiments. Local deviations, such as for the blue circles, are mostly due to either a change of sintering stage or the onset of grain growth. Hence next the density and grain size evolution will be considered.

The simulation measurements in terms of density ρ, grain size G and GB area A_{gb} are collected in fig. 9.5. Focus first on the diamonds in fig. 9.5a: These represent the density of simulations with suppressed grain growth. The base case (teal), as well as the simulations in which only surface diffusion D_s is reduced (purple, orange), have essentially the same densification behaviour. This is due to vacancy absorption happening fast enough that surface diffusion contributes relatively little to neck growth compared to vacancy absorption. There is a small effect of reduced densification rate with reduced surface diffusion up to $\approx 90\,\%$ density, after which the densification rate with reduced surface diffusion is larger. This density-dependent influence of the surface diffusion is likely due to the inversion of the surface mass flux observed by Luo et al. [198]. In contrast, decreasing the GB diffusion D_{gb} (green) significantly reduces the densification rate throughout the process. In this case a significant amount of neck growth is due to surface diffusion filling the neck without concomitant vacancy absorption. Hence decreasing the surface diffusion (blue) for this case does significantly speed up densification ($\approx$ factor 3 less time to 80% density), though not to the original levels. The two simulations with reduced grain boundary diffusion (green, blue) will also henceforth be called slowly densifying, in contrast to the quick densification exhibited by the remaining simulations.

Focus now on the effect of grain growth on densification by comparing the circular symbols (unsuppressed grain growth) and the diamonds (suppressed grain growth) in fig. 9.5a: For the quickly densifying simulations there is hardly any influence on the density evolution. This is due to densification happening so quickly that grain growth only really starts past about 90% relative density. Grain growth however does lead to pores detaching from the GBs, which at the end of the simulations causes about 1% porosity to remain in a detached state. As before, decreasing the GB diffusion causes a significant slowdown of densification, with grain growth further limiting the achievable density for a fixed time. Since grain growth has a significant effect on these, it will be discussed next.

The grain size evolution is depicted in fig. 9.5b. Comparing the base case (teal) with only reduced surface diffusion (purple, orange) shows a slight reduction of grain growth via pore drag, since pore motion is limited by surface diffusion. The effect is not particularly pronounced due to the quick densification removing pores quickly as well. Pore drag becomes much more evident when comparing the quickly densifying simulations to the

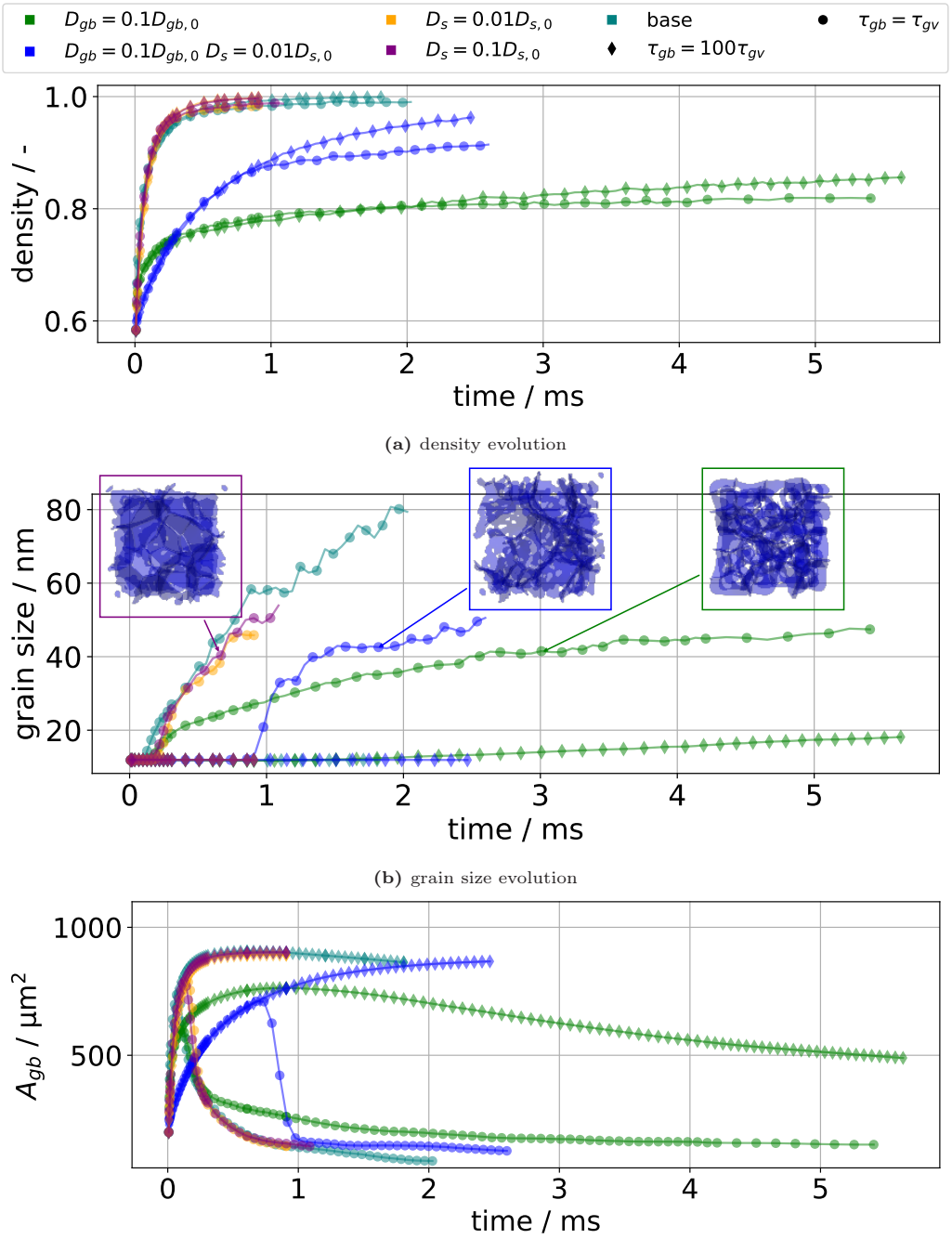

(a) density evolution

(b) grain size evolution

(c) GB area evolution

Figure 9.5: The influence of grain growth and variable interfacial diffusivity on densification (a), grain size (b) and total GB area A_{gb} (c). The GB networks (blue) for three simulations are shown as insets in (b) for similar grain sizes, with white space within the image indicating porosity.

slowly densifying ones: As densification proceeds more slowly, more pores will be present at the same time and hence grain growth is slowed down. Unexpectedly, when in addition to reducing the GB diffusion the surface diffusion is reduced as well, grain growth starts much later in term of time and density. This is likely due to the sintering neck being formed only slowly in this case ($D_{gb} = 0.1D_{gb,0}$ $D_s = 0.01D_{s,0}$, blue), which also suppresses grain growth: The flux of atoms leading to grain growth is the contact area times the flux density. The flux density is due to curvature differences between grains and will be roughly comparable between simulations prior to the start of grain growth, as the initial conditions are the same. The contact area evolution differs significantly however, as is shown in fig. 9.5c by identifying it with the GB area A_{gb}. The simulation $D_{gb} = 0.1D_{gb,0}$ $D_s = 0.01D_{s,0}$ (blue) indeed shows much slower GB area growth. For this particular simulation, once a few grains have achieved a sufficient neck size, these grow rapidly (up to 6 times the mean grain size) until they are slowed down by porosity again, leading to stagnant grain growth for a short interval. This heavier porosity loading on grain boundaries is shown via the insets in fig. 9.5b, which show the GB network for similar grain sizes: Both simulations with reduced GB diffusivity show increased porosity on grain boundaries, with their grain growth hence being more significantly affected by pore drag.

In order to quantify grain growth with respect to experiments, the grain growth law is evaluated by fitting the grain size G data for $G > 13\,\mathrm{nm}$ to power laws of the form $G = At^n$, with the plots showing the results being deposited with the supplementary material [196]. The grain size filter is employed to fit only the regime where grain growth is taking place. Exponents ranging from about $\frac{1}{3}$ to $\frac{4}{5}$ are observed; the experimentally observed range is $\frac{1}{4}$ to $\frac{1}{2}$ [20]. The simulations with $D_{gb} = 0.1D_{gb,0}$ show values close to $\frac{1}{3}$ which is often experimentally observed and can be due to pore drag. The simulations showing $n > \frac{1}{2}$ are likely due to the start of grain growth significantly deviating from the rest of the curve. For example, if the data is filtered to $G > 20\,\mathrm{nm}$, then these exponents move appreciably closer to $\frac{1}{2}$, whereas $D_{gb} = 0.1D_{gb,0}$ achieves $n = \frac{1}{3}$. Hence filters for larger grain sizes will cut off more of the initial regime, but also include more data in the regime of low grain numbers. Ideally a larger system containing more grains and hence capable of reaching steady state would have been simulated. But since the primary goal was investigating densification, a too small number of grains was chosen for the initial conditions.

Based on these observations, one may conclude that below a certain ratio of $\frac{D_s}{D_{gb}}$, densification will proceed unhampered by surface diffusion. The coarse spacing of the ratios of the present investigation does not allow a particularly accurate estimate of the critical ratio, but it should be in the interval $[1, 10]$, i.e. GB diffusion should at worst be only

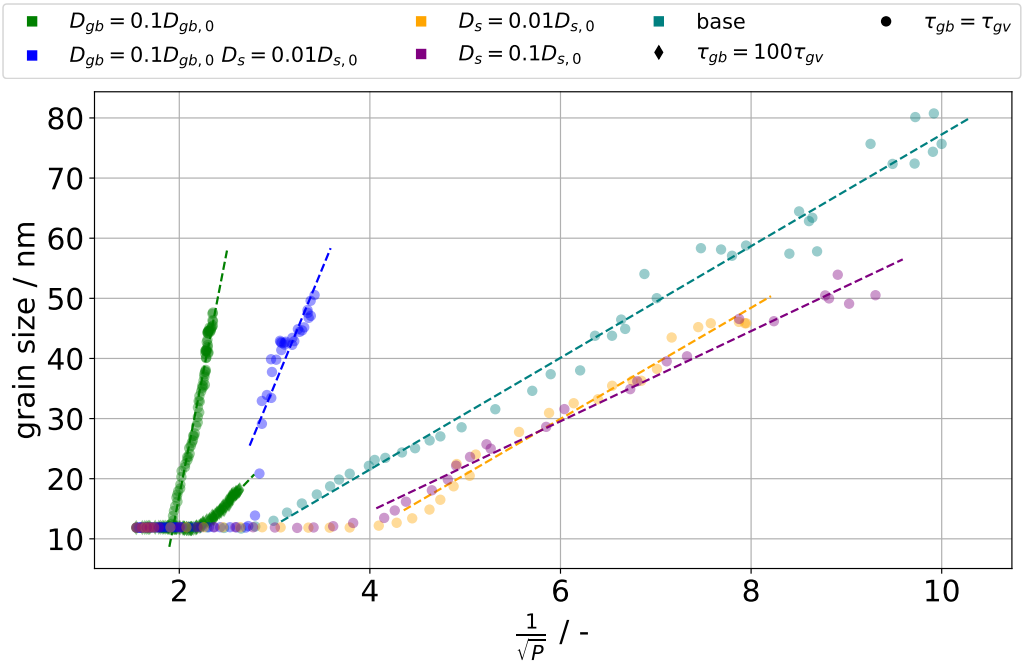

Figure 9.6: The inverse square root of porosity P is plotted against the grain size G. Once grain growth starts, a rather linear relationship is observed; the dashed lines indicate fits to data with $G > 13\,\text{nm}$ to account for this.

a magnitude slower than surface diffusion. Otherwise surface diffusion will inevitably account for major parts of neck growth and hence reduce the achievable density. Given that surface diffusion and GB diffusion are similar in their grain size dependence following Herring's scaling law, this should also extend to larger particle sizes and when grain growth occurs. At some point, however, volume diffusion becomes, in terms of total mass transported, relevant w.r.t. the interfacial fluxes as it is less affected by grain size.

Let us close the classical consideration by verifying the experimentally observed linear relationship between grain size and the inverse square root of porosity $G \propto \frac{1}{\sqrt{P}}$ [46] with $P = 1 - \rho$. This relationship is plotted for the simulations which exhibited grain growth ($G > 13\,\text{nm}$ at any point) in fig. 9.6 and shows a quite linear character once grain growth has started. This is quantified with linear fits, whose coefficient of determination is generally $R^2 > 0.97$, except for $D_{gb} = 0.1D_{gb,0}$ $D_s = 0.01D_{s,0}$ ($R^2 \approx 0.75$) with its stagnating grain growth. The scatter at high densities $\rho = 98\% \sim \frac{1}{\sqrt{P}} \approx 7$ is due to the density measurement being affected by surface roughness of the green body, which is effectively counted as open porosity. However, at this stage there are no pore channels

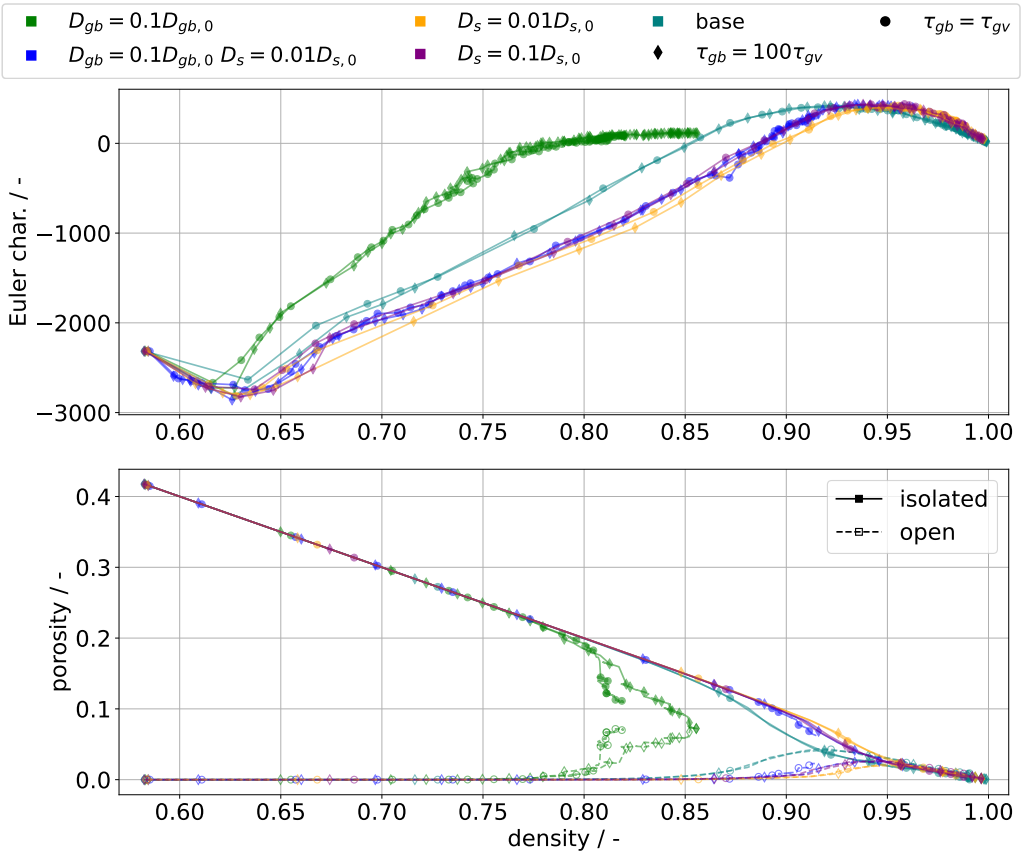

Figure 9.7: The Euler characteristic χ shows qualitatively similar behaviour compared to experimental data [101, 102]. Its evolution is influenced by both GB and surface diffusion, with little effect from grain growth.

left on the green body's surface, hence any "porosity" counted near the surface is a measurement error.

Besides the classical quantities of density and grain size, the microstructure can also be characterized via its shape. An integral approach to this characterization is the Euler characteristic χ of the pore space, which can be used to distinguish stages of sintering [101, 102]: The initial stage is characterized by a negative and decreasing value, with the intermediate stage continuously increasing the value up to a positive maximum value. In the final stage, the characteristic decreases towards zero for infinite time, representing a fully dense structure. The Euler characteristic is plotted over density in fig. 9.7 for the present simulation set and good accordance to the expectations is observed. Note that

grain growth has little effect on the evolution of the characteristic, since the symbols generally overlap. It is however influenced by GB diffusion via densification speed and by surface diffusion because it determines the time scale of pore evolution. In order to verify the suggestion of [102] that the maximum of χ indicates the final sintering stage, the bottom part also shows open and closed porosity separately over density. Assuming that the start of the final stage is given by the equality of isolated and open porosity, the suggestion is confirmed for the present simulations. Furthermore, it can be observed that isolated porosity is formed more slowly with lower surface diffusion. This is simply due to the pore instability being mostly limited by surface transport. Fast densification also has an apparent pore instability suppressing effect, since $D_s = 0.01 D_{s,0}$ (orange) has generally less isolated porosity than $D_{gb} = 0.1 D_{gb,0} D_s = 0.01 D_{s,0}$ (blue) at the same density. The likely origin of this is that densification progresses rapidly enough that the time to destabilization isn't reached before the pores are eliminated.

An approach which allows a more granular shape description is the calculation of shape factors characterizing individual objects. The factors employed are those of MacSleyne et al. [199] employing second moments of the mass distribution of the object to characterize its shape. These have three invariants $\widetilde{\Omega}_i$, $i \in \{1, 2, 3\}$, which are characteristic for a fixed shape e.g. a sphere, a tetrahedron or the truncated octahedron (tetrakaidecahedron) suggested by Coble [88] for modelling the intermediate and final stage grain shape. The invariants can be normalized to a specific shape s, $\Omega_i = \frac{\widetilde{\Omega}_i}{\widetilde{\Omega}_{i,s}}$, and thus the distance from this shape is related to how far from the value of 1 the normalized invariant Ω_i is. The sphere is chosen as a reference shape and the normalized variants are collected in a vector Ω. In order to summarize the invariants, we introduce the lumped invariant employing the Euclidean norm $\Omega_E = \frac{||\Omega||}{\sqrt{3}}$ of the vector Ω. The factor of $\sqrt{3}$ stems from the use of the Euclidean norm, such that $\Omega_E = 1$ still represents a sphere; the value itself can be interpreted in the same way as the components Ω_i. The invariants are separately calculated for the grains, isolated pores and detached pores, with the detached pores forming a subset of the isolated pores. Hence if only detached pores remain, their invariants will be the same as for the isolated pores.

The mean of Ω_E is plotted over density in fig. 9.8 for the separate structures. The standard deviation was also calculated, but in general it is quite large and hence would obscure the evolution. It was ensured that there are at least 5 objects of which the mean is calculated, as otherwise the initial trajectory is dominated by small, short-lived pores for the pores.

Focus first on the evolution of the isolated and detached pores: At high densities, reached by simulations with high GB diffusivity, both tend to $\Omega_E = 1$, which is consistent with

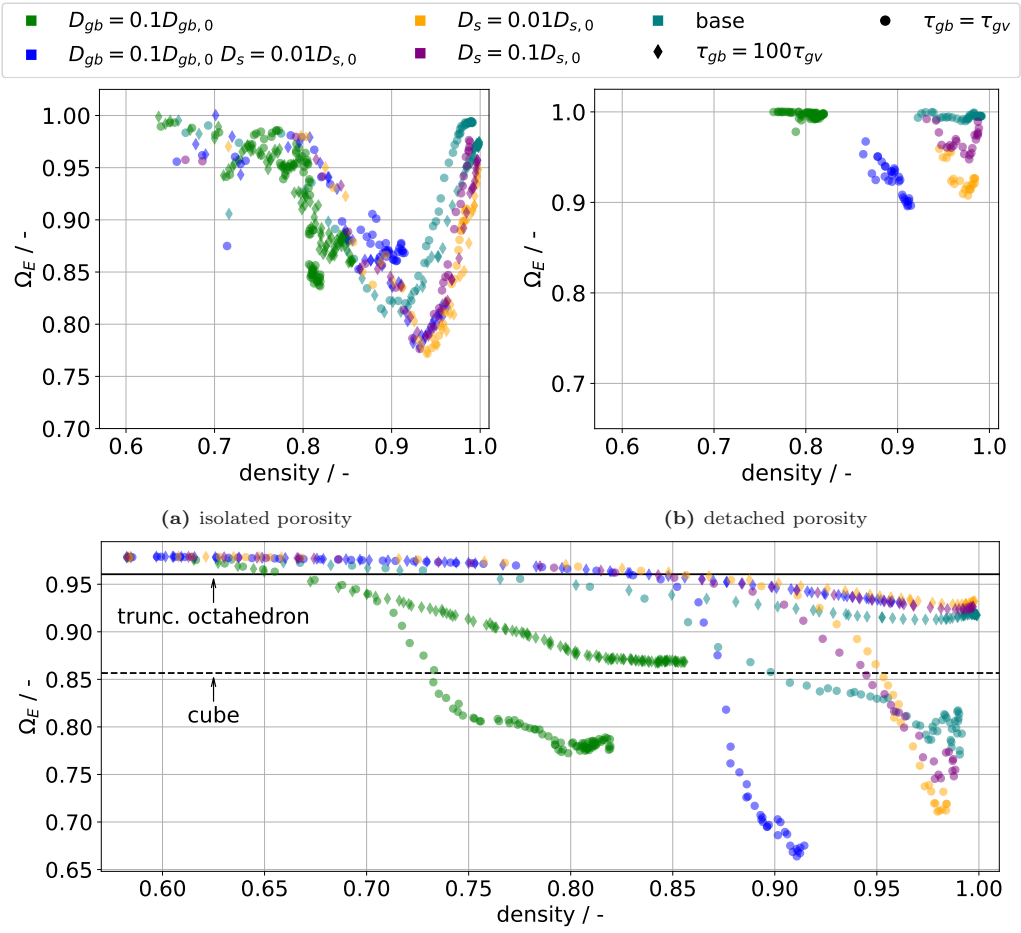

(a) isolated porosity

(b) detached porosity

(c) grains

Figure 9.8: The lumped invariant $\Omega_E = \frac{||\Omega||}{\sqrt{3}}$ of the normalized invariant vector Ω is plotted over density for all simulations, with the structures of isolated and detached porosity as well as the grains being shown separately. Given sufficient densification, the porosity tends to approximate spheres, i.e. $\Omega_E = 1$. The steady invariants for the grains depend on densification rate and grain mobility, with the latter influence likely due to finite size effects.

curvature minimization. The transitory period shows a non-monotonic behaviour, likely attributable to isolated networks of pores first forming, then splitting into single pores via Plateau-Rayleigh-like instabilities. These instabilities are likely induced via grain boundaries since this is typically faster than instability growth from perturbations. [90]. Since the timescale for this instability is dependent on the surface diffusion, the convergence to a spherical shape is also slower for reduced surface diffusion. High grain mobility allows pores to detach and afterwards spheroidize within the grains. This causes the invariant for the simulations with high grain mobility (circles) to generally be closer to that of the sphere than for those without, since pores on grain boundaries deform to reach the proper dihedral angle. In the slowly densifying cases (low GB diffusivity), the isolated pore networks still remain and tend to dominate the shape factor. Note that an entire pore network can become detached from the GB network, which significantly slows down its destabilization to isolated spheres. Hence apparently isolated porosity in 2D micrographs might very well be the same pore.

Focus next on the evolution of the grain structures: From the initial somewhat spherical shape, a mostly monotonic decrease is observed, with the speed being related to both interfacial diffusivities and the grain mobility. The dashed black line indicates the cube's invariant, with the solid black line indicating the truncated octahedron's invariant. All simulations pass the truncated octahedron's invariant, but do not converge towards it. One might argue that pore-laden structures have a different invariant compared to the pore-free structure. But even for the base case without grain growth, in which only few pores remain at the end, a value significantly different, i.e. $\approx \frac{1}{3}$ of the distance between a sphere and a cube, from that of the truncated octahedron is observed. Experimental observation of the annealing of dense ($\approx 99\%$) strontium titanate [200] also indicate that real grains do not show the invariants of the truncated octahedron, though these of course also have effects from crystalline anisotropy. Together with the evolution of grain coordination number before the final sintering stage [100, 115], this suggests that the assumption of truncated octahedra being representative of the grain structure during intermediate stage sintering should be dropped. However, the present results do not allow a constructive suggestion for a replacement shape. The generation of shapes from invariants, while possible, usually requires invariants of higher order moments as shown in [201]; furthermore, these shapes are likely not as analytically tractable as the truncated octahedron. Hence while the truncated octahedron is not a satisfactory approximation for the grain shape during intermediate stage sintering, it can still be used in geometric modelling while being aware that prefactors derived from it will likely be wrong.
As a final note, the invariants for simulations with unsuppressed grain growth will be affected by the initial green body shape in their later stages. This is due to the few

leftover grains approximating the original green body shape. Therefore, the grain invariants' values in the later stages with unsuppressed grain growth should not be taken at face value. The plots of the unlumped invariants, generally showing similar trends, are deposited with the supplementary material [196].

9.3 Sintering of structures produced by freeze-casting

Freeze-casting [45] is a novel process for the production of porous materials as well as near net shape casting. A suspension of a liquid, usually water and hence assumed thus, and a target material is mixed and frozen, resulting in a microstructure of the target material and ice. The ice is sublimated next, leaving a porous structure which is then usually sintered, completing the freeze-casting process chain. A previously developed model for the phase-field simulation of the freezing part of freeze-casting [202] is employed to generate a three-dimensional freeze-cast structure. The volume fraction of target material is known for each cell of the domain and is employed to generate a sphere packing approximate the freeze-cast body. Where a sufficient volume fraction is reached, spheres of $r = 8\,\mathrm{nm}$ are placed into a domain, approximating the continuous volume fraction field with a discrete packing of spheres. The freeze-casting simulation itself employed particles of radius 250 nm, with the change in sphere radius being for computational efficiency, as smaller particles will sinter faster; this does mean however that a smaller version of the actual structure is sintered next. The space of low volume fraction is left empty, producing macropores, and thus a rough approximation of the sublimation process is achieved. Finally, the resulting sphere packing is computationally sintered with the present model to completely simulate the process chain of freeze-casting for the first time ever.

The resulting microstructural evolution over time is shown in fig. 9.9. On the left the entire structure is shown, with grains being rendered as a copper-like material, since the materials parameters of table 8.2 approximate copper, and the dark lines within the structure represent grain boundaries and higher order junctions. As can be seen, even a complex, inhomogeneous structure can be sintered with the present model. Furthermore, some grain growth has occurred as would be expected from the low grain size. At the end of the simulation run, the particulate region is completely dense, with no isolated porosity remaining and no pore channels penetrating through the structure. On the right, a fracture surface is shown together with a rough approximation of the porosity, rendered with a water-like apperance. This porosity is continuously reduced, with many

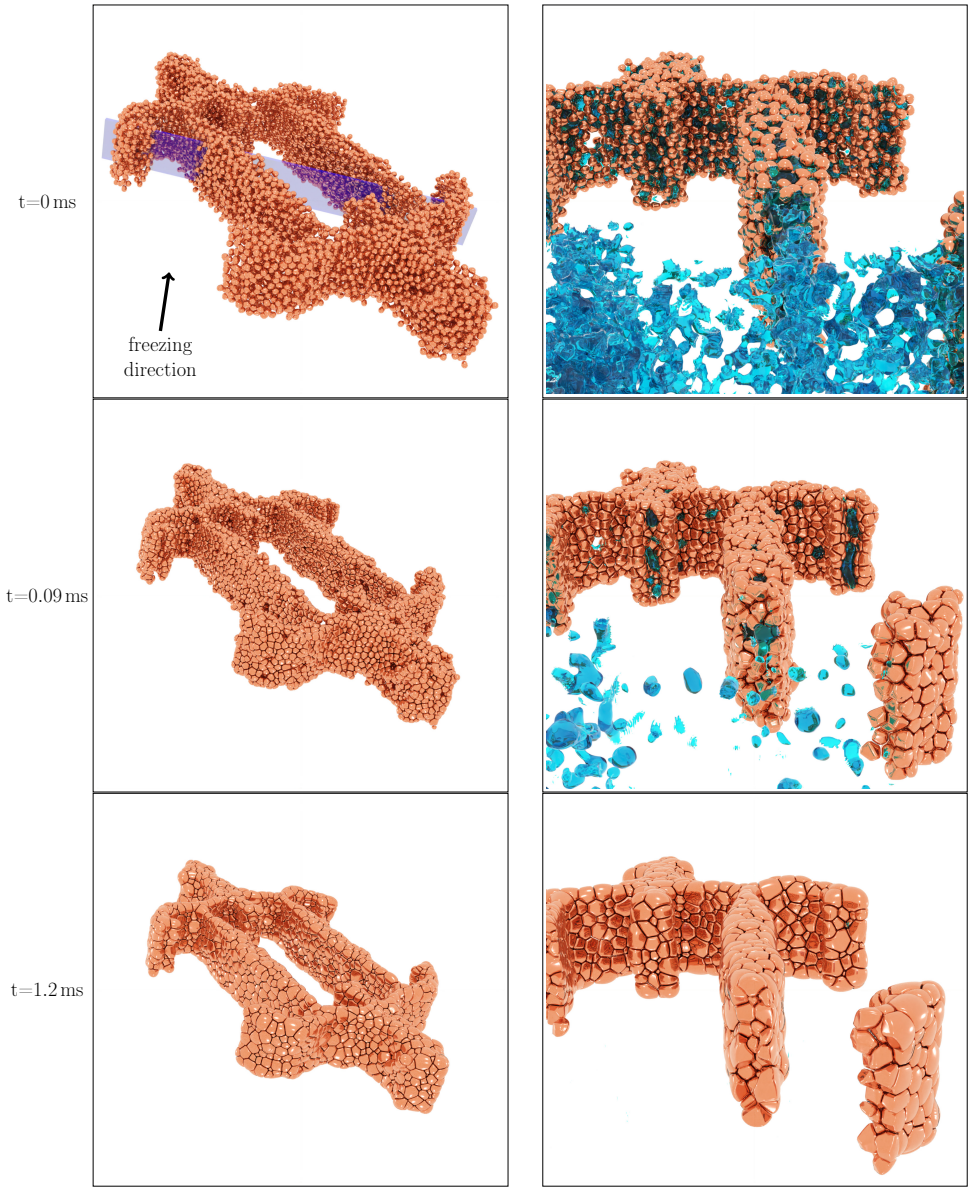

Figure 9.9: A freeze-cast structure with a macropore undergoing sintering. The structure itself shrinks while keeping the macropore intact. On the right a close-up for a fracture surface normal to the Y direction, also indicated by the blue plane at $t = 0\,\mathrm{ms}$, is shown, including a rough approximation of the porosity rendered with a water-like appearance. It can easily be seen that the porosity within the walls changes substantially between $t = 0\,\mathrm{ms}$ and $t = 0.09\,\mathrm{ms}$, with many grains already having eliminated their surrounding porosity.

grains already having eliminated their surrounding porosity at $t = 0.09\,\mathrm{ms}$, which limits their further contribution to densification. Note that almost no vertical motion is evident between $t = 0.09\,\mathrm{ms}$ and $t = 1.2\,\mathrm{ms}$. Densification in this direction has stopped at about $t = 0.09\,\mathrm{ms}$ and only the directions normal to it continue to densify. The surface in this direction also tends to have fewer grains, allowing these to bulge out more and thereby influence the strain measurement.

The shrinkage is characterized with the strain in each spatial dimension, which is found to be anisotropic: In the freezing direction, upwards and parallel to the macropore, a shrinkage of about 10 to 13% is observed, but in the directions normal to it, a shrinkage of 16 to 19% is observed. The strain range is due to inhomogeneous strain measurements. Experimental evidence of anisotropic shrinkage after freeze-casting exists [203, 204], but the experiments disagreed on which direction shrinks less. Farhangdoust et al.[203] observed that the freezing direction shrunk less, comparable to the present results. However, as Lichtner et al.[204] note, Farhangdoust et al. may not have removed the initial, isotropic structure generated by freeze-casting and neither the continuous skin formed on the outside of a freeze-cast cylinder. Lichtner et al. investigated the anisotropic shrinkage with experiments and the discrete element method, experimentally and simulatively observing less shrinkage in the plane normal to the freezing direction. Following Olevsky[205] it was argued that the anisotropic shape of the pores induces anisotropic shrinkage. The reason for this is that the sintering potential is proportional to curvature, and if the curvature is anisotropic, so is the sintering potential. Hence directions which exhibit a larger curvature will densify faster than others with smaller curvature. It should be said however that the macropores' macroscopic curvature is low and it is not clear whether it can cause the observed magnitude of shrinkage anisotropy. Another reason stated in the discussion of [204] was that particles within the walls will sinter isotropically, as their contacts are isotropically distributed. Particles on the walls' surface have missing contacts and hence will tend to move anisotropically. This disregards however that the sintering potential can also be distributed inhomogeneously and anisotropically.

The present results can be explained by analyzing the anisotropy of the sintering potential, represented by how much GBs deviate from their equilibrium concentration within the simulation. Define the anisotropy factor of a property Π as $f(\Pi) = \frac{\Pi_{YZ}}{\Pi_X}$, i.e. simply the ratio of the property in the YZ (average over both Y and Z directions) plane, normal to the freezing direction, to the property in the freezing direction X. The anisotropy factor of both the strain and sintering potential are plotted against each other in fig. 9.10. Two regimes are evident here: Initially, there is a slight anisotropy in the sintering potential, which is sufficient to cause the strain to become increasingly anisotropic. Although the anisotropy is small (≈ 1.05), this small anisotropy causes about half of the observed

anisotropy in the strain. This is due to the high driving forces for densification at this early stage. The anisotropy in the sintering potential increases eventually, due to the sintering potential being connected with the chemical potential (stress) on a particle's surface within the phase-field model. As the structure densifies, more and more grains completely lose their connection to the surface and become embedded in a surrounding grain matrix; this can easily be seen on the right of fig. 9.9. Once this happens, the model assumes that there is no additional stress due to curvature and correspondingly reduces the sintering potential of the associated grain boundaries. While this occurs isotropically, the average sintering potential in a direction is dependent on both such embedded grains and surface grains. A simple model of this effect could read as

$$\sigma^d = \frac{N_v \sigma_{iso} + N_s^d \sigma_s^d}{N_v + N_s^d}$$

i.e. the average sintering potential σ^d in a direction d is the addition of both a volume contribution $N_v \sigma_{iso}$, acting isotropically, and a surface contribution $N_s^d \sigma_s^d$, potentially inducing anisotropy. If $N_v \gg N_s^d$, isotropic behavior is observed, which was the case in the previous sections; though if the anisotropic contribution is the same in each direction, this would also result in net isotropic behavior. In the present geometry however, $N_v \approx 2N_s^d$ in the YZ plane since the walls are on average about 6 particles thin. In contrast to this, $N_v \approx 5N_s^d$ in the X direction (12 particles) and hence this direction will be affected less by the surface grains, especially compared to the Y and Z directions. Thus, the observed anisotropy of the sintering potential might be due to the phase-field model giving an unwarranted extra weight to particles with exposed surfaces by virtue of their increased sintering potential σ_s^d. Finally, the increase in the anisotropy of the sintering potential at roughly constant strain anisotropy is due to little to no porosity remaining. This correspondingly magnifies the aforementioned effects, though given that little to no densification is possible anymore, no further increase in strain anisotropy is observed. The non-monotonic behaviour in this final region is mostly due to measurement errors via grain growth, since densification has effectively stopped.

Three other confounding factors exist: First, the present geometry only contains a single macropore open to the surrounding vacuum, raising questions of representativeness. Second, within the present phase-field model it was observed that linear chains of particles only achieve particle count independent strain evolution starting from about 16 particles in the chain[115]. Up to that point, increasing the number of particles in the chain decreased the strain rate monotonically. The strain rate ratio between a four and sixteen particle chain, roughly comparable to how thick the freeze-cast structures is in the YZ and X directions, is on average about 1.17. This is in rough agreement with the initial

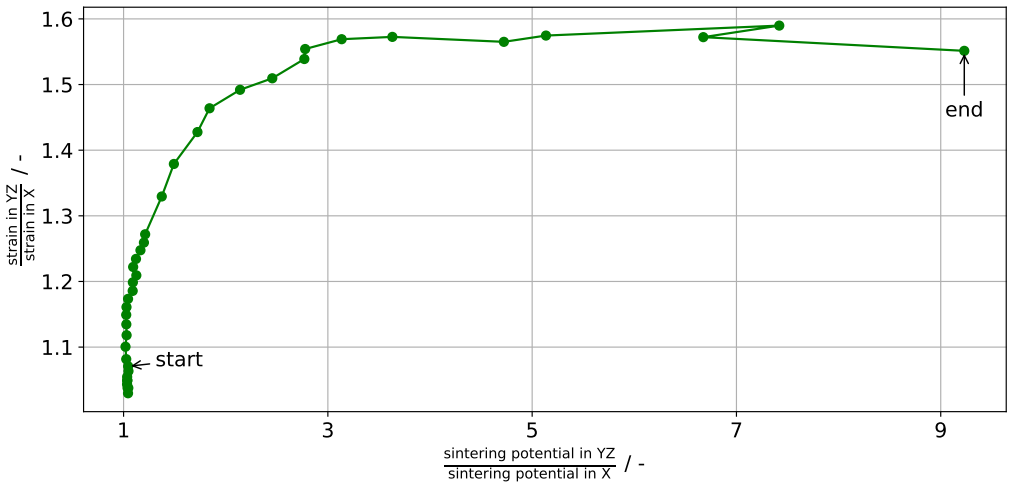

Figure 9.10: Anisotropy factor $f(\Pi) = \frac{\Pi_{YZ}}{\Pi_X}$ for the properties Π of strain and sintering potential.

increase of strain anisotropy up to about a factor of ≈ 1.2, after which the increase in sintering potential anisotropy becomes the dominant influence on the strain anisotropy. The change in strain rate between chains of different particle counts was explained via the differing sintering potentials of the chain's end particles. Since their shape evolution is only restricted by one grain boundary, they will generally have an average surface chemical potential which differs from the inner particles. Since there are many thin sections in the freeze-cast structure, this effect is present in freeze-casting sintering simulation as well, and is the likely origin of the sintering potential anisotropy. The final confounding factor is that some grain growth ($\approx 10\%$ average grain size increase) occurs. While for the present results it does not result in desintering [206], the green body resulting from freeze-casting is generally liable to experience this phenomenon — the bridges spanning the macropores are similar to the bridges spanning cracks in the classic work of Sudre and Lange [206]. Since desintering would generally reduce the connectivity normal to the freezing direction, it would support Lichtner et al's [204] experimental results. In total, while the present results are quite encouraging for relatively thick structures, further research and modelling work should be done on the calculation of the sintering potential within the model.

10 Overall conclusion and outlook

Within the present work the processes of solidification and sintering were investigated with the help of phase-field simulations.

In chapter 4, it was possible to verify a boundary curve separating eutectic growth from coupled dendritic-eutectic growth. Based on the assumptions for the boundary curve, this also suggests that during coupled dendritic-eutectic growth the isolated growth forms do not significantly influence each other. This conclusion is furthered by comparing the operating states of both dendrites and eutectics during coupled growth to their isolated forms at equivalent growth conditions with little difference being observed. Velocity changes were conducted to test for morphological hystereses and it was found that the transition from a dendritic-eutectic pattern to a eutectic pattern is easier than the reverse process. Large-scale two-dimensional simulations allowing for significant time spent in primary crystallization revealed that the distance between dendrite tips and the eutectic front plays a major role in the overall pattern formation: If the distance is large, the eutectic will simply grow along interdendritic liquid channels. During this growth, it is possible that the eutectic will nucleate anew in liquid pockets formed by secondary arms and thus eutectics of different dominant orientation should be found around dendrites. If the distance is small, then the growth of secondary dendrite arms is generally suppressed by the eutectic. The eutectic front itself exhibits a small-scale variation of phase-widths close to the dendrite due to solute rejection from the dendrite and is thus curved close to the dendrite. However, this curvature need not be due to the effects of the dendrite, as a eutectic after overgrowing a dendrite still showed a curved front.
Finally, three-dimensional simulations were conducted to verify whether the morphology of the eutectic changes in reaction to the coupled growth. At the same growth conditions, a eutectic composed of isotropic phases yielded a fiber-matrix arrangements, which was changed into a lamellar pattern once one of the phases had an anisotropic solid-liquid interface. Exploiting the morphological hystereses allowed the simulation of coupled growth at the very same growth conditions and the eutectic was observed to eventually form a lamellar pattern due to inclusion of anisotropic solid-liquid phases. Hence no conclusive statement can be made whether coupled growth can induce a morphological change in the eutectic. Future work could probe this in two possible ways: Simulate at concentrations

with a larger difference in phase fractions which would favour a fiber-matrix arrangement. If the phase fraction difference is sufficiently large, the isolated eutectic with anisotropic phases could, depending on the anisotropy strength, eventually keep the the fiber-matrix arrangement. Similarly, a change in the anisotropic formulation or strength could lead to the anisotropic dendritic phase not invading the initially isotropic eutectic. If at the same growth conditions a different morphology is observed for coupled growth, evidence of coupled growth's influence on morphology would be obtained.

The process of freeze-casting was modelled in chapter 5 by applying classical solidification phase-field methods with Gibbs energies approximating the peculiarities of colloidal suspensions. This resulted in dendritic structures, whose microstructural lengths were investigated subsequently. Hence the effects of solidification velocity, temperature gradient, solids loading and particle size on these lengths were revealed. One parameter which was not part of prior experimental focus, the temperature gradient, was found to have a significant effect on all three lengths, especially at smaller particle sizes. Hence by recording the temperature gradient experiments can be made more comparable.
Future work should re-evaluate the energetic description of the system, as right now it is based on combining data from quite different sources. One way of doing this would be to evaluate the enthalpy of a suspension as it freezes and use it as input for thermodynamic modelling; in the same way that the enthalpy is related to the Gibbs free energy, the reverse is true as well. Given that the suspended particles should not undergo any phase transformation, their enthalpic contribution should be mainly one of heat capacity and excluding volume of liquid which does not transform. Furthermore, a thin-interface analysis including a concentration-dependent diffusivity should be carried out, since the diffusivity in colloidal suspension is sensitive to both concentration and particle size.

Sintering was extensively studied (chapters 6 to 9) starting from a critical investigation of the most commonly used phase-field model for solid-state sintering. A multitude of unphysical behaviours were revealed and resolved in subsequent works. This allowed the matching with many qualitative observations of experiments: First, the newly developed model has a representative volume element for densification, unlike the literature model for solid-state sintering. This model also showed the expected behaviour of slower densification with larger grains. Furthermore, the co-evolution of the grain structure during sintering in terms of the grain coordination number could be shown to be similar to experiments.
Based on these results, further investigations with various process and geometry changes were carried out: The effect of pressure was included by modifying the equilibrium vacancy concentration at grain boundaries and found to yield the experimentally observed

and theoretically derivable linear increase of densification rate with pressure. By a projection method this isotropic pressure could be turned into an uniaxial stress, which is commonly employed in creep experiments. Simulations with a tensile, uniaxial stress showed the major qualitative features of creep: Constant strain rate after an initial transient, increase of porosity, and in the case of Coble creep, a linear dependence of strain rate on the applied stress. Next, the coupled processes of densification and grain growth were tackled by varying the interfacial diffusivities and grain mobilities. This effectively represents sintering at different temperatures or doping levels. With these variations it could be shown that as long as densification is fast, surface diffusion has little influence on the densification behaviour. The grain boundary diffusivity should not be much smaller than an order of magnitude than the surface diffusion in order to ensure this. Lower surface diffusion also increases the time to pore destabilization as well as the effect of pore drag on grain boundaries. The latter causes slightly less grain growth for otherwise the same parameters if surface diffusion is reduced. Grain growth itself seems to generally follow power laws after an initial transient, with the exponent depending on whether fast or slow densification occurs. This was observed to be due to pore drag, as fast densification implied little pore loading on grain boundaries, whereas slow densification led to severe pore loading on grain boundaries.
Due to the 4D information provided by simulations, it was possible to follow the shape evolution of each grain and pore during these simulations. Thanks to this, it was possible to determine that networks of isolated porosity form, which then undergo a grain boundary mediated form of the Plateau-Rayleigh instability to split into smaller units. If these units stay attached to grain boundaries, they generally deviate from a spherical shape, but if they are detached their shape tends towards a sphere. The grain shape was observed to generally be different from the usual assumption of the truncated octahedron, as shown by moment invariants. This explains a part of the deviation of classical sintering theory from experiments, as the prefactors are heavily dependent on the assumed geometry.
Finally, an inhomogeneous density distribution was shown to result in anisotropic shrinkage. The structure employed for this was a freeze-cast structure generated with the freeze-casting model presented in this work. While anisotropic shrinkage comparable to some experiments in literature was observed, some additional model complications were observed as well which will need to be addressed in future work.

Overall, the present work shows the wide applicability of the phase-field model to materials processing. This is not only limited to the classical phase-field application of solidification, but also to the intricate process of sintering. Furthermore, by simulating each step within a process chain with an appropriate method, a virtual replication of the

process chain can be established. This was exemplified with the freeze-casting process chain in the present work, but also applies to e.g. steel processing: The processes of refining the ore, casting into ingots which are then smithed into shape, potentially quenched and finally heat-treated to adjust the materials properties, are nowadays mostly analyzed in isolation. This necessitates assumptions on the state of the material prior to the investigated processing step, which might severely affect the reaction of the material to the processing.
By combining these steps into a coherent simulation chain, more quantitative results can be obtained. A key factor in such a coherent chain is the precise knowledge of input parameters, since these determine the spatiotemporal evolution of the system. One way of determining these could be data assimilation methods[207]: Based on experimentally observed data, the parameters of a computational model are adjusted to fit the experimental observations automatically. However, the computational model employed for this needs to capture all relevant processes correctly. An easy way to understand this is comparing the results of the sintering models developed in this work: The same density-time curve would result in radically different diffusion coefficients depending on the model, as one model can achieve a RVE, but the other cannot. Hence while the observation might be matched by the model without an RVE, the determined parameters will be unusable outside of the precise conditions the experiment was conducted at. The goal in the end is to determine the *physical* value of the parameter, and not one seen under the lens of an incorrect model. Thus these values need to be entirely transferable between different computational models handling different parts of a process as long as the material stays the same.

A Appendix

A.1 Formal equivalence of units

The specification of units for composition as well as energy density is rather free if the conversion factor is assumed to be constant. Say for the moment that the "correct" units to use for composition c would be the molar concentration $[c] = \mathrm{mol\,m^{-3}}$ as well as the volumetric Gibbs energy density $[g_v] = \mathrm{J\,m^{-3}}$ for energy density. The conversion to a specification in terms of molar fraction and molar Gibbs free energy would be $x = \frac{c}{V_m}$ and $g_m = g_v V_m$ under the assumption of constant molar volume V_m. Assume now that some nondimensionalization scales exist such that $[\bar{c}] = [\frac{c}{c_0}] = 1$ and $[\bar{g_v}] = [\frac{g_v}{g_{v,0}}] = 1$, with the units of the scales corresponding to the units of the quantities. Given that constant molar volume is assumed and that $[c] = [\frac{1}{V_m}]$ a natural choice is $c_0 = \frac{1}{V_m}$, as is generally done in this work; this directly implies equivalence of mole fraction and molar concentration in nondimensional concentration $\bar{c}$. With this choice of scale, a scale for the molar Gibbs free energy is given by $g_{m,0} = \frac{g_{v,0}}{c_0} = g_{v,0} V_m$. Using the earlier definitions we have

$$g_m = g_v V_m \tag{A.1}$$

$$\bar{g_m} = \frac{g_v V_m}{g_{v,0} V_m} \tag{A.2}$$

$$= \frac{g_v}{g_{v,0}} \tag{A.3}$$

i.e. given these choices of scales, the nondimensional molar Gibbs free energy is the same as the nondimensional volumetric Gibbs free density.

Note that if the molar volume is not constant, this relation would not hold since the choice of scale is fixed, but the conversion neccesarily happens on a local basis accounting for local conditions.

A.2 Further details of freeze-casting

This effectively reproduces the supplementary material of publication [80], showing the precise numerical values of the Gibbs free energy functions and the obtained steady-state microstructures.

A.2.1 Gibbs free energy parameters

This section details the numerical values employed to describe the Gibbs free energy of aqueous bentonite suspensions with particles of size 250 nm, 375 nm and 500 nm. All values are nondimensionalized based on the scales noted in the main text, with $g_{dim} = G \cdot E_0$. For each particle size, the Gibbs free energy of both the solid ice phase $g_i(c,T)$ and the liquid suspension phase $g_s(c,T)$ are reported. Both are of the form

$$g_\alpha(c,T) = A_\alpha(T)c^2 + B_\alpha(T)c + C_\alpha(T)$$

with $A_\alpha(T), B_\alpha(T), C_\alpha(T)$ being parabolic functions of temperature T. The functions $C_i(T), C_s(T)$ for the ice and suspension phases are independent of the particle size since they are based on the pure phase description following IAPWS.

Table A.1: particle size independent functions

$C_i(T)$	$-843.987154950033T^2 + 2668.14452736135T - 1823.8679855496$
$C_s(T)$	$-1862.28940047943T^2 + 3718.19539783286T - 1855.56475865368$

The functions $A_\alpha(T), B_\alpha(T)$ for the ice and suspensions phases are tabulated below for each particle size:

Table A.2: functions for 250 nm particles

$A_i(T)$	$-363.813052701955T^2 + 1038.42737506969T - 661.07371316661$
$A_s(T)$	$+624.781729505937T^2 - 2001.5373528048T + 1603.02054720731$
$B_i(T)$	$-14305.5893356235T^2 + 26721.0370280905T - 12534.9375540961$
$B_s(T)$	$-363.813052701955T^2 + 1038.42737506969T - 661.07371316661$

Finally, the full Gibbs energy functions for the different particle sizes are also given:

Table A.3: functions for 375 nm particles

$A_i(T)$	$8696450.19594392T^2 - 16499259.5809074T + 7827020.0745525$
$A_s(T)$	$+4419.53212429992T^2 - 9890.27278224592T + 5533.24950362982$
$B_i(T)$	$-130214.073750852T^2 + 245337.628150446T - 115442.978896433$
$B_s(T)$	$12514.870762504T^2 - 23252.2358392643T + 10773.1205717657$

Table A.4: functions for 500 nm particles

$A_i(T)$	$+995906.442526578T^2 - 2106381.19059346T + 1113015.48143482$
$A_s(T)$	$+10047.1312993791T^2 - 21246.3527768701T + 11224.7417646649$
$B_i(T)$	$-5645.19688672837T^2 + 11679.3939071022T - 6046.24602532013$
$B_s(T)$	$+2941.69029612794T^2 - 5300.34949864201T + 2371.22834220704$

$$\begin{aligned} g_{i,250\,\mathrm{nm}} =& (750591.374527449T^2 - 1.47463039577804 * 10^6 T + 743122.943915487) * c^2 \\ &+ (-14305.5893356235T^2 + 26721.0370280905T - 12534.9375540961) * c \\ &- 843.987154950033T^2 + 2668.14452736135T - 1823.8679855496 \end{aligned}$$

$$\begin{aligned} g_{s,250\,\mathrm{nm}} =& (1603.02054720731 - 2001.5373528048T + 624.781729505937T^2) * c^2 \\ &+ (-363.813052701955T^2 + 1038.42737506969T - 661.07371316661) * c \\ &- 1862.28940047943T^2 + 3718.19539783286T - 1855.56475865368 \end{aligned}$$

$$\begin{aligned} g_{i,375\,\mathrm{nm}} =& (8.69645019594392 * 10^6 T^2 - 1.64992595809074 * 10^7 T + 7.82702007455250 * 10^6) * c^2 \\ &+ (-130214.073750852T^2 + 245337.628150446T - 115442.978896433) * c \\ &- 843.987154950033T^2 + 2668.14452736135T - 1823.86798554960 \end{aligned}$$

$$
\begin{aligned}
g_{s,375\,\mathrm{nm}} =& (5533.24950362982 - 9890.27278224592T + 4419.53212429992T^2) * c^2 \\
&+ (12514.8707625040T^2 - 23252.2358392643T + 10773.1205717657) * c \\
&- 1862.28940047943T^2 + 3718.19539783286T - 1855.56475865368
\end{aligned}
$$

$$
\begin{aligned}
g_{i,500\,\mathrm{nm}} =& (703345.2040012840T^2 - 1.51219218860276 * 10^6T + 812645.048703083) * c^2 \\
&+ (-6458.38650416161T^2 + 13153.8099858636T - 6713.44791450838) * c \\
&- 843.987154950033T^2 + 2668.14452736135T - 1823.86798554960
\end{aligned}
$$

$$
\begin{aligned}
g_{s,500\,\mathrm{nm}} =& (7984.99647865678 - 14858.7003887071T + 6911.02343660797T^2) * c^2 \\
&+ (3754.87978653526T^2 - 6774.76533796470T + 3038.43011872479) * c \\
&- 1862.28940047943T^2 + 3718.19539783286T - 1855.56475865368
\end{aligned}
$$

A.2.2 Simulation snapshots of freeze-casting

The following images show simulation snapshots of all conducted simulations in their final state. The field shown is the phase-field of the ice phase, with yellow indicating ice and blue indicating suspension. The red-orange part in between is the diffuse interface.

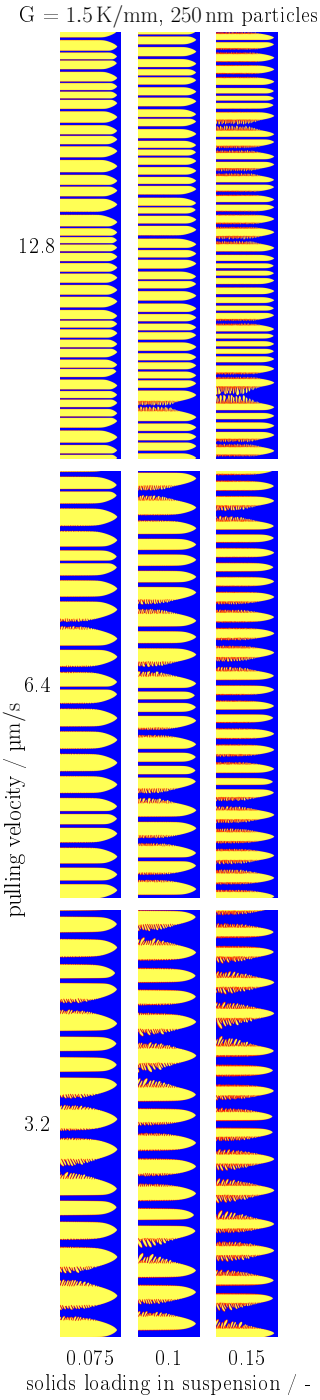
G = 1.5 K/mm, 250 nm particles
12.8
6.4
3.2
pulling velocity / µm/s
0.075
0.1
0.15
solids loading in suspension / -

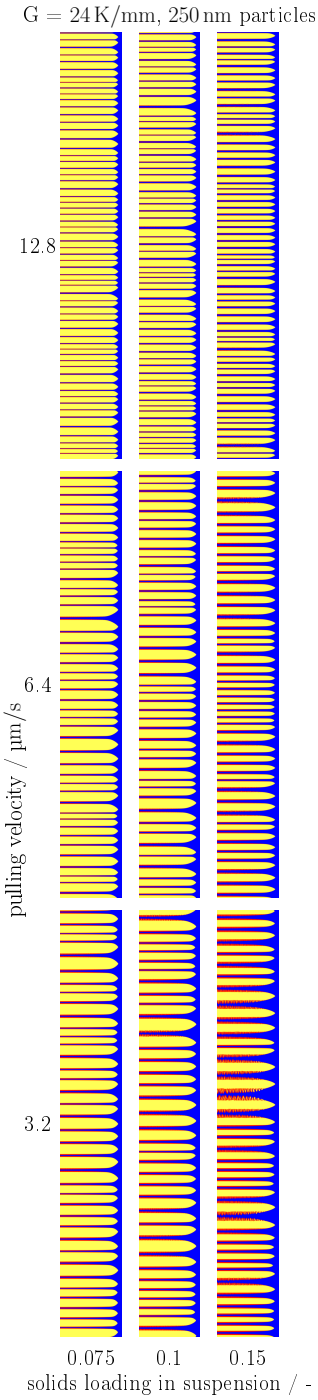
G = 24 K/mm, 250 nm particles
12.8
6.4
3.2
pulling velocity / µm/s
0.075
0.1
0.15
solids loading in suspension / -

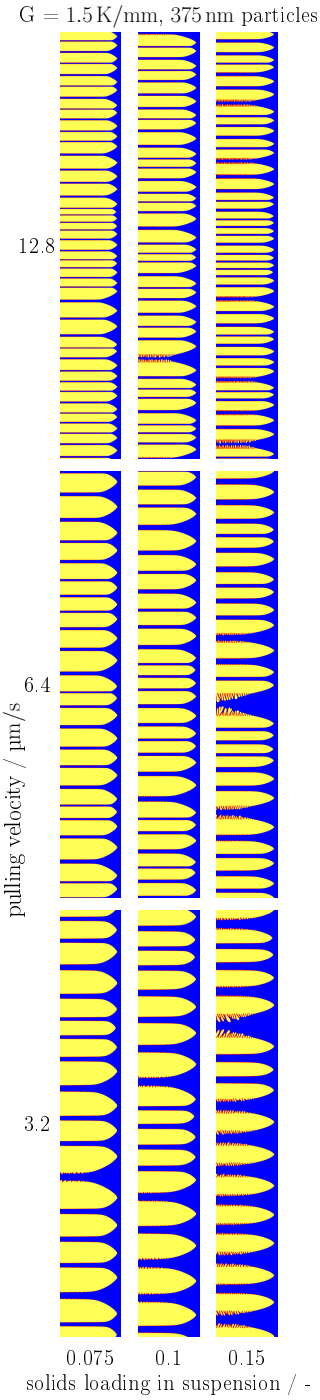
G = 1.5 K/mm, 375 nm particles
12.8
6.4
3.2
pulling velocity / µm/s
0.075
0.1
0.15
solids loading in suspension / -

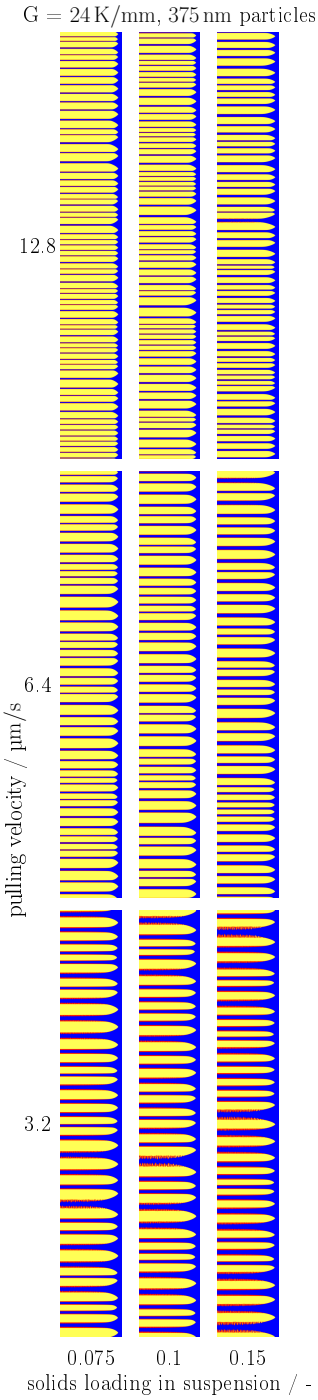
G = 24 K/mm, 375 nm particles
12.8
6.4
3.2
pulling velocity / µm/s
0.075
0.1
0.15
solids loading in suspension / -

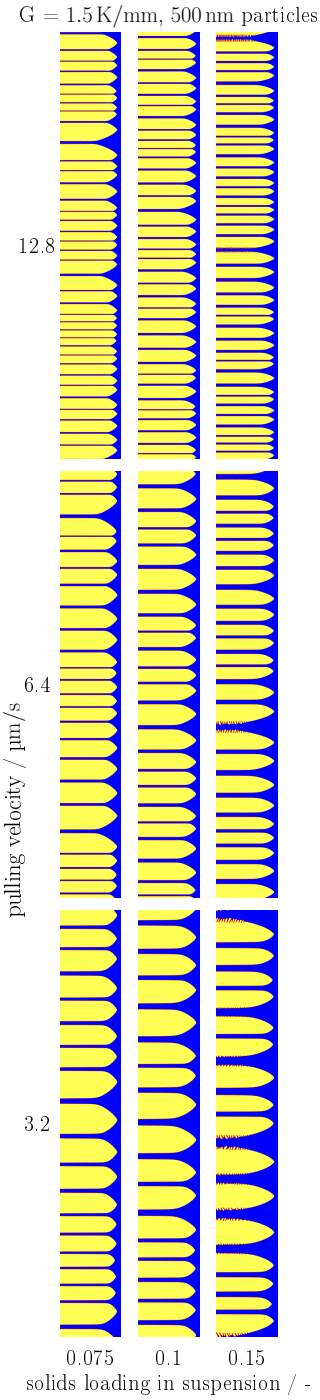
G = 1.5 K/mm, 500 nm particles
12.8
6.4
3.2
pulling velocity / µm/s
0.075
0.1
0.15
solids loading in suspension / -

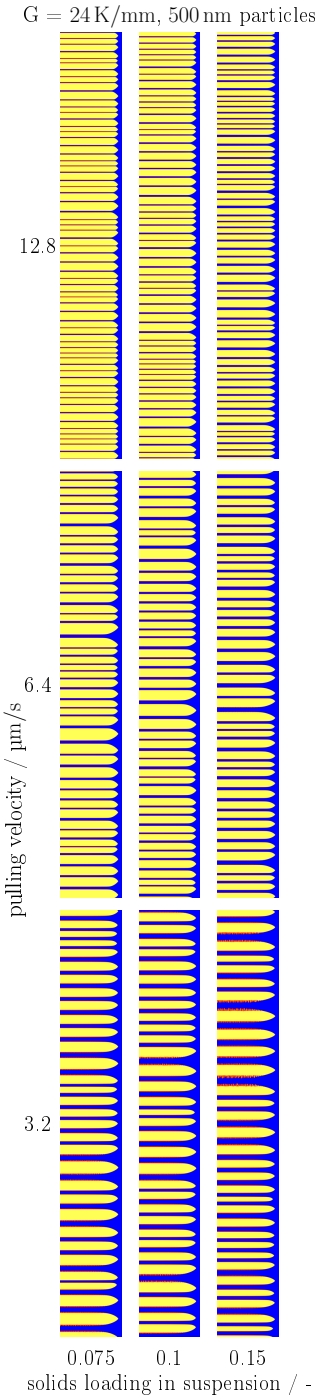
G = 24 K/mm, 500 nm particles
12.8
6.4
3.2
pulling velocity / µm/s
0.075
0.1
0.15
solids loading in suspension / -

List of Figures

List of Tables

Student theses supervised

During the writing of the dissertation several theses by students were supervised by the author.

- Heming Wang, M.Sc. thesis, “Stabilität von Porenkanälen während des Sinterprozesses”, KIT, 2019
- Nikita Tschumak, B.Sc. thesis, “Untersuchung der Plateau-Rayleigh-Instabilität in Polykristallen mithilfe der Phasenfeldmethode”, KIT, 2020
- Jan Hartmann, B.Sc. thesis, “Untersuchung des Einflusses von Material- und Geometrieparametern auf die Rayleigh-Instabilität in Bikristallen mit der Phasenfeldmethode”, 2021
- Ahmed Elmoghazy, seminary thesis, “Grain growth in stretched isotropic systems”, KIT, 2021
- Nikita Tschumak, seminary thesis, “Anpassung von Gefügemorphologien bei gerichteter Erstarrung: Untersuchung des Einflusses von variabler Ziehgeschwindigkeit mit der Phasenfeldmethode”, KIT, 2023

List of Publications

The list of publication involving the author is identified via author acronyms instead of numbers in order to distinguish them from the regularly cited works within the thesis proper.

Journal articles

[DNKH+21] K. Dargahi Noubary, M. Kellner, J. Hötzer, M. Seiz, H.J. Seifert, and B. Nestler. Data workflow to incorporate thermodynamic energies from Calphad databases into grand-potential-based phase-field models. *Journal of Materials Science*, 56(20):11932–11952, 2021.

[HSK+19] Johannes Hötzer, Marco Seiz, Michael Kellner, Wolfgang Rheinheimer, and Britta Nestler. Phase-field simulation of solid state sintering. *Acta Materialia*, 164:184–195, February 2019. 10.1016/j.actamat.2018.10.021. Publisher: Elsevier BV.

[RHR+19] Veronika Rehn, Johannes Hötzer, Wolfgang Rheinheimer, Marco Seiz, Christopher Serr, and Britta Nestler. Phase-field study of grain growth in porous polycrystals. *Acta materialia*, 174:439–449, 2019.

[Sei22] Marco Seiz. Effect of rigid body motion in phase-field models of solid-state sintering. *Computational Materials Science*, 215:111756, December 2022. 10.1016/j.commatsci.2022.111756.

[SHN23a] Marco Seiz, Henrik Hierl, and Britta Nestler. An improved grand-potential phase-field model of solid-state sintering for many particles. *Modelling and Simulation in Materials Science and Engineering*, 31(5):055006, July 2023. 10.1088/1361-651X/acd56d.

[SHN23b] Marco Seiz, Henrik Hierl, and Britta Nestler. Unravelling densification during sintering by multiscale modelling of grain motion. *Journal of Materials Science*, 58(35):14051–14071, Sep 2023. 10.1007/s10853-023-08859-9.

[SHNR23] Marco Seiz, Henrik Hierl, Britta Nestler, and Wolfgang Rheinheimer. Revealing process and material parameter effects on densification via phase-field studies. 2023. 10.48550/arXiv.2308.09682.

[SKN23] Marco Seiz, Michael Kellner, and Britta Nestler. Simulation of dendritic–eutectic growth with the phase-field method. *Acta Materialia*, 254:118965, 2023. 10.1016/j.actamat.2023.118965.

[SN21] Marco Seiz and Britta Nestler. Modelling and simulation of the freeze casting process with the phase-field method. *Computational Materials Science*, 193:110410, June 2021. 10.1016/j.commatsci.2021.110410. Publisher: Elsevier BV.

[SOA+21] Marco Seiz, Philipp Offenhäuser, Stefan Andersson, Johannes Hötzer, Henrik Hierl, Britta Nestler, and Michael Resch. Lustre I/O performance investigations on Hazel Hen: experiments and heuristics. *The Journal of Supercomputing*, 77(11):12508–12536, April 2021. 10.1007/s11227-021-03730-7. Publisher: Springer Science and Business Media LLC.

Conference contributions

[BHE+19] Martin Bauer, Johannes Hötzer, Dominik Ernst, Julian Hammer, Marco Seiz, Henrik Hierl, Jan Hönig, Harald Köstler, Gerhard Wellein, Britta Nestler, and Ulrich Rüde. Code generation for massively parallel phase-field simulations. In *Proceedings of the International Conference for High Performance Computing, Networking, Storage and Analysis*, SC '19, New York, NY, USA, 2019. Association for Computing Machinery. 10.1145/3295500.3356186.

[HHS+20] Henrik Hierl, Johannes Hötzer, Marco Seiz, Andreas Reiter, and Britta Nestler. Extreme scale phase-field simulation of sintering processes. In *2019 IEEE/ACM 10th Workshop on Latest Advances in Scalable Algorithms for Large-Scale Systems (ScalA), Denver, CO, USA, 18-18 Nov. 2019*, page 25–32. Institute of Electrical and Electronics Engineers (IEEE), 2020. 10.1109/ScalA49573.2019.00009. 35.14.01; LK 01.

[RHK+18] V. Rehn, J. Hötzer, M. Kellner, M. Seiz, C. Serr, W. Rheinheimer, M. J. Hoffmann, and B. Nestler. The impact of pores on microstructure evolution: A phase-field study of pore-grain boundary interaction. In *High*

Performance Computing in Science and Engineering ' 17: Transactions of the High Performance Computing Center, Stuttgart (HLRS) 2017. Ed.: W. Nagel, page 485–502. Springer International Publishing, 2018. 10.1007/978-3-319-68394-2_29.

[SHH+20] Marco Seiz, Johannes Hötzer, Henrik Hierl, Stefan Andersson, and Britta Nestler. Bad nodes considered harmful: How to find and fix the problem. In *Sustained Simulation Performance 2018 and 2019 – Proceedings of the Joint Workshops on Sustained Simulation Performance, University of Stuttgart (HLRS) and Tohoku University, 2018 and 2019. Ed.: M. Resch*, page 123–130. Springer International Publishing, 2020. 10.1007/978-3-030-39181-2_11.

[SHH+21a] M. Seiz, P. Hoffrogge, H. Hierl, A. Reiter, D. Schneider, and B. Nestler. Phase-field simulations with the grand potential approach. In *High Performance Computing in Science and Engineering '20*, pages 561–577. Springer International Publishing, 2021. 10.1007/978-3-030-80602-6_37.

[SHH+21b] M. Seiz, J. Hötzer, H. Hierl, A. Reiter, K. Schratz, and B. Nestler. Accelerating phase-field simulations for HPC-systems. In *High Performance Computing in Science and Engineering '19*, pages 555–567. Springer International Publishing, 2021. 10.1007/978-3-030-66792-4_37.

Bibliography

[1] Peter Jordan. *Stahel und Eyssen, künstlich weych und hart zu machen, schrifft und bildwerck darinn zu etzen: Gold unnd silberfarben, auff ein yedes metal mancherley weyse zu machen. Auch mancherley lötung zu stahel, eysen und messing, kalt und warm ; Schmaltz flecken, öl flecken, oder was es nur für flecken seind, auss Gewandt, Sammat, Seyden, Güldinen stücken, Cleydern etc. leychtlich mitt wassern oder laugen, darzu bereyt, on schaden zu vertreiben : eins yeglichen gewandts verlorn farb wider zu bringen. Auch garn, Leynwath, Holtz, Beyn etc. Mancherley farben zu ferben.* bey Peter Jordan, Getruckt zu Meintz [Mainz], 1534. doi: 10.3931/e-rara-15203. URL `https://doi.org/10.3931/e-rara-15203`.

[2] D. Mackenzie. History of quenching. *International Heat Treatment & Surface Engineering*, 2:68–73, 06 2008. doi: 10.1179/174951508X358437. URL `https://doi.org/10.1179/174951508X358437`.

[3] Theophilus Presbyter and CR Dodwell. *De diversis artibus, in The Various Arts.* Translated by CR Dodwell. London: Thomas Nelson and Sons, Ltd., 1961.

[4] M.J. Peet. 6 - bainitic steels and alloys for power plants. In Amir Shirzadi and Susan Jackson, editors, *Structural Alloys for Power Plants*, Woodhead Publishing Series in Energy, pages 153–187. Woodhead Publishing, 2014. ISBN 978-0-85709-238-0. doi: 10.15339780857097552.2.153. URL `https://doi.org/10.1533/9780857097552.2.153`.

[5] A. Papapetrou. Untersuchungen über dendritisches wachstum von kristallen. *Zeitschrift für Kristallographie - Crystalline Materials*, 92(1-6):89–130, 1935. doi: doi:10.1524/zkri.1935.92.1.89. URL `https://doi.org/doi:10.1524/zkri.1935.92.1.89`.

[6] G.P. Ivantsov. Temperature field around spherical, cylinder and needle-like dendrite growing in supercooled melt. *Dokl. Akad. Nauk. SSSR*, 58:567–569, 1947.

[7] G.E Nash and M.E Glicksman. Capillarity-limited steadystate dendritic growth—i. theoretical development. *Acta Metallurgica*, 22(10):1283–1290, 1974. ISSN 0001-6160. doi: 10.10160001-6160(74)90141-2. URL https://doi.org/10.1016/0001-6160(74)90141-2.

[8] JS Langer and J Müller-Krumbhaar. Stability effects in dendritic crystal growth. *Journal of Crystal Growth*, 42:11–14, 1977.

[9] W. Kurz and D. J. Fisher. Dendrite growth at the limit of stability: tip radius and spacing. *Acta Metallurgica*, 29(1):11–20, 1981. ISSN 00016160. doi: 10.1016/0001-6160(81)90082-1. URL https://doi.org/10.1016/0001-6160(81)90082-1.

[10] J. Frenkel. Viscous flow of crystalline bodies under the action of surface tension. *J. Phys. (U. S. S. R)*, 9(5):385–391, 1945.

[11] Conyers Herring. Effect of change of scale on sintering phenomena. *Journal of Applied Physics*, 21(4):301–303, 1950.

[12] W D Kingery and M Berg. Study of the Initial Stages of Sintering by Viscous Flow, Evaporation—Condensation, and Self-Diffusion. *Journal of Applied Physics*, 26, 1955. doi: 10.1007/978-94-009-0741-6_22. URL https://doi.org/10.1007/978-94-009-0741-6_22.

[13] R.L. Coble. Initial Sintering of Alumina and Hematite. *Journal of the American Ceramic Society*, 41(2):55–62, 1958.

[14] D. Lynn Johnson and Ivan B. Cutler. Diffusion sintering: I, initial stage sintering models and their application to shrinkage of powder compacts. *Journal of the American Ceramic Society*, 46(11):541–545, 1963. doi: 10.1111j.1151-2916.1963.tb14606.x. URL https://doi.org/10.1111/j.1151-2916.1963.tb14606.x.

[15] A.J. Melendez and C. Beckermann. Measurements of dendrite tip growth and sidebranching in succinonitrile–acetone alloys. *Journal of Crystal Growth*, 340(1): 175–189, February 2012. ISSN 00220248. doi: 10.1016/j.jcrysgro.2011.12.010. URL https://doi.org/10.1016/j.jcrysgro.2011.12.010.

[16] Jianrong Gao, Mengkun Han, Andrew Kao, Koulis Pericleous, Dmitri V. Alexandrov, and Peter K. Galenko. Dendritic growth velocities in an undercooled melt of pure nickel under static magnetic fields: A test of theory with convection. *Acta Materialia*, 103:184–191, January 2016. ISSN 13596454. doi: 10.1016/j.actamat.2015.10.014. URL https://doi.org/10.1016/j.actamat.2015.10.014.

[17] P.K. Galenko, D.A. Danilov, K. Reuther, D.V. Alexandrov, M. Rettenmayr, and D.M. Herlach. Effect of convective flow on stable dendritic growth in rapid solidification of a binary alloy. *Journal of Crystal Growth*, 457:349–355, January 2017. ISSN 00220248. doi: 10.1016/j.jcrysgro.2016.07.042. URL https://doi.org/10.1016/j.jcrysgro.2016.07.042.

[18] Fabian Lemke. *Untersuchung des Sinterverhaltens von SrTiO3 unter Berücksichtigung der Defektchemie*. PhD thesis, Karlsruher Institut für Technologie (KIT), 2016. URL https://doi.org/10.5445/KSP/1000054013. doi: 10.5445/KSP/1000054013.

[19] George W. Scherer and David L. Bachman. Sintering of Low-Density Glasses: II, Experimental Study. *Journal of the American Ceramic Society*, 60(5-6):239–243, May 1977. ISSN 0002-7820, 1551-2916. doi: 10.1111/j.1151-2916.1977.tb14115.x. URL https://doi.org/10.1111/j.1151-2916.1977.tb14115.x.

[20] M.N. Rahaman. *Ceramic Processing and Sintering*. Materials Engineering. Taylor & Francis, Boca Raton, 2003. ISBN 9780824709884.

[21] R. Kobayashi. Modeling and numerical simulations of dendritic crystal growth. *Physica D: Nonlinear Phenomena*, 63(3):410 – 423, 1993. ISSN 0167-2789. doi: 10.10160167-2789(93)90120-P. URL http://dx.doi.org/10.1016/0167-2789(93)90120-P.

[22] A. Karma and W. Rappel. Quantitative phase-field modeling of dendritic growth in two and three dimensions. *Physical review E*, 57(4):4323, 1998.

[23] A. Karma and W.J. Rappel. Phase-field model of dendritic sidebranching with thermal noise. *Physical review E*, 60(4):3614, 1999.

[24] Tomohiro Takaki, Shinji Sakane, Munekazu Ohno, Yasushi Shibuta, and Takayuki Aoki. Large-scale phase-field lattice Boltzmann study on the effects of natural convection on dendrite morphology formed during directional solidification of a binary alloy. *Computational Materials Science*, 171(April 2019):109209, 2020. ISSN 0927-0256. doi: 10.1016/j.commatsci.2019.109209. URL https://doi.org/10.1016/j.commatsci.2019.109209.

[25] Britta Nestler, Harald Garcke, and Björn Stinner. Multicomponent alloy solidification: phase-field modeling and simulations. *Physical Review E*, 71(4):041609, 2005.

[26] R. Folch and M. Plapp. Quantitative phase-field modeling of two-phase growth. *Physical Review E*, 72(1):011602, 2005.

[27] Michael Kellner, Ioannis Sprenger, Philipp Steinmetz, Johannes Hötzer, Britta Nestler, and Martin Heilmaier. Phase-field simulation of the microstructure evolution in the eutectic NiAl-34Cr system. *Computational Materials Science*, 128(15): 379–387, 2017.

[28] Supriyo Ghosh and Mathis Plapp. Influence of interphase boundary anisotropy on bulk eutectic solidification microstructures. *Acta Materialia*, 140:140–148, November 2017. ISSN 13596454. doi: 10.1016/j.actamat.2017.08.023. URL https://doi.org/10.1016/j.actamat.2017.08.023.

[29] C.E. Krill III and L.Q. Chen. Computer simulation of 3-D grain growth using a phase-field model. *Acta Materialia*, 50:3057–3073, 2002.

[30] K. Ahmed, C. a. Yablinsky, A. Schulte, T. Allen, and A. El-Azab. Phase field modeling of the effect of porosity on grain growth kinetics in polycrystalline ceramics. *Modelling and Simulation in Materials Science and Engineering*, 21(6):065005, 2013. ISSN 0965-0393. doi: 10.1088/0965-0393/21/6/065005. URL https://doi.org/10.1088/0965-0393/21/6/065005.

[31] Johannes Hötzer, Veronika Rehn, Wolfgang Rheinheimer, Michael J. Hoffmann, and Britta Nestler. Phase-field study of pore-grain boundary interaction. *Journal of the Ceramic Society of Japan*, 124(4):329–339, 2016. doi: 10.2109/jcersj2.15266. URL https://doi.org/10.2109/jcersj2.15266.

[32] Eisuke Miyoshi, Tomohiro Takaki, Munekazu Ohno, Yasushi Shibuta, Shinji Sakane, Takashi Shimokawabe, and Takayuki Aoki. Ultra-large-scale phase-field simulation study of ideal grain growth. *npj Computational Materials*, 3(June):25, 2017. ISSN 2057-3960. doi: 10.1038/s41524-017-0029-8. URL https://doi.org/10.1038/s41524-017-0029-8. Publisher: Springer US.

[33] Yu U. Wang. Computer modeling and simulation of solid-state sintering: A phase field approach. *Acta Materialia*, 54(4):953–961, 2006. ISSN 13596454. doi: 10.1016/j.actamat.2005.10.032. URL https://doi.org/10.1016/j.actamat.2005.10.032.

[34] Sudipta Biswas, Daniel Schwen, Jogender Singh, and Vikas Tomar. A study of the evolution of microstructure and consolidation kinetics during sintering using a phase field modeling based approach. *Extreme Mechanics Letters*, 7:78–89, 2016. ISSN 23524316. doi: 10.1016/j.eml.2016.02.017. URL https://doi.org/10.1016/j.eml.2016.02.017.

[35] Johannes Hötzer, Marco Seiz, Michael Kellner, Wolfgang Rheinheimer, and Britta Nestler. Phase-field simulation of solid state sintering. *Acta Materialia*, 164:184–195,

2019. ISSN 1359-6454. doi: 10.1016j.actamat.2018.10.021. URL https://doi.org/10.1016/j.actamat.2018.10.021.

[36] Rongpei Shi, Marissa Wood, Tae Wook Heo, Brandon C. Wood, and Jianchao Ye. Towards understanding particle rigid-body motion during solid-state sintering. *Journal of the European Ceramic Society*, 41(16):211–231, 2021. ISSN 0955-2219. doi: 10.1016j.jeurceramsoc.2021.09.039. URL https://doi.org/10.1016/j.jeurceramsoc.2021.09.039.

[37] Daniel A. Cogswell. Quantitative phase-field modeling of dendritic electrodeposition. *Physical Review E*, 92(1):011301, July 2015. ISSN 1539-3755, 1550-2376. doi: 10.1103/PhysRevE.92.011301. URL https://doi.org/10.1103/PhysRevE.92.011301.

[38] Toshiyuki Koyama. Phase-field modeling of microstructure evolutions in magnetic materials. *Science and Technology of Advanced Materials*, 9(1):013006, January 2008. ISSN 1468-6996, 1878-5514. doi: 10.1088/1468-6996/9/1/013006. URL https://doi.org/10.1088/1468-6996/9/1/013006.

[39] D. Rodney, Y. Le Bouar, and A. Finel. Phase field methods and dislocations. *Acta Materialia*, 51(1):17–30, January 2003. ISSN 13596454. doi: 10.1016/S1359-6454(01)00379-2. URL https://doi.org/10.1016/S1359-6454(01)00379-2.

[40] Robert DeHoff. *Thermodynamics in Materials Science, Second Edition*. CRC Press, Boca Raton, 2006. ISBN 0849340659; 9780849340659.

[41] R. W. Balluffi, Samuel M. Allen, W. Craig Carter, and Rachel A. Kemper. *Kinetics of materials*. J. Wiley & Sons, Hoboken, N.J, 2005. ISBN 978-0-471-24689-3.

[42] W. Kurz. A brief history of the science of dendritic and eutectic growth until 1980. *Materials Science Forum - MATER SCI FORUM*, 508:313–324, March 2006. doi: 10.4028/www.scientific.net/MSF.508.313. URL https://doi.org/10.4028/www.scientific.net/MSF.508.313.

[43] Wilfried Kurz, David J. Fisher, and Rohit Trivedi. Progress in modelling solidification microstructures in metals and alloys: dendrites and cells from 1700 to 2000. *International Materials Reviews*, 64(6):311–354, August 2019. ISSN 0950-6608, 1743-2804. doi: 10.1080/09506608.2018.1537090. URL https://doi.org/10.1080/09506608.2018.1537090.

[44] Wilfried Kurz, Michel Rappaz, and Rohit Trivedi. Progress in modelling solidification microstructures in metals and alloys. Part II: dendrites from 2001 to 2018. *International Materials Reviews*, 66(1):30–76, January 2021. ISSN 0950-6608, 1743-2804.

doi: 10.1080/09506608.2020.1757894. URL https://doi.org/10.1080/09506608.2020.1757894.

[45] Sylvain Deville. *Freezing colloids : observations, principles, control, and use : applications in materials science, life science, earth science, food science, and engineering*. Springer, Cham, Switzerland, 2017. ISBN 3-319-50515-7. doi: 10.1007/978-3-319-50515-2. URL https://doi.org/10.1007/978-3-319-50515-2.

[46] Randall M. German. Sintering Trajectories: Description on How Density, Surface Area, and Grain Size Change. *JOM*, 68(3):878–884, March 2016. ISSN 1047-4838, 1543-1851. doi: 10.1007/s11837-015-1795-8. URL https://doi.org/10.1007/s11837-015-1795-8.

[47] L. Kaufman and H. Bernstein. *Computer Calculation of Phase Diagrams with Special Reference to Refractory Metals*. Notes and Reports in Computer Science and Applied Mathematic. Academic Press, New York, 1970. ISBN 9780124020504.

[48] Nigel Saunders and A Peter Miodownik. *CALPHAD (calculation of phase diagrams): a comprehensive guide*. Elsevier, New York, 1998. ISBN 0-08-0421296.

[49] Clarence Zener. Kinetics of the decomposition of austenite. *Trans. Aime*, 167:550, 1946.

[50] M. E. Glicksman, R. J. Schaefer, and J. D. Ayers. Dendritic growth-a test of theory. *Metallurgical Transactions A*, 7(11):1747–1759, Nov 1976. ISSN 2379-0180. doi: 10.1007/BF03186673. URL https://doi.org/10.1007/BF03186673.

[51] E. Ben-Jacob, Nigel Goldenfeld, J. S. Langer, and Gerd Schön. Dynamics of interfacial pattern formation. *Phys. Rev. Lett.*, 51:1930–1932, Nov 1983. doi: 10.1103/PhysRevLett.51.1930. URL https://doi.org/10.1103/PhysRevLett.51.1930.

[52] P. Pelce and D. Bensimon. Theory of Dendrite Dynamics. *Nuclear Physics B*, 2: 259–270, 1987.

[53] D. A. Kessler and H. Levine. Pattern selection in three dimensional dendritic growth. *Acta Metallurgica*, 36(10):2693–2706, 1988. ISSN 00016160. doi: 10.1016/0001-6160(88)90116-2. URL https://doi.org/10.1016/0001-6160(88)90116-2.

[54] A. Choudhury and B. Nestler. Grand-potential formulation for multicomponent phase transformations combined with thin-interface asymptotics of the double-obstacle potential. *Physical Review E*, 85(2):021602, 2012.

[55] A Pineau, G Guillemot, D Tourret, A Karma, and Ch-A Gandin. Growth competition between columnar dendritic grains–cellular automaton versus phase field modeling. *Acta Materialia*, 155:286–301, 2018.

[56] G. A. Santos, P. R. Goulart, A. A. Couto, and A. Garcia. Primary Dendrite ARM Spacing Effects upon Mechanical Properties of an AL–3Wt%CU–1Wt%LI Alloy. In Andreas Öchsner and Holm Altenbach, editors, *Properties and Characterization of Modern Materials*, pages 215–229. Springer Singapore, Singapore, 2017. ISBN 978-981-10-1602-8. doi: 10.1007/978-981-10-1602-8_19. URL https://doi.org/10.1007/978-981-10-1602-8_19.

[57] Joel Strickland, Bogdan Nenchev, and Hongbiao Dong. On directional dendritic growth and primary spacing—a review. *Crystals*, 10(7), 2020. ISSN 2073-4352. doi: 10.3390/cryst10070627. URL https://doi.org/10.3390/cryst10070627.

[58] Ch. A. Gandin, M. Eshelman, and R. Trivedi. Orientation dependence of primary dendrite spacing. *Metallurgical and Materials Transactions A*, 27(9):2727–2739, September 1996. ISSN 1073-5623, 1543-1940. doi: 10.1007/BF02652367. URL https://doi.org/10.1007/BF02652367.

[59] Erich Scheil. Über die eutektische kristallisation. *Z. Metallkunde*, 37(1-2):1–11, 1946. URL https://doi.org/10.1515/ijmr-1946-371-201.

[60] WH Brandt. Solution of the diffusion equation applicable to the edgewise growth of pearlite. *Journal of Applied Physics*, 16(3):139–146, 1945. Publisher: American Institute of Physics.

[61] MATS Hillert. Pressure induced diffusion and deformation during precipitation, especially graphitization. *Jernkont. Ann*, 141:157–181, 1957.

[62] K.A. Jackson and J.D. Hunt. Lamellar and rod eutectic growth. *Trans. Met. Soc. AIME*, 236:1129–1142, 01 1966. doi: 10.1016/B978-0-08-092523-3.50040-X. URL https://doi.org/10.1016/B978-0-08-092523-3.50040-X.

[63] R Trivedi, JT Mason, JD Verhoeven, and W Kurz. Eutectic spacing selection in lead-based alloy systems. *Metallurgical Transactions A*, 22(10):2523–2533, 1991.

[64] A Ourdjini, Jincheng Liu, and R Elliott. Eutectic spacing selection in Al-Cu system. *Materials Science and Technology*, 10(4):318–318, 1994.

[65] D. Lewis, J. Warren, W. Boettinger, T. Pusztai, and L. Gránásy. Phase-field models for eutectic solidification. *JOM*, 56(4):34–39, 2004.

[66] Silvère Akamatsu and Mathis Plapp. Eutectic and peritectic solidification patterns. *Current Opinion in Solid State and Materials Science*, 20(1):46–54, 2016.

[67] B. Nestler and A. Choudhury. Phase-field modeling of multi-component systems. *Current Opinion in Solid State and Materials Science*, 15(3):93–105, June 2011. ISSN 13590286.

[68] J. Hötzer, C. Seer, and B. Nestler. Generierung von dreidimensionalen Pulverstrukturen. *Forschung aktuell 2016*, pages 32 – 35, 2016. ISSN 1613-4958.

[69] Marco Seiz, Michael Kellner, and Britta Nestler. Simulation of dendritic-eutectic growth with the phase-field method. *Acta Materialia*, 254:118965, May 2023. ISSN 13596454. doi: 10.1016/j.actamat.2023.118965. URL https://doi.org/10.1016/j.actamat.2023.118965.

[70] M. H. Burden and J. D. Hunt. The extent of the eutectic range. *Journal of Crystal Growth*, 22(4):328–330, 1974. ISSN 00220248. doi: 10.1016/0022-0248(74)90178-X. URL https://doi.org/10.1016/0022-0248(74)90178-X.

[71] M Trepczyńska Lent. Coupled and competitive eutectic growth. *Archives of Foundry Engineering*, 11:237–240, 2011.

[72] J Eiken and M Apel. Eutectic morphology evolution and Sr-modification in Al-Si based alloys studied by 3D phase-field simulation coupled to Calphad data. *IOP Conference Series: Materials Science and Engineering*, 84:012084, June 2015. ISSN 1757-8981, 1757-899X. doi: 10.1088/1757-899X/84/1/012084. URL https://doi.org/10.1088/1757-899X/84/1/012084.

[73] Kai Wang and Lijun Zhang. Quantitative phase-field simulation of the entire solidification process in one hypereutectic Al–Si alloy considering the effect of latent heat. *Progress in Natural Science: Materials International*, 31(3):428–433, June 2021. ISSN 10020071. doi: 10.1016/j.pnsc.2021.04.009. URL https://doi.org/10.1016/j.pnsc.2021.04.009.

[74] Cheng Gu, Michael P. Moodispaw, and Alan A. Luo. Cellular automaton simulation and experimental validation of eutectic transformation during solidification of Al-Si alloys. *npj Computational Materials*, 8(1):134, June 2022. ISSN 2057-3960. doi: 10.1038/s41524-022-00824-5. URL https://doi.org/10.1038/s41524-022-00824-5.

[75] S. S. L. Peppin, J. a. W. Elliott, and M. G. Worster. Pressure and relative motion in colloidal suspensions. *Physics of Fluids*, 17(5):1–10, 2005. ISSN 10706631. doi: 10.1063/1.1915027. URL https://doi.org/10.1063/1.1915027.

[76] S. S.L. Peppin, J. A.W. Elliott, and M. Grae Worster. Solidification of colloidal suspensions. *Journal of Fluid Mechanics*, 554:147–166, 2006. ISSN 00221120. doi: 10.1017/S0022112006009268. URL https://doi.org/10.1017/S0022112006009268.

[77] Stephen S.L. Peppin, M. Grae Worster, and J. S. Wettlaufer. Morphological instability in freezing colloidal suspensions. *Proceedings of the Royal Society A: Mathematical, Physical and Engineering Sciences*, 463(2079):723–733, 2007. ISSN 14712946. doi: 10.1098/rspa.2006.1790. URL https://doi.org/10.1098/rspa.2006.1790.

[78] S. S. L. Peppin, J. S. Wettlaufer, and M. G. Worster. Experimental verification of morphological instability in freezing aqueous colloidal suspensions. *Physical Review Letters*, 100(23):1–4, 2008. ISSN 00319007. doi: 10.1103/PhysRevLett.100.238301. URL https://doi.org/10.1103/PhysRevLett.100.238301.

[79] Tsung Hui Huang, Tzu Hsuan Huang, Yang Shan Lin, Chih Hsiang Chang, Po Yu Chen, Shu Wei Chang, and Chuin Shan Chen. Phase-Field Modeling of Microstructural Evolution by Freeze-Casting. *Advanced Engineering Materials*, 20(3):1–13, 2018. ISSN 15272648. doi: 10.1002/adem.201700343. URL https://doi.org/10.1002/adem.201700343.

[80] Marco Seiz and Britta Nestler. Modelling and simulation of the freeze casting process with the phase-field method. *Computational Materials Science*, 193:110410, 2021. ISSN 0927-0256. doi: 10.1016j.commatsci.2021.110410. URL https://doi.org/10.1016/j.commatsci.2021.110410.

[81] Kaiyang Yin, Kaihua Ji, Louise Strutzenberg Littles, Rohit Trivedi, Alain Karma, and Ulrike G. K. Wegst. Hierarchical structure formation by crystal growth-front instabilities during ice templating. *Proceedings of the National Academy of Sciences*, 120(23):e2210242120, June 2023. ISSN 0027-8424, 1091-6490. doi: 10.1073/pnas.2210242120. URL https://doi.org/10.1073/pnas.2210242120.

[82] Henning Aufgebauer, Julia Kundin, Heike Emmerich, Maral Azizi, Christian Reimann, Jochen Friedrich, Thomas Jauß, Tina Sorgenfrei, and Arne Cröll. Phase-field simulations of particle capture during the directional solidification of silicon. *Journal of Crystal Growth*, 446:12–26, July 2016. ISSN 00220248. doi: 10.1016/j.jcrysgro.2016.04.032. URL https://doi.org/10.1016/j.jcrysgro.2016.04.032.

[83] B. Echebarria, R. Folch, A. Karma, and M. Plapp. Quantitative phase-field model of alloy solidification. *Physical Review E*, 70(6):061604, 2004.

[84] Gunnar Schubert. *Thick Film Metallisation of Crystalline Silicon Solar Cells*. PhD thesis, Universität Konstanz, 2006. URI http://nbn-resolving.de/urn:nbn:de:bsz:352-opus-25592; accessed October 2023.

[85] Cori N Bucherl, Karl R Oleson, and Hugh W Hillhouse. Thin film solar cells from sintered nanocrystals. *Current Opinion in Chemical Engineering*, 2(2):168–177, May 2013. ISSN 22113398. doi: 10.1016/j.coche.2013.03.004. URL https://doi.org/10.1016/j.coche.2013.03.004.

[86] Jorg Schube, Leonard Tutsch, Tobias Fellmeth, Martin Bivour, Frank Feldmann, Thibaud Hatt, Florian Maier, Roman Keding, Florian Clement, and Stefan W. Glunz. Low-Resistivity Screen-Printed Contacts on Indium Tin Oxide Layers for Silicon Solar Cells With Passivating Contacts. *IEEE Journal of Photovoltaics*, 8(5):1208–1214, September 2018. ISSN 2156-3381, 2156-3403. doi: 10.1109/JPHOTOV.2018.2859768. URL https://doi.org/10.1109/JPHOTOV.2018.2859768.

[87] B.J. Kellett and F.F. Lange. Thermodynamics of Densification: I, Sintering of Simple Particle Arrays, Equilibrium Configurations, Pore Stability, and Shrinkage. *Journal of the American Ceramic Society*, 72(5):725–734, 1989. doi: doi.org/10.1111/j.1151-2916.1989.tb06208.x. URL https://doi.org/doi.org/10.1111/j.1151-2916.1989.tb06208.x.

[88] R. L. Coble. Sintering Crystalline Solids. I. Intermediate and Final State Diffusion Models. *Journal of Applied Physics*, 32(5):787–792, May 1961. ISSN 0021-8979, 1089-7550. doi: 10.1063/1.1736107. URL https://doi.org/10.1063/1.1736107.

[89] F. A. Nichols and W. W. Mullins. Morphological changes of a surface of revolution due to capillarity-induced surface diffusion. *Journal of Applied Physics*, 36(6):1826–1835, 1965. ISSN 00218979. doi: 10.1063/1.1714360. URL https://doi.org/10.1063/1.1714360.

[90] Omar Hussein, D. Keith Coffman, Khalid Hattar, Eric Lang, Shen J. Dillon, and Fadi Abdeljawad. Plateau–Rayleigh instability with a grain boundary twist. *Applied Physics Letters*, 121(14):141601, October 2022. ISSN 0003-6951, 1077-3118. doi: 10.1063/5.0103658. URL https://doi.org/10.1063/5.0103658.

[91] Takuji Oda. Thermodynamic model for grain boundary effects on hydrogen solubility, diffusivity and permeability in poly-crystalline tungsten. *Fusion Engineering and Design*, 112:102–116, November 2016. ISSN 09203796. doi: 10.1016/j.fusengdes.2016.08.001. URL https://doi.org/10.1016/j.fusengdes.2016.08.001.

[92] Edvinas Navickas, Tobias M. Huber, Yan Chen, Walid Hetaba, Gerald Holzlechner, Ghislain Rupp, Michael Stöger-Pollach, Gernot Friedbacher, Herbert Hutter, Bilge Yildiz, and Jürgen Fleig. Fast oxygen exchange and diffusion kinetics of grain boundaries in Sr-doped $LaMnO_3$ thin films. *Physical Chemistry Chemical Physics*, 17(12): 7659–7669, 2015. ISSN 1463-9076, 1463-9084. doi: 10.1039/C4CP05421K. URL https://doi.org/10.1039/C4CP05421K.

[93] Jonathan M. Polfus, Bilge Yildiz, and Harry L. Tuller. Origin of fast oxide ion diffusion along grain boundaries in Sr-doped $LaMnO_3$. *Physical Chemistry Chemical Physics*, 20(28):19142–19150, 2018. ISSN 1463-9076, 1463-9084. doi: 10.1039/C8CP02443J. URL https://doi.org/10.1039/C8CP02443J.

[94] L. C. Liu and H. R. Gong. Hydrogen solubility and diffusivity at $\sigma 3$ grain boundary of PdCu. *RSC Advances*, 11(22):13644–13652, 2021. ISSN 2046-2069. doi: 10.1039/D0RA10133H. URL https://doi.org/10.1039/D0RA10133H.

[95] V. Rehn, J. Hötzer, W. Rheinheimer, M. Seiz, C. Serr, and B. Nestler. Phase-field study of grain growth in porous polycrystals. *Acta Materialia*, 174:439–449, 2019.

[96] E. Rabkin. On the grain size dependent solute and particle drag. *Scripta Materialia*, 42(12):1199–1206, jun 2000. ISSN 13596462. doi: 10.1016/S1359-6462(00)00359-6. URL https://doi.org/10.1016/S1359-6462(00)00359-6.

[97] M. Hillert. On the theory of normal and abnormal grain growth. *Acta Metall. Mater.*, 13:227–238, 1965.

[98] Guillaume Bernard-Granger, Nathalie Monchalin, and Christian Guizard. Sintering of ceramic powders: Determination of the densification and grain growth mechanisms from the "grain size/relative density" trajectory. *Scripta Materialia*, 57(2):137–140, 2007. ISSN 1359-6462. doi: 10.1016j.scriptamat.2007.03.030. URL https://doi.org/10.1016/j.scriptamat.2007.03.030.

[99] Randall M. German. Coarsening in Sintering: Grain Shape Distribution, Grain Size Distribution, and Grain Growth Kinetics in Solid-Pore Systems. *Critical Reviews in Solid State and Materials Sciences*, 35(4):263–305, 2010. ISSN 1040-8436. doi: 10.1080/10408436.2010.525197. URL https://doi.org/10.1080/10408436.2010.525197.

[100] Randall M. German. Coordination number changes during powder densification. *Powder Technology*, 253:368–376, February 2014. ISSN 00325910. doi: 10.1016/j.powtec.2013.12.006. URL https://doi.org/10.1016/j.powtec.2013.12.006.

[101] F. Wakai and O. Guillon. Evaluation of sintering stress from 3-D visualization of microstructure: Case study of glass films sintered by viscous flow and imaged by X-ray microtomography. *Acta Materialia*, 66:54–62, March 2014. ISSN 13596454. doi: 10.1016/j.actamat.2013.11.070. URL https://doi.org/10.1016/j.actamat.2013.11.070.

[102] Gaku Okuma, Daiki Kadowaki, Tsuyoshi Hondo, Satoshi Tanaka, and Fumihiro Wakai. Interface topology for distinguishing stages of sintering. *Scientific Reports*, 7 (1):11106, September 2017. ISSN 2045-2322. doi: 10.1038/s41598-017-11667-2. URL https://doi.org/10.1038/s41598-017-11667-2.

[103] V. Kumar, Z. Z. Fang, and P. C. Fife. Phase field simulations of grain growth during sintering of two unequal-sized particles. *Materials Science and Engineering A*, 528(1):254–259, 2010. ISSN 09215093. doi: 10.1016/j.msea.2010.08.061. URL https://doi.org/10.1016/j.msea.2010.08.061.

[104] Ian Greenquist, Michael R Tonks, Larry K Aagesen, and Yongfeng Zhang. Development of a microstructural grand potential-based sintering model. *Computational Materials Science*, 172:109288, 2020. ISSN 0927-0256. doi: 10.1016/j.commatsci.2019.109288. URL https://doi.org/10.1016/j.commatsci.2019.109288.

[105] A Kazaryan, Y Wang, and Bruce R Patton. Generalized phase field approach for computer simulation of sintering: incorporation of rigid-body motion. *Scripta materialia*, 41(5):487–492, 1999.

[106] Fadi Abdeljawad, Dan S Bolintineanu, Adam Cook, Harlan Brown-Shaklee, Christopher DiAntonio, Daniel Kammler, and Allen Roach. Sintering processes in direct ink write additive manufacturing : A mesoscopic modeling approach. *Acta Materialia*, 169:60–75, 2019. ISSN 1359-6454. doi: 10.1016/j.actamat.2019.01.011. URL https://doi.org/10.1016/j.actamat.2019.01.011.

[107] Robert Termuhlen, Xanthippi Chatzistavrou, Jason D Nicholas, and Hui-Chia Yu. Three-dimensional phase field sintering simulations accounting for the rigid-body motion of individual grains. *Computational Materials Science*, 186:109963, 2021. ISSN 0927-0256. doi: 10.1016/j.commatsci.2020.109963. URL https://doi.org/10.1016/j.commatsci.2020.109963.

[108] Sudipta Biswas, Daniel Schwen, Jogender Singh, and Vikas Tomar. A study of the evolution of microstructure and consolidation kinetics during sintering using a phase field modeling based approach. *Extreme Mechanics Letters*, 7:78–89, 2016.

[109] Sudipta Biswas, Daniel Schwen, and Vikas Tomar. Implementation of a phase field model for simulating evolution of two powder particles representing microstructural changes during sintering. *Journal of Materials Science*, 53:1–27, 2018. URL https://doi.org/10.1007/s10853-017-1846-3.

[110] Branislav Dzepina, Daniel Balint, and Daniele Dini. A phase-field model of pressure-assisted sintering. *Journal of the European Ceramic Society*, 39:173–182, 2019. ISSN 0955-2219. doi: 10.1016/j.jeurceramsoc.2018.09.014. URL https://doi.org/10.1016/j.jeurceramsoc.2018.09.014.

[111] Xiao Wang, Yuan Liu, Like Li, Caleb O Yenusah, Yaohong Xiao, and Lei Chen. Multi-scale phase-field modeling of layer-by-layer powder compact densification during solid-state direct metal laser sintering. *Materials & Design*, 203, 2021. ISSN 0264-1275. doi: 10.1016/j.matdes.2021.109615. URL https://doi.org/10.1016/j.matdes.2021.109615.

[112] Vladimir Ivannikov, Fritz Thomsen, Thomas Ebel, and Regine Willumeit-Römer. Capturing shrinkage and neck growth with phase field simulations of the solid state sintering. *Modelling and Simulation in Materials Science and Engineering*, 29(7): 075008, sep 2021. doi: 10.1088/1361-651X/ac1f87. URL https://doi.org/10.1088/1361-651X/ac1f87.

[113] Marco Seiz. Effect of rigid body motion in phase-field models of solid-state sintering. *Computational Materials Science*, 215, 2022. ISSN 0927-0256. doi: 10.1016/j.commatsci.2022.111756. URL https://doi.org/10.1016/j.commatsci.2022.111756. Publisher: Elsevier B.V.

[114] Marco Seiz, Henrik Hierl, and Britta Nestler. An improved grand-potential phase-field model of solid-state sintering for many particles. *Modelling and Simulation in Materials Science and Engineering*, 31(5):055006, July 2023. ISSN 0965-0393, 1361-651X. doi: 10.1088/1361-651X/acd56d. URL https://doi.org/10.1088/1361-651X/acd56d.

[115] Marco Seiz, Henrik Hierl, and Britta Nestler. Unravelling densification during sintering by multiscale modelling of grain motion. *Journal of Materials Science*, 58 (35):14051–14071, Sep 2023. ISSN 1573-4803. doi: 10.1007/s10853-023-08859-9. URL https://doi.org/10.1007/s10853-023-08859-9.

[116] Marco Seiz, Henrik Hierl, Britta Nestler, and Wolfgang Rheinheimer. Revealing process and material parameter effects on densification via phase-field studies. 2023. doi: 10.48550/arXiv.2308.09682. URL https://doi.org/10.48550/arXiv.2308.09682.

[117] A. Choudhury, K. Reuther, E. Wesner, A. August, B. Nestler, and M. Rettenmayr. Comparison of phase-field and cellular automaton models for dendritic solidification in Al–Cu alloy. *Computational Materials Science*, 55:263–268, 2012.

[118] M. Fleck, L. Mushongera, D. Pilipenko, K. Ankit, and H. Emmerich. On phase-field modeling with a highly anisotropic interfacial energy. *European Physical Journal Plus*, 126(10):1–11, 2011. ISSN 21905444. doi: 10.1140/epjp/i2011-11095-7. URL https://doi.org/10.1140/epjp/i2011-11095-7. ISBN: 2190-5444.

[119] Johannes Hötzer, Oleg Tschukin, Marouen Ben Said, Marco Berghoff, Marcus Jainta, Georges Barthelemy, Nikolay Smorchkov, Daniel Schneider, Michael Selzer, and Britta Nestler. Calibration of a multi-phase field model with quantitative angle measurement. *Journal of Materials Science*, 51(4):1788–1797, 2015. ISSN 1573-4803. doi: 10.1007/s10853-015-9542-7. URL https://doi.org/10.1007/s10853-015-9542-7.

[120] Simon Daubner, Paul W. Hoffrogge, Martin Minar, and Britta Nestler. Triple junction benchmark for multiphase-field and multi-order parameter models. *Computational Materials Science*, 219:111995, February 2023. ISSN 09270256. doi: 10.1016/j.commatsci.2022.111995. URL https://doi.org/10.1016/j.commatsci.2022.111995.

[121] N. Moelans. A quantitative and thermodynamically consistent phase-field interpolation function for multi-phase systems. *Acta Materialia*, 59(3):1077–1086, 2011. ISSN 1359-6454. doi: 10.1016j.actamat.2010.10.038. URL http://dx.doi.org/10.1016/j.actamat.2010.10.038.

[122] Samuel M. Allen and John W. Cahn. A microscopic theory for antiphase boundary motion and its application to antiphase domain coarsening. *Acta Metallurgica*, 27(6):1085–1095, June 1979. ISSN 00016160. doi: 10.1016/0001-6160(79)90196-2. URL https://doi.org/10.1016/0001-6160(79)90196-2.

[123] Sumanth Nani Enugala. *Some refinements in the phase-field and sharp interface treatments of eutectic growth*. PhD thesis, Karlsruher Institut für Technologie (KIT), 2021. URL https://doi.org/10.5445/IR/1000134170. doi: 10.5445/IR/1000134170.

[124] M. Plapp. Unified derivation of phase-field models for alloy solidification from a grand-potential functional. *Physical Review E*, 84(3):031601, 2011.

[125] James A. Warren and J. S. Langer. Prediction of dendritic spacings in a directional-solidification experiment. *Phys. Rev. E*, 47(4):2702–2712, April 1993. doi: 10.1103/Ph

ysRevE.47.2702. URL https://doi.org/10.1103/PhysRevE.47.2702. Publisher: American Physical Society.

[126] Julia Kundin, Hedieh Farhandi, Priya Kamatchi Ganesan, Renato S M Almeida, Kamen Tushtev, and Kurosch Rezwan. Phase-field modeling of grain growth in presence of grain boundary diffusion and segregation in ceramic matrix mini-composites. *Computational Materials Science*, 190:110295, 2021. ISSN 0927-0256. doi: 10.1016/j.commatsci.2021.110295. URL https://doi.org/10.1016/j.commatsci.2021.110295. Publisher: Elsevier B.V.

[127] Klara Asp and A John. Phase-field simulation of sintering and related phenomena – A vacancy diffusion approach. *Acta Materialia*, 54:1241–1248, 2006. doi: 10.1016/j.actamat.2005.11.005.

[128] Clawpack Development Team. Clawpack software, 2020; accessed July 2023. URL https://doi.org/10.5281/zenodo.4025432. Version 5.7.1.

[129] Kyle T Mandli, Aron J Ahmadia, Marsha Berger, Donna Calhoun, David L George, Yiannis Hadjimichael, David I Ketcheson, Grady I Lemoine, and Randall J LeVeque. Clawpack: building an open source ecosystem for solving hyperbolic pdes. *PeerJ Computer Science*, 2:e68, 2016. doi: 10.7717/peerj-cs.68. URL https://doi.org/10.7717/peerj-cs.68.

[130] David I. Ketcheson, Kyle T. Mandli, Aron J. Ahmadia, Amal Alghamdi, Manuel Quezada de Luna, Matteo Parsani, Matthew G. Knepley, and Matthew Emmett. PyClaw: Accessible, Extensible, Scalable Tools for Wave Propagation Problems. *SIAM Journal on Scientific Computing*, 34(4):C210–C231, November 2012.

[131] Robert L. Coble. Diffusion Models for Hot Pressing with Surface Energy and Pressure Effects as Driving Forces. *Journal of Applied Physics*, 41(12):4798–4807, November 1970. ISSN 0021-8979, 1089-7550. doi: 10.1063/1.1658543. URL https://doi.org/10.1063/1.1658543.

[132] Chao Yang, Houbing Huang, Wenbo Liu, Junsheng Wang, Jing Wang, Hasnain Mehdi Jafri, Yu Liu, Guomin Han, Haifeng Song, and Long-qing Chen. Explicit Dynamics of Diffuse Interface in Phase-Field Model. *Advanced Theory and Simulation*, 4(1):2000162, 2020. doi: 10.1002/adts.202000162. URL https://doi.org/10.1002/adts.202000162.

[133] Abhik Choudhury, Michael Kellner, and Britta Nestler. A method for coupling the phase-field model based on a grand-potential formalism to thermodynamic databases. *Current Opinion in Solid State and Materials Science*, 19(5):287–300, 2015.

[134] Rainer Feistel and Wolfgang Wagner. A New Equation of State for Ice Ih A New Equation of State for H2O Ice Ih. *Journal of Physical and Chemical Reference Data*, 35(2):1021–1047, 2006. doi: 10.1063/1.2183324. URL https://doi.org/10.1063/1.2183324.

[135] Marco Seiz, Michael Kellner, and Britta Nestler. Simulation of dendritic–eutectic growth with the phase-field method. 2023. doi: 10.48550/arXiv.2301.08593. URL https://doi.org/10.48550/arXiv.2301.08593.

[136] Marco Seiz. Modellierung des gekoppelt dendritisch-eutektischen wachstums mit der phasenfeldmethode. Master's thesis, Karlsruhe Institute of Technology, 2017. (unpublished).

[137] J. Lipton, M. E. Glicksman, and W. Kurz. Dendritic growth into undercooled alloy metals. *Materials Science and Engineering*, 65(1):57–63, 1984. ISSN 00255416. doi: 10.1016/0025-5416(84)90199-X. URL https://doi.org/10.1016/0025-5416(84)90199-X. ISBN: 0025-5416.

[138] V. Witusiewicz, U. Hecht, S. Fries, and S. Rex. The Ag–Al–Cu system: Part I: Reassessment of the constituent binaries on the basis of new experimental data. *Journal of alloys and compounds*, 385(1):133–143, 2004.

[139] Michael Fleck, Felix Schleifer, and Patrick Zimbrod. Frictionless motion of diffuse interfaces by sharp phase-field modeling. 2022. doi: 10.48550/arXiv.1910.05180. URL https://doi.org/10.48550/arXiv.1910.05180. _eprint: arXiv:1910.05180v3.

[140] Abhik Choudhury, Mathis Plapp, and Britta Nestler. Theoretical and numerical study of lamellar eutectic three-phase growth in ternary alloys. *Physical Review E*, 83(5):051608, 2011.

[141] P. Steinmetz, Y.C. Yabansu, J. Hötzer, M. Jainta, B. Nestler, and S.R. Kalidindi. Analytics for microstructure datasets produced by phase-field simulations. *Acta Materialia*, 103:192–203, 2016.

[142] Michael Kellner, Johannes Hötzer, Ephraim Schoof, and Britta Nestler. Phase-field study of eutectic colony formation in NiAl-34Cr. *Acta Materialia*, 182:267–277, 2020.

[143] Marco Seiz. Supplementary Data to "Simulation of dendritic- eutectic growth with the phase-field method" by Seiz et al., January 2023. URL https://doi.org/10.5281/zenodo.7516370. accessed October 2023.

[144] William Silversmith. Connected components on multilabel 3d images. https://pypi.org/project/connected-components-3d/. Accessed: June 2023.

[145] Martin Zimmermann, Alain Karma, and Michel Carrard. Oscillatory lamellar microstructure in off-eutectic Al-Cu alloys. *Physical Review B*, 42(1):833–837, jul 1990. ISSN 0163-1829, 1095-3795. doi: 10.1103/PhysRevB.42.833. URL https://doi.org/10.1103/PhysRevB.42.833.

[146] Andrea Parisi and Mathis Plapp. Defects and multistability in eutectic solidification patterns. *EPL (Europhysics Letters)*, 90(2):26010, 2010.

[147] László Rátkai, Gyula I. Tóth, László Környei, Tamás Pusztai, and László Gránásy. Phase-field modeling of eutectic structures on the nanoscale: the effect of anisotropy. *Journal of Materials Science*, 52(10):5544–5558, May 2017. ISSN 0022-2461, 1573-4803. doi: 10.1007/s10853-017-0853-8. URL https://doi.org/10.1007/s10853-017-0853-8.

[148] S R Coriell, S C Hardy, and R F Sekerka. A non-linear analysis of experiments on the morphological stability of ice cylinders freezing from aqueous solutions. *Journal of Crystal Growth*, 11:53–67, 1971.

[149] D. R. H. Jones. The measurement of solid-liquid interfacial energies from the shapes of grain-boundary grooves. *The Philosophical Magazine: A Journal of Theoretical Experimental and Applied Physics*, 27(3):569–584, 1973. doi: 10.1080/14786437308219232. URL https://doi.org/10.1080/14786437308219232.

[150] S C Hardy. A grain boundary groove measurement of the surface tension between ice and water. *The Philosophical Magazine: A Journal of Theoretical Experimental and Applied Physics*, 35:471–484, 1977. doi: 10.1080/14786437708237066. URL https://doi.org/10.1080/14786437708237066.

[151] László Gránásy, Tamás Pusztai, and Peter F James. Interfacial properties deduced from nucleation experiments: A Cahn-Hilliard analysis. *Journal of Chemical Physics*, 117:6157–6168, 2002. doi: 10.1063/1.1502652. URL https://doi.org/10.1063/1.1502652.

[152] T Kuroda and R Lacmann. GROWTH KINETICS OF ICE FROM THE VAPOUR PHASE AND ITS GROWTH FORMS. *Journal of Crystal Growth*, 56:189–205, 1982.

[153] Richard Handel, Ruslan L Davidchack, Jamshed Anwar, and Andrey Brukhno. Direct Calculation of Solid-Liquid Interfacial Free Energy for Molecular Systems : TIP4P Ice-Water Interface. *Physical review letters*, 036104(January):1–4, 2008. doi: 10.1103/PhysRevLett.100.036104. URL https://doi.org/10.1103/PhysRevLett.100.036104.

[154] Ruslan L Davidchack, Richard Handel, Jamshed Anwar, and Andrey V Brukhno. Ice Ih-Water Interfacial Free Energy of Simple Water Models with Full Electrostatic Interactions. *Journal of Chemical Theory and Computation*, 8(7):2383–2390, 2012. doi: 10.1021/ct300193e. URL https://doi.org/10.1021/ct300193e.

[155] Peter V Hobbs. *Ice physics*. Oxford university press, New York, 1973.

[156] Minoru Maruyama, Yuko Kishimoto, and Tsutomu Sawada. Optical study of roughening transition on ice I h (1010) planes. *Journal of Crystal Growth*, 172:521–527, 1997.

[157] Kazushige Nagashima and Yoshinori Furukawa. Nonequilibrium effect of anisotropic interface kinetics on the directional growth of ice crystals. *Journal of Crystal Growth*, 171:577–585, 1997.

[158] T. Waschkies, R. Oberacker, and M. J. Hoffmann. Investigation of structure formation during freeze-casting from very slow to very fast solidification velocities. *Acta Materialia*, 59(13):5135–5145, 2011. ISSN 13596454. doi: 10.1016/j.actamat.2011.04.046. URL https://doi.org/10.1016/j.actamat.2011.04.046.

[159] Sylvain Deville, Eduardo Saiz, and Antoni P. Tomsia. Ice-templated porous alumina structures. *Acta Materialia*, 55(6):1965–1974, 2007. ISSN 13596454. doi: 10.1016/j.actamat.2006.11.003. URL https://doi.org/10.1016/j.actamat.2006.11.003.

[160] Sylvain Deville. Freeze-casting of porous ceramics: A review of current achievements and issues. *Advanced Engineering Materials*, 10(3):155–169, 2008. ISSN 14381656. doi: 10.1002/adem.200700270. URL https://doi.org/10.1002/adem.200700270.

[161] Stefan Flauder, Uwe Gbureck, and Frank A. Müller. Structure and mechanical properties of β-TCP scaffolds prepared by ice-templating with preset ice front velocities. *Acta Biomaterialia*, 10(12):5148–5155, 2014. ISSN 18787568. doi: 10.1016/j.actbio.2014.08.020. URL https://doi.org/10.1016/j.actbio.2014.08.020.

[162] F. Parhami, R. M. McMeeking, A.C.F. Cocks, and Z. Suo. A model for the sintering and coarsening of rows of spherical particles. *Mechanics of Materials*, 31:43–61, 1999.

[163] Rowland M Cannon and W. Craig Carter. Interplay of Sintering Microstructures, Driving Forces, and Mass Transport Mechanisms. *Journal of the American Ceramic Society*, 72(8):1550–1555, 1989.

[164] W Villanueva, K Grönhagen, G Amberg, and J Ågren. Multicomponent and multiphase simulation of liquid-phase sintering. *Computational Materials Science*, 47 (2):512–520, 2009. ISSN 0927-0256. doi: 10.1016/j.commatsci.2009.09.018. URL https://doi.org/10.1016/j.commatsci.2009.09.018.

[165] Qingcheng Yang, Arkadz Kirshtein, Yanzhou Ji, Chun Liu, Jie Shen, and Long-Qing Chen. A thermodynamically consistent phase-field model for viscous sintering. *Journal of the American Ceramic Society*, 102(2):674–685, 2019. doi: 10.1111/jace.16021. URL https://doi.org/10.1111/jace.16021.

[166] J. Hötzer, V. Rehn, W. Rheinheimer, M. Hoffmann, and B. Nestler. Phase-field study of pore-grain boundary interaction. *Journal of the Ceramic Society of Japan*, 124(4):329–339, 2016. doi: 10.2109/jcersj2.15266. URL https://doi.org/10.2109/jcersj2.15266.

[167] Chaitanya Joshi, T.A. Abinandanan, Rajdip Mukherjee, and Abhik Choudhury. Destabilisation of nanoporous membranes through gb grooving and grain growth. *Computational Materials Science*, 139:75–83, 2017. ISSN 0927-0256. doi: 10.1016j.commatsci.2017.07.026. URL https://doi.org/10.1016/j.commatsci.2017.07.026.

[168] Creative Commons. Cc-by 4.0 deed. URL https://creativecommons.org/licenses/by/4.0/.

[169] Pengtao Yue, Chunfeng Zhou, and James J Feng. Spontaneous shrinkage of drops and mass conservation in phase-field simulations. *Journal of Computational Physics*, 223:1–9, 2007. doi: 10.1016/j.jcp.2006.11.020. URL https://doi.org/10.1016/j.jcp.2006.11.020.

[170] A Suzuki and Y Mishin. Atomic mechanisms of grain boundary diffusion : Low versus high temperatures. *Journal of Materials Science*, 40:3155–3161, 2005.

[171] Daniel B. Butrymowicz, John R. Manning, and Michael E. Read. Diffusion in Copper and Copper Alloys. Part I. Volume and Surface Self-Diffusion in Copper. *Journal of Physical and Chemical Reference Data*, 2(3):643–656, July 1973. ISSN 0047-2689, 1529-7845. doi: 10.1063/1.3253129. URL https://doi.org/10.1063/1.3253129.

[172] Marco Seiz, Henrik Hierl, and Britta Nestler. Supplementary Material to "An improved grand- potential phase-field model of solid-state sintering for many particles", March 2023. URL https://doi.org/10.5281/zenodo.7755462. accessed October 2023.

[173] Ole Tange. Gnu parallel 20221222 ('chatgpt'), December 2022. URL https://doi.org/10.5281/zenodo.7465517. GNU Parallel is a general parallelizer to run multiple serial command line programs in parallel without changing them.

[174] A. P. Thompson, H. M. Aktulga, R. Berger, D. S. Bolintineanu, W. M. Brown, P. S. Crozier, P. J. in 't Veld, A. Kohlmeyer, S. G. Moore, T. D. Nguyen, R. Shan, M. J. Stevens, J. Tranchida, C. Trott, and S. J. Plimpton. LAMMPS - a flexible simulation tool for particle-based materials modeling at the atomic, meso, and continuum scales. *Comp. Phys. Comm.*, 271:108171, 2022. doi: 10.1016/j.cpc.2021.108171. URL https://doi.org/10.1016/j.cpc.2021.108171.

[175] T Hawa and M R Zachariah. Development of a phenomenological scaling law for fractal aggregate sintering from molecular dynamics simulation. *Journal of Aerosol Science*, 38(8):793–806, 2007. doi: 10.1016/j.jaerosci.2007.05.008. URL https://doi.org/10.1016/j.jaerosci.2007.05.008.

[176] T Hawa and M R Zachariah. Molecular dynamics simulation and continuum modeling of straight-chain aggregate sintering: Development of a phenomenological scaling law. *Physical Review B - Condensed Matter and Materials Physics*, 76:054109, 2007. doi: 10.1103/PhysRevB.76.054109. URL https://doi.org/10.1103/PhysRevB.76.054109.

[177] Bingqing Cheng and Alfonso H W Ngan. The sintering and densification behaviour of many copper nanoparticles : A molecular dynamics study. *Computational Materials Science*, 74:1–11, 2013. ISSN 0927-0256. doi: 10.1016/j.commatsci.2013.03.014. URL https://doi.org/10.1016/j.commatsci.2013.03.014. Publisher: Elsevier B.V.

[178] Lifeng Ding, Ruslan L Davidchack, and Jingzhe Pan. A molecular dynamics study of sintering between nanoparticles. *Computational Materials Science*, 45(2):247–256, 2009. ISSN 0927-0256. doi: 10.1016/j.commatsci.2008.09.021. URL https://doi.org/10.1016/j.commatsci.2008.09.021. Publisher: Elsevier B.V.

[179] Aidan P Thompson, H Metin Aktulga, Richard Berger, Dan S Bolintineanu, W Michael Brown, Paul S Crozier, J Pieter, Axel Kohlmeyer, Stan G Moore, Trung Dac, Ray Shan, Mark J Stevens, Julien Tranchida, Christian Trott, and Steven J Plimpton. LAMMPS - a flexible simulation tool for particle-based materials modeling at the atomic , meso , and continuum scales. *Computer Physics Communications*, 271, 2022. ISSN 0010-4655. doi: 10.1016/j.cpc.2021.108171. URL https://doi.org/10.1016/j.cpc.2021.108171. Publisher: Elsevier B.V.

[180] S. M. Foiles, M. I. Baskes, and M. S. Daw. Embedded-atom-method functions for the fcc metals cu, ag, au, ni, pd, pt, and their alloys. *Phys. Rev. B*, 33:7983–7991,

Jun 1986. doi: 10.1103/PhysRevB.33.7983. URL https://doi.org/10.1103/PhysRevB.33.7983.

[181] Alexander Stukowski. Visualization and analysis of atomistic simulation data with OVITO-the Open Visualization Tool. *MODELLING AND SIMULATION IN MATERIALS SCIENCE AND ENGINEERING*, 18(1), JAN 2010. ISSN 0965-0393. doi: 10.1088/0965-0393/18/1/015012. URL https://doi.org/10.1088/0965-0393/18/1/015012.

[182] J. D. Hunter. Matplotlib: A 2d graphics environment. *Computing in Science & Engineering*, 9(3):90–95, 2007. doi: 10.1109/MCSE.2007.55. URL https://doi.org/10.1109/MCSE.2007.55.

[183] Peter Mahler Larsen, Søren Schmidt, and Jakob Schiøtz. Robust structural identification via polyhedral template matching. *Modelling and Simulation in Materials Science and Engineering*, 24(5):055007, may 2016. doi: 10.1088/0965-0393/24/5/055007. URL https://doi.org/10.1088/0965-0393/24/5/055007.

[184] R.T. DeHoff. A Cell Model for Microstructural Evolution during Sintering. In *Materials Science Research*, pages 23–34. Springer US, Boston, MA, 1984. doi: 10.1007/978-1-4613-2761-5_2. URL https://doi.org/10.1007/978-1-4613-2761-5_2.

[185] R.T. DeHoff. Stereological theory of sintering. In *Science of Sintering*, pages 55–71. Springer US, Boston, MA, 1989. doi: 10.1007/978-1-4899-0933-6_3. URL https://doi.org/10.1007/978-1-4899-0933-6_3.

[186] Andrew Lawson and Hassel Ledbetter. Coupled temperature dependences of volume and compressibility. *Philosophical Magazine - PHILOS MAG*, 91:1425–1440, 04 2011. doi: 10.1080/14786435.2010.537702. URL https://doi.org/10.1080/14786435.2010.537702.

[187] J. Hötzer, A. Reiter, H. Hierl, P. Steinmetz, M. Selzer, and Britta Nestler. The parallel multi-physics phase-field framework pace3d. *Journal of Computational Science*, 26:1 – 12, 2018. ISSN 1877-7503. doi: 10.1016j.jocs.2018.02.011. URL https://doi.org/10.1016/j.jocs.2018.02.011.

[188] Blas Pedro Uberuaga, Louis J Vernon, Enrique Martinez, and Arthur F Voter. The relationship between grain boundary structure, defect mobility, and grain boundary sink efficiency. *Scientific Reports*, 5:9095, 2015. doi: 10.1038/srep09095. URL https://doi.org/10.1038/srep09095.

[189] Stephen Boyd, Neal Parikh, Eric Chu, Borja Peleato, and Jonathan Eckstein. Distributed Optimization and Statistical Learning via the Alternating Direction Method of Multipliers. *Foundations and Trends® in Machine Learning*, 3(1):1–122, 2011. ISSN 1935-8237, 1935-8245. doi: 10.1561/2200000016. URL https://doi.org/10.1561/2200000016.

[190] Hao Ji and Yaohang Li. Block conjugate gradient algorithms for least squares problems. *Journal of Computational and Applied Mathematics*, 317:203–217, 2017. ISSN 0377-0427. doi: 10.1016j.cam.2016.11.031. URL https://doi.org/10.1016/j.cam.2016.11.031.

[191] Christopher C. Paige and Michael A. Saunders. Lsqr: An algorithm for sparse linear equations and sparse least squares. *ACM Trans. Math. Softw.*, 8(1):43–71, mar 1982. ISSN 0098-3500. doi: 10.1145/355984.355989. URL https://doi.org/10.1145/355984.355989.

[192] Amy Henderson Squillacote, James Ahrens, Charles Law, Berk Geveci, Kenneth Moreland, and Brad King. *The paraview guide*, volume 366. Kitware Clifton Park, NY, 2007.

[193] Marco Seiz, Henrik Hierl, and Britta Nestler. Supplementary Material to "Unravelling densification during sintering by multiscale modelling of grain motion", May 2023. URL https://doi.org/10.5281/zenodo.8215289.

[194] M. P. Harmer and R. J. Brook. The effect of MgO additions on the kinetics of hot pressing in Al2O3. *Journal of Materials Science*, 15(12):3017–3024, December 1980. ISSN 0022-2461, 1573-4803. doi: 10.1007/BF00550370. URL https://doi.org/10.1007/BF00550370.

[195] R. L. Coble. A Model for Boundary Diffusion Controlled Creep in Polycrystalline Materials. *Journal of Applied Physics*, 34(6):1679–1682, June 1963. ISSN 0021-8979, 1089-7550. doi: 10.1063/1.1702656. URL https://doi.org/10.1063/1.1702656.

[196] Marco Seiz, Henrik Hierl, Britta Nestler, and Wolfgang Rheinheimer. Supplementary Material to "Revealing process and material parameter effects on densification via phase-field studies", August 2023. URL https://doi.org/10.5281/zenodo.8263533. accessed October 2023.

[197] S. Schleef, H. Löwe, and M. Schneebeli. Influence of stress, temperature and crystal morphology on isothermal densification and specific surface area decrease of new snow. *The Cryosphere*, 8(5):1825–1838, October 2014. ISSN 1994-0424. doi: 10.5194/tc-8-1825-2014. URL https://doi.org/10.5194/tc-8-1825-2014.

[198] Wendong Luo and Jingzhe Pan. Effects of Surface Diffusion and Heating Rate on First-Stage Sintering That Densifies by Grain-Boundary Diffusion. *Journal of the American Ceramic Society*, 98(11):3483–3489, November 2015. ISSN 00027820. doi: 10.1111/jace.13662. URL https://doi.org/10.1111/jace.13662.

[199] J P MacSleyne, J P Simmons, and M De Graef. On the use of moment invariants for the automated analysis of 3D particle shapes. *Modelling and Simulation in Materials Science and Engineering*, 16(4):045008, June 2008. ISSN 0965-0393, 1361-651X. doi: 10.1088/0965-0393/16/4/045008. URL https://doi.org/10.1088/0965-0393/16/4/045008.

[200] A. Trenkle, M. Syha, W. Rheinheimer, P.G. Callahan, L. Nguyen, W. Ludwig, W. Lenthe, M. P. Echlin, T. M. Pollock, D. Weygand, M. De Graef, M. J. Hoffmann, and P. Gumbsch. Nondestructive evaluation of 3D microstructure evolution in strontium titanate. *Journal of Applied Crystallography*, 53(2):349–359, April 2020. ISSN 1600-5767. doi: 10.1107/S160057672000093X. URL https://doi.org/10.1107/S160057672000093X.

[201] Marcin Novotni and Reinhard Klein. Shape retrieval using 3d zernike descriptors. *Computer-Aided Design*, 36(11):1047–1062, 2004. ISSN 0010-4485. doi: 10.1016j.cad.2004.01.005. URL https://doi.org/10.1016/j.cad.2004.01.005. Solid Modeling Theory and Applications.

[202] Marco Seiz and Britta Nestler. Modelling and simulation of the freeze casting process with the phase-field method. *Computational Materials Science*, 193:110410, June 2021. ISSN 09270256. doi: 10.1016/j.commatsci.2021.110410. URL https://doi.org/10.1016/j.commatsci.2021.110410.

[203] S. Farhangdoust, A. Zamanian, M. Yasaei, and M. Khorami. The effect of processing parameters and solid concentration on the mechanical and microstructural properties of freeze-casted macroporous hydroxyapatite scaffolds. *Materials Science and Engineering: C*, 33(1):453–460, January 2013. ISSN 09284931. doi: 10.1016/j.msec.2012.09.013. URL https://doi.org/10.1016/j.msec.2012.09.013.

[204] Aaron Lichtner, Denis Roussel, Daniel Röhrens, David Jauffres, Julie Villanova, Christophe L. Martin, and Rajendra K. Bordia. Anisotropic sintering behavior of freeze-cast ceramics by optical dilatometry and discrete-element simulations. *Acta Materialia*, 155:343–349, 2018. ISSN 1359-6454. doi: 10.1016j.actamat.2018.06.001. URL https://doi.org/10.1016/j.actamat.2018.06.001.

[205] Eugene A. Olevsky. Theory of sintering: from discrete to continuum. *Materials Science and Engineering: R: Reports*, 23(2):41–100, June 1998. ISSN 0927796X.

doi: 10.1016/S0927-796X(98)00009-6. URL https://doi.org/10.1016/S0927-796X(98)00009-6.

[206] Olivier Sudre and Fred F. Lange. The Effect of Inclusions on Densification; III, The Desintering Phenomenon. *Journal of the American Ceramic Society*, 75(12): 3241–3251, December 1992. ISSN 0002-7820, 1551-2916. doi: 10.1111/j.1151-2916.1992.tb04417.x. URL https://doi.org/10.1111/j.1151-2916.1992.tb04417.x.

[207] T. Wu, B. Rosić, L. De Lorenzis, and H. G. Matthies. Parameter identification for phase-field modeling of fracture: a bayesian approach with sampling-free update. *Computational Mechanics*, 67(2):435–453, Feb 2021. ISSN 1432-0924. doi: 10.1007/s00466-020-01942-x. URL https://doi.org/10.1007/s00466-020-01942-x.